Determination of the controlling parameters of agglomeration of Mn dusts in order to improve process predictability

John-Lee Dubos

université PARIS-SACLAY

Determination of the controlling parameters of agglomeration of Mn dusts in order to improve process predictability.

Thèse de doctorat de l'université Paris-Saclay

École doctorale n°579 Sciences mécaniques et énergétiques, matériaux et géosciences (SMEMAG)
Spécialité de doctorat: Science des matériaux
Unité de recherche : Université Paris-Saclay, CNRS, GEOPS, 91405, Orsay, France
Référent : Faculté des sciences d'Orsay

Thèse présentée et soutenue en visioconférence, le 30/11/2020, par

John-Lee DUBOS

Composition du Jury

Olivier HUBERT Professeur, École Normale Supérieure Paris-Saclay (LMT)	Président
Jean COLOMBANI Professeur, Université Claude Bernard Lyon 1 (ILM)	Rapporteur & Examinateur
Eric SERRIS Ingénieur de recherche, École des mines de Saint-Étienne (PMMG)	Rapporteur & Examinateur
Beate ORBERGER Maîtresse de conférence (HC-HDR), Université Paris-Saclay (GEOPS)	Directrice de thèse
Jean-Michel MILAZZO Ingénieur Expert pyrometallurgie, Eramet IDEAS	Co-Directeur de thèse
Simon BLANCHER Chef du département Geometallurgie, Eramet IDEAS	Co-Directeur de thèse

Thèse de doctorat
NNT : 2020UPASJ009

Acknowledgements

As most things nowadays, this Ph.D. would not have been possible without fundings. I would hence like to thank financial support of the KIC-EIT RawMaterials through the Go-4-0 project N°15046, and that of the ANRT through the CIFRE N°2017/0326.

Additionally, this work could not have been achieved on my own. Thus, I would like to thank my thesis supervisors, **Beate Orberger**, **Jean-Michel Milazzo** and **Simon Blancher**, without whom this project never have been possible. They helped me at all the steps of the way, from the methodology to the redaction, guiding me to always improve my ideas.

I would also like to thank the members of my jury, **Olivier Hubert, Jean Colombani** and **Éric Serris**, who took upon their time to examine and judge my work. Your feedbacks were much appreciated, and the discussion we had after the presentation were very enlightening.

My thanks also goes to the people at Eramet who gave me the opportunity to perform this Ph.D. thesis, namely **Laurent J.**, **Yves**, **Mireille**, **Vincent P.** and **Caroline**.

It is important to thank the people who helped me with the practical aspect of my thesis. **Sebastien, Odile, Christophe, Marion, Yann H., Laurent D., Marie-France, Vincent, Quentin**, thank you for showing me how to properly prepare and analyze my samples. **Laurent K.**, I would never have been able to perform any of my agglomeration experiments if you did not show me the ropes first, so I would like to thank you for that. **Christian** and **Cédric**, we did not work very long together, but it was very informative and interesting. I hope the gas analysis tool will be properly finished someday.

Of course, my supervisors were not the only person to help me. **Julien**, you were a critical help, both in terms of agglomeration and "scientific behavior". **Thomas**, I will always remember of our Qemscan sessions and endless talks. In both of you, I found mentors and friends. **Johannes Lützenkirchen** and **Maksym Dosta**, you were also key players in this project, helping me understand scientific fields I knew nothing of. I wish I could have had time to go further in both those areas and thank you once again for those invaluable experiences. Maybe we will be able to work together again in the future?

But this thesis, spent mostly at **Eramet**, would not have been the same without all my wonderful colleagues from the pyrometallurgical department. **Cedrik**, you've always been supporting of me no matter how strange I could be, and for that I can never be thankful enough. Let's hunt Monsters again sometimes. **Laure**, you were the first ever to remember to call me for lunch. **Noémie**, you've always been a little thing full of energy who puts a smile on everyone's face. I could write another thesis just talking about all the escape games, boardgames and small chat and exchanges I had with you **Piwies**, Keep being yourselves, fiery, proud and kind. **Alexy**, you helped me a great deal with handling Python, and thanks for that. However, try to keep your shirt on a bit more… **Axel, Matthieu**, **Thibault**, you arrived much later, but I enjoyed our existential talks and cinematographic exchanges very much. Let's do that again around a pool table someday soon! **Bertil**, the eternal intern, keep working hard and smile harder. **Nicole**, we did not share an office for very long, but it was a pleasure, nonetheless.

And of course, all the technicians of this wonderful department, **Michel**, **Gao**, **Sylvain**, **Nicolas Bondouy, Nicolas Louet**, **Olivier**. I had an amazing time with all of you. I will especially remember those shifts during the Go-4-0 pilot where we could cast metal together. It was an incredible experience, and I'll cherish it forever. You are an unruly, grumpy bunch, but I love you guys anyway and I'll teach you how to actually play boardgames someday. **Odile**, you may not

have been in this department, but it's all the same to me: after all, you're just as grumpy as them, and just as kind.

Christophe, **Valère**, **Romain** we may not have shared the same department, but I'll sing with you until dawn again, whenever you're ready. You have always made me feel welcome, and I hope I can repay you your kindness one of these days.

David, how incredibly funny was it to see you arrive after meeting you in Poland a few months earlier. It was a pleasure to be able to climb along with you. Keep at it, and let's meet on a mountaintop someday. **Marc** keep working on those digs and smashes, and let's play again together. I really enjoyed playing volleyball with you. And thank you **Kateryna** for creating those opportunities, as well as being part of them, with your infectious smile.

Thanh, we did not work together as much as we should have. But you were undeniably essential in this thesis, showing me how to properly handle my data with Python, how to represent and understand them. And for that, thank you.

Thank you, **Anne-Lise**, for your help in navigating the administrative swamps that I struggled with.

But Eramet was only one side of the people I had the pleasure to meet, for I had the pleasure of belonging to the **GEOPS** laboratory. Although I did not spend as much time with you, I thoroughly enjoyed all of it; starting with the "Old Ones", already present when I started. **Floumiche** of course, the Tarot Queen, who invited me to play straight away. Your mellow, easy-to-live personality really helped me into the GEOPS community. It took some time to actually know you, but it was worth it. **Maxime**, always taunting Floumiche and laughing, thank you for being so easy-going. I feel like entering you guys office was like playing the lottery, never knowing what kind of weird yet hilarious shenanigans you would be up to. **Quentin** and **Ludo**, already gone yet always there, amongst other things to play tarot. **Maxence**, with your weird knowledge and facts which are interesting most of the time. Being around you crazy bunch always made me feel a bit saner. And **Claire**, **Fanny**, **Mustafa, Axel** don't think a single second that you're much better than those people. **Inès**, you may have been the only one able to stabilize them, and your departure for sunnier places made it so much more difficult. And **Johanna**, we may never have worked together, but I am grateful I met you anyway.

And then the younger ones, whom I saw grow and bloom into fine scientists. **Margaux**, your calm voice always able to make people move along and do what they were supposed to. You teamed-up perfectly with **Louise** when it came to organize everything. You two truly were the mothers of this batch, and it may not always have been easy. But anyway, I'm happy I could meet you, for you always had the others concerns in mind. **Maxime** and **Orianne**, often quiet in a corner. We may not have talked much, but I enjoyed doing so on the occasion. It was restful, especially compared to all the other specimens. On the other side of the spectrum, there's you, **Hadrien**. It is not always easy talking with you, but when you stop running from one sport court to another or making jokes, it is a pleasure to do so. I hope we may play again together in a near future.

Alexys, always so chill I sometimes wanted to check for your pulse. I'll keep climbing so that maybe someday we can climb some interesting ways together, rather than just watch you from the ground. **Lara**, with your amazing stories about Alaska and Siberia. You proved once and for all that being tall is definitely not all it takes to be a good climber. I'll catch up to you, too.

Maher, I don't really know how you fit in all that, old man. It was truly mind-blowing meeting you again so many years after the bachelor. Your calm and wits are refreshing, and I'm glad for the time I could spend with you.

And **Sir Robert Polochon**, your class and nobility is only matched by those represented on the walls of your house.

But there are also those with whom I never actually worked, and yet supported me all throughout those three years, and far longer than that. **Venceslas**, always there to help me change my mind when I need to. You helped me through thick and thins, and for that I won't ever thank you enough, Brother. **Tan**, with your chill lookout on life, never bothered and always ready to have a good time. **Yohan**, you never talk much, but you are always paying attention. I truly appreciate being able to count on you if I need to. **Hai**, always optimizing everything. Thank you for preventing me many headaches. **Bénédicte**, always here with a smile, ready to motivate everyone. **Jordan, Jonathan, Séb,** always quick with a joke and ready to play.

Hossayn and **Émilie**, you may have moved in a faraway land, but that doesn't mean I forgot you. You are here when I truly need it and when I need advice, and I am all the better for it.

And last but not least, I would like to thank all of my **Family**. They bore with my many flaws, when I felt overwhelmed, or did not take the time to communicate with them, and they found the strength to always forgive me anyway. We do not choose our family, but I am very glad for the one I have.

There are of course many other people I did not mention, because I am a forgetful person, and because another thesis wouldn't be enough to write about everyone I met. I am often being told than I am a lucky person, for many reasons. But the reason I consider myself luckiest is the chance to have so many wonderful, amazing persons in my life. I found that at every paragraph I wrote, I wanted to add "let's see each other again" because I want to keep in touch with everyone of you.

I am grateful for everything you all bring me, and I love each and every one of you.

Synthèse

Le travail effectué au cours de cette thèse a été rédigé en anglais. Conformément à la règlementation en vigueur au sein de l'Université Paris Saclay et de l'école doctorale SMEMaG, le lecteur francophone qui le souhaite trouvera ci-dessous une courte synthèse de mon travail, rédigée en français.

Les industries minière et métallurgique produisent chaque année d'important volumes de matériaux fins (<3 mm) aux diverses étapes de leurs procédés. Ces boues et poussières posent des problèmes économiques et environnementaux, en plus de perturber la bonne marche des procédés de valorisation. Afin de circonvenir à ces problèmes, la meilleure solution est l'agglomération. Afin de réduire les impacts environnementaux des procédés, une agglomération à froid et sans liant est préférable.

Diverses méthodes d'agglomération existent sur le marché, produisant graduellement une densification des matériaux, une déformation de ses particules et la fracture de ces dernières. Les méthodes des basses pressions telles que le bouletage densifient le matériau, mais requièrent beaucoup de liant, d'humidité et un traitement thermique afin de donner des propriétés mécaniques satisfaisantes aux agglomérés. L'accroissement de la pression réduit le besoin en liant et en humidité des matériaux, mais réduit également le tonnage annuel que peut délivrer la méthode. La méthode de compression uniaxiale délivre la plus grande pression disponible sur le marché, et permet d'obtenir des agglomérés satisfaisant avec une utilisation de liant faible à nulle. Toutefois, ces méthodes sont susceptibles aux variations des éléments entrants, et leur calibration est ardu. Il est donc difficile de prédire leurs résultats.

Au travers de ces différentes méthodes, les forces principales maintenant les agglomérés varient. Toutefois, l'exclusion de l'utilisation des liants ôte la possibilité de créer des ponts solides et des réactions chimiques, et limite les forces principales intervenant durant l'agglomération aux forces interparticulaires : les forces électrostatiques, dont les force de Van der Waals, et les ponts capillaires en présence d'humidité. L'objectif de ce travail est de lier les paramètres de ces forces avec les caractéristiques des matériaux agglomérés afin d'améliorer la prédictibilité de l'agglomération.

Pour ce faire, un échantillonnage a été réalisé sur l'ensemble de la chaîne de production de ferromanganèse de l'usine d'Eramet Norway Sauda, incluant : (1) des fines de minerais (Minerai de COMILOG, Moanda, et Asman et Gloria, ASSMANG, Afrique du Sud), (2) des poussières et boues de four à arc submergé, (3) des poussières de raffinage ainsi que (4) des poussières de métal. Les propriétés chimiques, physiques et morphologiques des matériaux ont été caractérisés de façon étendues grâce aux méthodes suivantes : Fluorescence en rayons X (XRF), Combustion, Perte au feu (PAF), Diffraction des rayons X (DRX), Microscopie Electronique à Balayage (MEB), QEMSCAN, granulométrie laser (CILAS) et optique (QICPIC), Mesure de la surface spécifique par la méthode Brünauer-Emmett-Taylor (BET), Capacité d'Echange Cationique (CEC) et le potentiel zeta.

Les résultats de ces méthodes ont été utilisés en conjonction avec des considérations théoriques et empiriques afin de prédire qualitativement l'agglomérabilité des différents matériaux. Des hypothèses ont été formulées à partir d'une comparaison avec des liants commerciaux, tels que la bentonite, et des tests préliminaires d'agglomération :

- Les principaux paramètres affectant l'agglomérabilité d'un matériau sont : sa teneur en minéraux à feuillet, sa distribution granulométrique, la dureté et la forme de ses particules ainsi que leur charge de surface.
- La présence de minéraux avec une structure en feuillet augmente la facilité d'un matériau à produire des agglomérés résistants.
- Il en va de même avec une distribution granulométrique plus importante, la présence de minéraux à faible dureté avec des particules de forme complexes.
- Les charges de surfaces peuvent être bénéfiques si les différentes particules possèdent des charges de surface opposées, ou délétères si elles sont équivalentes.
- Les fines de minerais de Moanda possèdent le meilleur potentiel d'agglomération grâce à ses particules dures enrobées de lithiophorite, un minéral avec une structure en feuillet et une faible dureté.
- Il pourrait être possible d'utiliser les fines de minerais comme une matrice pour recycler les autres produits avec une agglomérabilité inférieure, tel que la hausmannite, afin de les valoriser sans recourir à un liant.

Afin de tester ces hypothèses, des tests de compaction uniaxiale ont été réalisés sur quatre matériaux : (1) la bentonite, un liant commercial principalement composé de montmorillonite, une argile gonflante, (2) la kaolinite, une argile non gonflante, (3) un concentré de minerai enrichi en pyrolusite et (4) de la hausmannite. Les conditions de pression (0-450 MPa), la teneur en eau (0-10 wt. %), et le pH (4, 7, 11) furent variés afin d'étudier leur impact sur les résultats de l'agglomération. Les matériaux furent testés séparément, mais également mélangés deux à deux.

Les résultats montrent que l'accroissement de la pression est bénéfique pour les oxides, mais que les minéraux à feuillets voient leur performance se dégrader au-delà de 250 MPa à cause de l'intensification du mécanisme de rebond élastique. L'ajout d'humidité jusqu'à 4 wt. % améliore la tablétabilité des matériaux, accroissant la dureté des tablettes et réduisant leur production de fines et leur reprise élastique. Au-delà d'environ 6 wt. % (la valeur exacte dépendant du matériau), la résistance diamétrale décroît de façon importante. La présence de matériaux à structure en feuillets (argiles, lithiophorite) est un facteur crucial pour une agglomérabilité importante des échantillons. Ces tests ont également démontré que les fines de minerais enrichies s'agglomèrent seules de façon satisfaisante, sans utilisation de liant. Leur tenue est assez forte pour permettre de les mélanger avec les poussières de hausmannite pour recycler ces dernières sans liant additionnel. Les résultats optimaux de ces mélanges présentant le meilleur compromis de taux de recyclage et de dureté est obtenu pour un mélange minerai enrichi/hausmannite de 80/20 %, avec 4 wt. % d'eau ajoutée.

Suite à ces résultats, une tentative de reproduction via une modélisation par éléments discrets a été entreprise en utilisant le minerai enrichi comme matériau de comparaison. Les paramètres mécaniques du matériel, indisponibles dans la littérature, ont été estimés par comparaison à partir du comportement mécanique des autres matériaux lors de l'agglomération. L'étude portait principalement sur la variation du module d'Young ainsi que la taille et la force des liaisons entre les particules. Bien qu'il ne fût pas possible de reproduire les conditions expérimentales à la fois d'un point dureté des agglomérés et style de cassure, l'impact de chacun des paramètres a pu être étudié. Augmenter le module d'Young diminue la résistance diamétrale des agglomérés, mais tend à créer des cassures à la périphérie des tablettes, tandis que sa diminution favorise le bris selon une fracture traversant le diamètre. Une taille de liaison importante augmente la résistance diamétrale de l'agglomeré, mais également sa rigidité. Elle tend ainsi à favoriser une fracture diamétrale des tablettes. Une force des liaisons plus importantes permet d'exprimer les effets des variations du

module d'Young et de la taille des liens. En effet, si les liens sont trop faibles, ils se briseront à faible pression et l'on observera un émiettage graduel de la tablette.

Afin d'être capable de reproduire les résultats empiriques par la modélisation, il faudrait effectuer des tests de caractérisations supplémentaires pour déterminer ses propriétés mécaniques de façon plus précises. Il faudrait également être capable de retranscrire les propriétés des liens dans les paramètres de la modélisation.

Contents

Foreword

This manuscript is entirely in English, except for the summary which is in both English and French. It is organized in 6 chapter, including 2 accepted scientific publications in Powder technology (Chapters 2 and 3). The supplementary materials and additional data used with these papers were shifted into the appendixes, along with the data generated during the agglomeration experiments and modelling tests. The proceedings and conference abstract produced during the course of this thesis are also presented in the appendixes. The references used are gathered at the end of the manuscript.

Chapitre 1 - Introduction

1. Toward a circular economy

Metals are essential to our daily lives, but its resources are limited. However, an increasing awareness at global and EU scale for resource sustainability is becoming a priority for humanity. The EU circular economy action plan aims at reducing the strain on the earth's resources by reducing the need for primary resource extraction and processing, which are responsible for about 50% of the total greenhouse gas emissions and more than 90 % of biodiversity loss and water stress (European Commission, 2020). This plan aims at increasing industrial cooperation to improve resource efficiency through recycling and innovative reuse of secondary resources (Fig. 1.1).

Fig. 1.1. Scheme for the raw materials in circular economy by the EU (eit.RawMaterials, n.d.)

At a global scale, the iron and steel sectors are the biggest metal industries with 2.8 billion metric tons of iron ores extracted each year and 1.8 billion metric tons of crude steel produced to supply global demands (U.S. Geological Survey, 2020). Most of the iron resources are extracted from Australia, Brazil, China and India. However, ore processing into steel takes place in China, EU, Russia and India (Fig. 1.2).

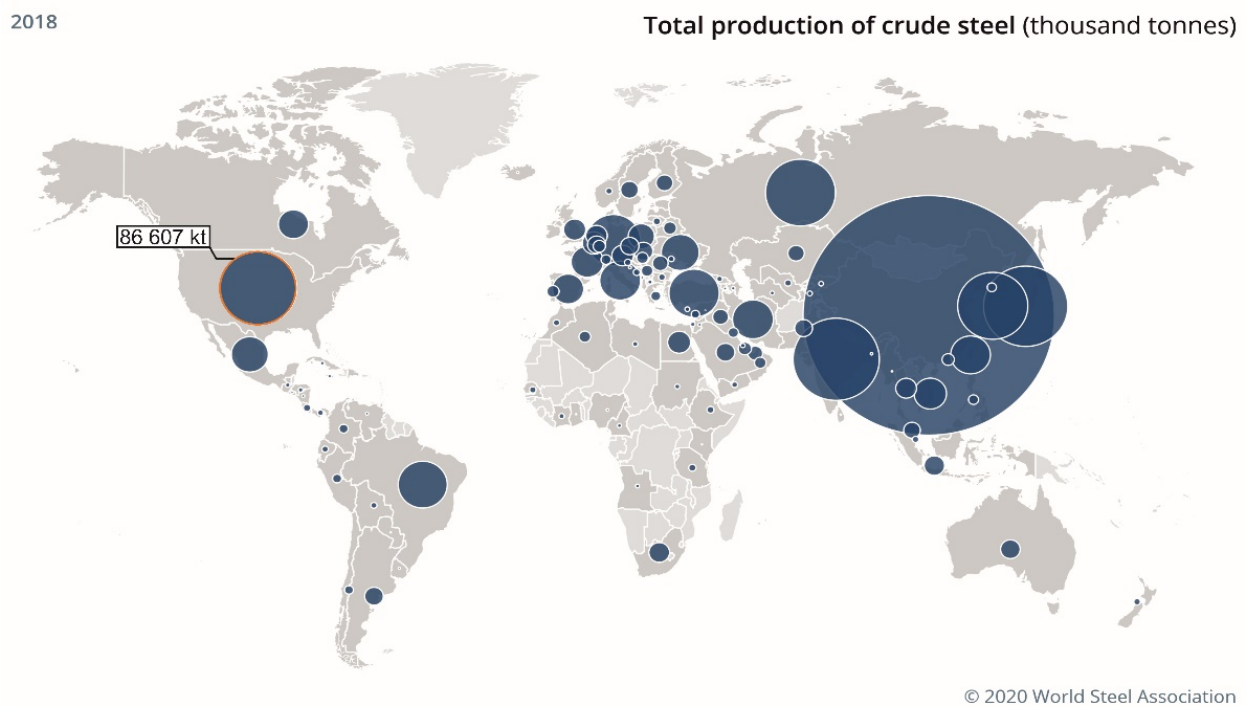

Fig. 1.2. Geographic repartition of crude steel production by country in 2018. The size of the circle is proportional to the amount of steel used. As an order of magnitude, USA steel production (86.607 million tons) was highlighted. The global crude steel production is around 1.816 billion tons (modified from Worldsteel, 2020).

EU produces 148 Mt of crude steel equivalent and consumes 189 Mt of it each year (Fig. 1.2, Fig. 1.3; Worldsteel, 2020). This industry is essential to the EU economy, both from its intrinsic value, and its link, as supplier, to major manufacturing sectors, such as automotive, aeronautic, construction and technological industries.

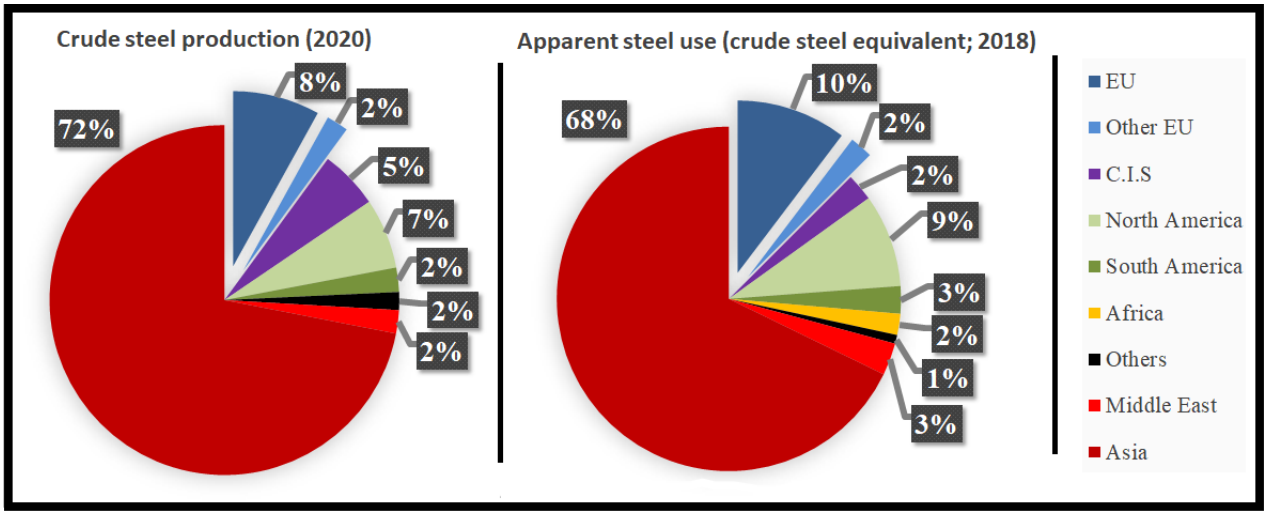

Fig. 1.3. Crude steel production in 2020 and Apparent steel use in 2018. EU amounts for 10 wt.% of the worldwide production and 12 wt.% of the worldwide consumption of steel. (Data from Worldsteel, 2020).

2. Manganese, essential for steel production

Manganese is a metal used as an additive in steel making to improve its hardenability and tensile strength. Manganese is an essential alloying element which deoxidizes the alloy while enhancing its mechanical strength and castability (Olsen et al., 2007). Therefore, the steel and alloy sector represents 90 % of the global manganese consumption, despite increasing demands for battery production (Roskill information services, 2019). About 65.4 million tons of ores of various grades have been extracted last year, mainly in South Africa, Australia and Gabon (USGS, MCS2020). This equals to 19 million tons of manganese metal extracted, a figure that has increased by about 30 % since 2006. Manganese processing takes place in China, India, Ukraine, Norway to produce a total amount of 24.1 million tons of SiMn and FeMn (Silicomanganese and Ferromanganese, respectively) alloys (IMnI, 2020).

During ore extraction and processing into alloys, wastes are generated at multiple steps. Those wastes take different forms, such as gangue minerals and slag, for the mining and metallurgical industries, respectively. Both industries also produce very fine (<3 mm) materials (Fig. 1.4). These granular materials are produced at each process step, from the ore extraction to the alloy refining including their handling. Each step's product has different properties, but all of them still contain metals, mostly manganese. Some of them, such as the refining dusts, even reach 70 wt.% manganese, compared to the ~50 wt.% manganese of the richest natural ores in Moanda, Gabon (Olsen et al., 2007).

Internal measurement performed at ERAMET plants in Norway estimates the production of fine-grained wastes at about 167 kg/t of alloy produced, for 1.35 t of CO_2. This is equivalent to 50,000 t of dusts and 30,000 t of sludges each year, amounting to ~16 wt.% of the FeMn production (Eramet Norway, 2018). Extended to the global scale and at the assumption that all processes produce an equivalent quantity of fines, the fine generations in the manganese pyrometallurgical industries can be estimated to 3.84 million tons per year. It is important to note that this number does not consider the dusts produced during mining and transport activities.

Due to their fine-grained nature, these particles can easily become airborne and pollute the surrounding of the metallurgical plants. In the proximity of foundries, manganese atmospheric concentrations have been found to rise to an annual average of 200–300 ng/m^3 and to over 500 ng/m^3 around SiMn and FeMn plants (Davis et al., 1994). The highest concentrations of airborne manganese in the working environment have been reported from manganese mining operations, with concentrations of up to 250 mg/m^3. Other industries with a high airborne manganese content are plants dedicated to ore-processing, dry-cell battery manufacturing and FeMn production. These numbers are 17-50 times higher than for areas remote from industries or other manganese resources, with manganese contents in ambient air ranging between 10 ng/m3-30 ng/m^3. It is also 1.3 to 5 times higher than the World Health Organization guidelines of 150 ng/m^3 (World Health Organization, 2000). Moreover, it has been found that these fine particles are hazardous to the human health when assimilated, especially at a neurological and respiratory level (Aschner and Aschner, 1991; Mergler et al., 1999).

Important efforts have been performed in order to prevent these airborne emissions and improve abating technologies to prevent these environmental and health issues (Kero et al., 2019). These fine dusts and sludge must be handled. Unlike coarser by-products such as gangue minerals and slags, they cannot be reused in that form in other industries, such as fillers for cements and roadworks. Classified as hazardous wastes due to their heavy metal contents, they must be disposed of properly. The common solution is landfilling, providing a risk of leakage of the landfill liners, and subsequent leaching of the heavy metal to the soil and aquifers.

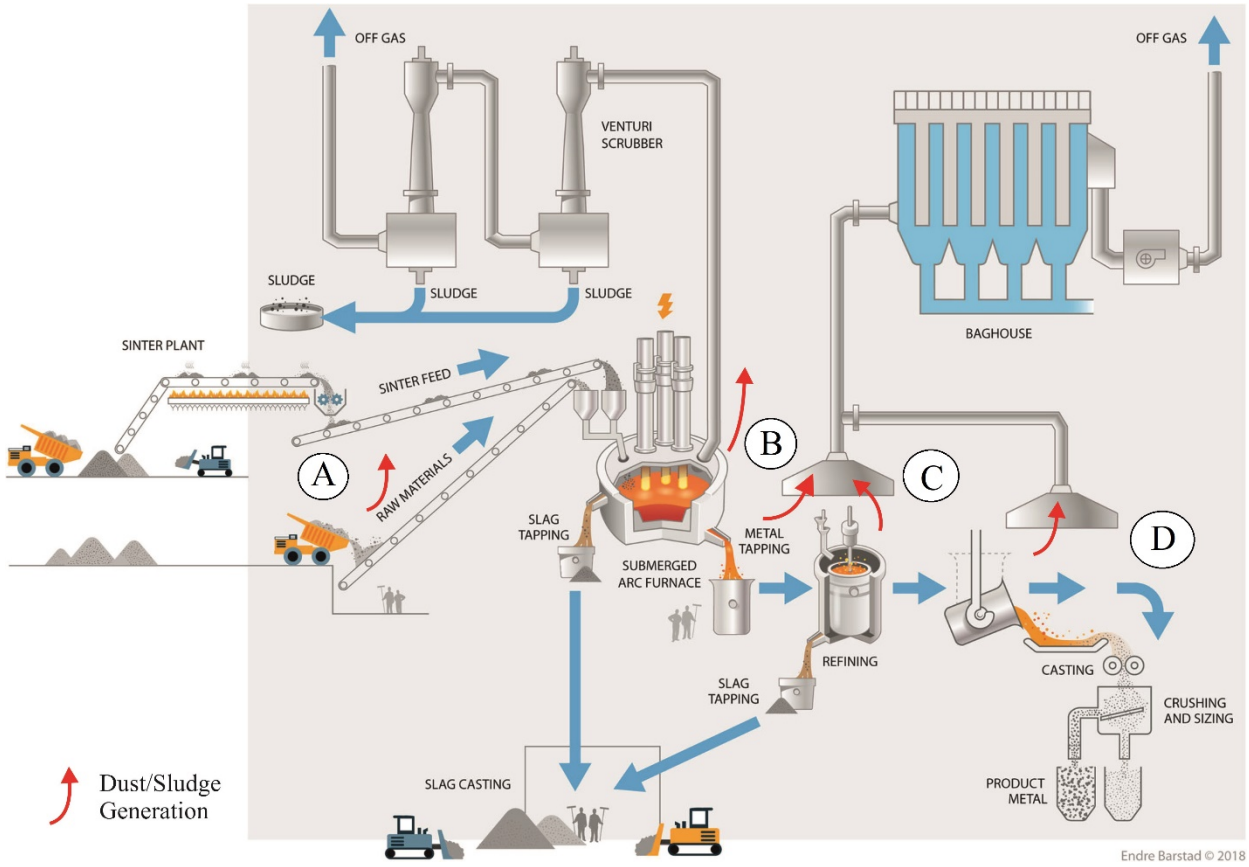

Fig. 1.4. Dust and sludge generation across a FeMn processing plant (Kero et al., 2019) with A) ore transport and handling, B) ore smelting, C) metal refining and D) metal casting.

Furthermore, landfilling and landfill management is expensive. Landfilling costs increased over the last years, and EU plans to keep using financial tools as a deterrent for landfill use and promote circular economy (European Commission, 2020).

Additionally, economic metals are landfilled, but can be valorized in relevant industries. An approximate estimation based on a production of 80,000 t/year (dust + sludges at Eramet Norway plants; Eramet Norway, 2018), an average manganese content of 40 wt.% of these waste materials gives 32 kt of manganese. The market price of the manganese is calculated on the basis of the Dry Metric Ton Unit (DMTU), which is the tonnage of manganese content calculated at 9 wt.% humidity. One DMTU Mn is equivalents to 10 kg of manganese and is valued around 2.8 $ per DMTU in the High Carbon Silicomanganese processing chain (as a rich slag equivalent), and around 4 $ per DMTU in the High Carbon Ferromanganese processing chain (as a rich ore equivalent). This represent a minimal shortfall of 90 k€ and 128 k€ respectively.

It hence appears logical to recycle those materials into the process chain from both economic and environmental point of view, as it is already widely performed in the iron ore industry (Moraes et al., 2018).

3. Challenges and solutions for recycling of metal waste fines

The fine grain-size (< 3 mm) of these materials hinders their direct recycling possibilities.

- If not moisturized, the <100 µm fines will be dispersed into the atmosphere.
- When handled, oscillations and vibrations (such as during transport by boat, lorry…) cause the granular materials to behave like liquids (Melhus and Aranson, 2012). This causes boats to capsize when transporting granular material.
- If the fines are reintroduced directly into the furnaces, they will block pathways of the gases across the burden, which are essential for the proper functioning of the process. This can lead to process instability or even furnace explosion due to pressure build-up or moisture-molten metal contact (Olsen et al., 2007).

Those fine materials must hence be reshaped to bigger grain sizes before being reintroduced in the furnace in order to preserve the porosity of the burden. This process, called agglomeration, is seeing a wide use in number of sectors such as pharmaceutical and food as well as mining and metallurgical industries (Pietsch, 2002). Agglomeration is a generic term and includes different methods to increase material granularity. In order to improve the resulting properties of the agglomerates, binders from organic and inorganic origins, or mixes of both, are often used (T. C. Eisele and Kawatra, 2003). Those binders are expensive and increase the amount of wastes such as slags produced during pyrometallurgical processes (Olsen et al., 2007). Reducing or avoiding binder use is hence recommended. However, according to the complexity of the materials and the various parameters influencing agglomeration, fundamental studies need to be performed.

Furthermore, different agglomeration methods are used according to the target materials. These methods can be adapted and fine-tuned when material properties are known.

Mining and metal industries use mainly pelletization, briquetting and high temperature sintering thanks to their ability to process high tonnage (Beloborodov et al., 2016; Pietsch, 2002; Zhu et al., 2014). For example, the estimated pelletizing capacity for the iron industry across the world amounts at about 480 million tons (Moraes et al., 2018). For manganese ore, after beneficiation, sintering is mainly used at the mine site (Olsen et al., 2007). Pelletizing usually requires a heat treatment or a storage time for the pellets to acquire adequate properties, while sintering is a heat-based process. Both processes require the use of binders (Pietsch, 2002).

However, all agglomeration processes used in mining and pyrometallurgical industries apply complex mechanisms, such as uniaxial compression, to heterogeneous, multiphase materials, which make fundamental studies more difficult. Due to the industrial requirement for productivity, most agglomeration studies performed are empirical, material specific, cost-expensive and time-consuming. The process is fine-tuned to the studied material, but not robust enough to deal with compositional changes of the materials which influence the agglomerate quality. Adjusting the process to the new material characteristics requires a new iteration of the agglomeration study.

Therefore, it is necessary to make a breakthrough towards a quantitative predictive approach**.**

In order to support the EU's Green Deal plan for an improved circular economy, EIT RawMaterial is funding R&D projects aiming at recycling industrial wastes into raw material. The KIC-EIT Go-4-0 project (2016-2020), aimed at reintroducing pyrometallurgical iron and manganese wastes into ferromanganese furnaces through agglomeration, while reducing environmental impact. This project was led by Eramet Ideas, operating plants at Eramet Norway and producing 10,000 t of dusts and sludge per year. Arcelor Mittal (France), producing more than 200,000 t of blast furnace sludges per year, participated with their experience from the iron ore sector. At present, these

wastes are landfilled. It represents an annual cost of 1 M€ for Eramet at 100 € /t of wastes, and 30 M€ for ArcelorMittal at 150 € /t of wastes.

Further participates in the Go-4-0 project were the CRM laboratory (Liège, Belgium) and EUROTAB (St Etienne, France) with their experience in industrial agglomeration, as well as CometTreatments (Charleroi, Belgium), producer of recycled carbon material to be used as a reductant.

The project performed agglomeration optimization trials using two methods: tableting, a new experience for the metallurgical sector, and briquetting. Moreover, various binders of inorganic (bentonite, Portland cement) or organic (Peridur, lignosulfonate) origins were used, along with various blends of fine materials. Go-4-0 also studied the behavior of agglomerates during thermal treatment for removal of metals impacting pyrometallurgical operation (K, Zn, Pb) and at high temperature to estimate the behavior of agglomerates when recycled into the furnace. The focus was set on cold agglomeration methods, as they are environmentally friendlier than sintering. However, these studies relied on experiments using an empirical approach, and the results would hence be specific to the materials used in the Go-4-0 project (Mn dusts and sludges, Fe sludges).

In order to study fundamental characteristics of the different materials under controlled agglomeration conditions in the view of predicting agglomeration behavior of fines, the KIC-EIT, ANRT and Eramet cofinanced this Ph.D. thesis in the frame of the Go-4-0 project (CIFRE contract n° 2017/0326).

The aim of this thesis is to contribute to the understanding of the fundamental mechanisms of the agglomeration processes of manganese fines, and the factors impacting those mechanisms. This insight will allow for a modelling of agglomeration processes, applicable to various materials and blends if a proper characterization of the material parameters is priorly performed. Through the understanding of the fundamental parameters of agglomeration, the target is to optimize binder use, or even forgo it if the studied material presents characteristics fitting those of commercial binder.

A new path was also taken choosing tabletization as an agglomeration method for mineral materials, a method which is usually operated for pharmaceutical products (Awad et al., 2019; Charinpanitkul et al., 2008; Johansson and Alderborn, 2001). It consists of a die where granular material is set before a punch comes down and press it in the shape of a small cylinder. It commonly sees limited use in the mining and metallurgical sectors due to its lower tonnage capacity compared to pelletization, briquetting and sintering, but it delivers higher compaction pressure that may allow avoiding the use of binders, which is one of the objectives of this study.

Experiments can be performed quickly and with low quantities of material. Moreover, tableting machines are easier to instrument and the process is easier to control than for other methods. It enables the recording of multiple data during processing, that can be used to understand the mechanisms occurring.

4. Thesis outline

The thesis comprises four main chapters: (1) theoretical considerations on agglomeration, a literature review; 2) characterization of material fines covering the entire manganese processing chain from ore to metal; 3) agglomeration experiments on four selected mineral concentrates; 4) modeling of the tableting behavior by Discrete Element Method (DEM) and data driven methods, based on real data acquisition.

Predicting the behavior of a material during agglomeration requires understanding the material properties and the agglomeration method it is subjected to. The latter subject is covered by a literature review on the different agglomeration methods, presented in the first chapter of this thesis.

The first step of this study was a comprehensive characterization of the different materials produced along the FeMn processing chain, from ore to metal. Mineralogical and chemical (both qualitative and quantitative) analyses were performed and coupled to theoretical considerations to estimate their agglomeration potential. This study allowed to qualitatively estimate agglomeration behavior. The results are presented in chapter 2 as a research paper published in Powder Technology in 2019.

The second step consisted in a series of tableting experiments which were performed at EUROTAB. Four products were selected in order to perform experiments under controlled pressure, moisture, and pH. Two products were parts of the manganese processing chain: manganese laterite ore fines from Moanda, Gabon and metal refining dusts from the Sauda plant in Norway, both sites being owned by Eramet. The two other products were clays with different properties: bentonite, a common industrial binder rich in montmorillonite, a swelling clay, and kaolinite, a non-swelling clay. A full mineralogical and chemical characterization was performed on the samples prior to the experiments, and on tablets after the experiments. The objective was to better observe the variations on the agglomerate properties based on the material properties. The results are presented in chapter 3 in form of a research article which is under review for the journal Powder Technology.

The third step of the thesis aimed at reproducing the empirical agglomeration results through numerical simulation of the process. Discret Element Method (DEM) was used to study the variations occurring with the modifications of the bond parameters (Young's modulus, diameter and strength). This is presented in the chapter 4 of this study in form of a research article under preparation for Powder Technology.

A general discussion chapter summarizes and analyses the outcomes of the thesis and its contribution to the improvement of agglomeration predictability. The conclusion provide recommendations for academic research and industrial applications to improve the results of this work. These additional works would help getting more information and increase overall prediction accuracy.

Chapitre 2 - Agglomeration methods and processes: a literature review

1. Introduction

Agglomeration processes of micrometric particles are the quintessential definition of a pluridisciplinary, multiscale phenomenon. Indeed, the particles are in a size range small enough so that molecular forces have an impact and big enough so that particles physics impact their agglomeration behavior. This scale forces to consider both chemistry and physics to explain the reactions, while crystallography is needed to understand particle's mechanical behavior. This domain between scientific disciplines makes it difficult to clearly define and predict the phenomenon taking place during agglomeration (Pietsch, 2002; Schulze, 2008).

There are multiple types of agglomeration methods, each with their own characteristics and mechanisms (Pietsch, 2002). This literature review has the objective of developing those different aspects of agglomeration, both technological and scientific, to establish the state-of-the-art regarding cold agglomeration. It is the first milestone toward my aim of understanding and modelling the agglomeration processes.

The agglomeration technologies will first be presented, followed by the mechanisms identified as the most important for agglomeration. In a third section, parameters impacting those mechanisms are developed. Those parameters are measurable, which can be varied to optimize the results obtained during agglomeration.

2. Agglomeration methods

All agglomeration methods have their advantages and drawbacks. Some of them are well investigated and understood thanks to their extensive use in the industry, such as the sintering (hot agglomeration process) (Pietsch, 2002; Zhu et al., 2014). This study aims at reducing the environmental impact and the financial cost of agglomeration, particularly in limiting energy consumption to a minimum. Therefore, it is focused on cold agglomeration processes.

During cold agglomeration processes, binders, additives that improve particles adherence to each other, are used to improve agglomeration results. Different types of binders exist, with different origins (organic or inorganic) and different chemical and mineralogical compositions (Halt and Kawatra, 2014). Each has its own properties, but all of them usually increase (i) the slag amounts (mostly considered as a waste) of the subsequent pyrometallurgical processes in which the agglomerates are used, and (ii) the energy consumption as this additional material also needs to be melted (T.C. Eisele and Kawatra, 2003). Additionally, some of them contain deleterious impurities which may alter the processes performance, such as alkalis, P, S, Cl... (Olsen et al., 2007).

The cold agglomeration processes can be classified into 4 categories (Fig. 2.1).

This section is mainly based on Wolfgang Pietsch's book (2002); Agglomeration processes: Phenomena, Technologies, Equipment. However additional sources are considered and cited.

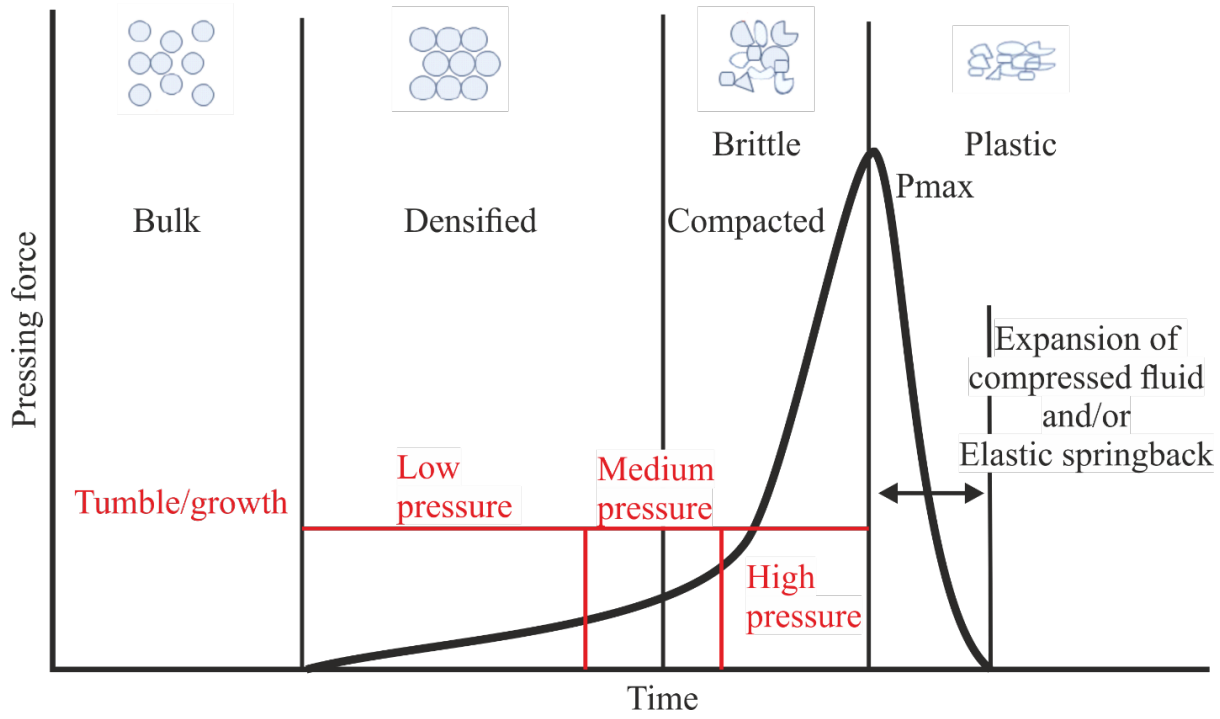

Fig. 2.1: Different domains of properties of the different types of agglomeration, differentiated by their actions on the particles. (modified from Pietsch, 2002).

2.1 Tumble/growth agglomeration

This type of agglomeration is mostly represented by pelletization (see Fig. 2.2). The main mechanism of this type of agglomeration is the rebound mechanism. This mechanism relies on the balance between the kinetic impact of the two particles and their bonding ability. The bonding probability depends on the kinetic force of the particles, their volume and mass. Electrostatic attraction should also be considered. The speed balance is delicate, since a higher speed means higher impact force, and a higher impact force means a higher bonding strength, if the particles stick to each other. However, if the speed is too high, then the particles will just bounce off each other, without adhering to each other. Additionally, if a bond is too weak, the next impact of a particle with its constitutive elements may break instead of creating a new bond. Given the particles characteristics, it may be possible to calculate a critical speed below which the particles will bond, and above which they will bounce. Since most of the impact speed will be provided by the "fall" of the particles during the disc's revolution, calculating this speed can help deciding the tilt angle and the rotation speed in order to produce more "successful" impacts.

The critical point of this process is the nucleation of the first agglomerates. At the same size, two particles will tend to bounce off each other, while at different sizes, the bigger particle is more likely to absorb the impact and stay close to the impacting particle. This is due to the law of energy conservation, resulting in a lesser speed for a particle of higher mass, at a constant kinetic energy. This explains why ore is a good candidate for tumble/growth agglomeration. Its broad particle size distribution increases the probability of nucleation. It also explains why industrials sometimes reintroduce part of their granulated material into the next batch, to provide the first nucleus and circumvent the nucleation part.

High moisture/binder content is required. This has two effects: the presence of a water film which creates capillary bridges and further reduces the kinetic energy of the particles, while improving the success rate of the agglomeration. Here, the particles are tumbled in a trommel or a pelletizing plate (see Fig. 2.2). The use of binders, curing time and/or heat treatment is often required.

Fig. 2.2: Disc pelletizer (Mars Mineral, 2020). The particles are agglomerated together thanks to their collision, if they do not rebound from each other.

2.2 Low pressure agglomeration

This type of agglomeration is basically regrouping methods where an initially sticky material is passed through a sieve, thanks to the “pressure” of a sweeping blade (Fig. 2.3). The material is rearranged to show a higher packing density than prior to the process. As for tumble/growth agglomeration, binder, curing time and/or heat treatment is nearly always mandatory.

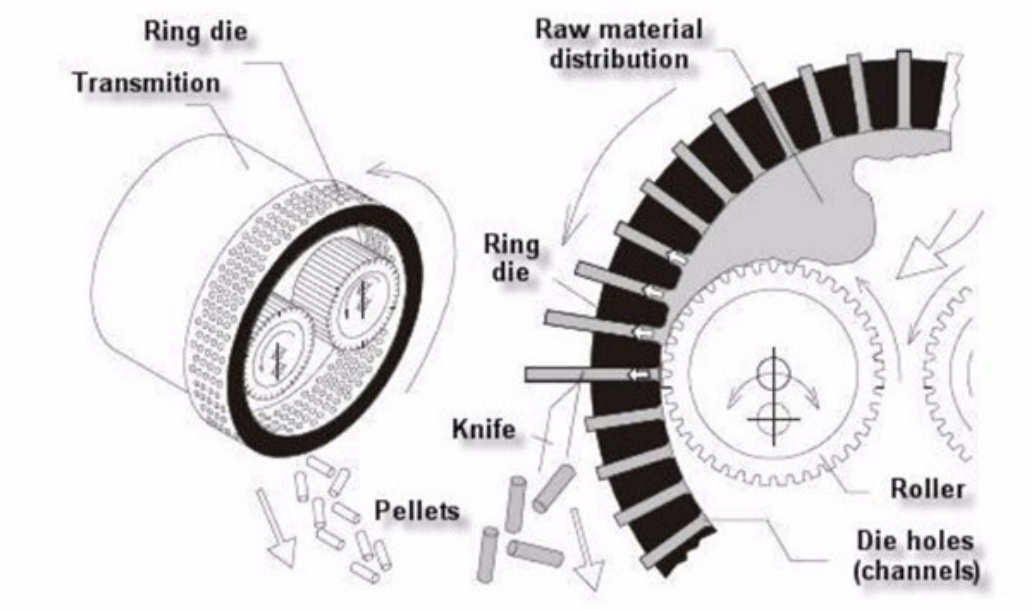

Fig. 2.3. Low pressure extruding machine, pushing the material into a ring die, decreasing its interparticular pore volume. Extruded are cut out by a knife (Zabava et al., 2018).

2.3 Medium pressure agglomeration

This regime of agglomeration shifts from a simple rearrangement of the particles to particle breakage at the intraparticular bonds. This creates fresh surfaces where the different atoms are not yet at equilibrium. In other words, bringing two of those “freshly broken” surfaces together may strongly bond them by creating Van der Waals forces.

However, this breakage phenomenon is limited due to the grain size of the material. Reaching the Heckel critical diameter of a material will transition its behaviour from brittle to plastic, preventing breakage (Heckel, 1961). This critical size is linked to the material’s mechanical properties and is specific to each.

Medium pressure agglomeration is usually performed through means of extruding machines, with a screw feeder or with briquetting machine (Fig. 2.4).

Fig. 2.4. Tangential wheels press (Komarek, 2020).

For the extruding machines the exit is the small end of a cone. Inside, the friction forces of the material against the sides lead to pressure build up, resulting in more compact agglomerates.

2.4 High pressure agglomeration

This type of agglomeration reaches the limit of particle breakage and starts to deform plastically them. One of the technologies is the uniaxial press, also called compaction or tabletization, where two punches apply high pressure on the powder (Fig. 2.5). High pressure agglomeration presents a high potential for use in mineral industries but introduces limits due to the high pressure applied. The materials may elastically rebound, which can partly or completely destroy the agglomerate (Fig. 2.10). Although there are some ways to circumvent this rebound, it is severely limiting the freedom of agglomeration.

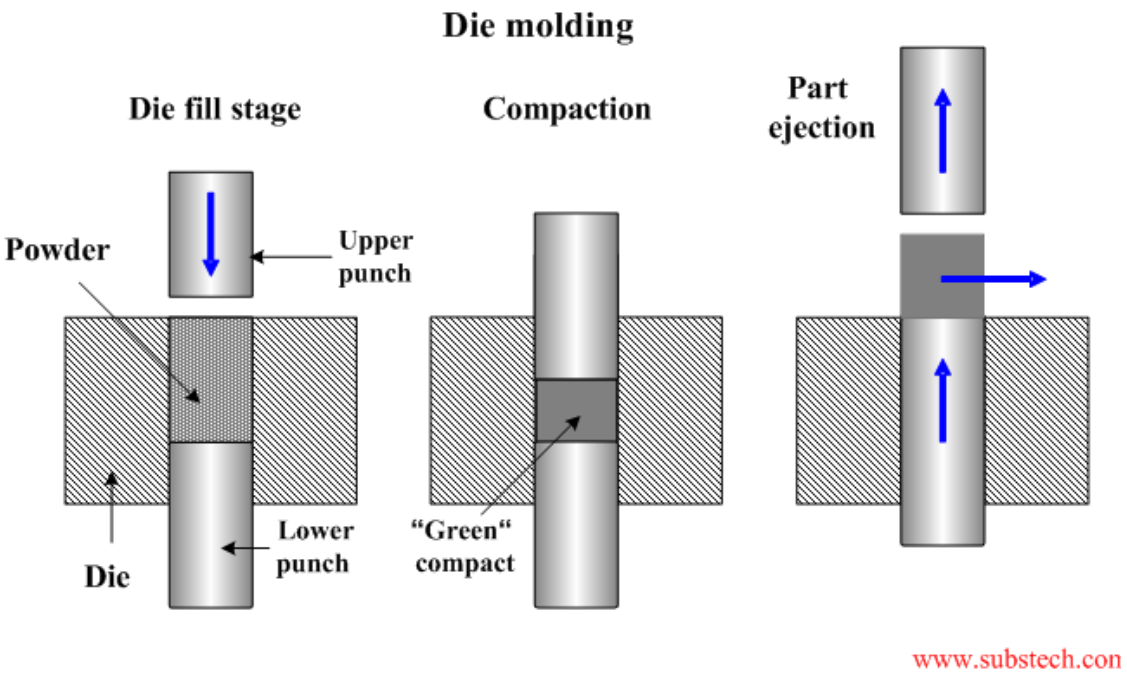

Fig. 2.5: Uniaxial high pressure press (Kopeliovich, 2012). The die is filled with powder before the upper punch comes down to press the powder into a tablet. The lower punch then goes up to extract it.

The moisture content is also drastically limited at <10% H20, since liquids are incompressible. Otherwise fluid lenses are created within the agglomerate, which prevents bonding of the material. However, high-pressure compaction requires less binders than other agglomeration methods, if any.

3. Interaction forces

Agglomeration is considered successful when all particles stick together and a cohesive solid is obtained. This implies, that the total strengths bringing the particles together must exceed the strengths keeping them apart (such as gravity, the different shocks the agglomerate may endure during transport). The forces keeping the particles together are depending on the agglomeration processes. The different possibilities are compiled in Fig. 2.6.

The main forces taking place during cold agglomeration processes are the capillary bridges, and the interparticular forces, such as Van der Waals and electrostatic forces.

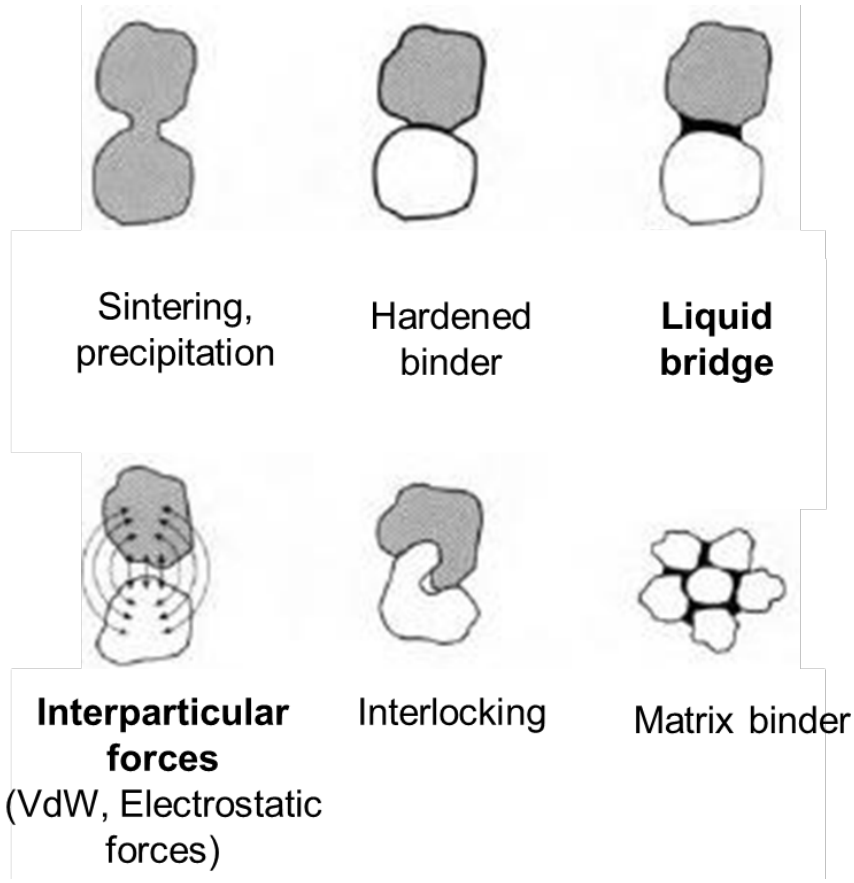

Fig. 2.6: Different phenomena occurring during agglomeration. Liquid bridges and interparticular forces are the most important. They can occur without any binder addition, or only with water. Sintering occurs when a material is heated until partial melting. Precipitation requires chemical agent. Interlocking can occur without binder. (modified from Pietsch, 2002).

3.1 Van der Waals forces

Van der Waals forces act when two particles are in very close contact. Those forces come from the rearrangement of the electronic cloud surrounding the molecules, creating a bond between the two particles. They range over a few Angstroms and decrease sharply with the separation distance. Along with the liquid bridges, they are considered as the strongest contributors to the agglomeration forces (Pietsch, 2002). They are impacted by the size of the particles and their distribution (Mu and Su, 2007). The moisture content also has a strong impact on those forces. An increasing amount of liquid leads to a decreasing intensity of the Van der Waals forces (Yang et al., 2016). There are many studies on the Van der Waals forces and their calculations in solids, but they are often calculated with Van der Waals theory, considering only two spherical particles next to each other, with set sizes (Fig. 2.7).

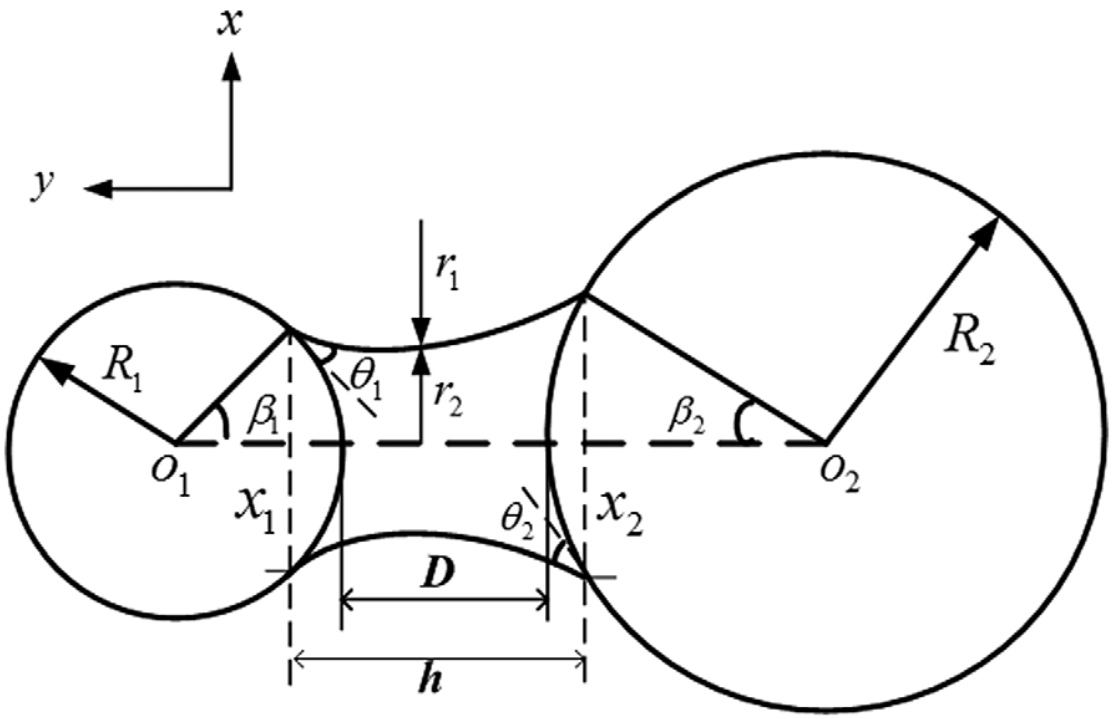

Fig. 2.7: Scheme of a liquid bridge between smooth spherical particles in humid environment. R is the spherical particle radius, Θ is the liquid–solid contact angle, β is the half-filling angle of the liquid with particle which characterize the amount of liquid, and D is closest separation distance between the particles. Subscripts 1 and 2 refer to the left and the right particles surfaces, respectively (Yang et al., 2016).

The limitations of this theory imply that this case will not happen during agglomeration. Particles are always surrounded by and interacting with other particles, which impacts induced Van der Waals forces. The Lifshitz theory deals with this limitation. It considers the impact of each surrounding particle on the interaction between two particles, by calculating its participation to the force through a projection on the interaction axis going through the middle of the two particles mainly considered (Lifshitz, 1956).

3.2 Liquid bridges

Capillary forces develop between two particles due to the presence of a liquid phase. Polarised molecules in the liquid create bonds between the particles. Similar to the Van der Waals forces, the particle size variation will increase the strength of the capillary bridges. However, an increase of liquid content will increase their intensity (Yang et al., 2016). However, the compressive strength of the overall solid will be reduced, although the tensile strength increases. Depending on the amount of liquid present in the mix solid/liquid, the solid will have different states: (i) pendular, with a S_L (Liquid Saturation) < 0.25, (ii) funicular, with a S_L < 0.9, (iii) capillar with S_L<1, with a slurry state > 1 (Fig. 2.8). The slurry state is characterised by the shift to an overall liquid behaviour, while the pendular and capillary states belong to the solid state. This difference in S_L has an impact on the way to calculate the strength of the liquid bridges, since the water repartition impacts the way the tensile strength is distributed in the water (Louati et al., 2017).

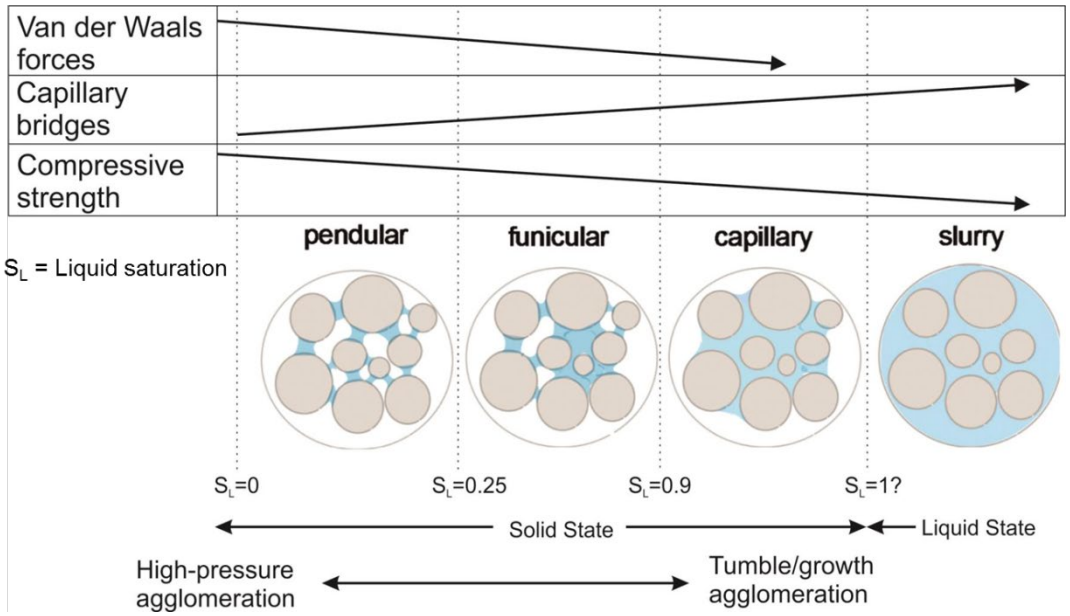

Fig. 2.8: Impact of water content on Van der Waals forces and capillary bridges during agglomeration (modified from Louati et al., 2017).

3.3 Electrostatic forces

Electrostatic forces develop from charge deficits inside the structure of the material. Depending on the crystallography of the material and its environmental conditions, those charge deficits can be intrinsic to its nature and defects or can be acquired through alteration/lixiviation. One of the most common examples is the isomorphic substitutions of Si^{4+} by Al^{3+}. This gives one less positive charge in the initially electrically neutral system (Zhu et al., 2016).

Those charges will act like magnet, bringing particles together if of opposite signs, repulsing them if of the same sign. In this last case, for homogeneous material, those surface charges will hence hinder agglomeration. Neutral surfaces will facilitate the processes, since other forces have been shown to be able to act upon this sticking (Pietsch, 2002). The best-case scenario for heterogeneous material remains to be determined, since it has not been investigated.

Models exist to calculate those forces, using Coulomb' law and Gauss' law. However, some deviations are observed. Additional studies are being performed to decrease those inaccuracies. The surface state may have been overlooked in those models (Grosshans and Papalexandris, 2017). Indeed, depending on the environment, part of those electrostatic charges can be compensated with ions from the surrounding environment of the particle (Zhu et al., 2016). Those are likely part of the parameters to consider for agglomeration efficiency.

3.4 Summary on interacting forces

Those three forces are considered as the main actors of agglomeration. However, they are very short ranged compared to macroscopic scale forces. Depending on the distance separating the particles, the strength and importance of those bonds may vary strongly. Fig. 2.9 presents values

for these forces calculated by Schulze (2008). However, it must be kept in mind that electrostatic forces are also dependent on particle charge. Additionally, this force is extensive.

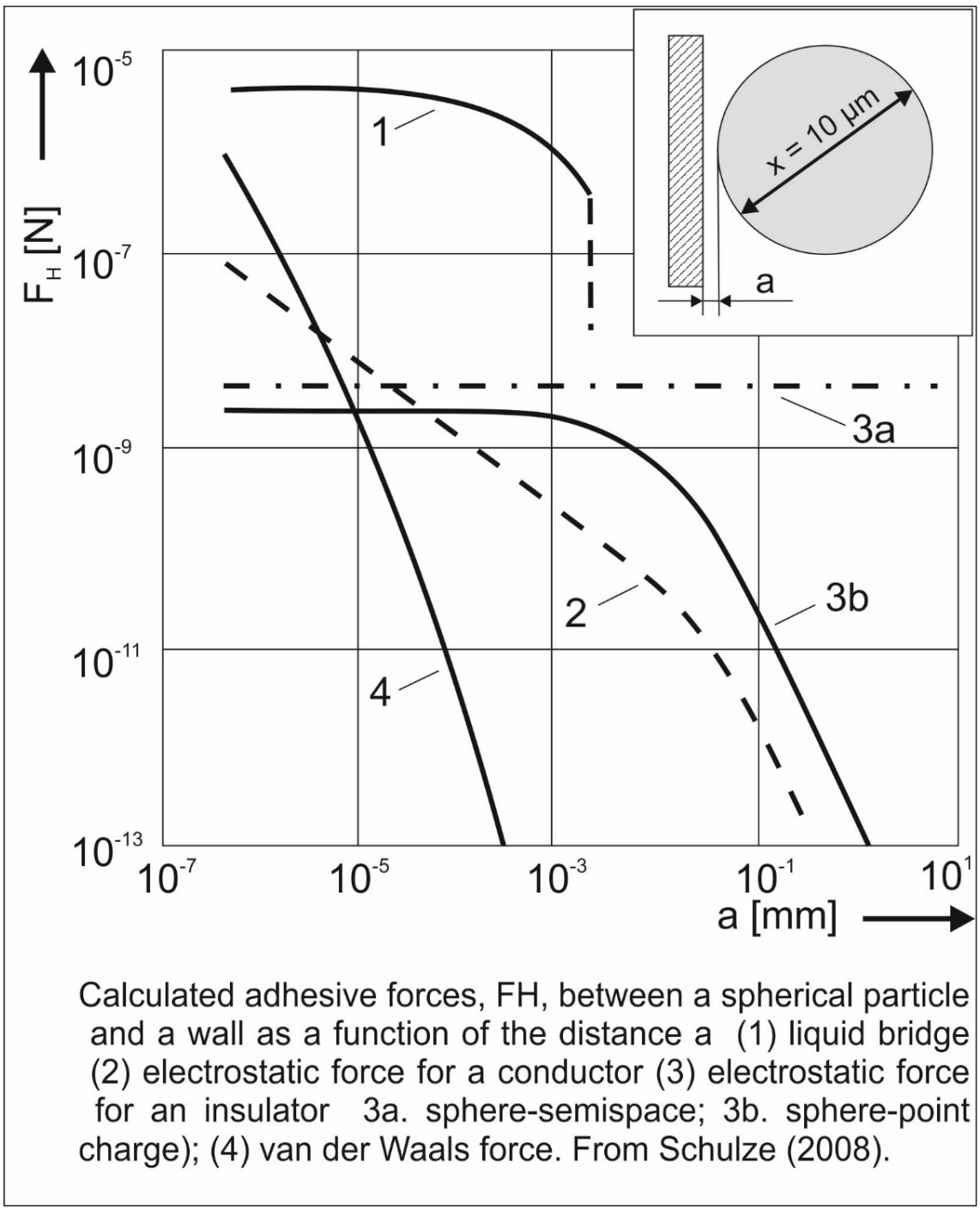

Fig. 2.9: Comparison of the intensity of the different adhesive forces (Schulze, 2008).

4. Key parameters for agglomeration

Measuring the above-mentioned forces is not straightforward, since there are few to no methods available. On the other hand, we know the parameters of those forces, and how to calculate them. It is hence possible to measure data, and then try to model the forces accordingly to those values.

Those parameters defining the intensity of the mechanisms occurring during agglomeration will hence be defined as Key Parameters (KP). They will be classified in three categories:

- Internal properties of the particles: Led by the mineralogy and mineralogical associations of the particles. Those properties are intrinsic to the materials.
- Physical properties of the particles: Impacted by the particle history and its environment. Those parameters describe the shape, size and size distribution of the particles.
- Environmental parameters: such as the moisture, the pressure applied, and the temperature, depend on the environmental and experimental conditions of the agglomeration processes.

The three categories are described below, to define in a more precise way the impact and variation induced on agglomeration's mechanisms by the variation of those parameters.

4.1 Internal properties of the particles

4.1.1 Mineralogy

This characteristic is obtained from crystallography and mineral chemistry. Crystallography can allow, by knowing elements in presence and the way they are bound to each other, to understand the chemical and mechanical behaviour of a particle. It hence determines the intrinsic properties of the particles: magnetic susceptibility, density, crystalline water content (Klein and Dutrow, 2008; Maxbauer et al., 2016).

A simple model using those parameters considers particles of pure mineralogy (Mu and Su, 2007; Yang et al., 2016a). It will simplify the calculations, while decreasing the accuracy. On the other hand, a more complex model includes mixed particles in order to create classes based on observations, hence fitting more with reality (Herting and Kleinebudde, 2007; Mansa et al., 2008; Wallmach, 2017). This is a choice to be made by every modeller between a model that is "lighter" to use, and a very accurate one.

The interface surface between particles in a material is usually considered negligible regarding the overall behaviour of the material. However, this is not true for smaller particle sized powders (< 0.1 mm). Indeed, the ratio of volumes between interface and particles then highly increases, and the behaviour of those interfaces becomes more important (Parker, 1993).

The new consideration brought to those interaction areas leads to more complex, but also more comprehensive settings, to develop numerical models (Logan, 2015; Parker, 1993). Research have been performed especially by the pharmaceutical industry (Herting and Kleinebudde, 2007; Johansen and Schæfer, 2001; Mansa et al., 2008), but also the mineral industry (Antonyuk et al., 2011; Debrincat et al., 2008). The goal was to perform more detailed model. However, the authors mostly circumvent the modelling of the processes to link the input parameters to the output characteristics using neural network, or empirical observations. Alternatively, most attempts at modelling the processes are performed on simplified particles morphology. On the other hand, material scientists are working on modelling interactions of the surfaces and their impact regarding the agglomeration results (Maximenko et al., 2008; Spettl et al., 2015). However, much work needs to be done until a comprehensive modelling of those systems can be reached.

Internal studies have also been performed at Eramet IDEAS (Trappes) on different materials (Mn ore fines, nickel laterites) to evaluate their ability to agglomerate (Bondouy and Milazzo, 2016, Fig. 2.10). Although these materials are similar to the samples studied here (manganese oxides), their mineralogical compositions are different. The samples of the manganese processing chain contain as major phases, lithiophorite ($(Al,Li)Mn^{4+}O_2(OH)_2$, trigonal, cleavage perfect on 001),

pyrolusite (MnO_2, tetragonal, cleavage perfect on 110, brittle), hausmannite (Mn_3O_4, tetragonal, cleavage nearly perfect on 001, indistinct on 112, 011, brittle), and clays (foliated, hydrated silicates). After tableting experiments, the best results are obtained with the lithiophorite-rich sample, followed by the pyrolusite-rich sample, with the haussmanite-rich sample presenting low agglomeration potential (Fig. 2.10 A, B and C respectively).

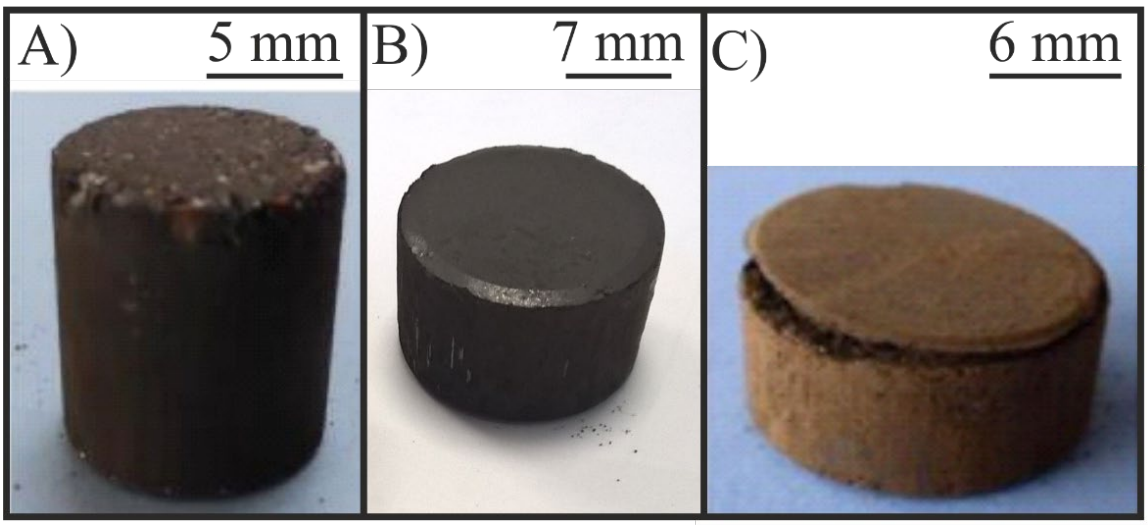

Fig. 2.10: Agglomeration results from the different studies: A) Tablet composed of lithiophorite-rich Mn fines from the Moulili sand, B) Tablet composed of Mn ore fines from Moanda (Gabon, Comilog) C) Tablet composed of metal refining dusts. All those tablets have been performed without additional binder use, with a uniaxial high-pressure press at Eurotab (From Bondouy and Milazzo, 2016).

Blancher and Laugier (2014) have performed a QEMSCAN study on nickel briquettes. The results present the distribution of smectites, swelling clay minerals, in a binder free briquette. The presence of the smectite made briquetting successful. This observation is further supported by results obtained by Eisele and Kawatra (2003), which states that bentonite (mainly composed of montmorillonite, a swelling clay mineral) is one of the main inorganic binders used for iron ore pelletization.

4.1.2 Behaviour under compression

The crystallography determines the atomic repartition inside the structure of a mineral (Klein and Dutrow, 2008). Some of the key considerations are developed in the following paragraphs. The atomic repartition and bonding between atoms (and molecules) are defined for each mineral. These parameters define the resistance of a mineral to stress. When a mineral is anisotropic, it will result in a resistance to stress depending on the stress direction.

Weaker bonds create weaker cleavage planes, and thus present fragile zones in the structure of a mineral (Fig. 2.11). Cleavages are qualified from *perfect* to *poor*, with *perfect* being an easy to break and very smooth resulting surfaces, while *poor* will need more strength to break, and may be less regular. Cleavages lead to brittle behavior of a mineral.

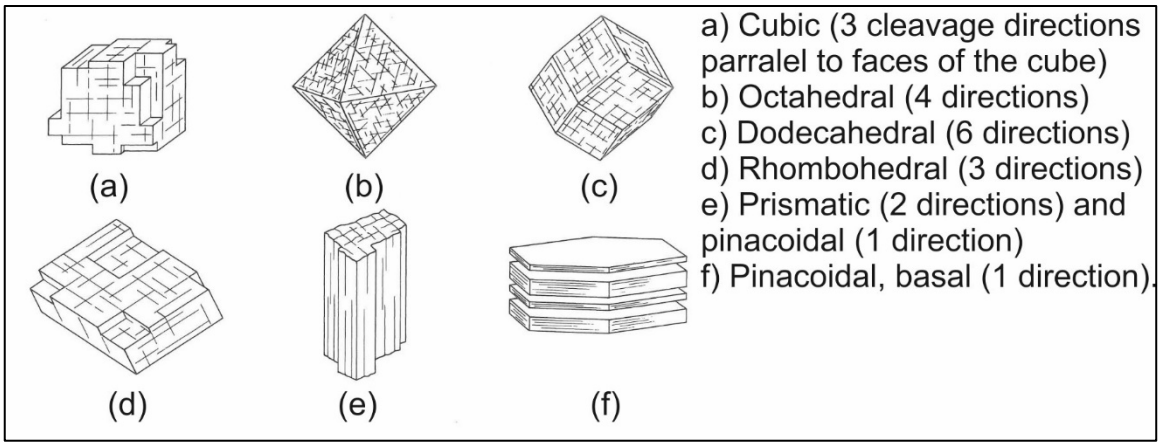

Fig. 2.11: Cleavage and its relationship to forms (Klein and Dutrow, 2008).

A second parameter of fragilization mineral structures are crystal defects. These defects can be point defect, linear defects or planar defects (Fig. 2.12). They may have different origins, such as the misplacement of an atom or its displacement for point defects, or empty sites. Some minerals have a higher tendency to have defects in their structures than others. Crystallographic defects lead to plastic behavior of a mineral (Klein and Dutrow, 2008).

When put under strain, those weak zones will be the location where it is accommodated. The plastic behavior of minerals under stress is related to a displacement of the defects inside the structures. For example, in the case of the absence of an atom (case 1 on Fig. 2.12), the pressure will push another atom in the empty space, and so on. The brittle behavior of minerals under stress is due to the activation of the cleavage planes, when the weaker bonds will not be able to withstand the pressure anymore.

Those parameters can help or hinder agglomeration mechanisms (Fig. 2.13; Pietsch, 2002). There is no predictive model of those phenomena yet. To evaluate these parameters, a set of compression experiments is needed, to fit the obtained curves with the models' equations. The four main models are those of Cooper and Eaton, (1962); Heckel, (1961); Kawakita and Lüdde, (1971); Sonnergaard, (2000), giving useful information about the brittle/viscous behaviour of a particular particle, but also other parameters, like flowability.

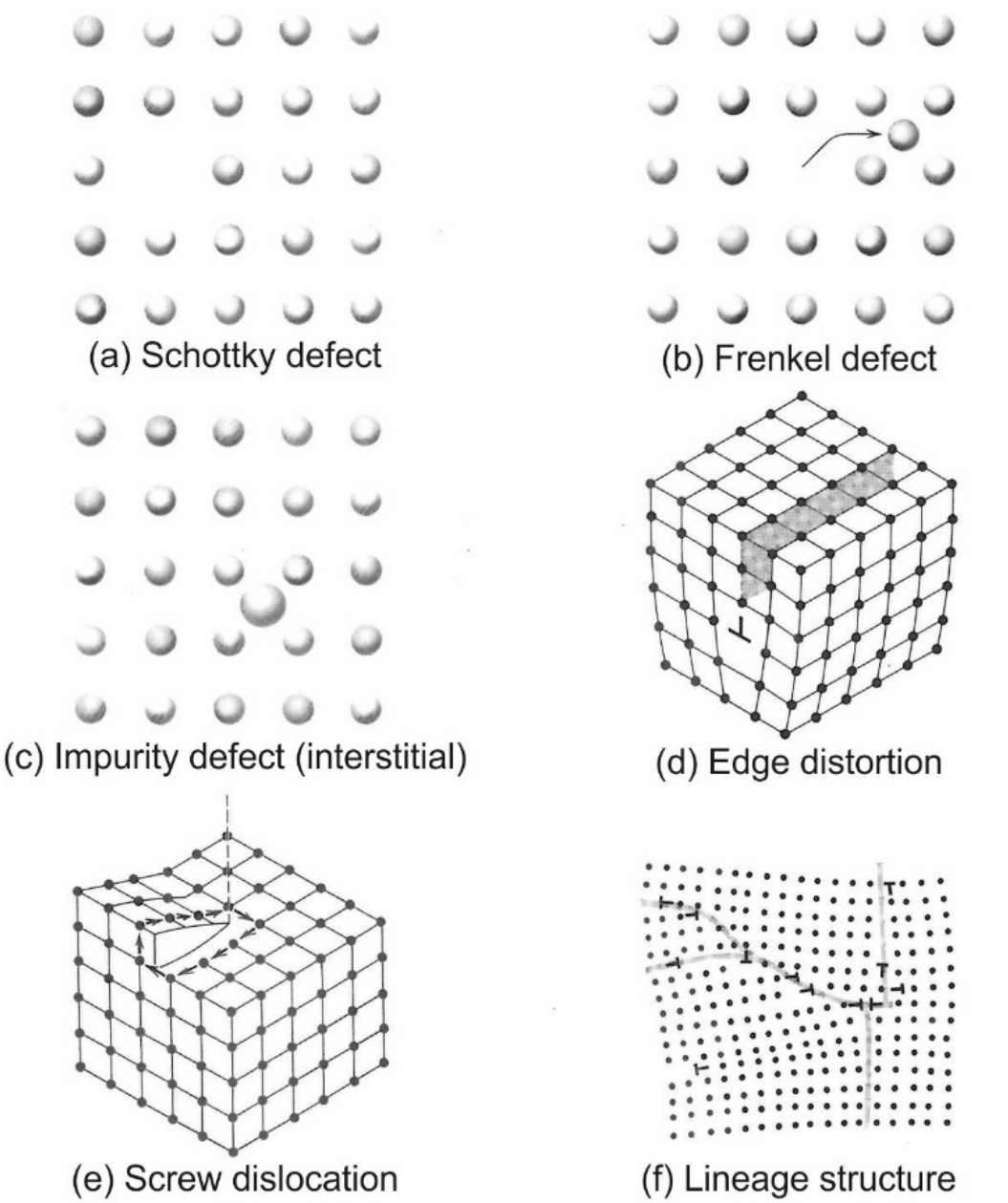

a) An ion (or atom) is missing from the structure
b) An ion (or atom) is displaced from its normal site
c) An interstitial impurity is randomly lodged in an otherwise regular structure.
d) A plane of atoms that stops along a dislocation line (the edge of dislocation is shown by the graphical symbol T)
e) A screw dislocation line (dashed) about which atomic planes wind a helical form.
f) A crystal made of a mosaic of domains that differ only slightly in orientation. The irregular zones (which are planes in three dimensions) of defects are *lineage structures*.

Fig. 2.12: Different types of crystal defects (Klein and Dutrow, 2008).

This information is valuable for both the agglomeration, and its application as a continuous process. Some material or shapes are better suited to some uses than others and choosing the right one may be the key of a successful process. For example Bacher *et al.*, (2008) illustrate this issue by studying the impact of particle shapes on the filling of a die. At the same time, the mechanical behavior of the material can impact the result of agglomeration. A pressure release from an agglomerate, whose material has an elastic behavior, may lead to an elastic rebound and cleave it orthogonally with respect to the pressure direction (Pietsch, 2002). It is hence important to be able to measure the importance of those elastic properties or predict them.

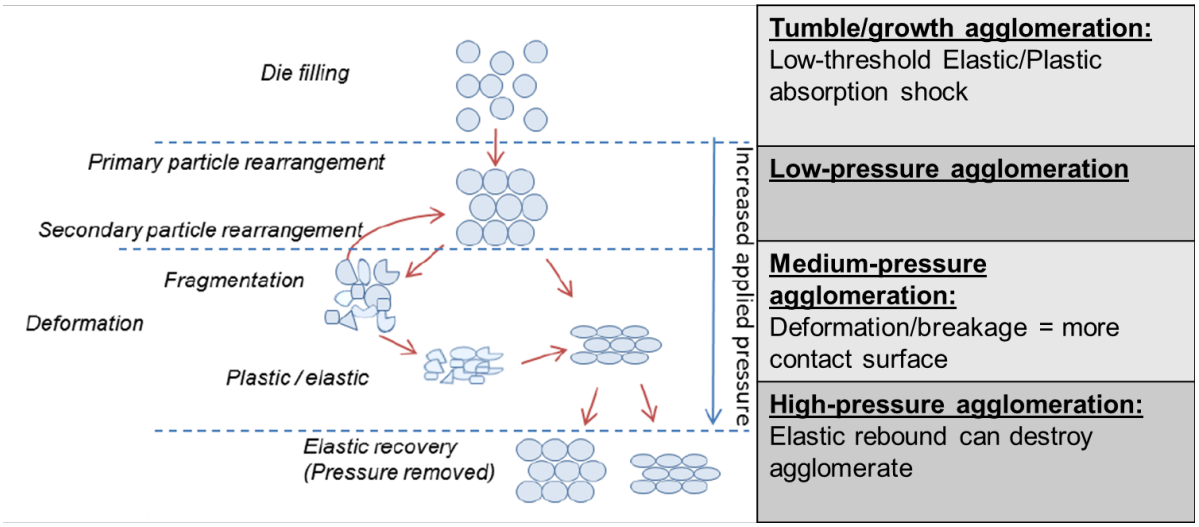

Fig. 2.13: Behaviour under the different degree of compression using different methods.

4.1.3 Surface potential

The surface potential of a mineral is a value determined by the interaction between the crystallography/mineralogy of a particle and its environment. The intrinsic mineral properties determine the "theoretical value" of this potential (Zhu et al., 2016), and the interaction with the environment (moisture, pH) modifies it again to obtain the "experimental" value. Indeed, interactions with the environment may change the surface state of the particles, for example oxidizing it, or attenuating the effect of the particle's charge by adsorbing ions.

Two measurable parameters describe the results of the interaction with the environment, the Zeta potential and the Cationic Exchange Capacity (CEC). While the surface potential for a given particle should be stable, those two parameters will change depending on the environment.

The Zeta potential represents the electric potential at the shear boundary (Fig. 2.14). This shear boundary is the limit between the ions stuck to the surface of the molecule, that are going to move with it, and the ions that are impacted by its surface charges and revolve around it, but are not stuck to it (Al Mahrouqi et al., 2017; Lowke and Gehlen, 2017).

The CEC (Cation Exchange Capacity) gives the theoretical number of ions that can be adsorbed by the particle (Leroy et al., 2015). When the CEC reaches its limit, the Zeta potential should reach 0, since the entire surface charges are compensated by the adsorbed ions. However, this CEC value is usually measured in a standard setting, where ion exchange occurs. Depending on the valence and the radius of the ions being exchanged, the CEC can be reached before the Zeta potential falls

to 0. Thus, the measurement conditions and the used settings must be known to appropriately consider the Zeta potential and CEC (Leroy et al., 2015).

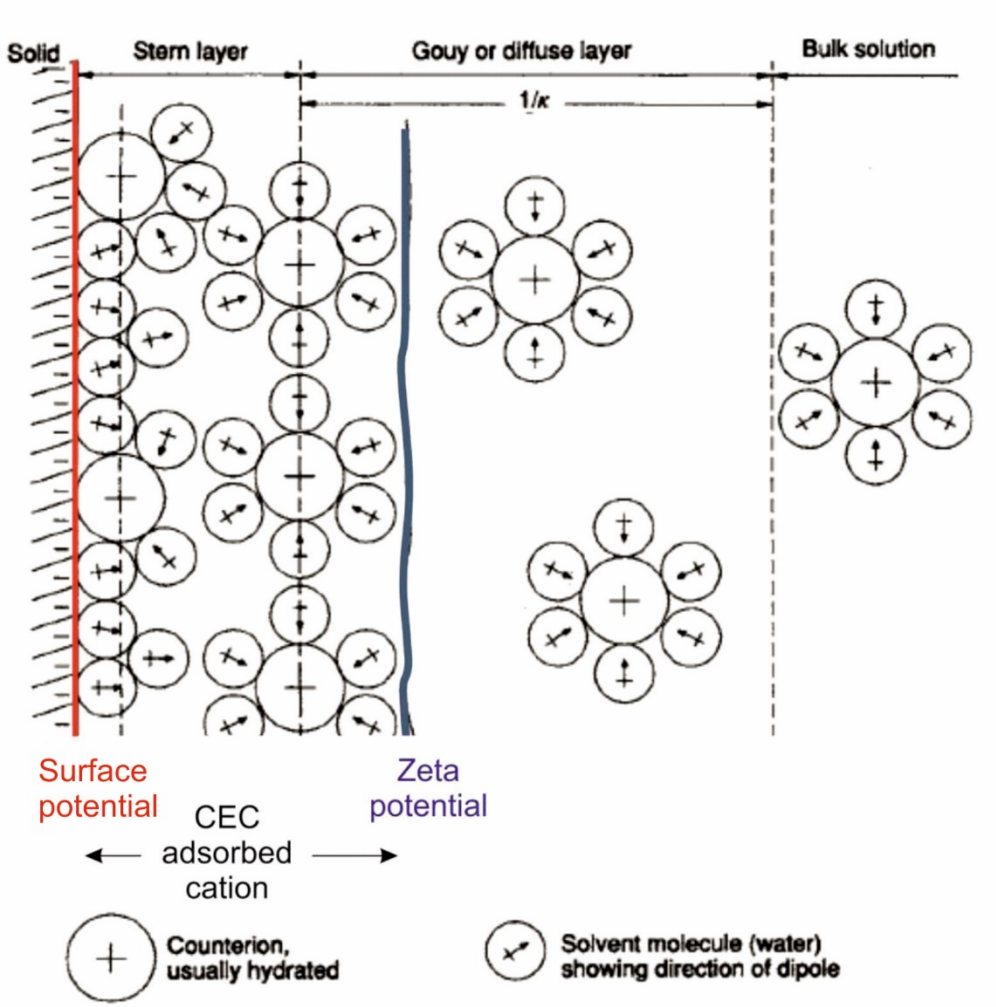

Fig. 2.14: Scheme showing the physical meaning of the zeta potential, CEC and surface potential around the particles considered (modified from Leroy et al. 2015).

However, the surface potential can be calculated from the CEC and zeta potential. It should be stable over the range of different environment. It should be possible for the value of the CEC and Zeta potential can be calculated independently of the physicochemical conditions of the particles. However, this needs a better understanding of the relationship between the different parameters. Hou et al. (2009) proposed a model linking the surface potential to the zeta potential.

Regarding agglomeration, those forces are considered most useful at low pressure (tumble/growth agglomeration, low-pressure agglomeration), since the material is not highly compacted.

Furthermore, depending on the material's characteristics, when the particles get closer, particle attraction may inverse to repulsion. It then becomes a balance between close range forces of attraction (hence VdW and capillary bridges) and repulsion (surface potential) (Pietsch, 2002). This change in particle behaviour needs to be further evaluated.

4.2 Physical properties of the particles

4.2.1 Shape

The shape of the particles influences directly the number of contact point and the surface area in contact between the particles Angular and jagged particle shapes show better agglomeration results than spherical shapes. (Fig. 2.15) They also need less binder, due to higher contact area (Johansen and Schæfer, 2001).

During tumble/growth agglomeration, particles enter in collision with one another. If the velocity of both is below a critical velocity (that depends on their mechanical properties and masses), then they agglomerate together instead of rebounding (Gensch and Weber, 2017).

It can be assumed that for a particle with jagged edges and/or needle-like overgrowth, these parts break more easily. This breakage would then help dissipate some of the kinetic energy of the grains, thus increasing the probability of successful agglomeration.

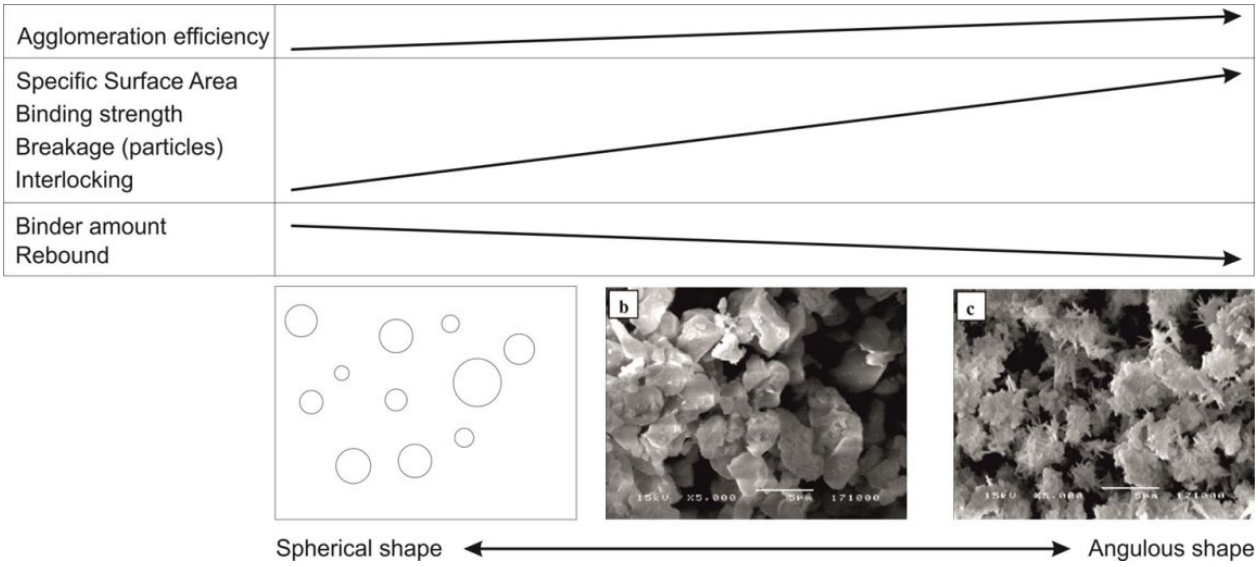

Fig. 2.15: Impact of the shape on different agglomeration characteristics and mechanisms (modified from Johansen and Schæfer, 2001).

4.2.2 Particle size and particle size distribution

These parameters determine the number and strengths of bonds. Understanding the correlation between the strength of the bonds linking two grains and the size of those grains was studied e.g. by Mu and Su, (2007) and Yang et al. (2016). It has been shown that the bigger the particle size (up to 100µm), the higher the bonding strength (Fig. 2.16).

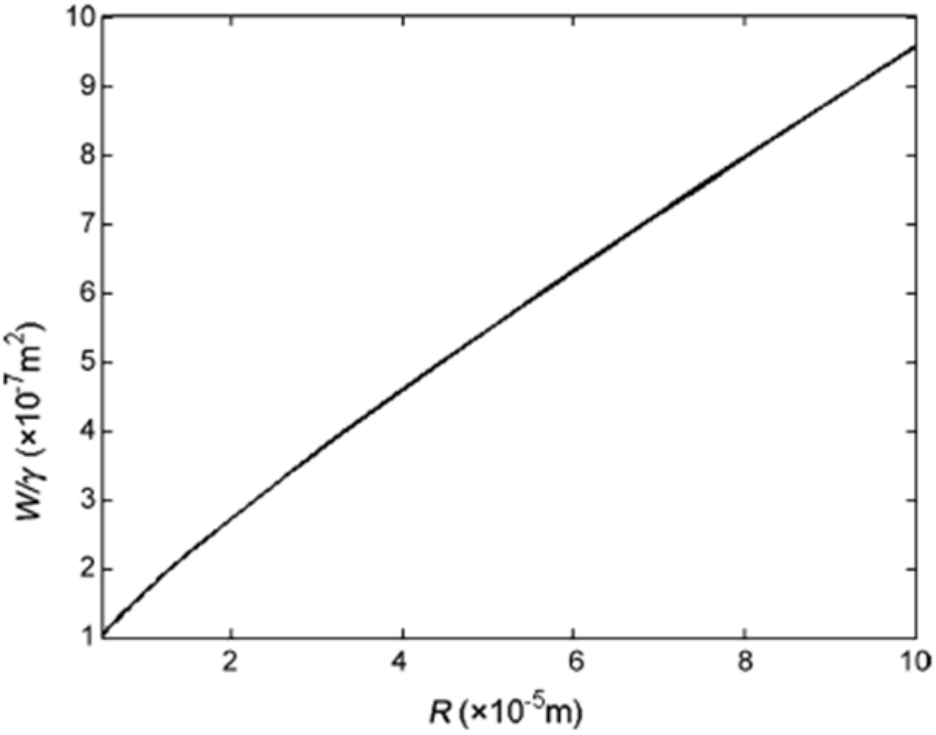

Fig. 2.16: Relationship between rupture energy (W/γ) and particle size (R) for capillary bridges (from Mu and Su, 2007).

However, this does not translate directly to the agglomerates as large particles imply larger separation distance. The separation distance here is the distance left between the surfaces of two neighbour particles (Fig. 2.17). The forces in action – Van der Waals, capillary bridges, electrostatic forces- are very sensitive to this gap. Therefore, particle size distribution must be considered as well.

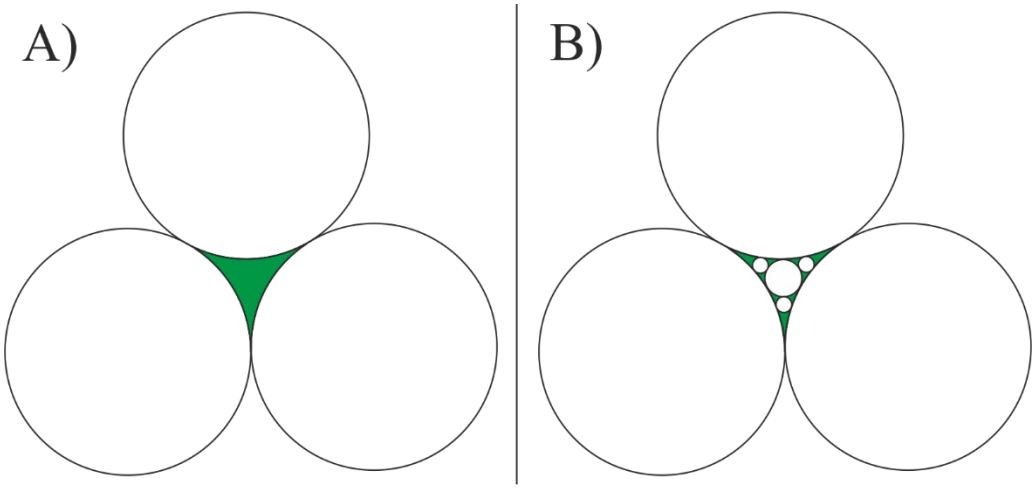

Fig. 2.17: Packing density, with the separation distance in green. On the left-hand side, there is only one grain size, ending up with a higher porosity (Separation distance). On the right-hand side, smaller grain sizes are added to the mix, which are going to fill the porosity, and decrease it (hence the smaller green surface).

Indeed, in the case of a wider particle size distribution, the packing density is increased (McGEARY, 1961) and the separation distances is reduced (Fig. 2.17 B). This does not decrease the intensity of the agglomeration forces as much as with only one particle size. This leads to a stronger agglomerate that will not crumble under its own weight (Debrincat et al., 2008; Herting and Kleinebudde, 2007; Pietsch, 2002).

4.3 Environmental parameters

While it is very important to have an in-depth knowledge of the physicochemical and mechanical properties of the particles, it is also important to understand the conditions of the particle environment and their interactions. Some of the environmental conditions can modify the internal properties of the particles and modify thus the agglomeration potential.

One of the examples that have already been presented, is the moisture of the sample (Fig. 2.8) that can increase or decrease the forces (Van der Waals and Capillary bridges; Louati et al., 2017). Its impact on the electrostatic forces is yet unknown but needs to be investigated. The Fig. 2.1 also presents the different behaviour depending on the pressure applied (Pietsch, 2002).

Furthermore, the zeta potential will change its value depending on the pH of the surrounding moisture (Fig. 2.18).

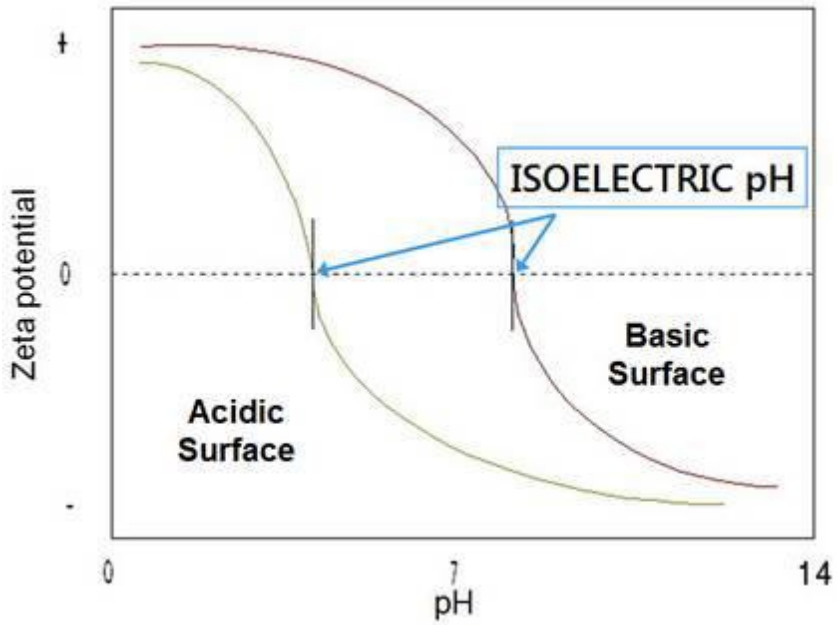

Fig. 2.18: pH versus Zeta potential: depending on the pH, the zeta potential will change for a same particle. The isoelectric pH is the pH at which the value of the Zeta potential changes signs (Horiba, 2020).

Moreover, the agglomeration temperature (e.g. sintering) impact on the material's properties (Chaim, 2017; T.C. Eisele and Kawatra, 2003). However, sintering (> 1000°C) is not the topic of

this study. In some machines (e.g.: extruding machines), however, the frictions in the material may increase temperature to > 50°, and may modify very low temperature minerals, hence changing the properties of the material.

It is thus important to choose the right agglomeration method, as the last type of environmental parameters. Each agglomeration method and apparatus have its own mechanisms, with its particular settings (the way of applying pressure, of compacting the particles and so on, are very specific). As such, it is important to keep in mind that each method will be optimized through different settings.

5. Conclusion

This literature review had an objective of evaluating the different phenomena likely to occur during cold agglomeration. This was done successfully, and some gradation was even given by some authors (Pietsch, 2002) to evaluate the respective importance of the different phenomena. The main forces that are going to take place during agglomeration are the Van der Waals forces, the capillary bridges, and the electrostatic forces. Another very important phenomenon is the behavior under compression of the particles considered.

The importance of those characteristics depends on key parameters, such as highlighted here:

- The internal properties of the particles, mainly given by the crystallography;
- The physical properties of the particles with their shape, size and size distribution;
- The environment of the particles: e.g. moisture, pH, etc. impact on agglomeration efficiency.

In the frame of this PhD, the objective is to understand how those parameters interacts to produce the capillary bridges and the electrostatic and Van der Waals forces, and how to model selected parameters in order to predict material behavior.

This task requires estimating the random repartition of the different sizes of particles, before adding the different nature on top of those different sizes, and then finding a way to calculate the resulting bonding strengths by taking into account the presence of particles into a bulk, and not just two by two. None of those steps has ever been completed before.

However, Wollborn et al. (2017) linked the bonding strength to the tensile strength of an agglomerate for modeling. Using Rumpf's (1970) model, his team used the breakage strength of the agglomerate to calculate the adhesion forces of the particles, and they obtained a good fit. However, they found that the controlling parameters had to be adjusted for each material, and that the process parameters need to be considered.

Linking this with the information collected in this document, it may be possible to refine the calculations in order to extend the links here, going from the material, to the adhesion forces, and then to the agglomerate strength. It could allow the introduction of new handles to manipulate agglomeration's results.

Chapitre 3 - Agglomeration potential evaluation of industrial Mn dusts and sludges based on physico-chemical characterization

Dubos, J.L. [1/2], Orberger, B. [2/3], Milazzo, J.M.,[1] Blancher, S.[1], Wallmach, T. [1], Lützenkirchen, J. [4] Banchet, J. [5]

1. Eramet IDEAS, 1 Avenue Albert Einstein, 78190 Trappes-en-Yvelines, France
2. GEOPS, Université Paris Sud, Université Paris Saclay, Bâtiment 504, 91405 Orsay, Cedex France
3. CATURA Geoprojects, 2 rue Marie Davy, 75014 Paris
4. INE, Karlsruhe Institute of Technology-KIT, 76344 Eggenstein-Leopoldshafen, Germany
5. EUROTAB, ZAC des Peyrardes, St Just St Rambert,, France

Published in Powder Technology.

DOI: https://doi.org/10.1016/j.powtec.2019.10.101

1. Abstract

Fine particles (<3 mm) are important, environmentally hazardous wastes of the mining and metallurgical industries that still contain valuable metals. Agglomeration, mainly using binders, is a common process to safely recycle those materials. This study aims at mastering cold agglomeration through understanding natural binder properties of the material. For the first time, a comprehensive physico-chemical characterization was performed on 13 samples from a manganese processing chain including ore fines. The main parameters to predict the agglomeration potential of the materials used in the present study are the presence of layer- and/or tunnel-structured phases along with the particle and grain size distribution, hardness and shapes, and particle surface charges. The Gabon ore fines show the best agglomeration potential. The soft, layer-structured plastic minerals (clays, lithiophorite) present naturally coat the hard grains (pyrolusite, cryptomelane) forming particles with enhanced binding potential. Blending these ore fines with low agglomeration potential dusts avoids binder use in the agglomeration process.

2. Graphical abstract

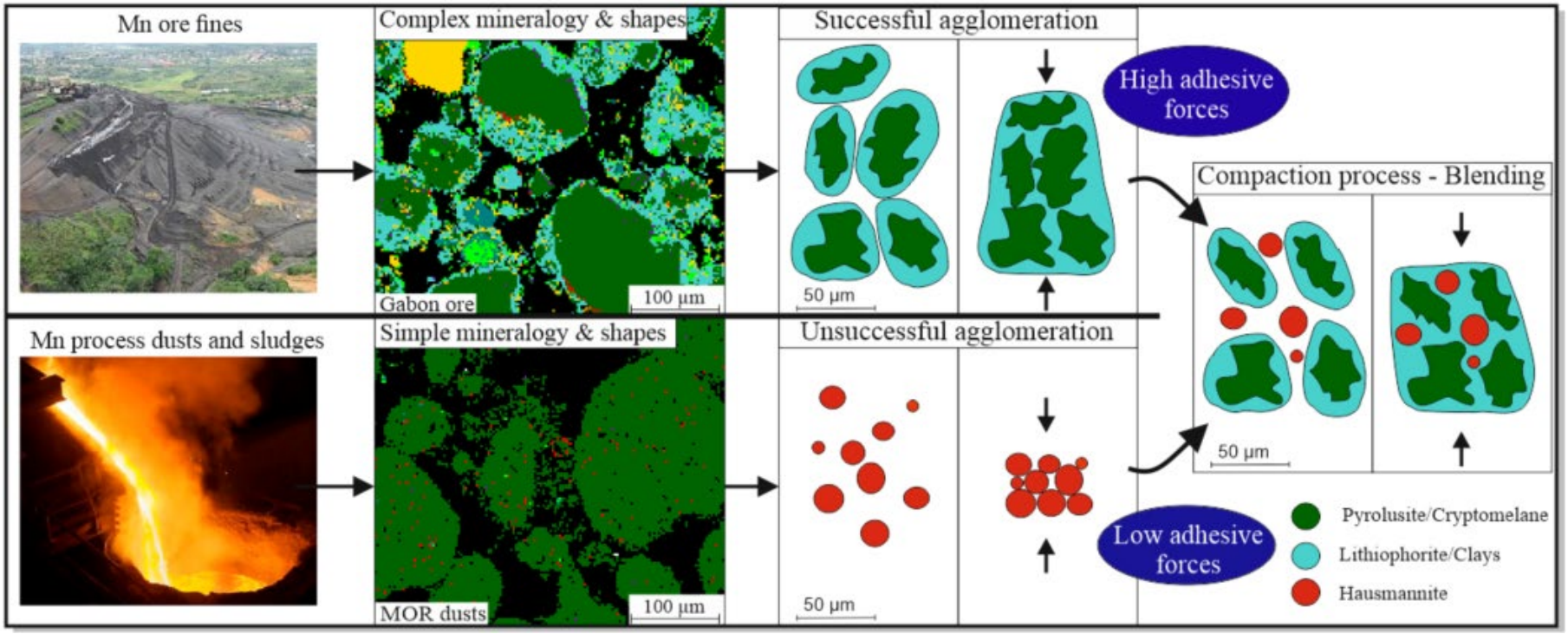

Fig. 3.1. Graphical abstract showing an estimation of the agglomeration potential based on characterization results. This is applied to two different materials, and hints at the possibility to blend them together to overcome one's low potential.

3. Introduction

Industrial dusts, here defined as particles sized below 3 mm, and sludges, composed of fine particles (<100 µm) suspended in aqueous solution, are the most important wastes of mining and pyrometallurgical industries. For example, the wastes related to manganese production amount to 15 kt/y of dusts and 10 kt/y of dried sludges from all the treatment processes of the sole Eramet Norway production plants. These numbers exclude dusts produced during mining, beneficiation and handling of ore fines. The installed pelletization capacity worldwide estimated at about 481 million tons per year (Tuck and Virta, 2015) translates well the scale of the fines issue**.**

Until the late 20th century, those dusts were mostly released into the atmosphere. Technologies to filter out dust have evolved since 1975 (Stellman, 2000). The fines also had to be handled and were at first stored in landfills. However, this solution was costly and could sometimes cause environmental issues (Fernández et al., 2003), due to the lixiviation of metals still present in the dusts. The metal content amounted up to 70 wt.% (Olsen et al., 2007), i.e. 30 wt.% higher than in the original ores. Liebman (Liebman, 2000) estimated that only 35 wt.% of the Electric Arc Furnace (EAF) dusts were recycled, part of it through agglomeration.

Reintroducing those dusts into the metal producing processes would increase the overall yield and decrease the waste. However, this would require an increase in particle sizes. Indeed, the direct introduction of loose dust and water bearing sludges into furnaces will decrease the gas permeability in the burden, where it may cause gas accumulation, leading to pressure build-up, which may in turn end up in a furnace explosion. Particle size upscaling can be achieved through high temperature agglomeration (sintering) (Chaim, 2017; Debrincat et al., 2008), cold agglomeration (briquetting, tableting) or with both cold and hot agglomeration steps (pelletization). The latter is widely used in the iron ore industries (T.C. Eisele and Kawatra, 2003).

Each method outputs different products, each with different chemical and mechanical properties. The predominantly considered properties are the mechanical resistance of the agglomerates and the generation of fines of the latter. Most technical approaches involve binders and/or moisture to increase agglomeration performance. Moisture enhances capillary forces and surface tension, but the impact may decrease when particles dry. Therefore, binders are used. The most common binder is bentonite for iron ore pelletization. Organic binders (e.g. lignosulfonate (Thomas By, 2017) or KemPel (Moraes et al., 2018)) are becoming a popular replacement for inorganic binders as only low amounts of impurities are added to the furnace. Presently, companies try to agglomerate their own dusts and sludges based on empirical experiments, as no universal agglomeration process is available.

In our case, the following agglomeration requirements must be met: (i) sufficient mechanical strength in order to allow packing, transporting and storage, without generating new dust, (ii) a chemical and mineralogical composition that is easily reducible in the furnace and (iii) properties that will not deteriorate gas permeability (e.g. (Pietsch, 2002)).

Cold agglomeration without using a binder is the best economical and ecological option for complex industrial dusts but it has not yet been studied to sufficient detail. The process was essentially investigated for monophasic powders in pharmaceutical (Herting and Kleinebudde, 2008a; Johansen and Schæfer, 2001), food (Rondet et al., 2016) and material industries (Kotzé, 2002; Wollborn et al., 2017).

Pietzsch (2002) and Schulze (2008) outlined that the most important forces controlling cold, binderless agglomeration are capillary bridges linked to moisture, and interparticular (Van der Waals and electrostatic) forces. Consequently, the physico-chemical characteristics (hardness,

nature, structure, surface states…) of the materials and the mechanics/physics of the agglomeration method have all to be taken into account.

Industrial dusts and sludges are complex materials. Being multiphased and heterogeneous in particle size, they provide variable physico-chemical properties during agglomeration. Particle size distribution is an important factor for agglomeration: for example, during granulation particles of about 1- 3 mm act as nucleation site of the granules, while particles smaller than 0.2 mm act as an adhesive layer (Pan et al., 2016). The mineralogy and its associated textures, the crystallography and the various grain/phase morphologies are important factors. Bulk and phase chemistries of the materials and physical parameters (e.g. Cation Exchange Capacity (CEC), Specific Surface Area (SSA)) are also to be taken into account. All these parameters are rarely investigated in this context, and no comprehensive systematic study currently exists.

This paper is the first part of a larger project. The objective of this study is to define key parameters for cold agglomeration of dusts from the manganese pyrometallurgical processing chain, based on characterization work and theoretical consideration. Future communications will address agglomeration experiments and a predictive modeling of agglomeration potential based on material characteristics, respectively. In the present study and for the first time, a systematic mineralogical, chemical and physical characterization of 13 representative samples from ore feed, processing dusts and sludges from the ferromanganese process chain of the Sauda plant (Eramet NORWAY) was performed. A multi technique approach was chosen for mineralogy and chemistry (XRD, XRF, SEM-EDS, QEMSCAN), particle size distribution (laser granulometer, QICPIC) in order to compare and evaluate the performance of each technique. In addition, parameters such as CEC, SSA, using the Brunauer-Emmet-Taylor (BET) method) and zeta potential, at present rarely studied for those materials (Johansen and Schæfer, 2001), are presented.

Thirteen samples from the manganese pyrometallurgical plant of Eramet in Norway (Sauda; Fig. 3.2) were studied. Six samples represent the feed material: (i) lateritic manganese ore and its sintered (reduced) product from the Mn-mine of Moanda, Gabon (Eramet COMILOG; 1 and 2 in Fig. 3.2, respectively), (ii) mixed carbonate-oxide ore from Gloria and Asman, both from South Africa (ASMANG; 3, 4 Fig. 3.2), (iii) recycled Metal Oxygen Refining (MOR) slag and onsite material spilled during handling (respectively remelt, 5, and spillmix+metal, 6, Fig. 3.2). The raw materials are referred to as: GO (Gabon ore), AO (Asman ore) and GlO (Gloria ore). Those materials are converted into manganese alloy in the furnaces. Other samples originate from (i) the environmental hood (located above the furnaces hall, 7, Fig. 3.2), (ii) dust generated during metal tapping from the furnace (8), and (iii) sludges produced in a water treatment plant processing dusts collected in Venturi filters (9). Samples 7, 8 and 9 will be referred to as smelting dusts hereafter. MOR low density ultrafines (<100 µm) do not contain metal droplets (10) while, two types of Cooler dusts (medium density ultrafines, <100 µm, and high density medium sized fines, 100-500 µm) do (11, 12). Samples 10, 11 and 12 will hereafter be referred to as refining dusts. The last sample is ferromanganese dust, generated during the crushing of the alloy.

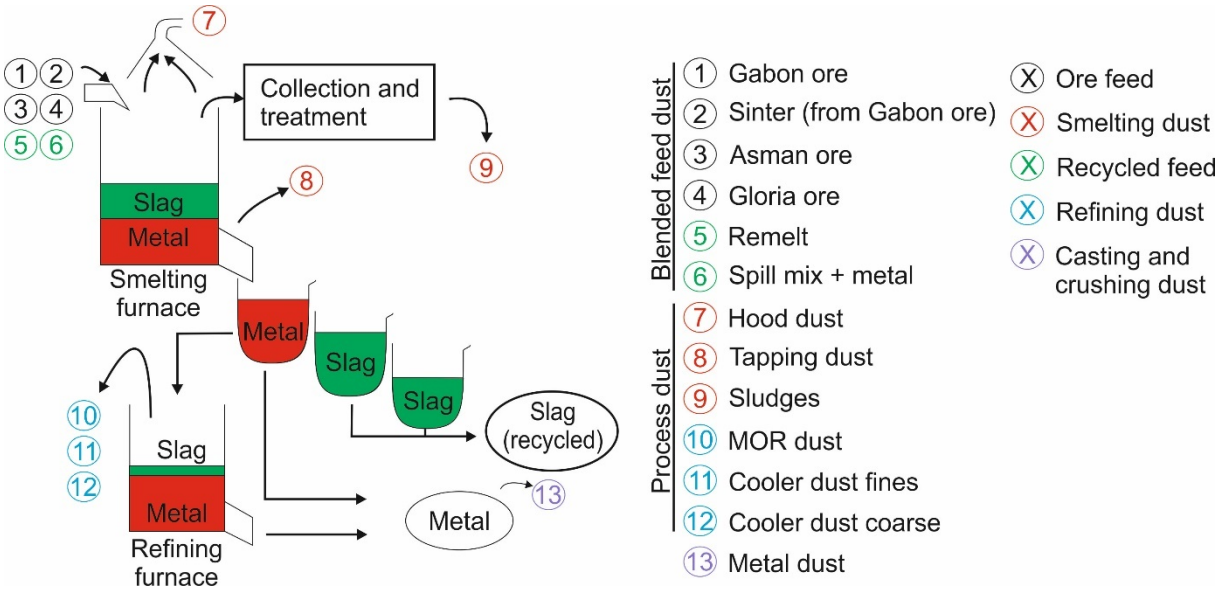

Fig. 3.2. Schematic sampling location across the treatment process of the ferromanganese production plant Sauda (Eramet Norway).

4. Methodology

4.1 Sampling & handling

According to Lyman, a sampling operation must be mechanically and methodologically correct, which means that every particle in the material feed have an equal probability to be sampled (Lyman, 2014). In the present study, our specimens were not acquired according to these principles, hence we can't certify their representativity. However, they fit the objective, which is to obtain a qualitative characterization of the different products across the production chain. Each material line has a very specific mineralogy, as is later shown later in this paper (See part 5.2). The mineralogy assessed in this paper is similar to the specifications defined in the literature ((Eissa et al., 2012; Hooper, 1968; Li and Robertson, 1997; Tangstad and Olsen, 1997)) and the proportions are within natural, limited variations. Once a deeper comprehension is obtained, it will be possible to recreate the properties of the different variations of a given dust to predict their behavior.

All the materials were manually taken inline of the process: from the feeding lines of the furnace for the feeds, and from their collecting recipient (big bags) for the process dusts.

All subsequent division of homogenized samples were performed using a riffle split to keep sample representativity.

All samples were wet sieved to separate the following fractions: *C* (Coarse: >1 mm), *M* (Medium: 1-0.1 mm), and *F* (Fines: <100 µm). Chemical and mineralogical analyses were performed at Eramet IDEAS, Trappes (France).

The scale used to determine the results of the sieving have an accuracy of 0.05 g.

4.2 Bulk chemistry

For chemical analyses, all samples were grinded to <100 µm and subsequently dried at 105°C for about 12h. The Loss On Ignition (LOI) was determined through a 2h calcination at 1000 °C to ensure that each element reaches its highest oxidation state. LOI may assume both positive and negative values. A positive value (weight loss) indicates volatile loss, while negative values indicate oxidation of highly reduced material (metals, monoxides, spinel-type oxides). Such highly reduced materials are metastable at ambient temperatures, but will revert to their stable state when heated, which involves higher oxidation states.

All bulk samples and their different size fractions were analyzed for major, minor and trace elements by means of X-Ray Fluorescence spectroscopy (XRF; PANalytical AXIOS Minerals equipped with a Co-anode). Total sulphur and carbon contents were analyzed by combustion (C/S Horiba EMIA 320V analyzer). Chlorine was determined by ion chromatography (881 Compact IC Pro. Colonne anionique Metrosep A Sup3- 250/4.6, Metrohm) and Boron by ICP-OES (720, Agilent).

All the detection limits and uncertainty are reported along with the analytical results in the research data linked to this paper.

4.3 X-Ray Diffraction (XRD)

Qualitative mineralogical analyses were performed using X-Ray Diffraction (XRD, PANalytical X'PERT PRO, with a Cu-anode, measuring time about 1h per sample). Prior to measurements, samples were grinded to about 40 µm. The obtained diffractograms were evaluated using HighscorePlus software and the Crystallography Open Database (Day, n.d.).

4.4 Mineralogical quantifications estimations

Based on bulk chemistry and qualitative mineralogy, the modal mineralogy of each sample fraction was calculated. The theoretical compositions of mineral endmembers were used to perform these calculations. This approach is naturally erroneous as the present phases are frequently composed of solid solutions. The mineralogy varies in the different samples. The methodology is described in Fig. 3.3.

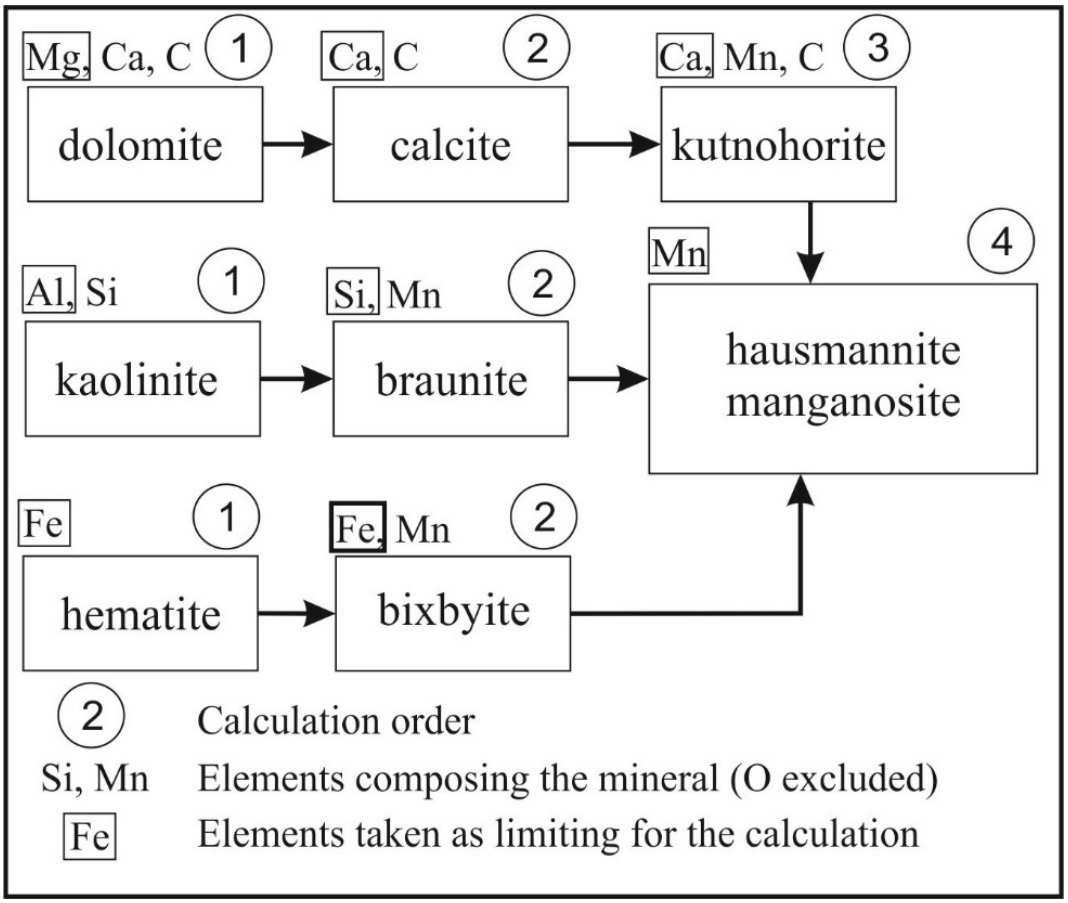

Fig. 3.3. Modal mineralogy calculation methodology. The minerals with exclusive elements are calculated first, and then the next until all elements have been accounted for.

When no discriminant element exists (e.g. between calcite $CaCO_3$ and kutnohorite $(Ca, Mn)(CO_3)_2$ in Fig. 3.3), a "repartition coefficient" is introduced to distinguish between both minerals. This coefficient is calculated for each case, following two rules: (i) involvement of at least 2 wt.% in both minerals to fit the XRD detection limit (~2 vol.%), (ii) total mineral quantification closest to 100 wt.%. The calculation does not consider the oxidation state of the elements (e.g. Mn) as they are not available. Because this method does not consider chemical variations in each mineral phase, it remains approximative and may lead to misinterpretation if used without additional information. Its accuracy is also dependent on the chemical analyses uncertainties.

4.5 Polished section preparation

Dusts and block samples were prepared to fit into molds. Fluid resin, methyl methacrylate, was poured over the samples. Samples were hardened in an autoclave at 45 °C and 80 bars for 48h: Since small (<1 mm) gaz bubbles are produced during the hardening, smaller/less dense particles (e.g. rhodochrosite: 3.69, pyrolusite: 4.80) may have been displaced upwards. Although most of the material is concentrated at the bottom of the sample, some of the samples may exhibit an under-representation of the smaller/less dense material in the polished section. The mount was then polished (Rotoforce 3/Rotopol 31, Struers, France). All samples were coated with an approximately 25 nm thick carbon layer for SEM/QEMSCAN investigations.

4.6 Scanning electron microscopy (SEM) and Qemscan

A high-resolution SEM-FEG Zeiss Supra 55 equipped with a 30 mm² Bruker SDD EDS detector was used in the Back Scattered Electron (BSE) and Secondary Electron (SE) modes to study the morphologies and textures of the dust particles at an accelerating voltage of 15 kV, with a diaphragm dimension of 120 µm, and a working distance of 8.6 mm. Energy Dispersive Spectroscopy (EDS) was used to obtain qualitative elemental composition of the grains.

A FEI Quanta 650F FEG, equipped with 2 Bruker Xflash 30 mm silicon drift EDX detectors, was used in BSE mode. The results were automatically treated with an associated QEMSCAN® system (Quantitative Evaluation of Minerals by SCANning electron microscopy, at 25kV and 10 nA, average counting time 5h per section). The iMeasure v5.4 software allows the collection of statistical data on mineralogy, and quantitative textural analyses of samples, which are classified and processed using the iDiscover v5.4 software suit. Due to the very fine particle size, the field image measurement option was selected. X-Ray data were collected with a 2.5 µm resolution, and total X-Rays count of 2000 counts per spectrum. The software compares the analyses to a database to identify the mineralogy of each pixel. It then calculates the mineralogical quantification based on the assumptions that (i) the surface proportions of the minerals are representative of their 3D distribution and (ii) the theoretical density of each mineral can be applied in the samples. The classification used in this study was verified by the XRD and bulk chemistry results to ensure the best fit between the different methods.

The challenge in studying fine particles such as industrial dusts with the QEMSCAN®, is two-fold:

(i) The resolution of the equipment defined by the spot size (about 1 µm) resulting in interferences of analyses (2.44 µm). This makes it difficult to have a clear-cut signature of very small particles or complex textures, thus complicating phase identification. As each microanalysis could be a mixture of several phases, mineral quantification needs to be statistically resolved. This was done by classifying EDS analyses to the dominant phase of mixes.

(ii) The characterization of a wide range of materials (semi-carbonated to oxide ores, products along the pyrometallurgical processing chain) with one single database. Usually a database is built for a specific purpose on a given sample type. A universal database demands larger constraints, as there are phases with quasi-identical chemical compositions. In order to overcome this issue, the boundaries between minerals were identified by statistical data treatment of raw EDS Qemscan data. The (Mn+Fe)/O elemental ratio was used to discriminate between Mn oxides (pyrolusite, haussmanite), allowing a good but not perfect distinction. Iron was included as it substitutes for Mn in the crystal structures.

The shape factor used in this paper is a built-in function of the QEMSCAN software. It calculates the ratio of the square of the perimeter to the area of a particle and gives an estimation of the roundness of particles.

4.7 Granulometry and granulomorphology

Apart from the QEMSCAN software, two methods were used to assess the Particle Size Distribution of the samples: laser granulometry, using a CILAS 1064L, and optical granulometry, with a Sympatec QICPIC apparatus. The analytical cycle is similar for both machines: a few milligrams of sample material are injected into the apparatus in an aqueous medium, and

ultrasound is used to separate the particles from each other. Water is set to flow through the apparatus for the analyses. While the CILAS relies on laser diffraction to measure particle sizes, assuming spherical particles, the QICPIC uses optical measurement and image analysis to measure and calculate morphological properties of the particles (e.g. Equal Projection Circle (EQPC), aspect ratio, convexity, sphericity). The theoretical calculations applied by the software are presented on the Sympatec website (Qicpic, n.d.). The CILAS ideally analyzes fine particles with a resolution of 0.1 µm, while the QICPIC is ideal for larger particles (up to 1 mm) with a resolution of ~5 µm for size analyses, and ~ 20 µm for calculated properties. For both machine, each analysis was repeated until three consecutive measurements showed similar curves. The values were then averaged to obtain the curves presented in this paper. Both methods were used and compared in this study. The QICPIC and QEMSCAN results were also compared.

4.8 Specific Surface Area (SSA) and Cation Exchange Capacity (CEC)

Specific Surface Areas (SSA) were analyzed for fractions <100 µm (except the Cooler dusts) in using the Brunauer-Emmett-Taylor (BET) method (Brunauer et al., 1938). Measurements were performed at the Études Recherches Matériaux laboratory (ERM, Poitiers, France) using a TRISTAR II 3020 from Micromeritics®. The CEC was analyzed at BRGM (Orléans, France) using cobaltihexamine following the NF X-130 (1999) norm. Since this reactant is a chloride compound, it may artificially increase its reactivity with a sample containing chlorides such as sylvite (KCl) in the hood dust and sludges. The obtained CEC values therefore have to be considered inconclusive for these kinds of samples. The uncertainty of those tests is reported in the research data linked to this paper.

4.9 Zeta potential

Zeta potential is the electric potential at the shear boundary, the interface between the outer Helmholtz plane and the bulk of the solution (Lu and Gao, 2010). Zeta potential measurements (Nanobrook 9000plus PALS with green laser) were performed at the Karlsruhe Institute of Technology (KIT, Germany). These analyses require particles ≤ 1 µm. The AO and GlO ores did not generate sufficient amount of fines, hence a suitable fraction is only available among the ores for GO. Analyzed samples included the <100 µm fraction of GO, sinter, tapping dust, sludges, MOR dust and metal dust. The material was suspended in MilliQ (ultrapure) water. The suspension material was extracted for measurements. The zeta potential was calculated from the electrophoretic mobility using the Smoluchowski model (von Smoluchowski, 1903). A single result is the average value of ten sets, composed of ten measurements each.

In a first series, the measurements were performed by injecting the suspended material into MilliQ water and measuring the pH. This was applied to all the above-mentioned samples.

However, the zeta potential is pH dependent, and the IsoElectric Point (IEP), which corresponds to the pH value where the zeta potential reaches 0 mV, is considered the most favorable for particle agglomeration (Lu and Gao, 2010). To find the IEP, the pH was monitored and adjusted between two measurements of the same material. This enables to obtain the correlation between pH variations and zeta potential variations. The adjustment was made through the addition of a base (NaOH) to increase, or an acid (HCl) to decrease the pH. This second series involving pH-variation is time consuming and was therefore applied to only four samples: GO, sludges, MOR dusts and metal dusts.

5. Results

Due to the important number of samples, and the volume of data generated by the XRF and XRD analyses, this paper will present synthetic charts. The exhaustive tables can be found in the research data linked to this paper (Appendix 1 to 4).

5.1 Bulk chemistry

The complete results, including the minor elements (Ba, Cu, Na, P, Sr, Ti, Zn, S, B and Cl) are presented in research data linked to this paper. Figure Fig. 3.4 shows the elemental composition of the sample specific granulometric fractions. It illustrates the differences in major elements, major changes during the pyrometallurgical processing, and the variations of the minor elements (See research data).

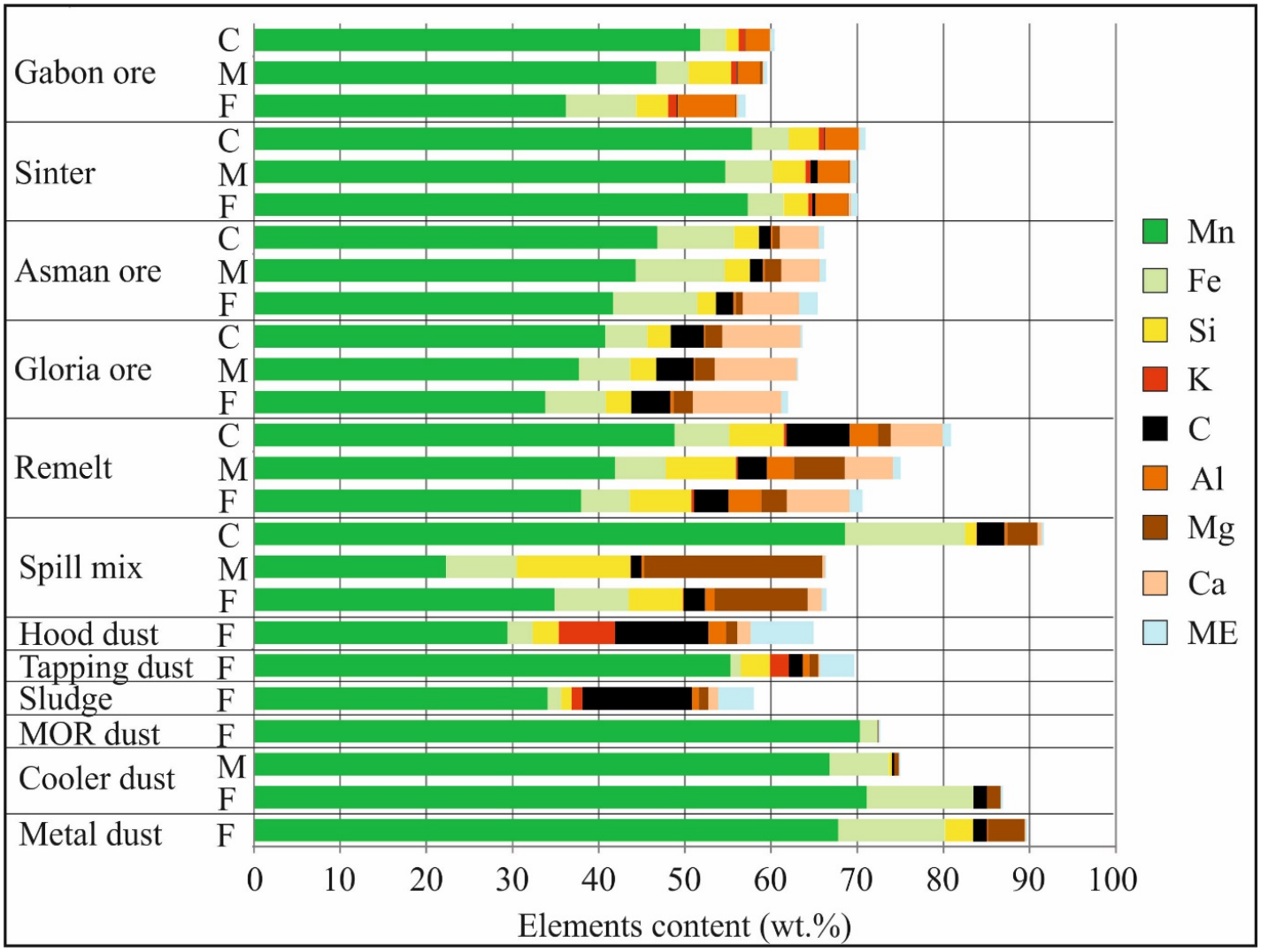

Fig. 3.4. Elemental concentrations (wt.%) of the samples from Mn-ores (top) to metal (bottom). Granulometric fractions were analyzed separately, represented as *C* (Coarse, 500 µm – 2 mm), *M* (Medium, 100-500 µm) and *F* (Fine, < 100 µm). ME (Minor elements): Ba, Cu, Na, P, Sr, Ti, Zn, S, B and Cl. The difference to 100% represents oxygen (not measured).

The element contents are reported in weight percent. Manganese is the main element of interest. Si, C, K, Al, Mg and Ca impact the pyrometallurgical processes. Therefore, we discuss the elements showing major changes.

Manganese and iron are present in different oxidation states from feed material to final product (Mn 0, 2+, 3+, 4+; Fe: 0, 2+, 3+). The chemical analyses are presented as elements, since we do not have exact information regarding the oxidation state (see research data). The LOI of the analyzed samples shown in Table 3.1 vary between +15 to -26 wt.%, representing a gradual decrease in oxidation state of the samples along the processing chain. The values presented for the ores are averaged across all fractions.

Table 3.1. Loss On Ignition (LOI) for each sample, averaged across all samples. The positive values show an effective mass loss due to volatile elements loss, while the negative values corresponds to a mass gain due to an oxidation of highly reduced material.

Sample	GO	AO	GlO	Sinter	Remelt	Spillmix	Sludges	Hood dust	Tapping dust	MOR dust	Metal dust
LOI (wt.%)	14.3	8.1	15.7	-0.3	-5.0	-9.6	35.4	22.0	3.9	-0.1	-26.1

Remelt (recycled material) seems to have similar ratios between its elements (Mn excepted), but an increasing oxidation state with decreasing fraction size (LOI: -15.49 (C), -11.77 (M), -3.19 wt.% (F)). The sinter fractions exhibit similar compositions (3 wt.% Mn variation being the highest observed in Fig. 3.4), while the spillmix has more variable composition.

For the fine fractions, the elemental composition and the oxidation state appear to be controlled by the pyrometallurgical process (Fig. 3.2). Since the process transforms oxides into metal, this seems obvious. However, sludges and hood dust are more oxidized than the tapping dust, although the three are extracted at the same process step.

As expected during Fe-Mn production, the Mn content increases from about 40 wt.% in the feed to ~70 wt.% in the final products. This is related to the decrease in contents of both oxygen and minor elements. The feed materials also contain Al, K, Ca and minor elements (as listed above), which are void or diminished in content in the final products (metal/MOR).

Some dust types generated along the ferromanganese production process act as elemental traps. For example, K is present in small amounts in GO and the sinter feed. It is most concentrated in the hood dust. A small amount of K is also present in sludges and tapping dust, but not in the subsequent material. Minor elements having low evaporation temperature (Zn, Pb…) are also concentrated in the smelting furnace dusts. Silica is concentrated in the smelting and refining slags, but some silica is still present in the metal dusts (Fig. 3.4).

GlO and AO contain Ca and C. The carbon content in GlO (~4.3 wt.%) is about twice as high as in AO. Sludges and hood dusts contain higher C than in the ores (12.7 and 10.8 wt.% respectively). Carbon is related to Ca-Mg carbonates in the AO and GlO and Mn carbonates in the smelting dusts. The subsequent material contains C <1.6 wt.%, (Fig. 3.4, Research data).

Sulfur is present to a significant extent only in the AO *F* fraction (0.48 wt.%), remelt (~0.23 wt.%) and smelting dusts (hood dusts: 0.98 wt.%, tapping dusts: 1.14 wt.%, sludges: 0.32 wt.%). Chlorine is present in significant amounts in hood (1.56 wt.%) and tapping (0.33 wt.%) dusts.

5.2 Mineralogy

Based on XRD analyses, the feed material is composed of two types of ores (oxidized and semi-carbonated; Fig. 3.5). GO hosts oxides (pyrolusite, cryptomelane), hydroxides (lithiophorite, goethite, gibbsite), clay minerals (kaolinite and illite), and quartz. Clays and gibbsite are concentrated in the *F* fraction. Cryptomelane is present in the *C* and *M* fractions. The semi-carbonated AO and GIO ores contain oxides (AO: hausmannite, bixbyite, hematite; GlO: hausmannite), hydroxides (AO: manganite), silicates (AO, GlO: braunite) and carbonates (AO, GlO: kutnohorite, calcite, dolomite). Contrary to GlO, the only difference between the fractions is the presence of dolomite solely in the *F* fraction of the GlO. The sinter, produced from GO, is only composed of spinel-type oxides (manganosite, hausmannite, galaxite) and silicates (tephroite, quartz). The remelt contains oxides (manganosite, hausmannite, galaxite), silicates (glaucochroite, quartz, forsterite) and carbonates (dolomite, calcite). The fraction-related variations are linked to the carbonates. Calcite is absent from the *C* fraction, dolomite is absent from the *M* fraction. The spillmix contains metals, oxides (manganosite and hausmannite), carbonates (dolomite and calcite) and silicates (forsterite). The smelting dusts also show different typologies. Sludges mostly contain carbonates (rhodochrosite, kutnohorite, smithsonite), while tapping dust mainly consists of oxides (hausmannite, manganosite) and traces of quartz. Hood dust mostly displays manganosite and hausmannite, but also rhodochrosite and kutnohorite. All three samples contain sylvite (KCl). The mineralogical simplification continues in the refining dusts composed of manganosite, hausmannite and ferromanganese. Forsterite is present in the *C* fraction of the cooler dusts. Metal dusts are composed of FeMn and forsterite.

Fig. 3.5 presents the quantitative mineralogy from QEMSCAN analyses and modal calculations performed based on XRD-XRF correlation. QEMSCAN analyses allowed the distinction and quantification of the solid solution in the same mineral group (e.g. calcite, dolomite, kutnohorite). The quantification of the Mn-bearing and non-Mn-bearing phases by QEMSCAN shows the chemical complexity of those structures, with Mn substituting for Ca, Mg and Fe. Classification was simplified into Mn-bearing and non-Mn-bearing phases (threshold at about 20 wt.%), presented in Figures 4 and 5. Furthermore, QEMSCAN indicates mineral phases below 2 vol.% in the sample (below detection limit of XRD), such as FeMn in the MOR dusts and hydroxides in remelt. The mixed phases, such as kutnohorite or galaxite ($MnAl_2O_4$) are considered as Mn-bearing phases.

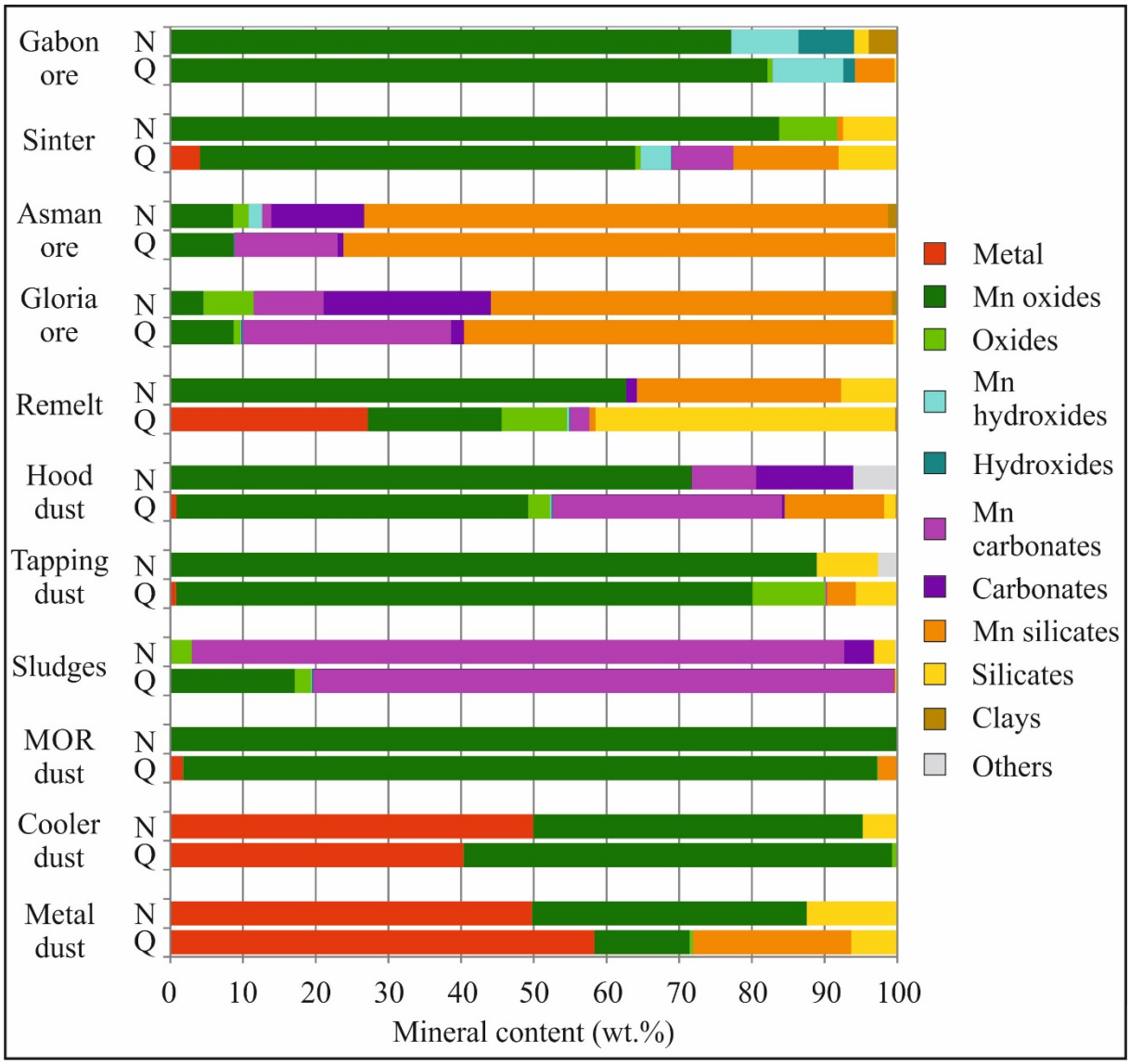

Fig. 3.5. Mineralogical quantification performed on the samples during this study. The bottom line (Q) presents QEMSCAN data. The top line (N) presents the modal quantification based on the combination of XRD phase identification and XRF chemical quantification, normalized to 100%.

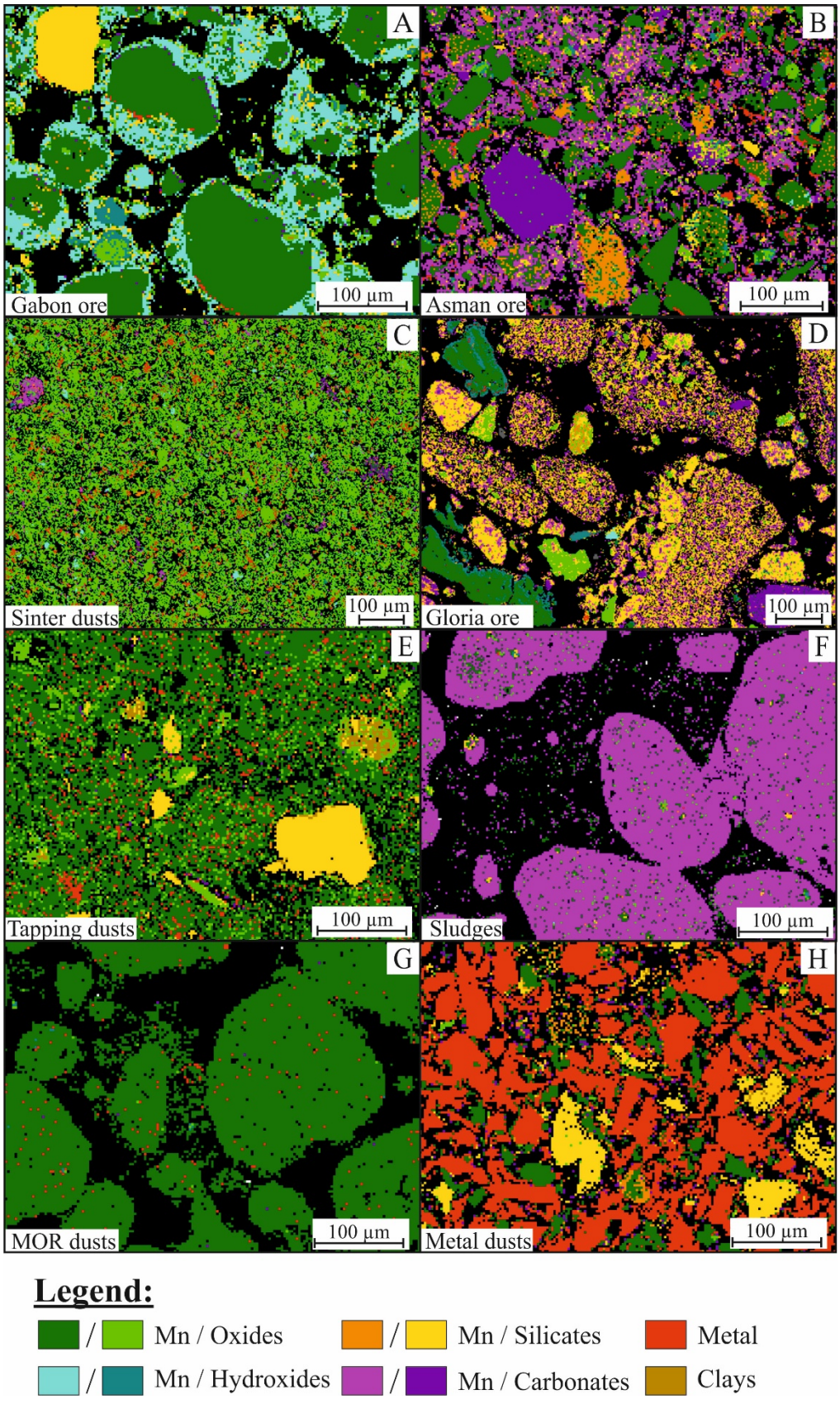

Fig. 3.6. QEMSCAN classification of *F* fractions of samples across the FeMn production. A) Gabon ore, B) Asman ore, C) Sinter dusts, D) Gloria Ore, E) Tapping dusts, F) Sludges, G) MOR dusts and H) Metal dusts.

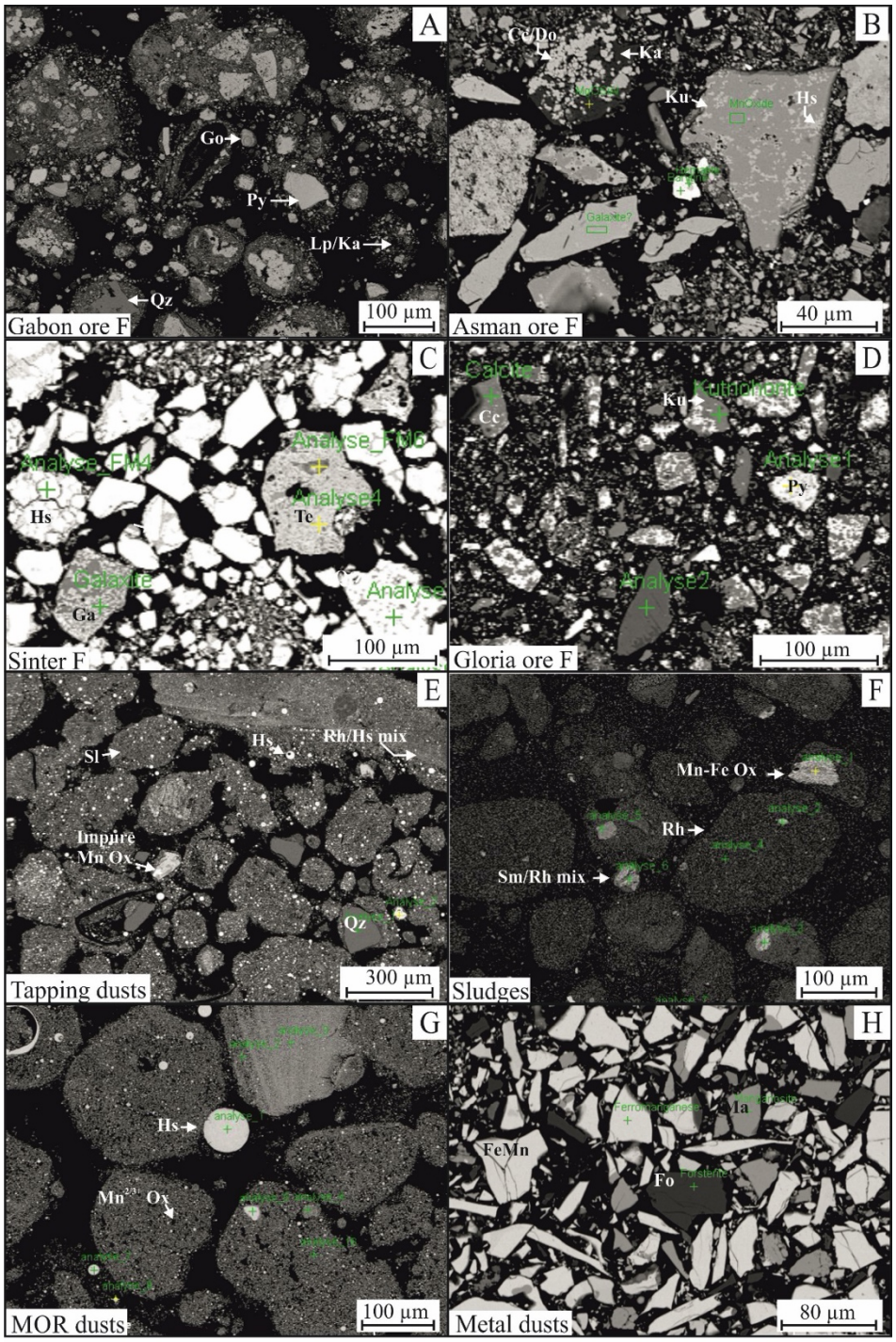

Legend:

Cc:	Calcite	Hs:	Hausmannite	Py:	Pyrolusite
Ba:	Barite	He:	Hematite	Qz:	Quartz
Do:	Dolomite	Ka:	Kaolinite	Rh:	Rhodochrosite
FeMn:	Ferromanganese	Ku:	Kutnohorite	Sm:	Smithsonite
Fo:	Forsterite	Lp:	Lithiophorite	Sl:	Slag-like matrix
Ga:	Galaxite	Ma:	Manganosite	Te:	Tephroite
Go:	Goethite	Ox:	Oxides		

Fig. 3.7. SEM-BSE pictures of samples across the FeMn production, with HV = 15 kV and a working distance of 8.3 mm. A) Gabon ore, B) Asman ore, C) Sinter dusts, D) GlO, E) Tapping dusts, F) Sludges, G) MOR dusts and H) Metal dusts.

In general, the mineral group estimates between the two quantification methods are consistent. Differences are observed for GO involving the absence of clay minerals in the QEMSCAN analysis. This is related to the small particles size (see section 2.1). In this sample, the estimated Mn silicate content signifies mixing of silicates and clays with Mn-bearing phases (oxides and hydroxides) due to the low resolution of QEMSCAN with respect to particle size (Fig. 3.6).

QEMSCAN analyses of the sinter show notable differences with the modal calculated mineral content (Fig. 3.5), by displaying metal and carbonate phase quantification. This may be due to variable pore sizes and high porosity of the material, unlike the other feeds. Such porosity increases the probability of analyzing resin or void along with the sample. This "perturbated" signal will create an overestimation of certain phases (e.g. carbonate if mixed with resin, or metal if mixed with void). These overestimations are corrected for by chemical assessment between QEMSCAN and XRF, and by QEMSCAN data base calibration using specific microprobe analysis (Blancher et al., 2015).

5.3 Morphology

GO (Fig. 3.6A and Fig. 3.7A) includes particles (10-200 µm) composed of angular Mn-oxides (pyrolusite) and goethite, which are surrounded by a mixture of Mn-hydroxides (lithiophorite) and clays, forming composite rounded particles (Fig. 3.6A). Rare angular quartz particles of ~100 µm are present. Neoformed lithiophorite and clay minerals occur as needles and/or web-like porous structures. Fibrous illite involves aggregates of linear grains mixed with kaolinite (Fig. 3.8).

The AO (Fig. 3.6B) shows highly variable mineralogy, bimodal grain sizes for the Mn carbonates (~1 and ~100 µm), Mn-silicates and clays. The large angular particles are composed of kutnohorite mixed with hausmannite, and angular grains of galaxite. The latter form elongated grains (40 to 20 µm in length), with slightly smoother edges. Micron-size carbonates (kutnohorite, calcite, dolomite, and magnesite) are intergrown with kaolinite and quartz, forming angular to rounded aggregates (about 35 µm). Those composite aggregates form a matrix surrounding the angular grains. Rare barite grains (~10 µm) occur.

The sinter dusts show grain sizes below 100 µm (Fig. 3.6C and Fig. 3.7C). While QEMSCAN represents particles around 20 µm, SEM shows higher variability. Grains are mainly angular, where particles are either rounded or angular. Tephroite particles are composed of microcrystalline needles while hausmannite particles consist of ~10 µm large, euhedral crystals. Hausmannite may also form grains of variable sizes (1 to 80 µm).

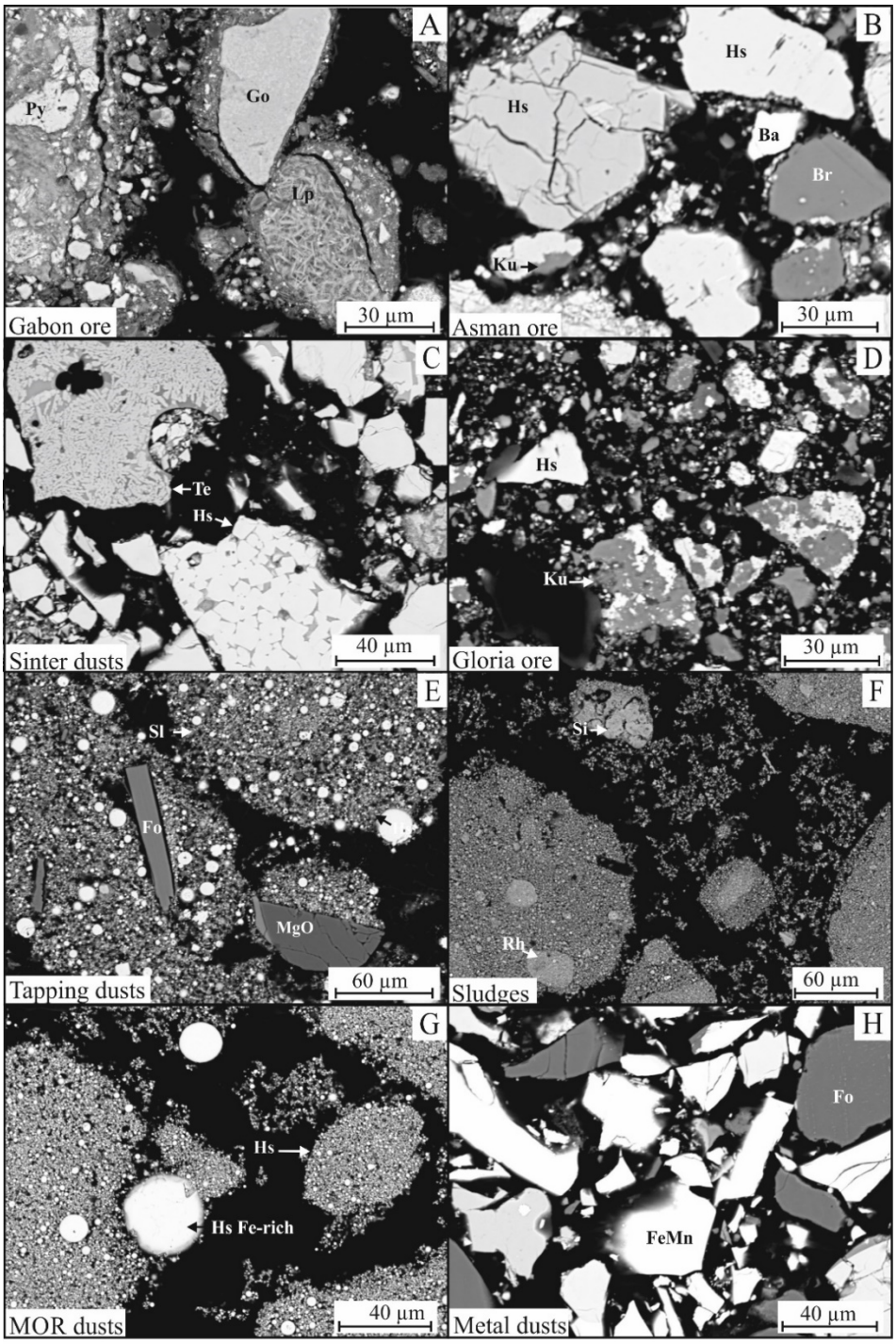

Legend:

Cc:	Calcite	Go:	Goethite	Ox:	Oxides
Ba:	Barite	Hs:	Hausmannite	Py:	Pyrolusite
Do:	Dolomite	He:	Hematite	Rh:	Rhodochrosite
FeMn:	Ferromanganese	Ka:	Kaolinite	Si:	Siderite
Fo:	Forsterite	Ku:	Kutnohorite	Sl:	Slag-like matrix
Ga:	Galaxite	Lp:	Lithiophorite	Te:	Tephroite

Fig. 3.8. SEM pictures at higher magnification than Fig. 3.7 of samples across the ferromanganese production sample with HV = 18 kV and a working distance of 8.3 mm. A) Gabon ore, B) Asman ore, C) Sinter dusts, D) Gloria ore, E) Tapping dusts, F) Sludges, G) MOR dusts and H) Metal dusts.

GlO is dominated by 2 types of particles: (1) silicate-carbonate mixes which are most abundant, and (2) Mn oxides-hydroxides composites. Interestingly, "particles in particles" are observed in the silicate-carbonate mixtures, with the included particles being non-Mn-bearing silicate-rich. This is probably related to the impregnation process. Figures 6D and 7D show that particles dominate over individual grains of various sizes (< 70 µm), presenting angular hausmannite and garnet (pyrope).

The tapping dust is composed of rounded particles (~100 µm) hosting spherical hausmannite grains (1-10 µm; Fig 7C). This matrix embeds 10-60 µm long forsterite needles and half-spherical periclase (MgO). Large particles composed of rhodochrosite and hausmannite (~600 µm long, 150 µm large) occur, as well as angular quartz grains (Fig. 3.7C). The bigger particles (20-40 µm) are porous. The EDS analyses show pure Mn oxides for the bigger ones (20-40 µm), but Mn-Fe oxides with traces of Zn for the smaller ones. The QEMSCAN image (Fig 5C) displays more cohesive material (Mn-oxides dominated) including some angular quartz grains (1-100 µm).

Sludges are composed of rounded Mn-carbonate particles a few 100 µm large which are sometimes in contact (Fig. 3.6D). These particles are composed of rhodochrosite grains (1-20 µm; Fig. 3.8D). Smaller particles are rare, and constitute a mixture of smithsonite/rhodochrosite or Mn-Fe oxides, most likely spinels based on EDS results (Fig. 3.7D).

The matrix of both sludge and tapping dusts samples is made of very fine spherical grains, being (i) a mix of dark grains with slag signature (O, Al, Si, K, Mn) and light grey grains presenting a mix of hausmannite/rhodochrosite in the tapping dusts, and (ii) pure dark grey rhodochrosite, with K traces in the sludges.

MOR represents the last step of the pyrometallurgical process. Nearly all particles are spherical and < 100 µm and are Mn-Fe oxides (spinel) (Fig. 3.7G and Fig. 3.8G). Some rare occurrences are white and elongated grains with rounded edges. Based on EDS spectra normalized to 100%, this is a FeMn alloy, composed of about 84 wt.% Mn, 16 wt.% Fe. The matrix is composed of dark grey submicrometric pure hausmannite (Mn_3O_4) particles.

MOR is composed of similar rounded particles as the sludges, but the fraction of intermediate particle sizes (a few tens of µm) is more important (Fig. 3.6, Fig. 3.7, Fig. 3.8E). Mn-oxides (hausmannite) are present instead of Mn-carbonates. Similarly, to the tapping dusts, hausmannite forms spherules. Those grains range from submicrometric to 40 µm, forming both the matrix and the bigger grains of the sample.

Metal dust (Fig. 3.6, Fig. 3.7, Fig. 3.8 F) includes homogenous and angular particles where Mn-metal dominates. Mn oxides (manganosite) show elongated shapes and occur interstitial to the Mn metal. Forsterite is present as large angular grains, interstitial to the Mn-metal.

Figure Fig. 3.9 presents the shape factor analyzed by the QEMSCAN with respect to the mineralogy for the samples presented in figures Fig. 3.6, Fig. 3.7 and Fig. 3.8. The shape factor is the ratio between the squared perimeter and the surface area. It describes the complexity of the shape of a particle: the more complex the shape (convoluted particles, jagged edges...), the higher the ratio, hence the shape factor. A perfect circle and a square have shape factors of 12 and 16, respectively. The morphological parameters of particles < 15 µm tend to be erroneous, due to their size being comparable to QEMSCAN resolution, and were filtered out. This explains the absence of the classes "clays" and "others" which were identified with other methods. This is shown on the previous graphs (Fig. 3.5 and Fig. 3.6). All the mineral groups are considered as gangue material, when not specifically selected. We then calculate the shape factor for each particle. The weighted averages of the shape factors are presented below.

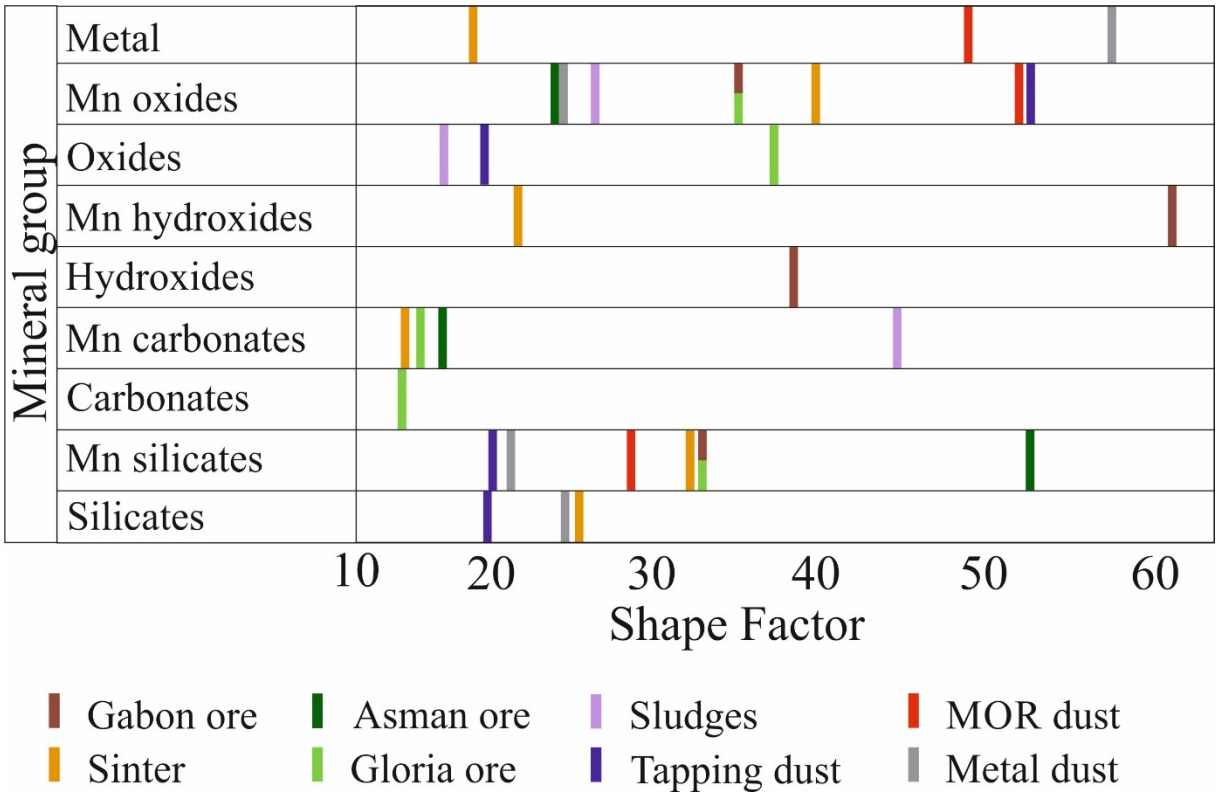

Fig. 3.9. Shape factor calculated by the QEMSCAN software for each sample and each mineral group, reflecting the shape complexity of the particles: higher shape factor means higher complexity.

The shape factor for each mineral type varies within one single sample. GO has similar shape factors (~35) for Mn silicates, Mn oxides and Mn-free hydroxides. However, Mn hydroxides have a complex shape factor around 60. The sinter sample presents two main shape factor groups: (1) metal, Mn hydroxides and silicates (18-25), and (2) Mn silicates and Mn oxides (32-40). For AO, the oxide shape factors are around 25. Mn silicates, on the other hand, have much more complex shapes, with a shape factor of around 52. The GlO presents two shape factor populations: (1) very smooth surfaced particles for CaMg carbonates and Mn carbonates, around 15, and (2) more complex shapes (e.g. serrated surfaces), between 32-37 for the other mineral groups (Mn silicates, Mn oxides and oxides).

Tapping dust exhibits a similar shape factor for the Mn silicates and oxides (~20). The Mn oxides present shape factor values around 52. Sludges show 3 distinct groups of shape factors, i.e.: 12 (oxides), 28 (Mn oxides), and 43 (Mn carbonates). QEMSCAN analyses cannot distinguish the different grains (crystals) for Mn carbonates, since the mineralogy is entirely dominated by the Mn carbonates, forming a bonding matrix. The MOR dust presents higher average shape factors: the lower ones are at 28 for the Mn silicates. Shape factors are 50 for the metal particles and 53 for the Mn oxides. The metal sample has low values for both Mn silicates (21) and Mn oxides (25), but a very high one (57) for the metal itself.

While QICPIC analyses also allow to determine the morphological properties of particles, it involves fundamental differences with respect to QEMSCAN: (1) it will analyze the morphological properties of the particles regardless of their mineralogy, (2) it involves a dynamic water flow, without cluster formation and (3) it acquires 2D projections of particles, while QEMSCAN acquires planar images across the particles that are numerically recalculated in volume.

Three values were calculated during QICPIC measurements: the convexity (amount of concave areas at particle surfaces), the sphericity (ratio between the EQPC (diameter of a circle of EQual Projection area) perimeter and the real perimeter of the particles), and the aspect ratio (minimum Feret diameter over maximum Feret diameter of the particles (Dražić et al., 2016)). For each of these metrics, the higher the value, the simpler particle morphology.

The obtained values (Fig. 3.10) confirm the QEMSCAN results, i.e. that the processed dusts tend to exhibit "simpler" morphology. Across all samples, sphericity values vary between 0.49 and 0.62, with higher values found in tapping, sinter, MOR dusts and GlO, and lower values in AO and GO. Convexities vary between 0.74 and 0.86, with the same distribution, with the sludges yielding high values. Aspect ratio varies between 0.68 and 0.81, with tapping, MOR and sinter showing higher values, and AO, GO and metal dusts showing lower values.

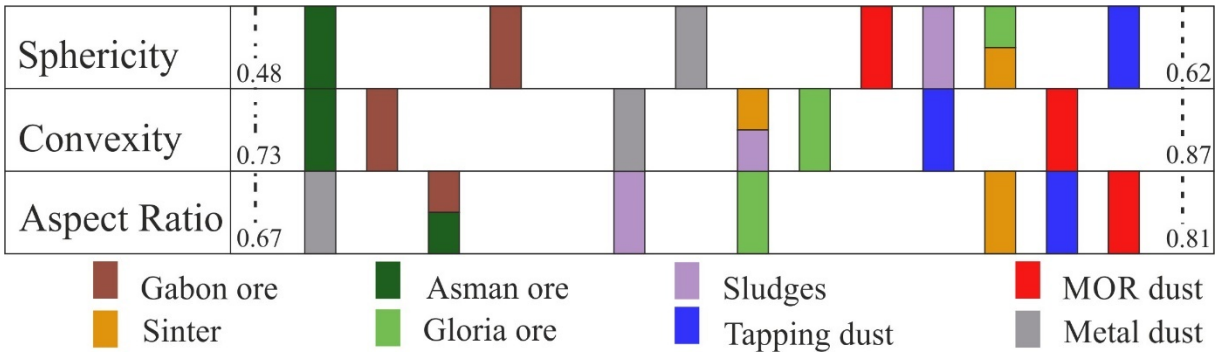

Fig. 3.10. QICPIC measurements results with Aspect ratio, sphericity and Convexity.

5.4 Grain and particle size distribution

Each material was wet screened, and results are shown in Fig. 3.11. Laser granulometry was performed on the *F* fraction for all samples. The amount of fines in GlO and AO was very low (Fig. 3.11). This amount was used for thin section preparation and chemical analysis but unfortunately the material left was not sufficient for granulometric measurements.

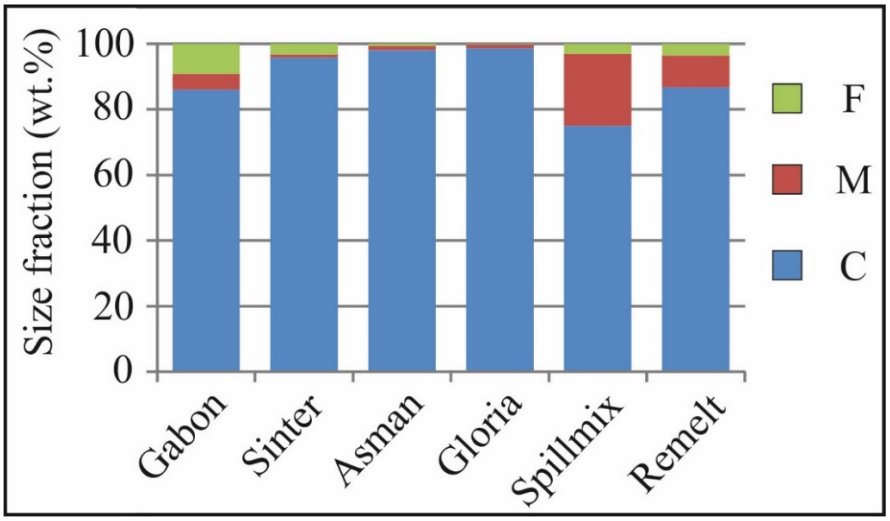

Fig. 3.11. Feed material separated through wet sieving in three fractions: F; Fines <100 µm, M; Medium 1-0.1 mm, C; Coarse >1 mm. Results are expressed in wt. %.

The studied samples exhibit two types of particle size distributions (Fig. 3.12): (A) samples with a main population between 1 and 10 µm (GO, sludges, hood, tapping, MOR and cooler fine dusts), and (B) samples with main population between 10 and 100 µm (sinter, remelt, spillmix, metal dust).

The type 1 (Fig. 3.12A) samples show a multimodal distribution. All dusts peak at 0.3 µm, except the sludges (0.6 µm). GO, tapping and hood dust show populations peaking at 30, 22 and 18 µm, respectively. The type 2 sample (Fig. 3.12B) also has a population peaking at 0.3 µm and a peak at 3.4 µm. For remelt and spillmix, as well as sinter and metal, the main population can be sub-divided with peaks (i) at 13 and 20 µm, respectively and (ii) at 36 µm. Sinter and metal samples are more homogeneous, but do show two populations peaking at (i) around 20 µm, and (ii) at 36 µm. Similar observations are made for the spillmix and remelt samples (Fig. 3.12B).

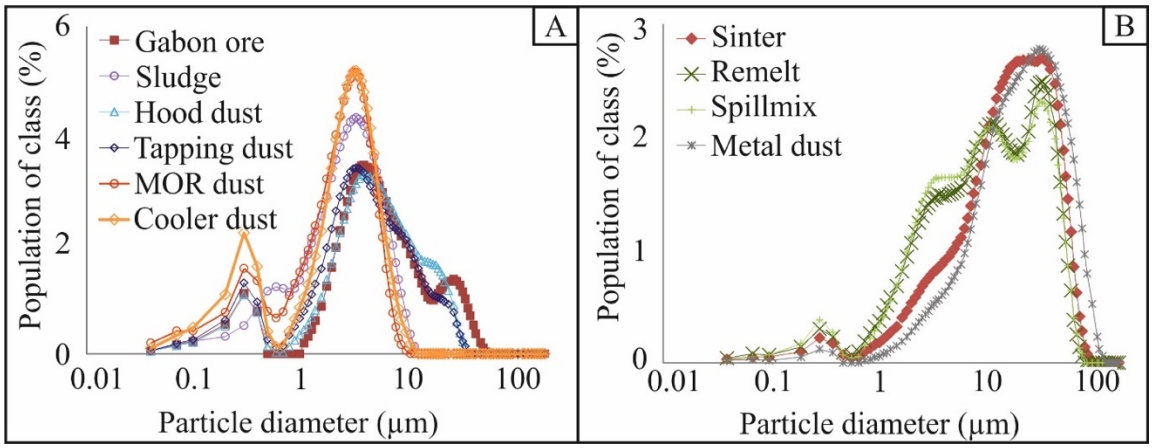

Fig. 3.12. Particle Size Distribution (PSD) of the measured samples. A) type 1 Samples: main population between 1 and 10 µm. B) type 2 Samples: main population between 10 and 100 µm.

5.5 CEC and Zeta potential

The CEC value (Table 3.2) measured for GO is about 8 times higher than for the other ores. The AO (0.3 meq/g) has only half the CEC value of the GlO (0.66 meq/g), although both ores have similar qualitative composition. However, AO has a slightly higher hydroxide content than GlO. The CEC values of the remelt and spillmix, at 4.4 and 3.4 meq/g, respectively are higher than for GO. Among the process dusts, the hood dust reaches 22.2 meq/g, the highest value of all samples. While the sludge is characterized by a CEC of 5.5 meq/g, the tapping dust has a low CEC (0.1 meq/g). The CEC of the metal is the second highest (9.1 meq/g) of all samples, while that of MOR is low (0.5 meq/g).

Table 3.2. Surface charges measurement across the samples. pH was measured during the zeta potential measurement in order to assess the modification induced by the dust on the pH of the added milliQ water. The results presented here are from the first set of measurements.

Sample	GO	AO	GlO	Sinter	Remelt	Spill mix	Sludges	Hood dust	Tapping dust	MOR dust	Cooler dust	Metal dust
CEC (meq/g)	4.03	0.3	0.66	0.49	4.39	3.35	5.52	22.2	0.1	0.48		9.11
Zeta potential (mV)	-18.5			-8.0			-17.4		7.0	-3.3	-25.0	-23.4
pH Zeta	4.8			6.7			5.2		7.8	4.7	5.8	6.2

The GO has a zeta potential value of -18.5 mV, while the sinter exhibits -8 mV (Table 3.2). The tapping dust has a slightly positive value of +7 mV when suspended in MilliQ water. The two tests performed on MOR show zeta potential values of -3.3 and +2.7 mV, i.e. close to zero. Cooler, metal dusts and sludges have negative values. The values determined in MilliQ water pertain to varying pH conductivity values among the samples. The observed linear relationship with CEC may hence be coincidental (Fig. 3.13) and would require further study.

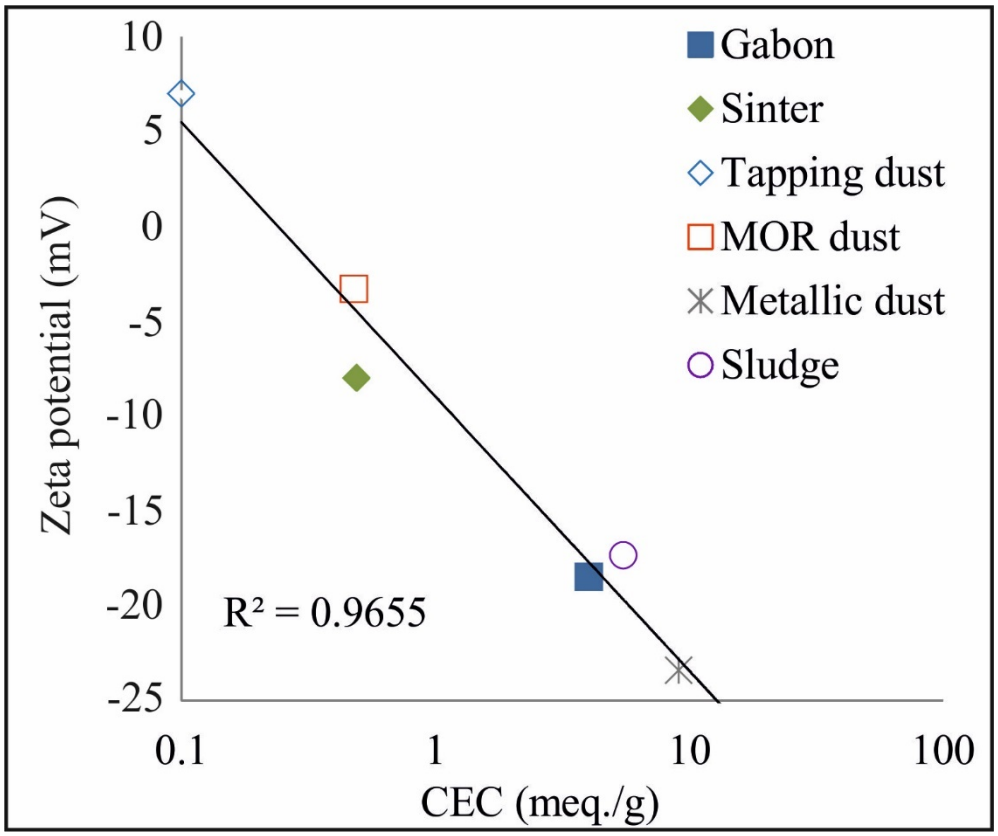

Fig. 3.13. Graph presenting zeta potential versus CEC using the data presented in Table 3.2.

The Isoelectric Point (IEP) was determined for four samples along the processing chain: GO fines, sludges, MOR and metal dusts (Fig. 3.14). The GO zeta potential shows a strong dependence with respect to pH changes, from 27 mV at pH 3.1 to -21 mV at pH 4.8. This is a typical curve for oxide

minerals with low ionic strength. The IEP is at ~pH 4.1. For sludges, the zeta potential is -18 mV at pH ~4. It seems to increase with decreasing pH, reaching zero zeta potential at pH 2. Although the metal dust zeta-potential reaches zero around a similar pH (~2.5), its evolution is not linear. The slope is steeper between pH 2.5 and 3 (0 to -12 mV) than for sludges (around -7 to -11 mV). The MOR dust behavior is peculiar. The points at pH 3.9/2.7 mV and pH 4.7/-3.3 mV, close to zero, are measured by simply suspending the sample in milliQ water. However, when acid or base is added, the values drastically change and align themselves on a curve that would yield an estimated IEP at pH ~2, and a zeta potential that decreases with increasing pH value.

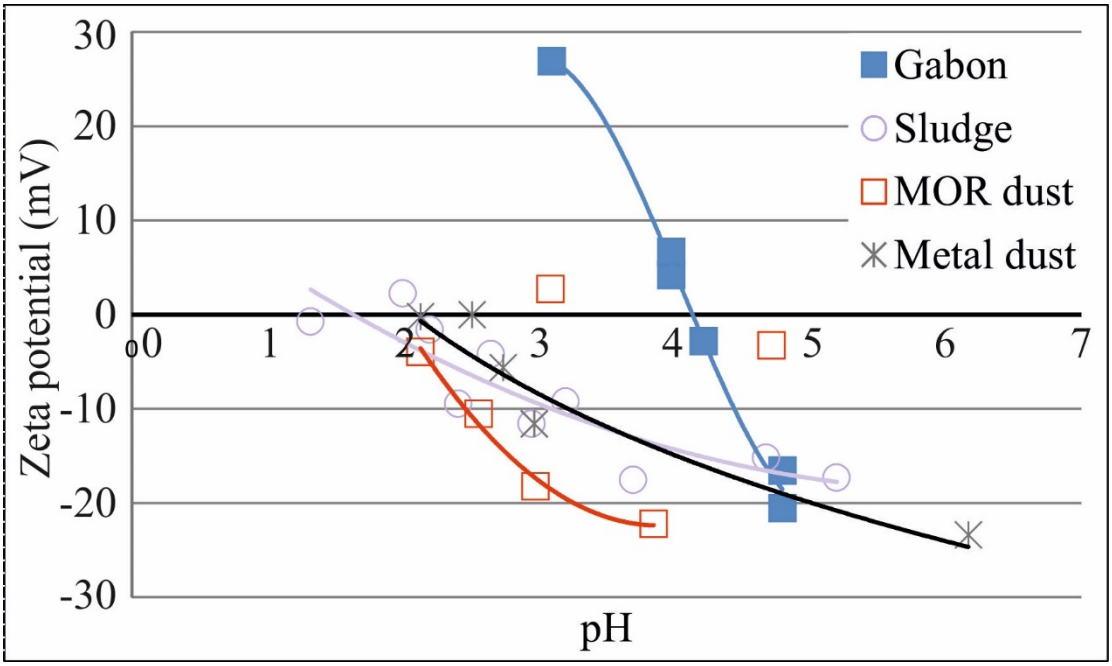

Fig. 3.14. Zeta potential evolution according to pH variations, for the Gabon ore, sludge, MOR dusts and Metal dusts samples.

The BET measurements yield a high variation among the feed material. GO has the highest value at 27 m²/g while AO (2 m²/g), GIO (2 m²/g) and sinter (below detection limit) show the lowest BET (Table 3.3). The recycled materials remelt and spillmix, have higher values at 13 and 20 m²/g, respectively. The values reached by the process dusts are decreasing with increasing degree of transformation, with the metal reaching below the measurable limit.

Table 3.3. Specific Surface Area measurement across the samples using the Brunauer-Emmett-Taylor (BET) method.

Sample	GO	AO	GlO	Sinter	Remelt	Spill mix	Sludges	Hood dust	Tapping dust	MOR dust	Metal dust
BET (m²/g)	27	2	2	0	13	20	7	7	4	3	0

6. Discussion

6.1 Efficiency and assessment of the methodologies

For the studied samples, ten different analytical techniques were coupled to obtain maximum information on each sample. Those methods and their performances regarding the different aspects of characterization are summarized in Table 3.4.

Table 3.4. Each method has specific strengths and weaknesses when dealing with fine material. The main aspects of each methods are summarized here, along with the agglomeration metrics each method allows to investigate.

	Information	Strength	Weakness	Associated metric
Bulk chemistry	Chemistry	Calibration for other methods		Metal content
XRD	Qualitative mineralogy	Reference method	Need chemical calibration Difficult for complex material	Mechanical behavior
SEM	Textural information	High resolution In-Situ chemistry	Low representativity or Highly time consuming	Mechanical behavior
Qemscan	Quantitative chemistry Quantitative mineralogy Granulomorphology	High representativity In-depth analysis Mineral based analyses	Sample preparation dependant High calibration time	Mechanical behavior Interaction surface
QICPIC	Granulomorphology	Low preparation time Good representativity	Low resolution No parameters crosscorrelation	Packing density Interaction surface
Cilas	PSD	High representativity High resolution	500 µm diameter max	Packing density
BET	SSA	Reference method for SSA		Interaction surface
CEC	Reactivity		Only targets ultrafine particles	Van der Waals forces Electrostatic forces
Zeta potential	Reactivity	Variable condition applicable	High preparation time Only targets ultrafine particles	Van der Waals forces Electrostatic forces

The bulk chemistry (in this study investigated via XRF, LOI, ICP-OES, combustion, ion chromatography) is essential to access the major, minor and trace element contents. Chemical characterization is also a key parameter to calibrate other methods (e.g. XRD, QEMSCAN) and the ensuing quantification. In the present study, high volatile (high LOI) bearing samples (GO, GlO, sludges and Hood dusts) are mainly composed of soft, plastic and sectile materials, such as carbonates and hydroxides but also Mn/Fe oxides formed in soils (Vodyanitskii, 2009). In contrast, highly negative LOIs were measured in metal dusts composed of hard, ductile and malleable materials. In our specific system, this information can hence be used as a first indicator of their oxidation state and mechanical properties.

XRD is essential for identification of the major minerals (>2 wt.%). However, the minor phases (e.g. swelling clays), which may act as binders during agglomeration, may be missed. Thus, carbonates were not detected in remelt, nor the Mn silicates in the tapping dusts (Fig. 3.5).

Furthermore, routine XRD lacks distinction between the solid solution of minerals of the same crystallographic system. To access such information, mineral separation and high counting time would be necessary. This would considerably increase the analyses time in industrial setting, and thus decision-making (Orberger et al., 2017).

For high-resolution SEM-EDS and QEMSCAN, sample preparation is a key issue (Lastra and Paktunc, 2016). Section preparation and the use of viscous resins leads to agglomeration due to adhesive forces (Shoyama et al., 2018). The preparation protocol caused a size-based segregation may occur due to different particle properties (Gonzalez et al., 2014; Thornton et al., 2012). Preparation with methylmetacrylate coupled to degassing enhanced segregation.

High-resolution SEM-EDS is performed to access qualitative phase chemistry and morphology. Although achieving representativity is time-consuming, SEM is mandatory to calibrate QEMSCAN results regarding µm-scale grain morphologies.

QEMSCAN analyses then allow quantification of the defined phases, as well as morphological information of particles (e.g. shape factor, grain sizes). When studying dusts <15 µm, as in the present study, the low resolution gives poorer morphological estimations.

For instance, when considering quasi-monomineralic dust samples (e.g. sludge, metal, MOR), the software is not able to deconvolute very fine grained particle aggregates. This leads to erroneous particle or grain sizes as well as shape factors. QICPIC involves less agglomeration issues as it relies on loose, ultrasound-separated sample material. However, it is unable to correlate the different properties of a particle.

CEC represents the cation adsorption potential of a material at a given pH. Higher values are usually considered to be correlated with the clay content. However, Kabata-Pendias (2001) also discusses the possibility that the Mn oxides content affects the CEC value. Indeed, Mn oxides such as pyrolusite or cryptomelane (present in GO) have tunnel structures, which may increase CEC values (Gulbinska, 2014). This is consistent with the results obtained for GO, AO and GlO, whereas CEC of GO is about ten times higher compared to the other two (Table 3.2). The CEC of metals has not been previously studied. The negative surface charge can explain the high CEC value obtained (~9 meq/g) .

The BET surface area, shown in Table 3.3, assesses the external and internal surface area of a sample, which depends on both granulo-morphology and mineralogy. The presence of clays is usually assumed to be the main factor in increasing the BET. However, impact must also be attributed to layer-structured and tunnel-structured phases. Lithiophorite for example has a structure very close to clay minerals, although it is a hydroxide. This fits with the values observed in our samples. The lithiophorite, pyrolusite and cryptomelane content of GO can explain the high

value (27 m²/g). Process dusts have intermediate values. Their formation occurs between the furnace bath and the atmosphere, where temperature decreases rapidly. This prevents the same compact crystallization that could occur in a slowly cooling system, and results in a more porous material, which increases the BET value despite the absence of clay minerals. The variation observed among process dusts is due to differences in crystallization kinetics (Dutta and Bose, 2012). First evaluation of QICPIC results for MOR and metal dusts lead to think that metal would have higher BET values. However, this is not the case, which may be explained by mineralogical differences. The resulting variation may hence be due to grain size and material properties.

The above methods, coupled with the understanding of agglomeration mechanisms, allow a critical extraction of information, such as metal content, mechanical behavior and packing density (Table 3.4). Those are key parameters affecting agglomeration processes (Pietsch, 2002).

6.2 Agglomeration parameters for the studied dusts

The main forces occurring during agglomeration are capillary, electrostatic, and Van der Waals forces (Schulze, 2008). There are two ways to impact these forces: modifying (i) directly one of the terms of the equation (e.g. (Schulze, 2008; Yang et al., 2016)) and (ii) indirectly one of the terms of the equation by altering a phenomenon occurring during the agglomeration cycle. One of the prime examples concerning the latter is the breakage of brittle particles under uniaxial pressure, leading to a more compact agglomerate. Shorter separation distances between particles must be achieved to obtain a hard agglomerate. The key parameter seems to be the mineralogy of a given material, including its variable crystallography and mutual interaction since they are linked in the material brittleness. Particle size distribution is also an important parameter for agglomeration. Pan *et al* (2016) found that a good mixture of particles < 200 µm and particles of 1-2 mm is most favorable, with little or no intermediate particle sizes. The reason is that the small particles will "fill the gaps" left by the large particles that undergo breakage. The following section will discuss the agglomeration potential of each material, estimated by the authors from a theoretical point of view. The main physical properties of each sample are shown in the Table 3.5.

Table 3.5. Summary of the shape properties of the samples investigated in this paper. The hardness values written X/Y* indicate the presence of two very distinct mineralogical family (e.g. Oxides and Clays in the GO) in terms of hardness.

	Hardness Moh	PSD			Sphericity	Convexity	Aspect ratio	Agglomeration potential
		1st decile	Average	10th decile				
GO	6/2*	0.247	4.347	21.623	0.53	0.75	0.70	High
AO	6/3*				0.49	0.74	0.70	Aberage
GlO	6/3*				0.60	0.81	0.75	Average
Sinter	6.5	2.568	17.884	51.314	0.61	0.81	0.79	Low
Tapping	6.0	0.284	2.793	12.763	0.62	0.84	0.80	Low
Sludge	3.0	0.645	2.068	4.849	0.69	0.81	0.73	Low
MOR	6.0	0.202	1.990	4.648	0.58	0.86	0.81	Negligible
Metal	6.5	4.892	23.609	66.386	0.56	0.78	0.68	Low

GO has the highest percentage of layered minerals (kaolinite, illite, lithiophorite, birnessite), with perfect cleavages, intrinsic Van der Waals bonding, and tunnel-structured minerals (pyrolusite and cryptomelane). The layer structure minerals occur as very fine (nm to µm) platy (clays) or needle-shaped (hydroxides) particles of low hardness (~2 on Moh's scale). They usually form soft coatings around the much harder (~6 on Moh's scale) tunnel-structured minerals (pyrolusite, cryptomelane). The layer structure minerals exhibit negative charges on their basal surfaces, and positive or negative charges on their edges depending on the pH. All those properties favor their adsorption on the tunnel-structured surfaces, and bonding among themselves when compressed (Fig. 3.15). Tunnel-structured minerals may incorporate cations and/or water molecules (Rakitskaya et al., 2018). This will in turn help increase the surface charges for the electrostatic and/or Van de Waals forces and/or the moisture content increasing capillary bridges. In a comparable fashion, nickel laterite ore from New Caledonia was successfully agglomerated using cold, binder-free briquetting (internal report ERAMET Ideas). QEMSCAN analyses (Fig. 3.16) show abundant layer-structured minerals (smectite). These swelling clays have properties similar to commercial bentonite, and thus naturally increase adhesive potential. The GO and nickel ores both have high amounts of tunnel and layer structure minerals. Considering the behavior of the material in Fig. 3.16, the overall adhesive potential of GO is assumed to be high. However, due to the coatings on the hard minerals (pyrolusite, cryptomelane…) by softer material, breakage is less likely, which in turn limits the creation of fresh surfaces during compaction.

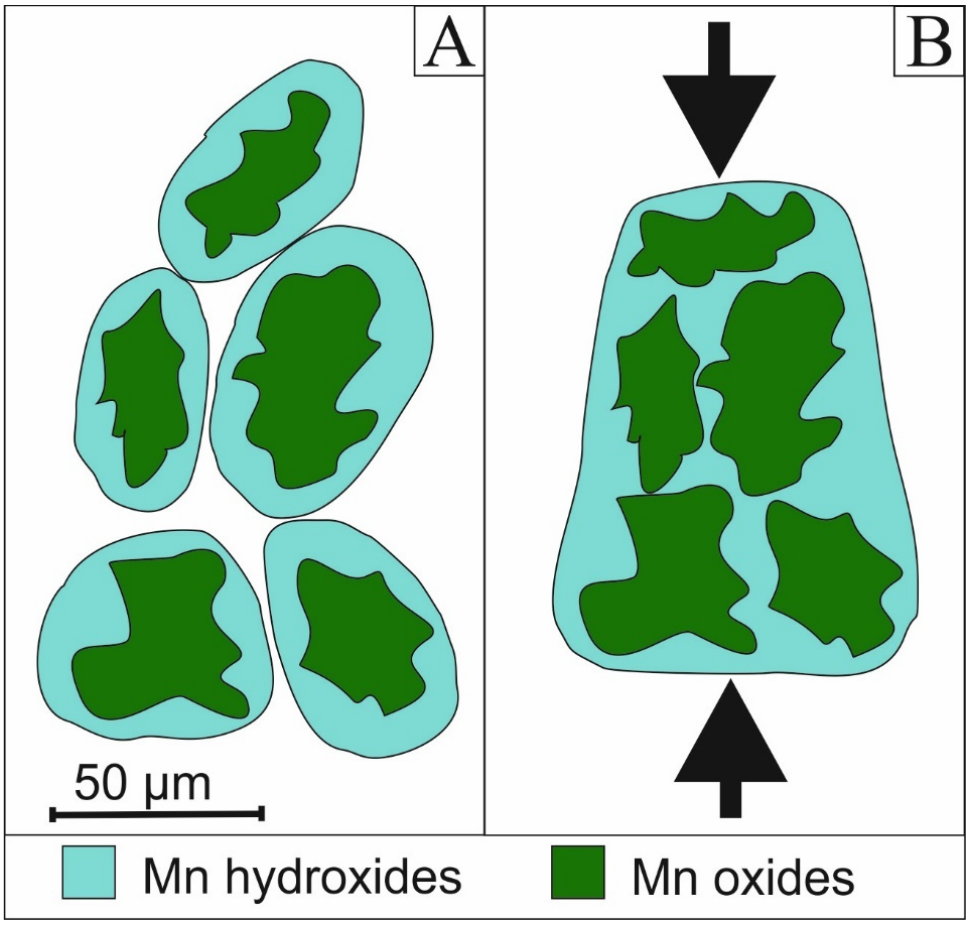

Fig. 3.15. Schematic of the hydroxide coating behavior under compression of the sample. The layered structured minerals behave plastically and fill the gaps, hence reducing the separation distance between the particle.

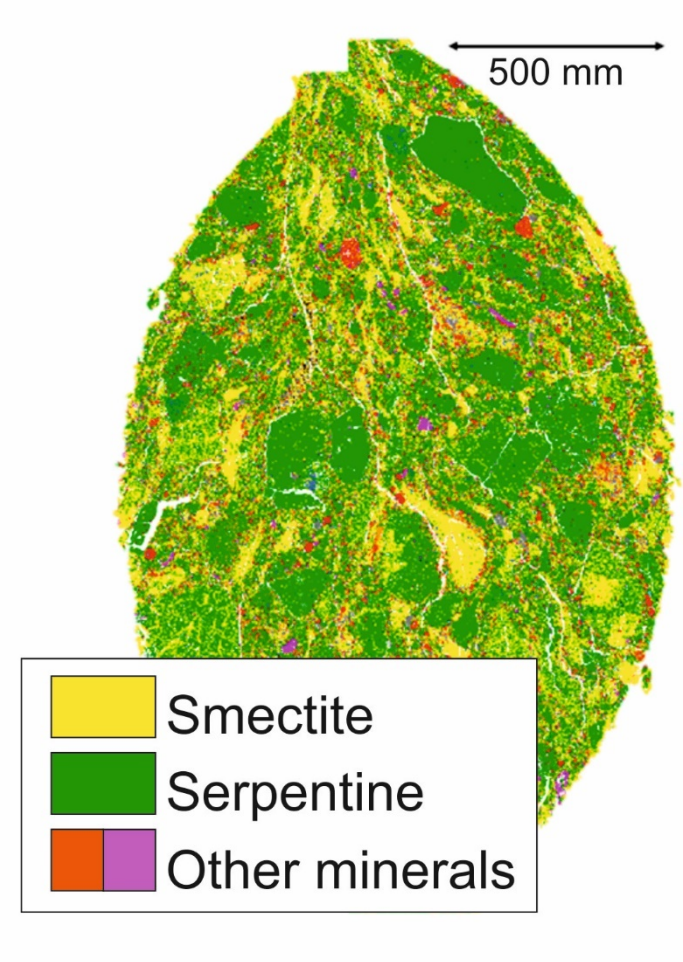

Fig. 3.16. QEMSCAN false color image of a nickel laterite ore pellet realized by ERAMET.

AO and GlO have similar properties. These samples are mostly composed of hard minerals (braunite, hausmannite, respectively 6.0 and 5.5 on Moh's scale) with low content of fine particles. They also contain soft carbonates (about 3 on Moh's scale) with perfect cleavages, which are brittle under compaction. However, particle breakage may be less efficient to reduce the separation distance between the particles than the clay deformation. Consequently, the adhesive potential of AO and GlO is lower than the one of GO. Instead, their low fine production reduces the need for agglomeration.

The sinter is composed of hard cubic spinels (hausmannite, galaxite) and tephroite having a hardness of 6.0 and 7.5 on the Mohs scale, respectively. All three minerals exhibit perfect cleavage. At room temperature (i.e. cold agglomeration temperature), spinels show rigid behavior (Stewart and Bradt, 1995). The resulting low breakability of the particles coupled to the low fine production of the sample will yield important separation distance between particles (Schulze, 2008). The complex shape of the particles may lead to physical interlocking of particles/grains. Spinels have good sorption capacities (Garcês Gonçalves et al., 2018), used for industrial remediation through nano-sized spinels (Sezgin et al., 2016). In our samples, the spinels are tens of microns in size, resulting in a smaller interaction surface area. Despite their good sorption capacity, the lack of good sorbent material in the sample suggests that the sinter will exhibit low adhesive potential under pressure.

The sludges have an essentially carbonated mineralogy (Moh's hardness around 3), but narrow PSD. They will hence exhibit low adhesive potential, although higher than that of the MOR. Indeed, the high hardness of the minerals (hausmannite, about 6 on Moh's scale), simple shape (spherical particles) and narrow PSD of the MOR dust suggest negligible adhesive potential. The tapping dusts have similar properties as the MOR. However, the broader PSD increases its adhesive potential.

The metal dust is the only sample with ductile behavior. Its high deformation threshold makes interlocking of particles difficult. Additionally, the shape of the particles is angular though simple. The PSD is narrow, and the mineralogy is homogeneous. This suggests rather low adhesive potential.

6.3 Increasing agglomeration potential

6.3.1 Moisture

The presence of moisture amidst the grains improves the cohesiveness of the material through an increase of the capillary forces. This will regulate the flow and deformation of the material (Mielniczuk et al., 2017). However, the presence of moisture also reduces Van der Waals forces. At liquid saturation, the material becomes a slurry (Fig. 3.17; (Louati et al., 2017)) which requires a balance between the tensile strength (capillary forces) and the compressive strength (Van der Waals forces).

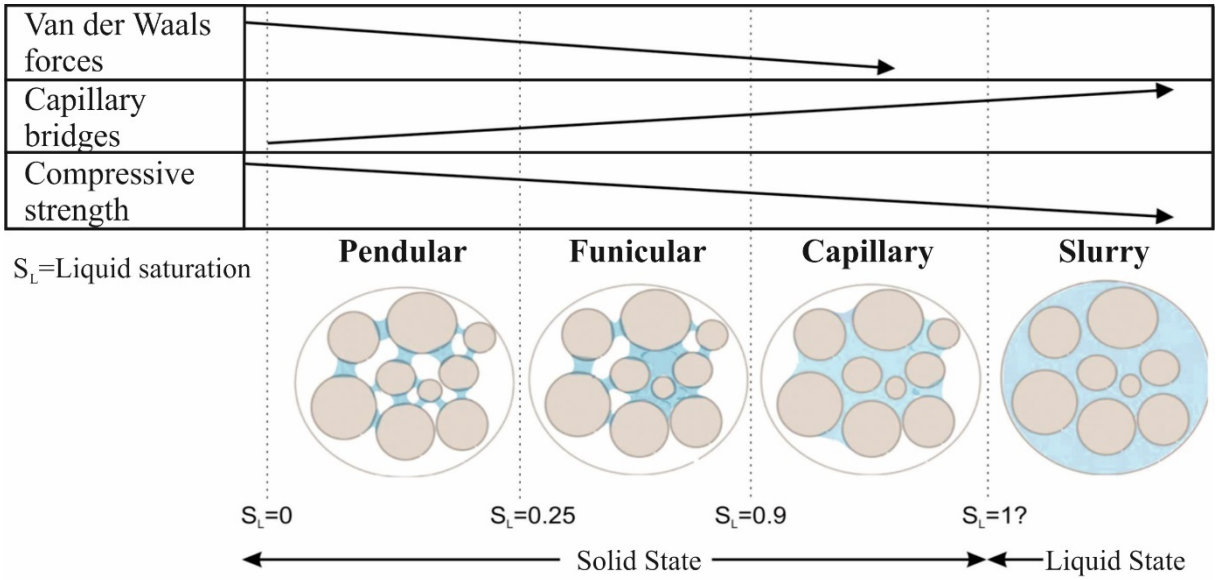

Fig. 3.17. Impact of moisture on the intensity of Van der Waals and Capillary forces. Agglomeration processes look for a high compressive strength, but capillary bridges help reduce the fine generation of an agglomerate. A balance is hence required. Modified from (Louati et al., 2017).

The surface charges mainly depend on the pH of the environment. It is therefore possible to control the surface state (physical and chemical) of the particles by conditioning the moisture added to the compacted material (Schoonheydt and Johnston, 2011), to manipulate the electrostatic attraction forces. For example, if the material is complex, with different phases, it would be possible to modify and adapt the pH so that different phases have opposite surface charges that cause attraction.

6.3.2 Blending

In order to optimize the overall agglomeration process for all dust types ensuring a constant valuable metal content of the agglomerates, blending could be necessary (Udo et al., 2018). In-depth material characterization allows to model optimum properties to achieve cold binder free agglomeration. In the present study, GO shows the best agglomeration potential. Future work will benchmark the blending proportion GO with the other materials and the compaction parameters.

7. Conclusions

1. A proper characterization of dusts must imperatively be pluridisciplinary, with a strong emphasis on mineralogy. Mineralogy and crystallography define the key parameters for agglomeration. Tunnel-structured must be considered along with layered-structure minerals for their helping roles in agglomeration. Further systematic study, relating Mn mineralogies and CEC would be required. Firstly, a laboratory study on the different dust materials should include SEM, QEMSCAN, XRD, XRF, CEC, BET and zeta potential studies. Then based on these results, key parameters of the material can be extracted and quantified (e.g. percentage of layer and tunnel structure minerals), to be used in the industrialized process scheme.
2. Considering dust generation along the processing chain, simplification of the mineralogy and the morphology was noticed.
3. Ores, especially GO in the present study, have the highest agglomeration potential due to their high amount of layer- and tunnel-structure minerals, highest among the analyzed materials. As GO is the most abundant dust and its agglomeration potential is high, blending of this high agglomeration potential matrix with the other materials should be studied and benchmarked further, along with the specificity of each agglomeration method. The two other ores (AO and GlO) have slightly lower agglomeration potential than GO. The process and sinter dusts have low agglomeration potentials, with the exception of MOR dust, of which exhibit negligible potential.
4. Additional work considers actual agglomeration experiments. Inclusion of such results will allow to design a predictive model for the agglomeration potential of samples.

8. Acknowledgments

We thank Eramet IDEAS, the GEOPS laboratory, the KIC-EIT RawMaterials Go4.0. The PhD is supported by a CIFRE project N° 2017/0326 and the ANRT for their logistic and financial support. A. Salaün, S Lafon and Q. Jallet (ER) are thanked for their help handling the samples. We thank the staff of ERAMET Norway SAUDA (B. Ravary, E.-D. Fatnes, D.-O. Hjertenes and E.-V. Hansen) for their help during the sampling mission.

Chapitre 4 - Binder-free tableting experiments on manganese oxides and industrial mineral powders

Dubos, J.-L. [1/2], Orberger, B., [2/3], Banchet, J.[4], Milazzo, J.-M.[1], Blancher, S. B.[1], Wallmach, T.[1], Lützenkirchen, J.[6]

1. Eramet IDEAS, 1 *Avenue Albert Einstein, 78190 Trappes-en-Yvelines, France*
2. GEOPS, Université Paris Sud, Université Paris Saclay, Bâtiment 504, 91405 Orsay, Cedex France
3. CATURA Geoprojects, 2 rue Marie Davy, 75014 Paris
4. *EUROTAB, ZAC des Peyrardes, St Just St Rambert, France*
5. Institute of Nuclear Waste Disposal (INE), Karlsruhe Institute of Technology (KIT), Hermann-von-Helmholtz-Platz 1, 76344 Eggenstein-Leopoldshafen, Germany

Published in Powder Technology.

DOI: https://doi.org/10.1016/j.powtec.2020.08.032

1. Abstract

Cold, binder-free tableting experiments under controlled pressure (0-450 MPa), water addition (0-10 wt.%) and pH (4, 11) were performed on powder of pyrolusite ore concentrates, refined hausmannite, bentonite, kaolinite, as well as blends of those materials. It has been shown that increased pressure was beneficial for agglomeration of oxide materials, but pressure > 250 MPa triggered an elastic recovery in the clay minerals. Water addition up to 4 wt.% improved tabletability, increasing diametral resistance and reducing elastic recovery and fines generation. Amounts above 6 wt.% decreased diametral resistance. The presence of layered-structure minerals (such as montmorillonite, kaolinite, lithiophorite) appeared to be key to determine the agglomeration potential of a sample. This study also showed that tableting provides good performances for recycling industrial manganese oxide fines by obtaining industrial-grade resistance for tablets made with an 80/20 pyrolusite concentrate/hausmannite blends and 4 wt.% H_2O.

2. Graphical abstract

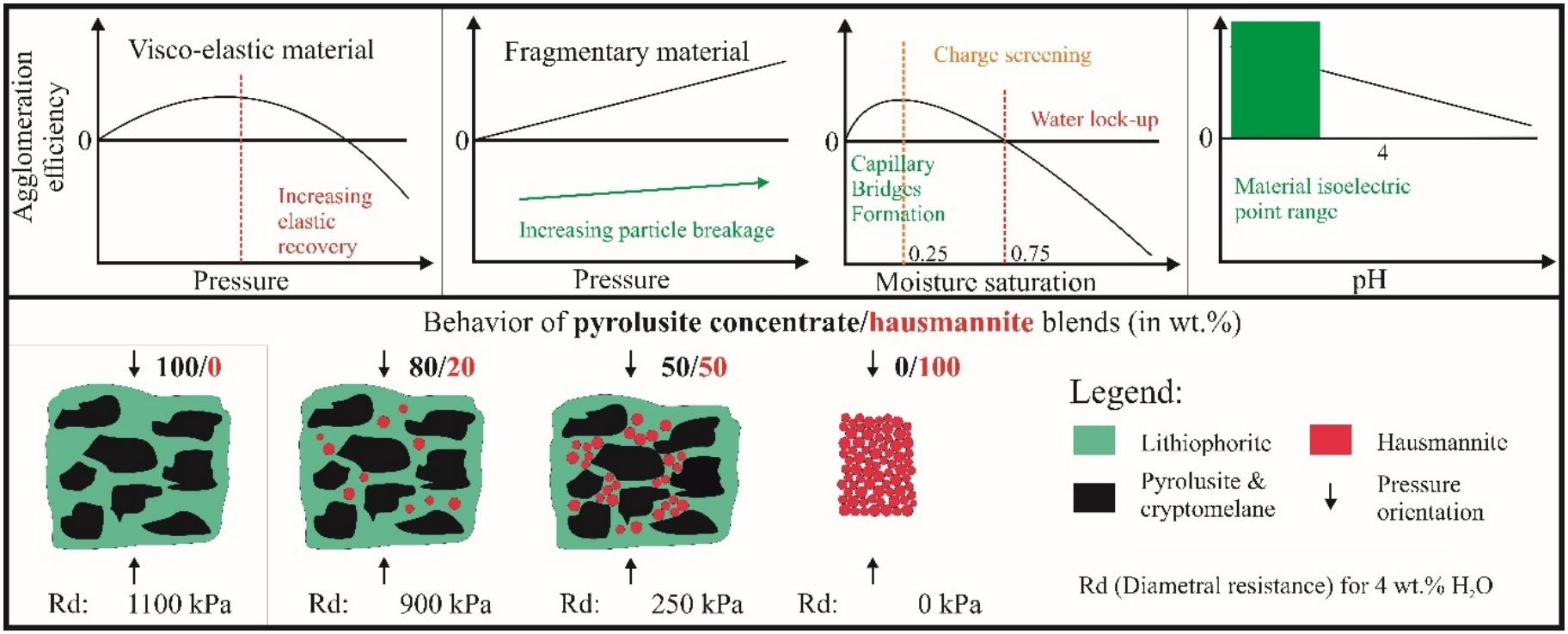

Fig. 4.1. Graphical abstract showing the impact of the different phenomena on the agglomeration efficiency, and the result of mixing in terms of material distribution and material resistance.

3. Introduction

Agglomeration is used in many industrial sectors such as powder technology, agriculture, food production, pharmacy, detergents, waste fines, catalysts and ore smelting (Darab et al., 1994; Dhanalakshmi et al., 2011; Fernández-González et al., 2018; Palzer, 2011). In the mining, industrial minerals and metallurgical sectors, agglomeration of fine grained (< 3 mm) materials (Dubos et al., 2019) is used to increase their granularity for metal recycling through pyrometallurgy (Olsen et al., 2007) and/or hydrometallurgy (Nosrati et al., 2012; Quaicoe et al., 2013). For example, along the ferromanganese production chain, the fines generated during the various process steps (crushing, screening of ore and intermediate metallurgical products) have Mn-contents of up to 70 wt.%, versus 40-50 wt.% in the oxide ore from Gabon (Dubos et al., 2019). Recycling of these fines and Mn-production from agglomerated fines will thus increase the profitability.

The choice of the applied agglomeration method depends on raw material and product applications. The mining and metallurgical sectors mainly use sintering, pelletization (also called granulation) and briquetting (T. By, 2017; Ordiales et al., 2016). For example, millions of tons of fines produced in the iron mining, metallurgical and steel industries lead to preferred use of pellets (Zhu et al., 2014). For material with high crystalline water content, such as manganese or nickel laterite ores, sintering, briquetting or extrusion are applied (Bizhanov et al., 2014; Ordiales et al., 2016) to allow subsequent use in pyrometallurgical processes.

For all these purposes, agglomerates need to be stable to avoid the recurrence of fines. High mechanical resistance is necessary to survive transport, storage and handling. High thermal resistance is required to allow introduction of these agglomerates into the furnaces without deteriorating the gas flow while maintaining a high reactivity through an optimal porosity and/or permeability (Olsen et al., 2007; Pietsch, 2002). These characteristics are at present obtained by using different types of binders. Common inorganic binders are bentonite and commercial Portland cements. Organic binders, such as lignosulfonate, usually provide sufficient cold strength, but decompose at temperatures around 500-1000°C (Halt and Kawatra, 2014). Ongoing research on natural and synthetic organic binders aims to improve and optimize their efficiencies (Linhares et al., 2019). Mixtures of organic and inorganic binders are also used (Halt and Kawatra, 2017; Ripke and Kawatra, 2000). The use of binders provides good mechanical and thermal resistance at low cost, but produces an increased amount of slag during reprocessing, and may introduce contaminants into the furnace. For example, potassium introduction may catalyze carbon from reductant oxidation (via the Boudouard reaction), whereas silicon addition modifies the basicity index and increases slag production (Halt and Kawatra, 2014; Olsen et al., 2007). In pyrometallurgical processing, binder addition consumes more energy, and will increase the cost per ton of cast metal. Furthermore, higher amounts of slags and CO_2/SO_2 emissions need to be managed to prevent environmental impacts (Olsen et al., 2007). As the global mining and metallurgical sectors present 34 % of global energy consumption (International Energy Agency, 2007), research and development projects (e.g. the EU Go40-project) target methods for binder free agglomeration (Eramet, 2018). At present, no study has been published on reliable, binder-free agglomeration in the mining and metallurgical industries.

However, in the industrial mineral sector, binder-free agglomeration, such as palletization, is applied to bentonite and kaolinite mainly for reaching higher bulk density for handling and transport (Darde et al., 2018; Heim et al., 2005, 2004; Sridharan et al., 1986).

Tableting is mainly applied to pharmaceutical products (Alkrad et al., 2017; Charinpanitkul et al., 2008; Kadiri et al., 2005; Stasiak et al., 2010). Recently, tableting has also been investigated as an agglomeration method for the mining and metallurgical sector, as it is time, cost and energy

efficient (He et al., 2015; Poirier, 2014). The difficulty is that the fines produced from ore and metallurgical processing are composed of multiple grain and particle sizes with different shapes, involving various phases (Dubos et al., 2019; Wünsch et al., 2019). This differs from the mainly mono-and biphasic pharmaceutical products of homogeneous particle size and grain shape.

Tableting of complex material still requires fundamental research, as the multiple micro-processes and their influencing parameters are not yet fully understood. As a consequence, empirical formulation and processing prevails (Wünsch et al., 2019).

The present study contributes to the understanding of the process and the involved micro phenomena of tableting. It also highlights the importance of such an approach for the industry. It is the first experimental study using tableting under controlled pressure, H_2O and pH conditions on powders (<125 µm) of pure industrial minerals (bentonite and kaolinite) and Mn-oxide concentrates (pyrolusite: MnO_2 as ore fines, and hausmannite (Mn_3O_4) of metallurgical origin). These materials were selected as they have different physico-chemical properties and mechanical behaviors. Tableting was also performed on mixtures of (1) pyrolusite-hausmannite, (2) kaolinite-pyrolusite and (3) kaolinite-hausmannite, with varying H_2O content and pressures. After the experiments, the diametral hardness (Rd) of each tablet was measured and selected tablets were analyzed via Scanning Electron Microscopy (SEM).

4. Material

Bentonite was selected for its known agglomeration capabilities. It is a common commercial binder composed of about 80 % of the swelling-clay montmorillonite, with about 20 wt.% of quartz, iron oxides, sulfides, and other clays, depending on the origin (Karland, 2010). The bentonite used in this study is a commercial product from Rockwood Clay Additives GmbH, procured by EUROTAB, France. Its main compound is Na-montmorillonite, classifying it as a Na-bentonite (Muurinen, 2011). Montmorillonite is a clay mineral belonging to the smectite (dioctahedral) group, i.e. the phyllosilicate family. These minerals are characterized by an average total exchange surface of about 800 m^2/g (20-90 and 700-800 m^2/g for the external and internal surfaces, respectively), using the Brunauer-Emmett-Taylor (BET) method. The montmorillonite structure is 2:1, with TOT M+ layers, with a charge of 0.2 to 0.6 electrons/lattice cell. The Cation Exchange Capacity (CEC) ranges between 80 and 150 meq./100g, depending on particle size, nature of cation and hydration degree (Salles, 2006). In all tables and figures hereafter, the bentonite is referred to as Bento.

Kaolinite was chosen as a non-swelling dioctahedral clay mineral of the phyllosilicate family. The kaolinite concentrate is a commercial product branded “Kaolin DC” in powdered form, procured by Imerys Ceramic France Kaolins de Bretagne (Lanvrian, Ploemeur). The usual Specific Surface Area (SSA), measured using the BET method, varies between 5 and 15 m^2/g (Diamond, 1956). It has a 1:1 structure, with TO layers. Due to the lower surface charge compared to bentonite, kaolinite CEC shows less variation (1-15 meq./100g). In all tables and figures hereafter, the kaolinite is referred to as Kao.

Pyrolusite is the main component of manganese laterite ore. The pyrolusite concentrate was obtained from Mn oxide ore (particle size >10 cm; Comilog, Moanda, Gabon) through jigging at Eramet Ideas (Rousseau et al., 2016). It contains mostly pyrolusite (75 wt.%), cryptomelane (11 wt.%), lithiophorite (8.2 wt.%), with small amounts of Fe oxyhydroxides and clays (3.6 and 1 wt.%, respectively). Pyrolusite concentrate is called “Pyro” in all figures and tables hereafter.

Hausmannite is the main product from pyrometallurgical processing (Olsen et al., 2007).

The hausmannite concentrate represents material from Metal Oxygen Refining dusts of the FeMn alloy production chain. It was sampled from the Eramet Norway Sauda plant. In all tables and figures hereafter, the hausmannite is referred to as Hs.

All four materials were fully characterized following the procedures described in Dubos et al. (2019). The results are presented in Table 4.2 and Table 4.3(Part 6.1). All samples were sieved to ensure a <125 µm grain size (Eramet Ideas, Trappes, France).

5. Methodology

Mineralogical and physico-chemical characterization of the four materials involved X-ray diffraction (XRD), X-Ray Fluorescence (XRF), laser and optical granulometry at Eramet Ideas. The Zeta potential was determined at the Institute of Nuclear Waste Disposal (INE), at Karlsruhe Institute of Technology (KIT), Germany. The CEC and BET values were subcontracted to the ERM laboratory (Poitiers, France). All methods have been described in detail in Dubos et al., (2019). Details are also given in supplement materials 1.

5.1 Bulk chemistry

All samples (<100 µm) were dried at 105 °C for 12h prior to analyses. A 2 h calcination at 1000 °C is necessary to analyze the Loss On Ignition (LOI). Major and minor elements were analyzed by X-Ray Fluorescence (PANalytical AXIOS Minerals, equipped with a CO-anode) at Eramet IDEAS.

5.2 X-Ray Diffraction

XRD was performed with a PANalytical X'PERT PRO using a Cu-anode on samples grinded < 40 µm for 1h. The diffractograms were analyzed using the HighscorePlus software coupled with the Crystallography Open Database (Day, n.d.).

5.3 Granulometry and Granulomorphology

Particle size distribution (PSD) was measured using a laser granulometer (CILAS 1064L) and an optical granulometer (Sympatec QICPIC). The laser granulometer has a high resolution of (~0.1 µm), assuming spherical particle shapes. However, the optical granulometer has a lower resolution (~5 µm) for measured and 20 µm for calculated shape properties, such as convexity, sphericity, aspect ratio (Qicpic, n.d.). Three repeatability tests were performed for each measurement on each apparatus.

5.4 Specific Surface Area and Cationic Echange Capacity

The SSA was determined using the BET method (Brunauer et al., 1938) using a TRISTAR II 3020 from Micromeritics ® (ERM Poitiers, France). The CEC was analyzed following the NF X-130 (1999) norm at BRGM (Orléans, France).

5.5 Zeta potential

A Nanobrook 9000 plus PALS equipped with a green laser was used to measure the electrophoretic mobility which was transferred to the zeta potential using the Smoluchowski model (von Smoluchowski, 1903). Each value is an average of ten measurements. Measurements can only be performed on suspended material in MilliQ (ultrapure) water with smaller size (<1 µm). Two series of measurement were performed. During the first test series only the pH and zeta potential of the afore-mentioned suspension was measured. The second series aimed at determining the IsoElectric Point (IEP), i.e. the pH value where the zeta potential is zero (0 mV). The absence of electrostatic charge is considered to present the best condition to agglomerate particles (Lu and Gao, 2010). The pH of the suspension was varied using NaOH or HCl to increase or decrease the pH, respectively.

5.6 Tableting

5.6.1 Apparatus

The tableting apparatus used is Cassiopée, a unique, custom-made, instrumented hydraulic uniaxial press constructed for EUROTAB (Andrézieux-Bouthéon, France; Fig. 4.2). It allows to set any compaction cycle parameter, i.e., compaction forces between 1 and 180 kN, punch speed from 1 to 300 mm/s, presence or absence of precompression and dwell time (time during which the highest pressure of the cycle is maintained at the end of the cycle before tablet release) between 20 and 5000 ms. Dies up to 55 mm diameter can be used. The apparatus is equipped with several sensors and associated software, real-time recording and imaging of both punches' positions, applied force, die seizure and tablet ejection seizure arising from the friction forces of the tablet against the die walls. The punches, made of carbide-tungsten, are 22 mm in diameter, with a 0.5 mm deep chamfer on each side. The die, made of the same material, has an inner conical shape to improve tablet ejection with an 0.6° half-angle (Fig. 4.2).

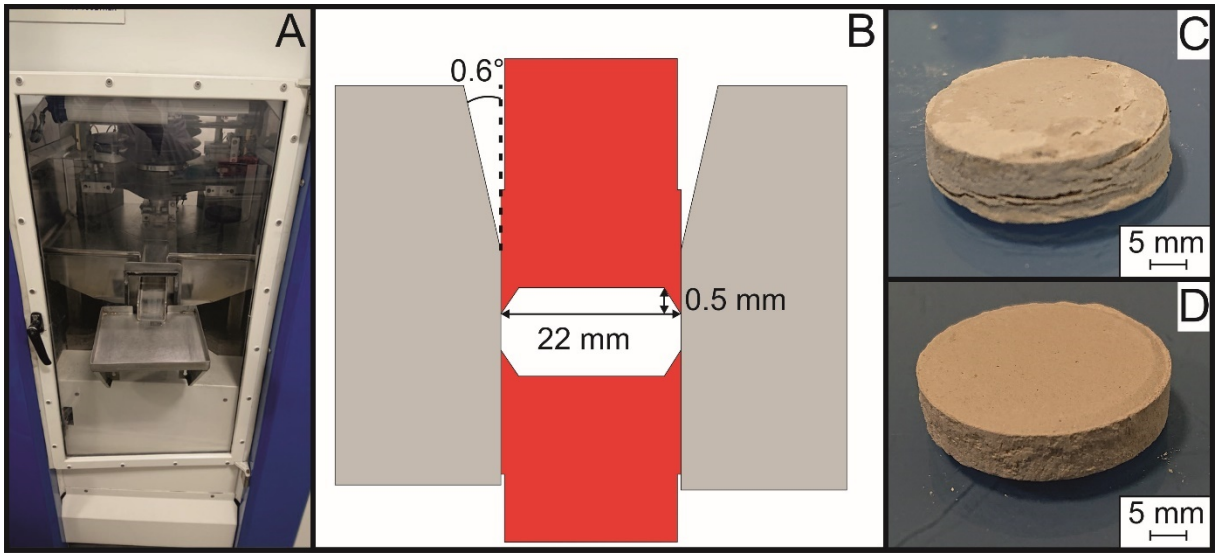

Fig. 4.2. Agglomeration apparatus with A) Picture of Cassiopée, EUROTAB's custom uniaxial press, B) Schematic drawing of the punches and die used for the agglomeration tests; C) and D) Examples of low-quality tablet (bentonite) and high-quality tablet (kaolinite), respectively.

5.6.2 Sample preparation

The first set of experiments is performed on pure concentrates. Only H_2O is added prior to agglomeration. A content of 1 wt.% H_2O corresponds to 0.3 g of water added to 30 g of sample, for a total sample mass of 30.3 g. H_2O is sprayed on top of thin layer of material at the buttom of the recipient, before the next layer of material is added and the process is repeated until the desired amount of H_2O is reached. The material is then mixed using a stirring rod, and the aggregates formed are crushed. Finally, the sample is placed into a rotating drum for 1 min with a revolution speed of 50 rotation per minute (rpm).

The pH-based experiments followed the same protocol, only replacing the tap water with HCl-buffered solution of pH 3 and NaOH-buffered solution to reach pH 7 and 11.

Furthermore, various blends were tested (Table 4.1). The blends were stirred mixed before the recipient is put for 1 min into a rotating drum with a revolution speed of 50 rpm. The same protocol as for the pure materials is applied to add H_2O and pH- buffering solutions.

Table 4.1. Blends performed during this study using the raw materials.

Blends	90/10 (wt.%)	80/20 (wt.%)	66.7/33.3 (wt.%)	50/50 (wt.%)	33.3/66.7 (wt.%)	30/70 (wt.%)	20/80 (wt.%)
Pyro/Hs		X	X	X	X	X	x
Pyro/Kao	X		X	X			
Hs/Kao	X		X	X			
Hs/Bento	X	X					

In order to have comparable filling settings for the matrix, the initial mass of the samples processed by tableting is 5 g for the bentonite and kaolinite, whereas it is 7.5 g for pyrolusite concentrate and hausmannite, the difference being due to the different densities of the materials.

The tableting cycle involves a precompression and a compression step, with a punch speed of 10 mm/s. The compaction during the compression step is maintained for 5 s (dwelling time). Preliminary tests showed that precompression and dwelling time have no impact on both pyrolusite concentrate and hausmannite. However, these parameters are relevant for the clay concentrates limiting their elastic recovery, hence increasing tablet quality.

5.6.3 Experimental protocol

It is supposed that the main forces during agglomeration are Van der Waals, electrostatic forces and capillary bridges (Pietsch, 2002; Schulze, 2008). These forces depend on e.g. the separation distance between particles, the liquid saturation and the surface charges of the different particles. When considering uniaxial pressure agglomeration, the separation distance will depend on the pressure applied to the sample, but also on the reaction of the sample to that pressure. The mineralogy and crystallography hence impact on the agglomeration results. The liquid saturation depends on the water content in the sample, and surface charges of the particles depend on their interaction with the added H_2O.

Based on these considerations the pressure set for agglomeration ranged from 0 to 450 MPa and the H_2O content was set between 0 to 10 wt.% at 2 wt.% steps. Each measurement was repeated 3 times. Fig. 4.3 shows the distribution of the experimental tests for each material.

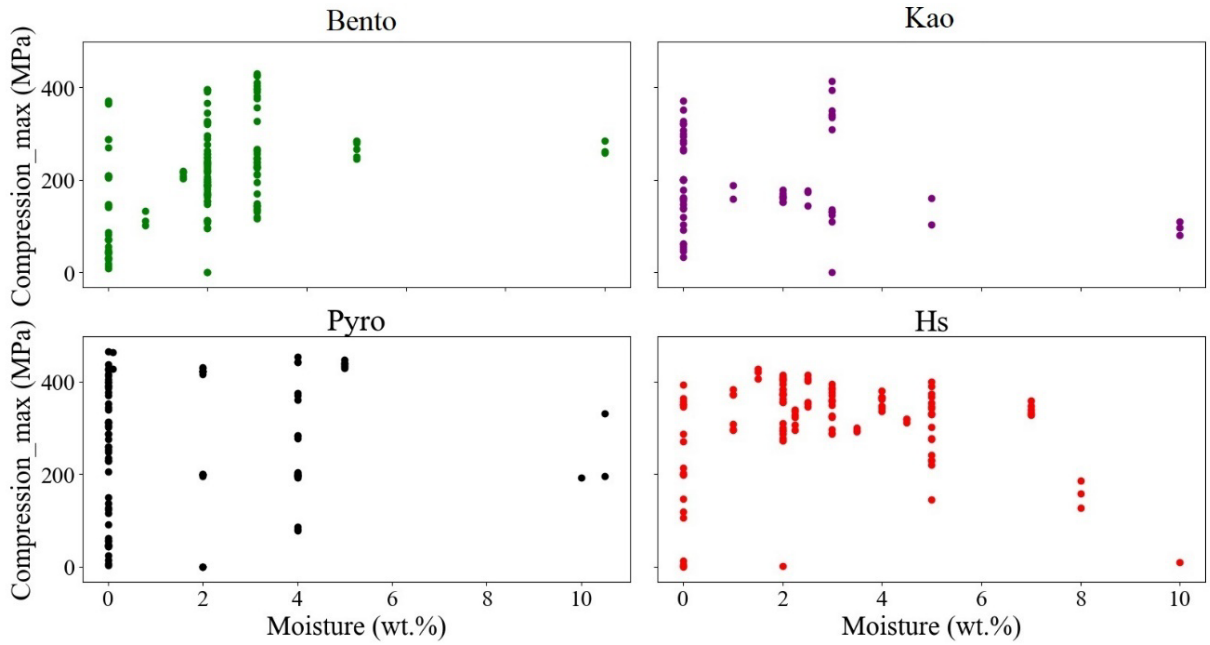

Fig. 4.3. Experimental condition of pressure and H_2O content for the tableting performed on A) Bentonite, B) Kaolinite, C) Pyrolusite concentrate (Pyro) and D) Hausmannite (Hs). Each point represents a unique couple of pressure and H_2O content investigated in this study.

5.6.4 Heckel's curve

The respective material behavior under compression was analyzed using Heckel's curve (Heckel, 1961b), which links the porosity of a material to the pressure applied. This curve has two regions, describing the particle behavior during compression. The first region is nonlinear and corresponds to the rearrangement of the particles, leading to a first degree of granular media densification. The lower the pressure delimiting the end of this first region, the easier it is to rearrange the material. In other words, curves with a short first non-linear region characterize a material that rearranges itself easily. The second region has a linear trend and shows the densification due to deformation or fragmentation of particles. It starts when the curve reaches a constant trend described by the equation (1), where D is the relative density of the material, and k and A are material specific constants. The inverse of k gives the yield pressure (Py) value of a material (MPa), corresponding to the energy necessary to plastically deform the material (He et al., 2019).

$$\ln\left(\frac{1}{1-D}\right) = kP + A \quad (1)$$

A material with Py < 60 MPa is plastic/viscoelastic, while for Py >120 MPa it is fragmentary (Ilkka and Paronen, 1993). Any value between 60 and 120 MPa indicates intermediate behavior between non-linear and linear, i.e. contributions from both fragmentary and viscoelastic properties.

5.6.5 Diametral resistance

The diametral resistance (Rd) of the tablets is assessed directly after coming out of the press. It is calculated using Eq. (2), where d and h are the diameter and height (mm) of the tablet, respectively, and F (N) the strength needed to break it. This strength is given by a Dr-Schleuniger-8M-durometer that compresses the tablet diametrically until it cracks.

$$Rd = \frac{2*F*1000}{\pi*d*h} \quad (2)$$

The internal surfaces of the two halves of the broken tablets are investigated by SEM in Secondary Electron (SE) mode.

5.7 Scanning Electron Microscopy (SEM)

A high-resolution SEM-FEG Zeiss Supra 55 equipped with a 30 mm² Bruker SDD EDS detector was used in Back Scattered Electron (BSE) and Secondary Electron (SE) modes at an accelerating voltage of 15 kV, with a diaphragm dimension of 120 µm, and a working distance of 8.6 mm. For raw material preparation, the resin was mixed with graphite particles to prevent agglomeration of the material, preserving shape and form of separate grains. This procedure did not give satisfactory results on the hausmannite sample. SEM observation of the tablets was performed on the broken halves after hardness tests, placed on carbon tape on the sample holder. Due to the fine-grained material of the tablets, the resin could not penetrate to the core of these agglomerates, and thus no polished sections could be prepared.

5.8 QEMSCAN®

The BSE of a FEI Quanta 650F FEG, set with 2 Brucker Xflash 30mm silicon drift EDX detectors was used. The QEMSCAN® (Quantitative Evaluation of Minerals by SCANning electron microscopy) software, iMeasure v5.4, enables the recording of statistical data on mineralogy and quantitative textural analyses of samples. The data were acquired at 25 kV and 10nA. For the study of raw materials, the field image setting was chosen due to the very fine particle sizes. In order to study the tablets, the Bulk Mineralogical Analysis (BMA) method was selected. The data are classified and processed using the iDiscover v5.4 software suit. X-Ray data were collected with a total X-Rays count of 2000 counts per spectrum at 2.5 µm resolution. The classification used in this study was cross-checked by XRD and bulk chemistry. The study of fine, micrometric particles using the QEMSCAN® is difficult to achieve due to (i) the spot size resolution (4-5 µm), and (ii) the chemical proximity of the materials studied (kaolinite and montmorillonite).

6. Results

6.1 Material characterization

6.1.1 Chemistry and mineralogy

The chemical and mineralogical compositions of the materials are presented in Tab. 2 and 3 respectively. The bentonite sample contains 32.3 wt.% Si and 7.3 wt.% Al. The Na content (1.9 wt.%) confirms that this bentonite can be classified as a Na-bentonite. Assuming pure montmorillonite, these contents should be 20.5 and 9.8 wt.% respectively. Additionally, the Ca

content of 1.2 wt.% may be attributed to the substitution of Na by Ca in the montmorillonite structure (Webmineral, n.d.). The Fe (1.2 wt.%) and Mg content (1.6 wt.%) are related to substitution in the clay minerals and to the presence of Fe-hydroxides (Fig. 4.4). XRD analyses reveal the presence montmorillonite, quartz, muscovite and albite (Tab. 3).

Table 4.2. XRF analysis of the four materials. Full analyses in oxides including traces (Ti, Zn, Ba, P) are available in supplementary material 1 (Appendix 5).

Sample	Fe (wt.%)	Mn (wt.%)	Si (wt.%)	Al (wt.%)	K (wt.%)	Ca (wt.%)	Na (wt.%)	Mg (wt.%)
Bento	1.21	0.08	32.3	7.25	0.53	1.24	1.94	1.6
Kao	0.61	<0.02	23.5	17.9	2.25	<0.08	<0.11	0.18
Pyro	2.47	52.9	0.82	2.56	0.69	<0.08	<0.11	<0.06
Hs	2.06	70.3	<0.14	<0.11	<0.06	<0.02	<0.07	0.1

The kaolinite sample has slightly lower Al (17.9 wt.%) contents compared to the theoretical value of 20.9 wt.% and slightly higher Si (23.5 wt.%) instead of the theoretical value of 21.8 wt.%) than a pure kaolinite. It also contains 2.3 wt.% of K (Webmineral, n.d.). These findings can be explained by the small amounts of muscovite and quartz confirmed by XRD (Tab. 3).

The pyrolusite concentrate sample has a lower amount of Mn than pure pyrolusite (52.9 instead of 63.2 wt.%). Its contents of Fe (2.5 wt.%), K (0.7 wt.%), Al (2.6 wt.%) and Si (0.8 wt.%) can be related to the presence of goethite, cryptomelane, lithiophorite, kaolinite and quartz, confirmed by XRD (Tab. 3).

Table 4.3. XRD analysis of the four materials.

Mineral	Pyro	Hs	Bento	Kao
Pyrolusite	x			
Cryptomelane	x			
Lithiophorite	x			
Goethite	x			
Quartz	x		x	x
Kaolinite	x			x
Hausmannite		x		
Muscovite			x	x
Orthoclase				x
Montmorillonite			x	
Albite			x	

The hausmannite sample contains 2.1 wt.% Fe, indicating the substitution of Mn by Fe in the crystal structure. The metal content (Mn+Fe) is 72.4 wt.%, very close to the theoretical value of 72 wt.% in pure Mn_3O_4. All other elements except Mg (0.1 wt.%) are below their detection limits.

6.1.2 Morphological and microtextural analyses

Figure Fig. 4.4 shows SEM images (A1, B1, C1, D1) and the corresponding QEMSCAN analyses (A2, B2, C2) of the morphology and hardness of the particles. The hardness is a weighted average of the Moh's hardness of the minerals composing each particle. Colors are used to differentiate the hardness of the different particles.

The bentonite sample is mostly composed of montmorillonite particles with sizes between 2 to 60 µm. They are rounded, platy and cracked. Muscovite has a morphology similar to that of montmorillonite. Quartz grains (30-50 µm) are angular. Albite forms shards of < 20 µm. Fe-oxyhydroxides, probably goethite, can be observed as scarce micrometric spherical particles (Fig. 4.4 A1).

In contrast to bentonite, the kaolinite grains have needle-like shapes up to 80 µm. This contrasts with its typically platy shape. This can be explained by its origin. The protolith of these kaolinite in the Armorican massif (Bretagne, France) are micaschists (Gaudin et al., 2015). The needle-like morphology is probably inherited from elongated micas prior to alteration into kaolinite. Muscovite displays plastic deformation features. The sample also contains quartz grains with jagged edges and angular orthoclase particles with a smooth surface. Both mineral grains are up to 30 µm in size (Fig. 4.4 B1). Orthoclase was not detected by XRD (Table 4.3).

The pyrolusite concentrate is essentially composed of pyrolusite and cryptomelane. Pyrolusite grains (0.1 -100 µm) have a smooth surface or show porous features. Cryptomelane grains display alteration features rich in Al, composing the biggest particles. They are often surrounded by very fine grained (< 2 µm) pyrolusite and cryptomelane mixes, embedded in a lithiophorite matrix (Fig. 4.4 C1). Some lithiophorite grains (< 20 µm) display needle-like features. Small round quartz grains (10 µm) are also present. A sample of the same origin (Comilog, Gabon ore) was described in detail in Dubos et al. (2019).

The hausmannite sample is pure. The grains are spherical (< 5 µm) with smooth surfaces. Micrometric particles form clusters (Fig. 4.4 D1).

The QEMSCAN® results fit well with observations by SEM (Fig. 4.4). Bentonite's main population has low Moh's hardness (2.0-1.5) and exhibits mostly low particle elongation (<1.8). It has a very low population with higher hardness (3-5), related to minor contributions from quartz, albite and orthoclase. The particles of the pyrolusite concentrate display a low elongation (<1.6), but higher hardness around 6. Particle hardness of 2.5 is related to lithiophorite (Moh's hardness: 2.5 - 3.0). The kaolinite shows two distinct populations. Low elongation (< 1.6) but high hardness (5.5 to 7.5) for the high-hardness minerals orthoclase and quartz. High elongation (~3.5) and low hardness (1.5-2.0) are related to kaolinite. The hausmannite displays elongation values around 1.4, corresponding to the spherical shape observed by SEM. The QEMSCAN® measurement could not be performed in proper conditions due to the sample properties.

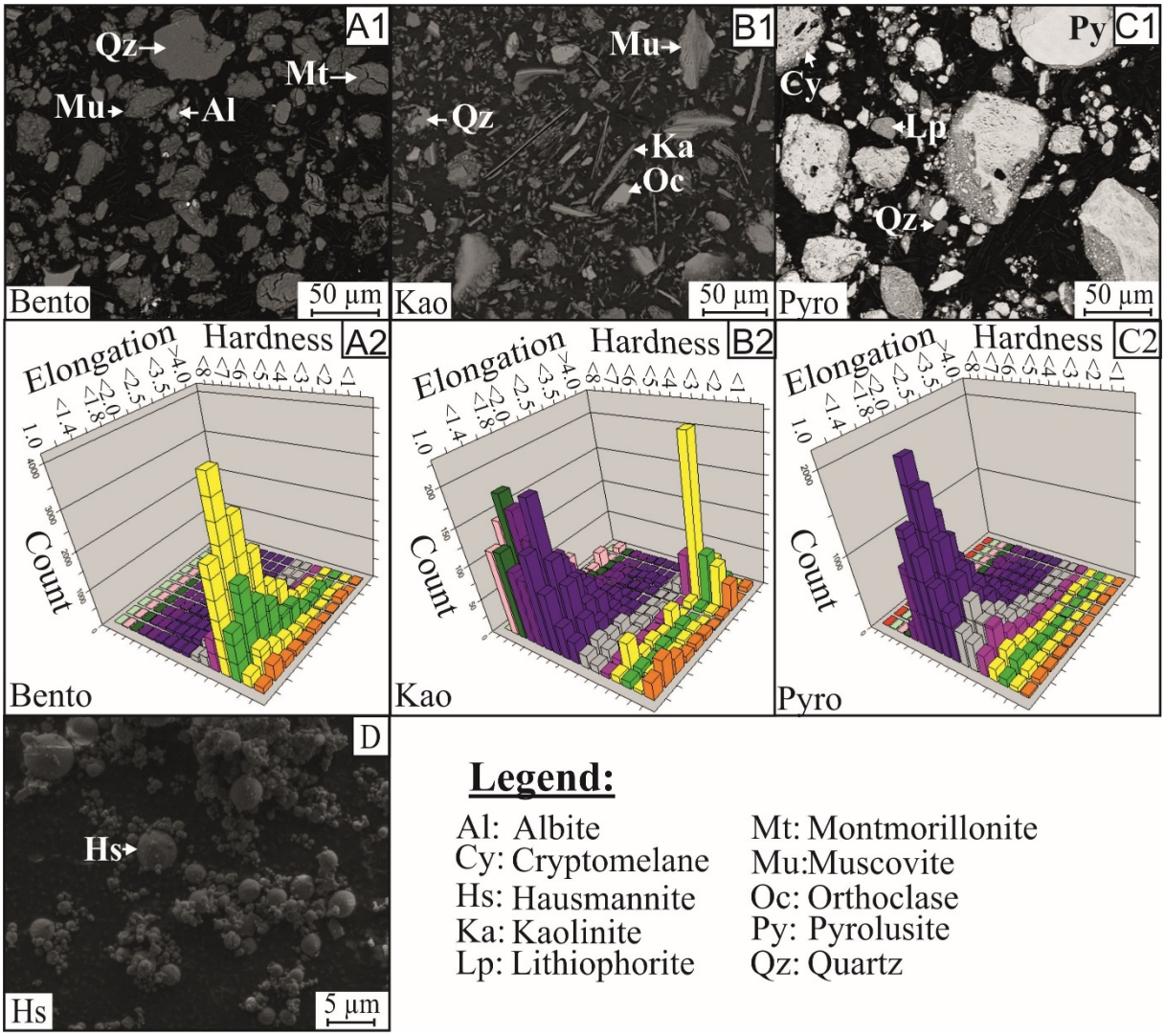

Fig. 4.4. SEM pictures with the associated QEMSCAN® calculations on the samples A) Bentonite, B) Kaolinite, C) Pyro and D) Hs. Pictures A1, B1 and C1 were taken at 15 kV using BSE, and D1 at 3 kV using SE. The QEMSCAN® calculations represent the particle counts for each combination of elongation and hardness (using Mohs scale) for the samples. The hausmannite measurements could not be performed due to the problems in sample preparation to obtain polished sections.

6.1.3 Particle size distribution (PSD) and grain morphology

Figure Fig. 4.5 shows the PSD of all samples for laser granulometry, while figure Fig. 4.6 shows morphological parameters based on calculations from optical QICPIC data.

The bentonite has a narrow distribution of particle sizes mostly between 10 and 100 µm, with some smaller particles around 3 µm. Those particles are irregular, as shown by low aspect ratio and convexity. The hausmannite has a low grain size (< 32 µm), and most of it is < 10 µm. It presents 3 distinct populations, centered around 0.6, 2.8 and 14 µm (Fig. 4.5). Contrary to the bentonite sample, its particles have more regular spherical shapes, fitting with SEM observations. The kaolinite and pyrolusite concentrate exhibit similar curves, increasing gradually from 1 µm, peaking around 60 µm and a subsequent sharp decrease due to sieving at 125 µm. However, the pyrolusite concentrate contains more fine particles (<10 µm).

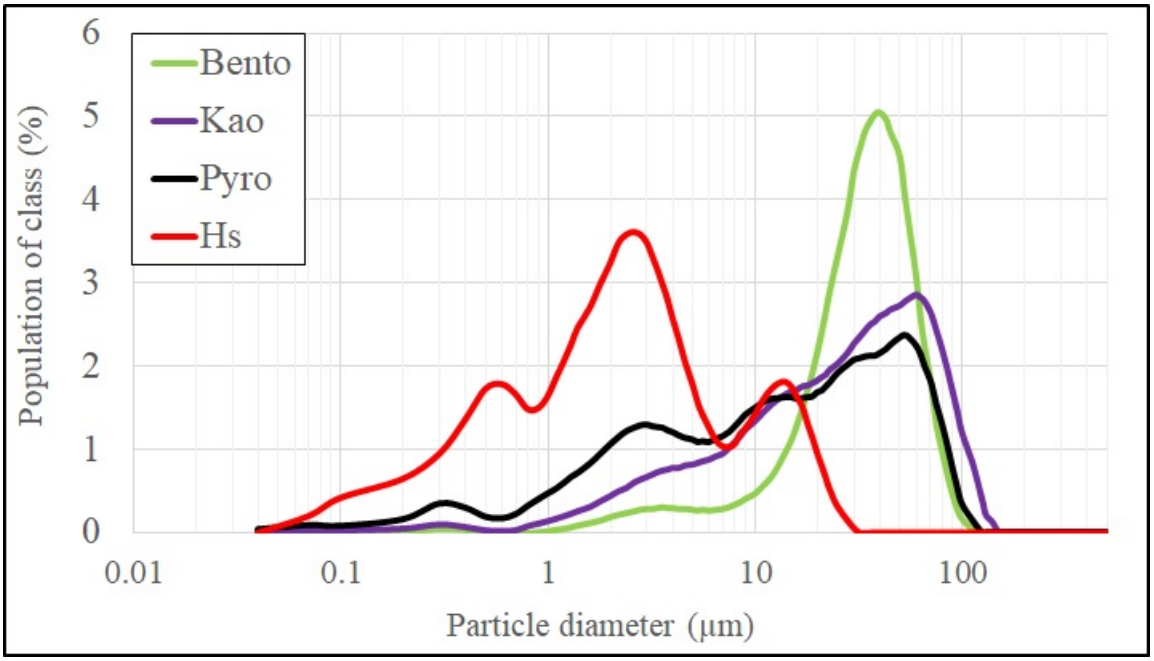

Fig. 4.5. Particle Size Distribution of all four samples using laser spectrometry. Pyro: pyrolusite concentrate, Hs: hausmannite.

The clay materials present the lowest values for all metrics across the samples. Kaolinite has the lowest values, with more elongate and ragged surfaces. The aspect ratio of the pyrolusite concentrate resembles that of the clay materials, showing more elongated particles than hausmannite. However, convexity and sphericity are higher for the pyrolusite concentrate than for hausmannite. This result contrasts with those obtained by SEM. The differences may be related to the methodologies. The very small particle size of the hausmannite (78 % are < 5 µm) gives lower precision to the optical measurement by QICPIC. Furthermore, ultrafine particles form aggregates. The ultrasound applied to separate these particles may have been insufficient. Hence QICPIC underestimates the spherical properties of the material (Fig. 4.6).

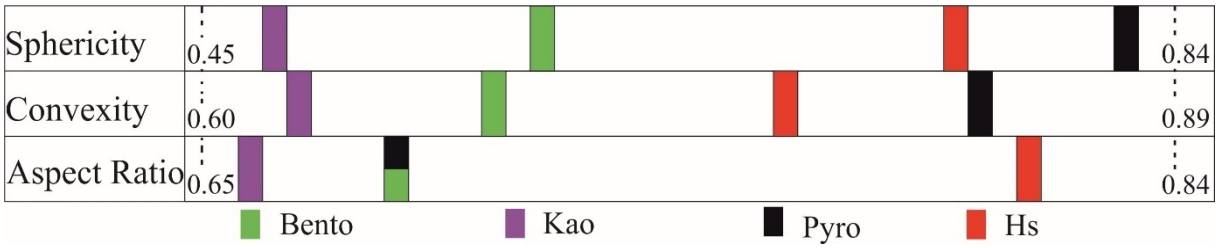

Fig. 4.6. Granulomorphological calculations for sample materials from QICPIC data. Hs, being very small sized, made it difficult to yield precise analyses. The morphological values of this sample are much lower and do not correspond to those observed by SEM.

6.1.4 CEC, BET and Zeta potential

Table 4.4 shows the CEC and BET for all samples. The bentonite displays the highest values in both CEC and BET (Table 4.4), indicating the highest potential reactivity of all samples. The CEC values measured for the bentonite are below the values for commercial Ca- and Na-bentonite, i.e.

60 and 78 meq/100g, respectively (Gul et al., 2014). BET values for commercial bentonite from Morocco (70 m²/g in El Miz et al, 2017) are also higher than the present measurement result (~59 m²/g), may be related to the presence of minor quartz, albite, muscovite and orthoclase.

Table 4.4. CEC and BET values measured for the samples under study (ERM laboratory).

Sample	CEC (meq./g)	BET (m²/g)
Bento	59.2	27
Kao	2.4	9
Pyro	0.5	14
Hs	0.0	2

Similarly to bentonite, the kaolinite CEC and BET values (2.4 meq/100 g and 9 m²/g) are lower than the average values found in the literature (1-15 meq/100g (Bouchet et al., 2000) and 5-15 m²/g (Dixon et al., 1977), respectively).

The pyrolusite concentrate BET value, higher than that of kaolinite in the present study (14 m²/g), is possibly due to the tunnel structures of pyrolusite and cryptomelane. Both have a 1x1 structure, but pyrolusite tunnels are half as large (2.3x2.3 Angström²) as those of cryptomelane (4.6x4.6 Angström; Julien and Mauger, 2017; Ferraris et al. 2004). The hausmannite shows a CEC below detection limit and a BET of 2 m²/g**.** These are the first CEC and BET values so far reported for Mn-oxide concentrates.

Figure Fig. 4.7 shows the zeta potential variations versus pH for all samples. Bentonite shows little impact of pH on its zeta potential value, going from -35 to -41 mV at pH 2 to 11, respectively. However, it does not reach the IEP in this pH range. The kaolinite has the lowest zeta potential values at higher pH (-51 mV at pH 10) and shows a pH dependence below pH 4. Although the IEP on the 2 to 11 pH range is not available, the trend seems to place it slightly below 2. The pyrolusite concentrate has -45 mV at pH 11 and a trend shift is obvious below pH 7. It reaches its IEP around pH 4.2. The hausmannite zeta potential is similar to that of bentonite at high pH (-40 mV at pH 9.5), but the trend between 6 and 11 shows increasing zeta potential with decreasing pH. A more significant trend shift change appears around pH 4, and the IEP is at pH around 3.

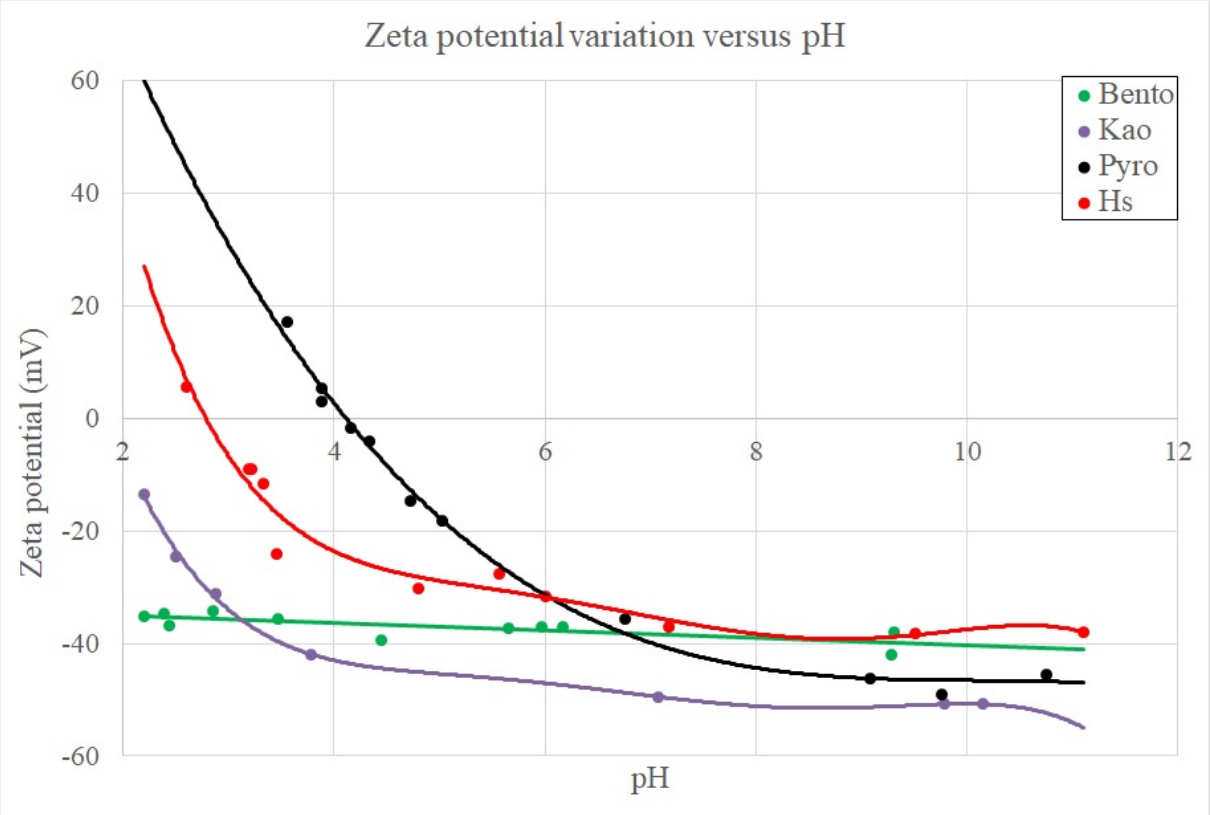

Fig. 4.7. Zeta potential variation versus pH for all materials. Only the pyrolusite concentrate and the hausmannite reach IEP in the pH range of 2 to 11, at pH 4.2 and 3 respectively.

6.2 Tableting results

The tableting experiments were first performed on the pure materials and concentrates under defined pressures (0-450 MPa), H_2O contents (0-10 wt.%) and with pH-buffered solution (3,7 and 11). Complementary tableting experiments were performed on blends, with an emphasis on hausmannite-pyrolusite concentrates (Table 4.1).

Various combinations of blends, pressure and H_2O content were tested. All the graphs in this chapter including the applied pressure and Rd display averaged values. The range of values used for each of these averages are displayed using error bars along the x and y axes. Values of the Rd were calculated from the tablet dimensions and its breakage force.

6.2.1 Raw material behavior

Figure Fig. 4.8 shows Heckel curves of all samples under pressure, describing their behavior during compaction. Bentonite has the longest particle rearrangement and the lowest Py. This indicates that reorganizing bentonite particles requires more energy than for the other materials, and bentonite keeps deforming as pressure increases. The Py value of 255 MPa is close to the limit of material with intermediate mechanical behavior. Kaolinite, pyrolusite concentrate and hausmannite show an easier rearrangement and a more fragmentary behavior (with Py values of 709, 1116, 5477 MPa respectively). The maximum pressure achieved for the clay samples is lower,

due to their small granularity and the mechanical behavior, which allows them to flow out of the die during compaction experiments.

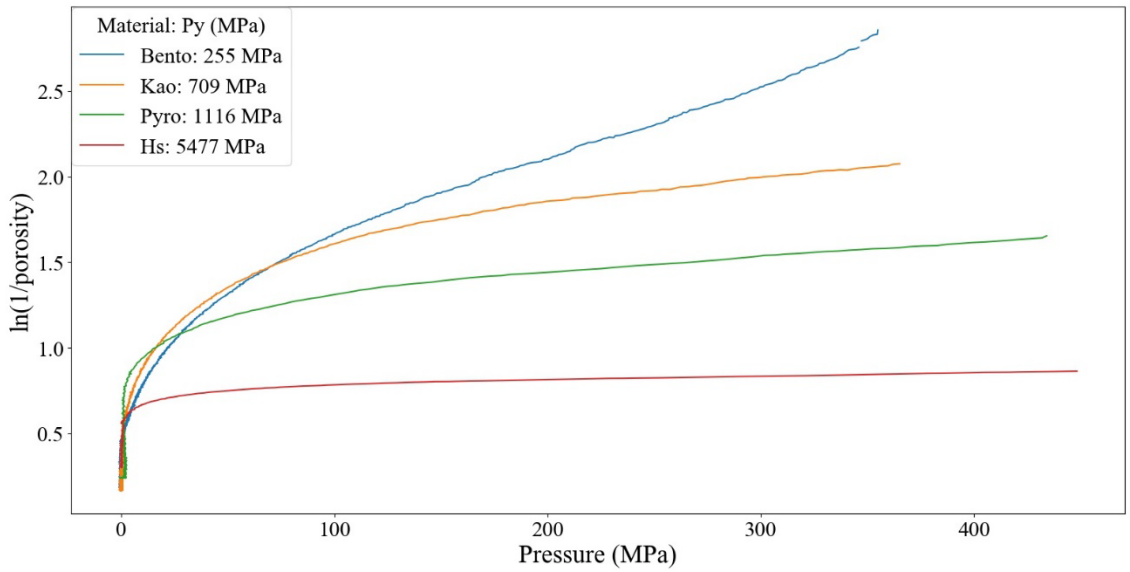

Fig. 4.8. Heckel curves for all samples, showing the behavior of each sample under pressure. For each sample, the yield pressure (MPa) has been calculated. Pyro: Pyrolusite concentrate, Hs: Hausmannite.

Figure Fig. 4.9 shows plots of the Rd against the pressure for the four materials. Due to the very fine granularity and matrix conicity, part of the samples exited the die, especially during dry tableting. This hampered the experiments above 400 MPa for the bentonite, kaolinite and hausmannite. Figure Fig. 4.9 represents all curves at 0 wt.% H_2O, which are reintroduced in the other graphs as reference curves. The vertical bars indicate Rd variability, showing that pyrolusite concentrate tablets are more reproducible than in the case of bentonite and kaolinite.

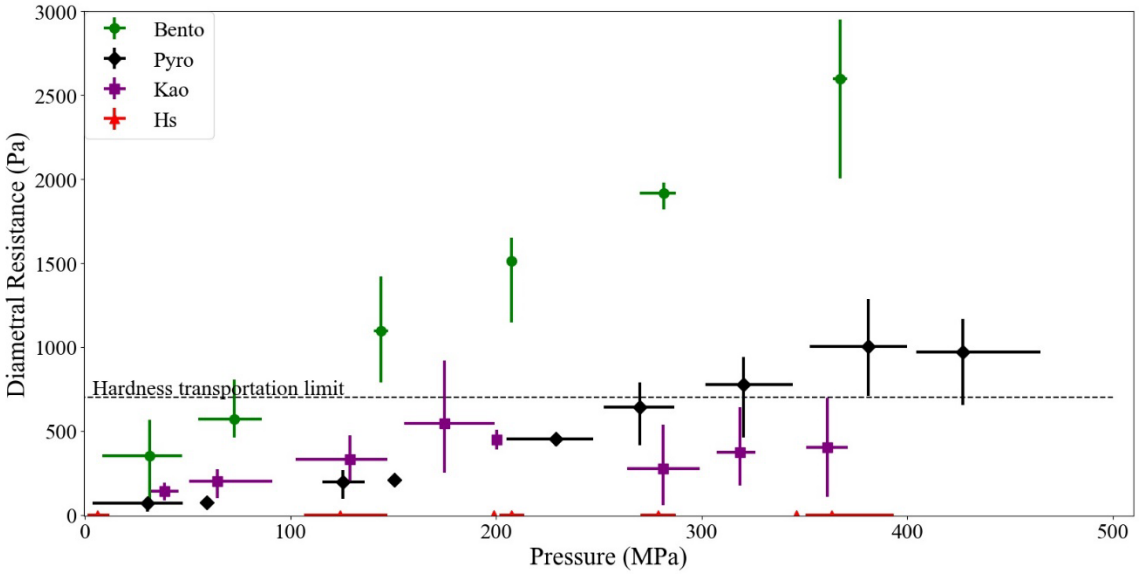

Fig. 4.9. Diametral resistance versus the pressure for all materials.

Bentonite shows the strongest correlation between Rd and pressure, reaching 2700 kPa Rd at 350 MPa. Kaolinite does not produce pressure-dependent agglomeration results, with near-constant Rd values around 500 kPa. Pyrolusite concentrate reaches the highest value at 1100 kPa for 420 MPa. It also shows an increase in Rd with pressure. Hausmannite shows no impact of pressure, and do not produce a self-adhesive agglomerate.

6.2.2 H_2O content

Figure Fig. 4.10 shows Heckel curves at various H_2O contents for all samples. The increased adhesion due to H_2O allows higher pressure to be applied for the clay minerals, revealing a threshold above which its porosity decreases sharply. This feature is typical of viscoelastic materials. At 3 wt.% H_2O, Py drops to 198 MPa, closer to the limit of intermediate materials. The addition of H_2O does not impact the kaolinite sample. The addition of H_2O to the pyrolusite concentrate increases rearrangement efficiency as well as Py. However, no significantly different behavior occurs between of 2 and 4 wt.% H_2O content. Water addition to hausmannite decreases its rearrangement efficiency and thus its final porosity.

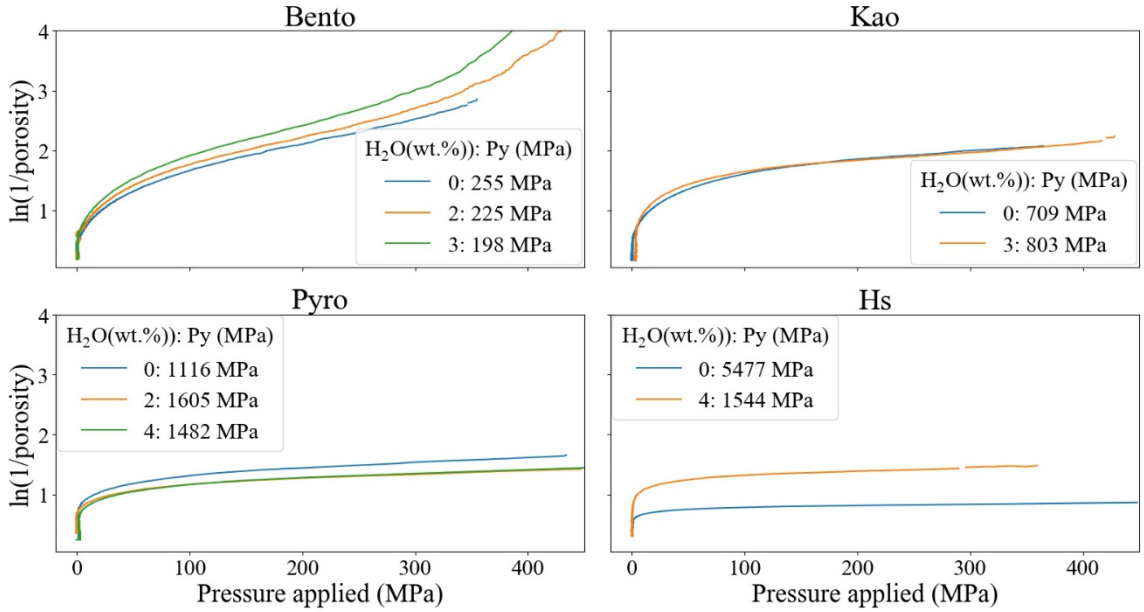

Fig. 4.10. Impact of H2O on the behavior of all four samples.

For bentonite, 2, 5 and 10 wt.% H_2O were studied. At 2 wt.% H_2O, Rd is about three times higher (1100 kPa instead of 400 kPa) at 50 MPa than without water. The maximum Rd of 1500 kPa is reached at 150 MPa. Rd drops significantly at 10 wt.% H_2O (Fig. 4.11). The kaolinite Rd shows little impact with the addition of water up to 5 wt.%. The addition of 10 wt.% H_2O causes a sharp Rd decrease (Fig. 4.11). For the pyrolusite the addition of water significantly increases Rd, but little difference is observed between 2, 4 and 10 wt.% H_2O. (Fig. 4.11).

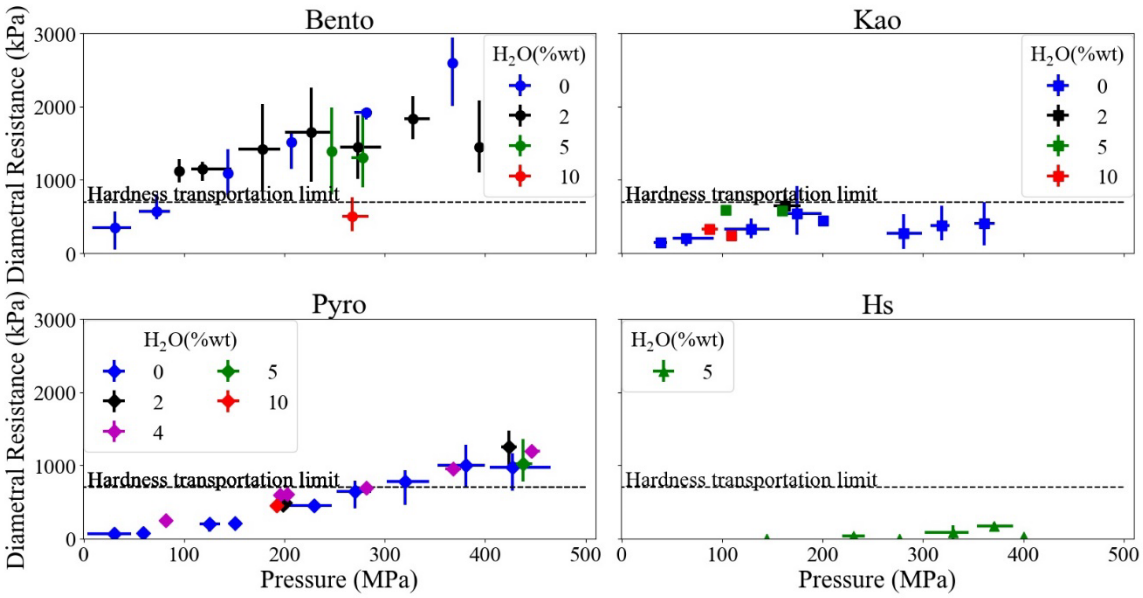

Fig. 4.11. Diametral resistance versus the pressure at various water content for bentonite, kaolinite, Pyro and Hs. Only the 5 wt.% H_2O curve is shown for the hausmannite, as all the other curves had lower Rd. The vertical bars indicate maximum and minimum for each setting.

Figure Fig. 4.12 shows a bentonite tablet with 3 wt.% H_2O compressed at 400 MPa. On Fig. 4.12 A an inner part with a sharp convex limit rim towards the outer part can be seen. This outer part is cracked from its contact with the inner part to the outer rim. The crack is perpendicular to those visible on the cross section of the tablet (Fig. 4.12B). The top part of the tablet (Fig. 4.12C) shows displacement of the material related to pressure. The crack (visible also in Fig. 4.12B) is not parallel to the surface as the crack at the bottom. The displacement may be related to elastic recovery at pressure release.

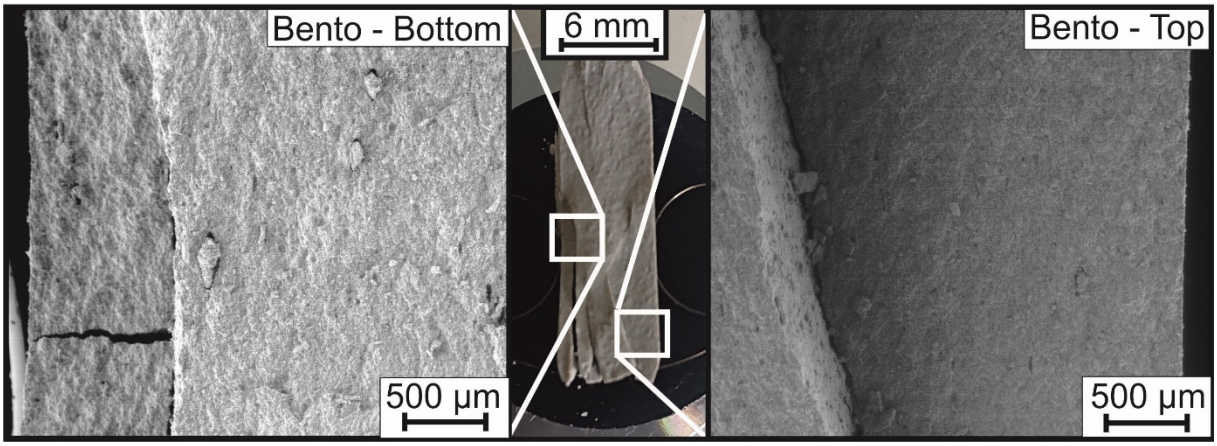

Fig. 4.12. SEM image (SE) of the top (A) and bottom (C) a bentonite tablet compressed at 400 MPa with 3 wt.% H2O, referenced around an optical picture (B). The central picture shows the section of a bentonite tablet fractured perpendicular to the pressure orientation due to elastic recovery at pressure release.

6.2.3 pH variation

The impact of pH on the material behaviors during tableting was evaluated. Figure Fig. 4.13 shows Heckel curves for all materials at 4% moisture and various moisture pH. At pH 3 and 7, bentonite has Py values of 238 and 191 MPa, i.e. very close to the intermediate behavior limit. At pH 11, its Py increases to 370 MPa, increasing its fragmentary behavior. Kaolinite is close to the intermediate behavior limit at pH 3 and 11, but pH 7 causes a higher Py. The impact of pH on the pyrolusite concentrate is negligible, while at pH 3.8 and 11, the fragmentary behavior of hausmannite is decreased (Fig. 4.13).

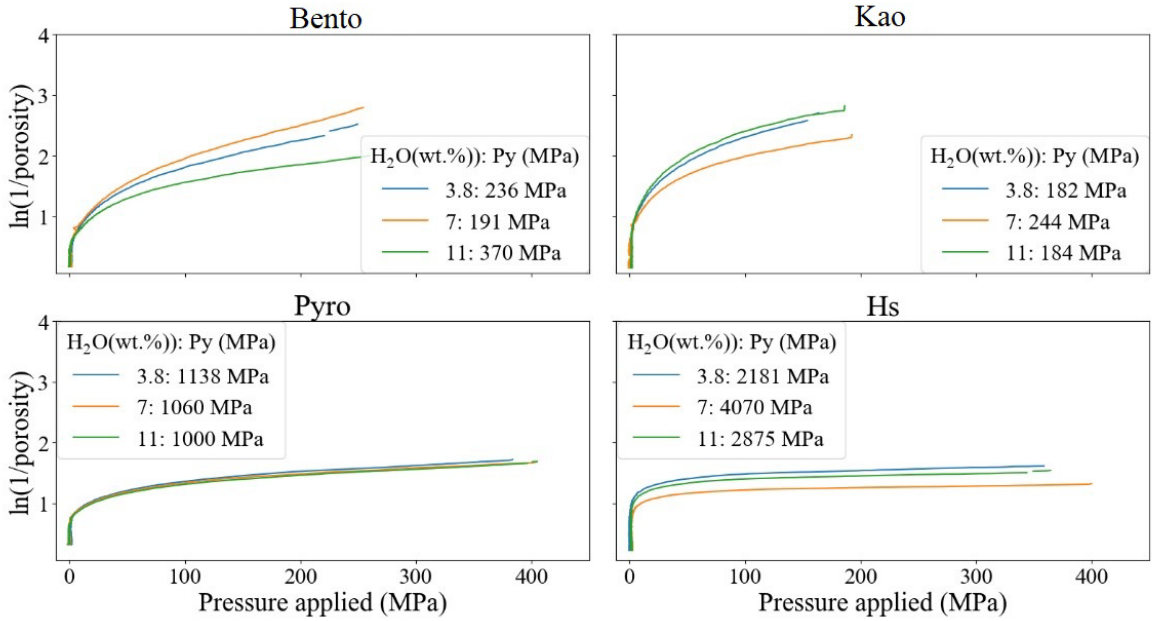

Fig. 4.13. Heckel curve for all material at 4 wt.% moisture and various pH. Pyro: pyrolusite concentrate, Hs: hausmannite.

Figure Fig. 4.14 shows Rd versus pH for all materials. The average Rd for bentonite decreases between pH 3.8 and pH 7 from 1250 to 750 kPa, but no significant variation can be observed between pH 7 and 11. However, these highy variable results must be taken with caution. Kaolinite shows a continuous Rd decrease (410, 340 and 240 kPa) with increasing pH, though three orders of magnitude lower than bentonite. The pyrolusite concentrate displays similar Rd compared to those of bentonite for pH 3.8 (1190 kPa) to pH 7 (840 kPa). However, it increases toward pH 11, reaching 1040 kPa. The hausmannite only produces a self-adhesive tablet at pH 3.8, at about 100 kPa.

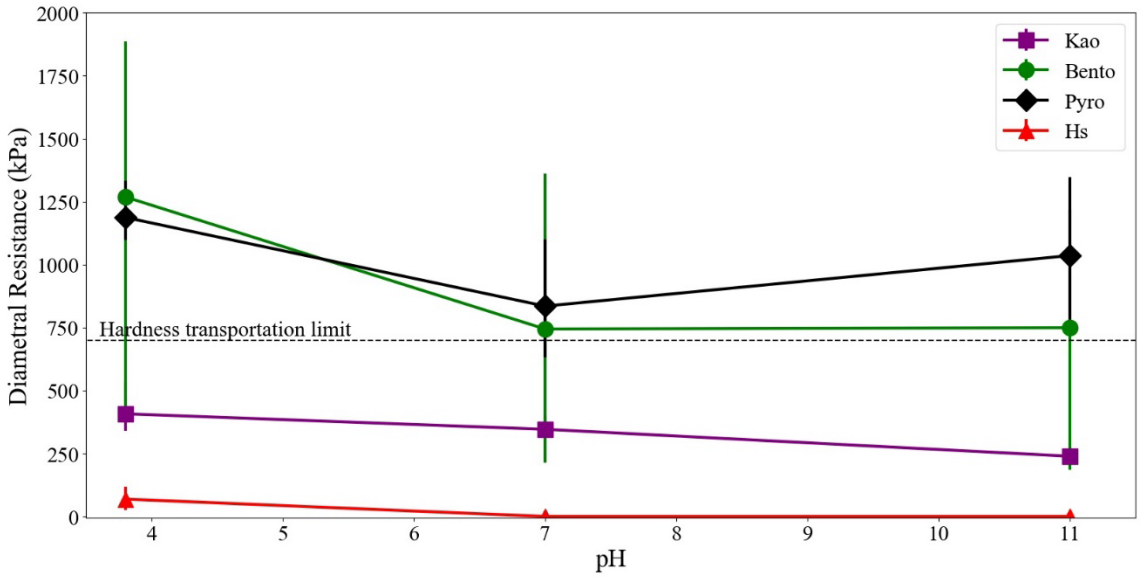

Fig. 4.14. Diametral resistance versus pH variation at 4 wt.% moisture for all four samples. The error bars show the maximum and minimum for each set of tests.

6.2.4 Blends of pyrolusite concentrate and hausmannite

Figure Fig. 4.15A presents Heckel curves of blends containing various pyrolusite concentrate content at 4 wt.% H_2O. The general trend is that lower pyrolusite concentrate content results in lower rearrangement time, lower final porosity and high Py, hence a more fragmentary material. This is coherent with the individual observation of the initial samples.

Figure Fig. 4.15B shows Heckel curves for 80/20 wt.% pyrolusite concentrate/hausmannite blends at various H_2O contents. H_2O addition up to 6 wt.% decreases the yield pressure of the blends. However, the yield pressure at 8 wt.% H_2O is higher than that at dry conditions.

Figure Fig. 4.16 presents the Rd of various pyrolusite concentrate and hausmannite blends at variable H_2O contents, at 300-450 MPa. The pressure varies depending on the blend compositions and the water content. Constant pressure could not be applied due to the variable mechanical behaviors of the blends. As in the previous experiments, H_2O content was set at intervals: 0, 2, 4, 6 and 8 wt.%.

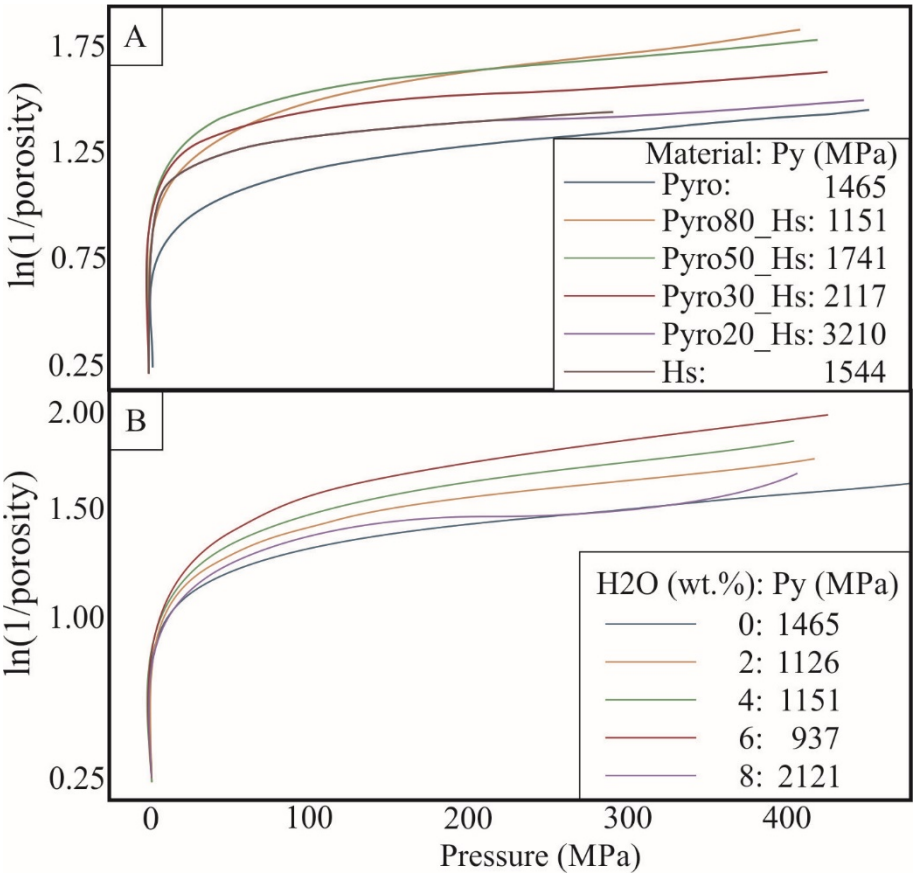

Fig. 4.15. Heckel curves for blends of A) variable pyrolusite concentrate (Pyro) content, at 4 wt.% H2O and B) blends of 80/20 Pyro/Hs blends, at various wt.% H2O content.

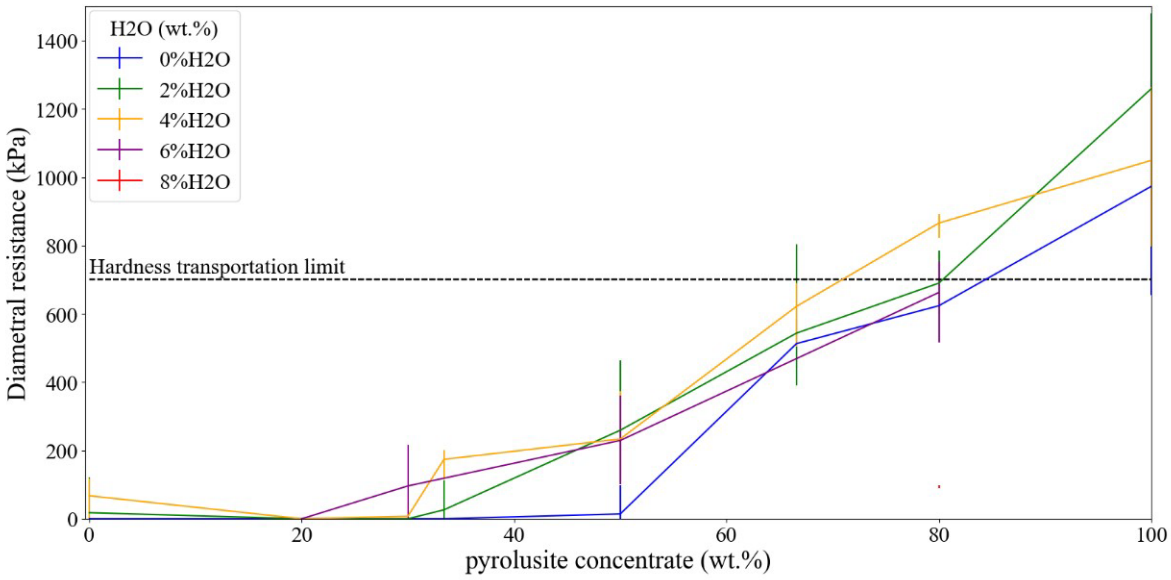

Fig. 4.16. Diametral resistance of blends among pyrolusite concentrate and hausmannite at various H2O content, at 300-450 MPa.

All blends show increasing Rd with increasing pyrolusite concentrate contents, regardless of H_2O contents. At 0 wt.% H_2O, tableting was not possible if the blend contained less than 50 wt.% pyrolusite concentrate. At 50 wt.% pyrolusite and 2, 4 and 6 wt.% H_2O, Rd increases up to 300 kPa whereas at 8 wt.% H_2O, Rd drops back to 0. The highest Rd for blends is reached at 4 wt.% H_2O and 80 wt.% pyrolusite concentrate addition, at about 900 kPa.

The results of the SEM investigations on the internal surface of the broken tablets are shown in Fig. 4.17. A blending 80 wt.% of a pyrolusite concentrate with 20 wt.% of hausmannite, results in a visible physical impact of H_2O on tableting. Higher H_2O content decreases the number of particles at the surface, and the edges of the tablets are flatter and smoother (Fig. 4.17 A, C, E).

In Fig. 4.17 B, C, D, F the impact of blend variations at 4 wt.% H_2O is presented. Tablets with higher pyrolusite concentrate content display rougher surfaces covered with angular particles, as well as smoother and straighter edges. Decreasing pyrolusite concentrate content results in cracks, (about 10 µm wide, 1.3 mm long, Fig. 4.17F), and shows an increasing number of hausmannite spheres (up to 170 µm in diameter).

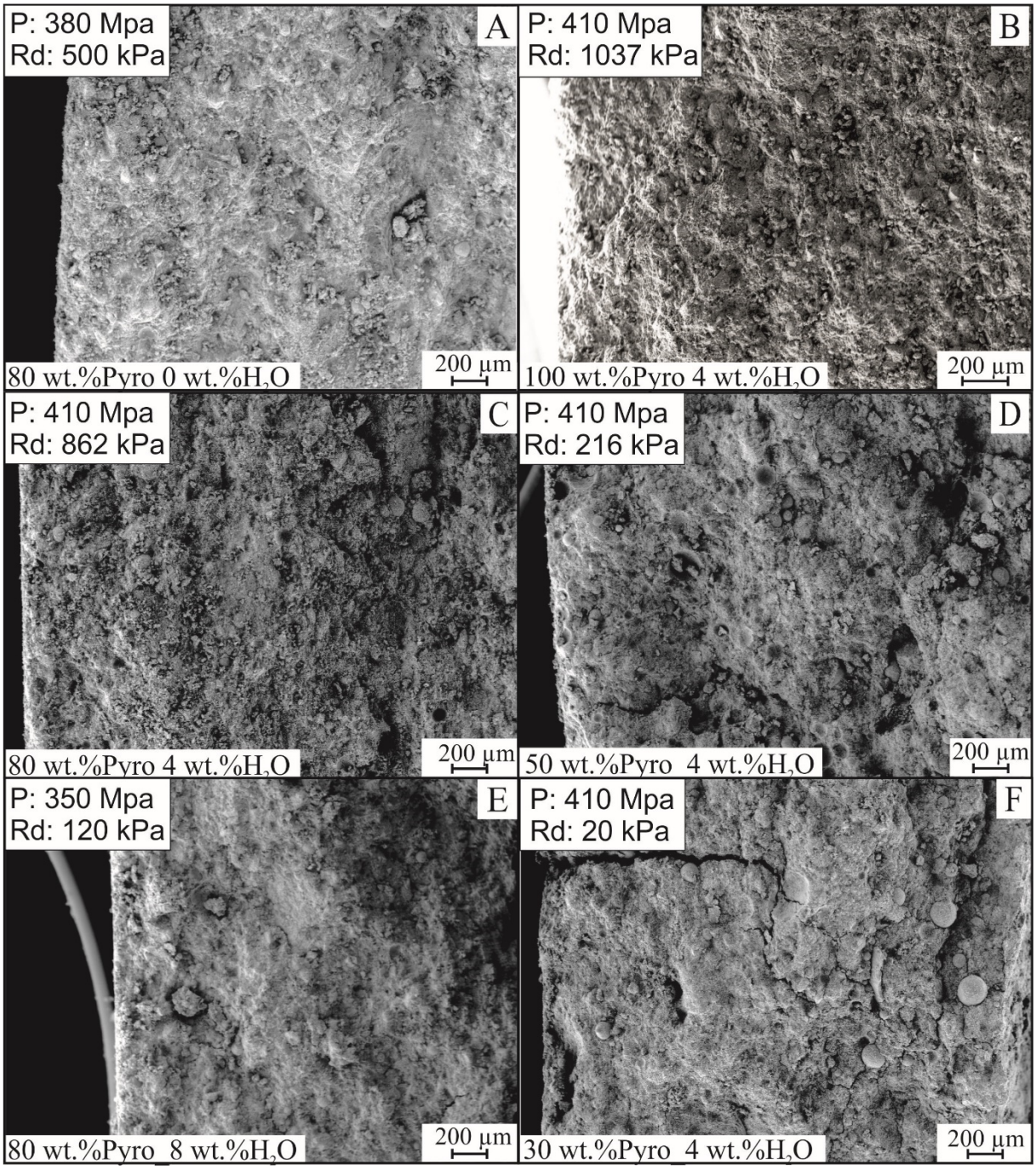

Fig. 4.17. SEM pictures (taken at 15 kV using SE) of the bottom part of blended agglomerated with A) 80 wt.% Pyro, 0 wt.% H2O, B) 100 wt.% Pyro, 4 wt.% H2O, C) 80 wt.% Pyro, 4 wt.% H2O, D) 50 wt.% Pyro, 4 wt.% H2O, E) 80 wt.% Pyro, 8 wt.% H2O, F) 30 wt.% Pyro, 4 wt.% H2O. The pressure applied during agglomeration (P) and resulting Rd is noted in the upper left corner.

Figure Fig. 4.18A displays the initial particles of the pyrolusite concentrate fixed on a tape, similarly to hausmannite in Fig. 4.4 D1. However, the particles in Fig. 4.18 show variable and angular habitus, and their surface appears rough, covered with sub-micrometric particles of kaolinite and lithiophorite.

The images in Fig. 4.18 B, C and D display zooms of the spherical particles from Fig. 16. Surfaces appear cracked and composed of polyhedral crystals. However, no cracks cut through the spherical particle. The cracks in Fig. 4.18C appear more irregular than those on Fig. 4.18D, which more likely follow grain boundaries.

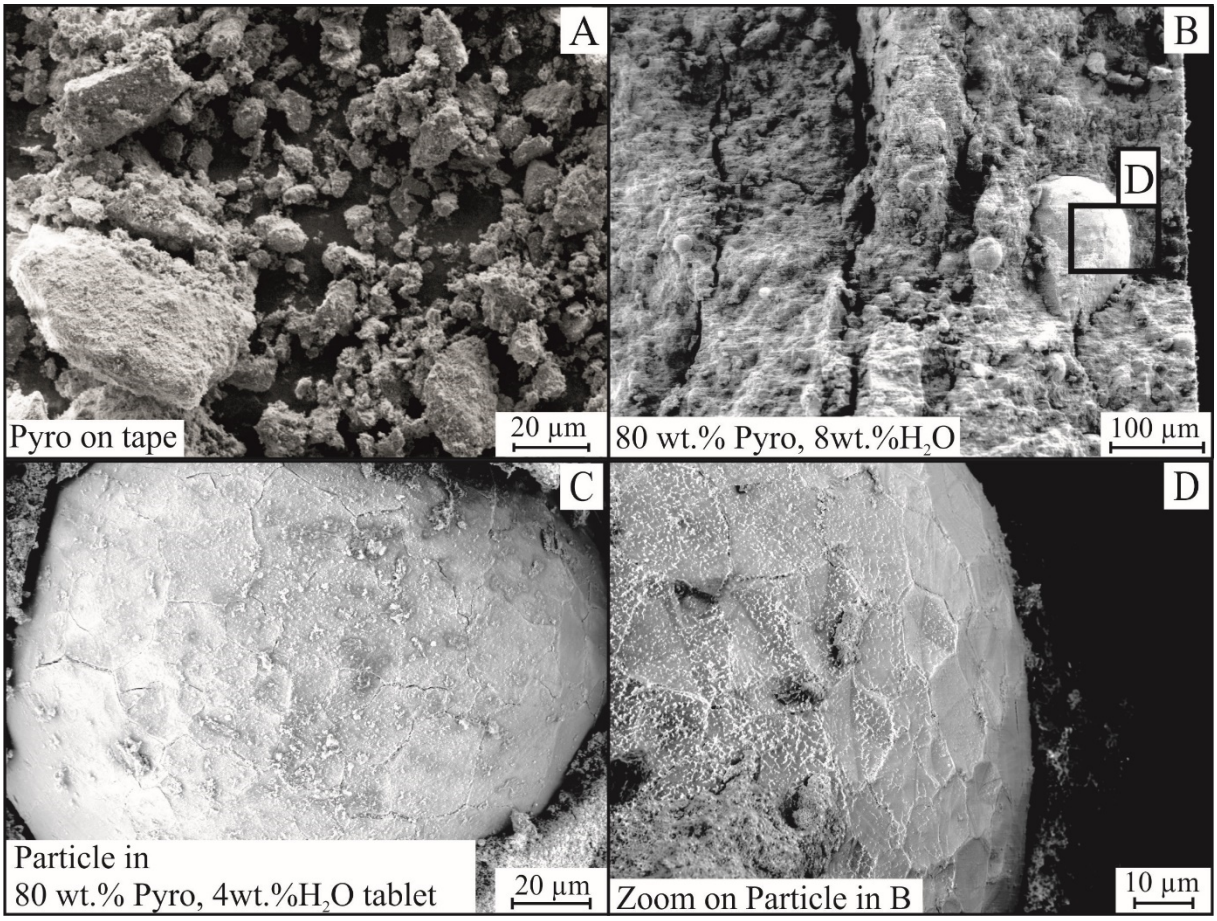

Fig. 4.18. SEM (SE) images: A) Pyrolusite concentrate, B) Top half of a tablet representing a blend of 80 wt.% pyrolusite concentrate and 20 % of hausmannite with 8 wt.% H2O, C) Rounded particle in a tablet of 80 wt.% pyrolusite concentrate and 20 % of hausmannite with 4 wt.% H2O (Note that the surface is deformed), D) Zoom on a particle shown in B, shown by the black rectangle, also in C. The surface is composed of polyhedric crystals of Mn-oxide, imbrication of the matrix material may have caused marks on the surface. The tablets in this figure were produced at 350 MPa.

6.2.5 Blends of pyrolusite concentrate/kaolinite and hausmannite/kaolinite

Figure Fig. 4.19shows Heckel curves for various blends of pyrolusite concentrate/kaolinite and hausmannite/kaolinite. The impact of adding kaolinite depends on the blend composition. Py drops from 1050 MPa at 90 wt.% pyrolusite concentrate to 850 MPa for 66 and 50 wt.% pyrolusite concentrate.

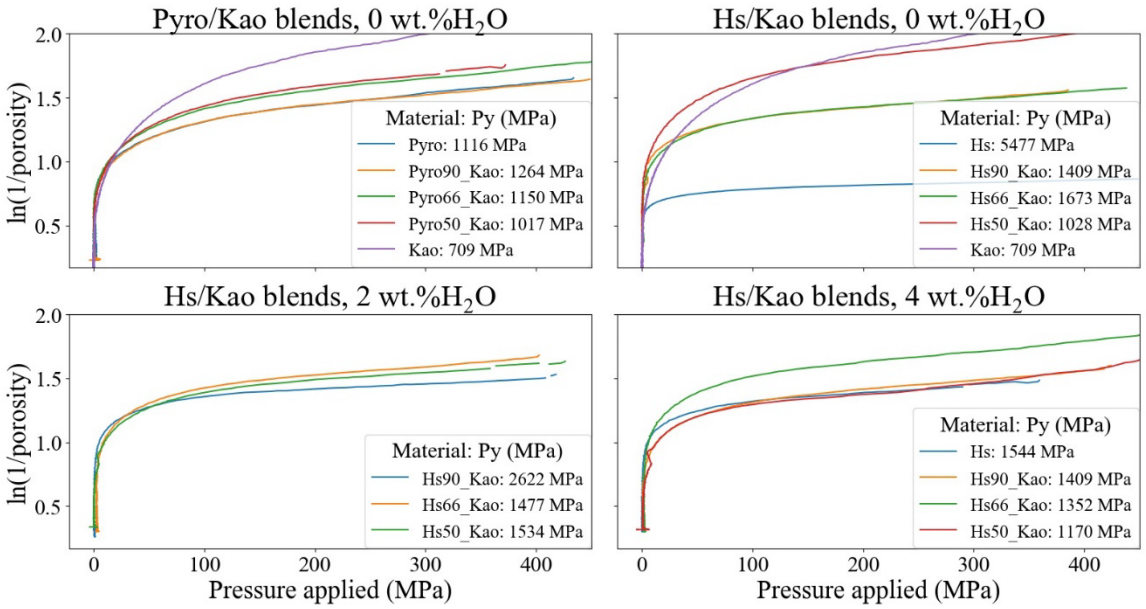

Fig. 4.19. Heckel curves for different levels of Pyro or Hs content, blended with kaolinite, at 0 wt.% H2O.

At 0 wt.% H_2O, the blend of hausmannite and kaolinite shows decreasing yield pressure and increasing final density with increasing kaolinite content. At 2 wt.% H_2O, increasing kaolinite content has much lower impact, although it correlates with decreasing Py. The variation in final density is much lower than at 0 wt.% H_2O. At 4 wt.% H_2O, the main visible difference is in the final density at 66.6 wt.% Hausmannite, which is higher than for the other blends. Py is similar among the different blends.

Experiments were performed on kaolinite/pyrolusite concentrate blends at 0 wt.% H_2O. The Rd increases up to 1400 kPa between 10 and 30 wt.% kaolinite, before dropping below 600 kPa at 50 wt.% kaolinite. The graph is presented in supplementary material 4 (Appendix 6).

Experiments were performed on hausmannite/kaolinite blends with various composition and H_2O content. When the blend is dry, no cohesive tablet can be obtained. At 2 wt.% H_2O, a cohesive tablet can be obtained at 50 wt.% hausmannite. At 4 wt.% H_2O, the blends with hausmannite content > 50 wt.% display self-adhesive yet low Rd (~ 200 kPa) tablets. The graph is presented as supplementary material 5 (Appendix 7).

6.2.6 Blends of hausmannite and bentonite

Experiments were performed on hausmannite/bentonite blends at 2 wt.% H_2O, with 90 and 80 wt.% hausmannite. Using Heckel's model, those blends show a more viscoelastic behavior (Py: 155 and 154 wt.%, respectively) than the hausmannite and bentonite concentrates (Py: 1459 and 225 MPa, respectively). Particles rearrangement of the blends is like that of bare hausmannite under low pressure. The graph is presented as supplementary material 6 (Appendix 8).

At 10 wt.% bentonite tablets are self-adhesive with Rd of 350 kPa. This value is below the industrial requirements of 700 kPa. Rd does not significantly change despite the presence of 10 wt.% bentonite.

7. Discussion

This is the first study so far using tableting without binder on bentonite, kaolinite, pyrolusite concentrate and hausmannite, under controlled conditions of pressure, H_2O content and pH. While tableting is one of the main agglomeration methods used in the pharmaceutical industry, it has become of increasing interest to the mining and pyrometallurgical industries in the last few years (He et al., 2015; Poirier, 2014). The advantages of this method are shorter processing time, lower energy consumption, and limited use of excipients and/or binders. In addition, a comprehensive characterization of those materials contributes to understanding the complex microprocesses occurring during tableting such as particle rearrangement, plastic and elastic deformation and particle fragmentation (Wünsch et al., 2019). This is expected to help predicting the structure and mechanical properties of final tablets, instead of relying on empirical approaches presently used in the formulation and process development of the agglomeration industries (Wünsch et al., 2019).

7.1 New insights into tableting processes

In this study, tablet strength is assimilated to its compressive strength. High compressive strength is achieved through high bonding surface area between the particles of a sample. During compaction, this bonding surface area is increased by 1) the rearrangement and 2) the plastic or fragmentary deformation of the tablet materials and of the particles (He et al., 2019).

7.1.1 Particle rearrangement

The rearrangement is the first step in tableting, chasing air from the sample and decreasing porosities (Veyera, 1994). It will result in an increase of the number of next neighbour particles and a decrease of the average contact surface (Martin et al., 2003). The energy necessary to rearrange the particles correlates positively with the interparticle frictional forces (Tay et al., 2019).

The interparticle frictional forces are influenced by changes in surface roughness and static charges (Kawashima et al., 1994). In this study, bentonite has the highest CEC (59.2 meq/100 g) and BET (27 m^2/g), and its particles are mainly non-convex (Fig. 4.4). Those properties should result in bentonite having the highest interparticle frictional forces of the four samples studied. In contrast, the hausmannite should have the lowest interparticle frictional forces, since it has the lowest CEC (<1 meq/100g) and BET (2 m^2/g), and convex (spherical) particle shape (Fig. 4.4). This is confirmed by the pressure necessary to achieve particle rearrangement, which amounts to 150 MPa and 50 MPa, for bentonite and hausmannite, respectively (Fig. 4.8). These values correspond to the pressure value at which the linear region of Heckel curves is reached.

Kaolinite and pyrolusite concentrate have CEC (2.38 and 0.54 meq/100g, respectively) and BET (4 and 9 m^2/g, respectively) in the same order of magnitude. Kaolinite particle morphology obtained by calculation from QICPIC data is non-convex, while that of pyrolusite concentrate is convex. However, SEM investigations (Fig. 4.4 and Fig. 4.19) shows that pyrolusite concentrate particles are covered by fine-grained material. This feature cannot be detected by the QICPIC, and it illustrates the bimodal nature of the pyrolusite concentrate and the complexity of its particles. It is mostly composed of pyrolusite and cryptomelane, both high hardness oxides composing the inside of the particles, but also contains lithiophorite occurring as a coating or an interstitial matrix. The latter consists of low-hardness phyllomanganate with a clay-like structure and charges on the surface of its layers (Manceau et al., 2005).

CEC, BET and zeta potential measurements were only determined on the bulk sample. No measurement was performed on pyrolusite and layered-structured lithiophorite separately, and no information was available in the literature. Such measurements could reveal much higher CEC and BET values for lithiophorite than for pyrolusite and cryptomelane. During rearrangement of these particles, the lithiophorite coatings are in contact with each other. Their effective charges and plastic behavior increase the interparticle frictional forces. The hard particles can also have an impact. A parallel can be drawn with the rheology of fluids, where the presence of particles increases its viscosity (Caricchi et al., 2007; Chen et al., 2010). The coexistence of high and low hardness minerals in the sample would increase interparticle frictional forces at material level, while the lithiophorite properties would increase these forces at particle level. This explains why kaolinite and pyrolusite concentrate show similar interparticle frictional forces, as illustrated by their particle rearrangement pressure around 130 MPa.

A higher pressure necessary to rearrange the particles of a material (e.g. bentonite versus hausmannite) is reflected by a higher flow resistance, and its poorer compressibility. Higher interparticle frictional forces lead to a strong interlocking of the particles, especially when the sample contains non-convex particles (e.g. bentonite, kaolinite and pyrolusite concentrate on Fig. 4.4 and Fig. 4.6). This interlocking produces a heterogeneous repartition of the structures inside the tablets and a low contact anisotropy resulting in an uneven load partitioning between the contact surfaces. Hence failure zones in the resulting agglomerates will be more dispersed.

7.1.2 Particle and material deformation

Deformation is observed at tablet and particle scales due to both compression and decompression. The energy available to deform the particles in the second step of tableting will decrease as the energy required during the particle rearrangement increases (Tay et al., 2019). The Py is the pressure that must be applied to overcome a material yield strength and deform it plastically. Thus, the decrease in the energy means that materials showing higher Py will not undergo plastic deformation. Such material with Py higher than the applied pressure can be deformed elastically or fragmentarily (He et al., 2019).

In our study, hausmannite, with a high Py, shows evidence of deformation. This material was initially composed of micrometric and spherical particles with smoothed surfaces which frequently form clusters (Fig. 4.20A) prior to deformation. After deformation at 350 MPa of hausmannite in a matrix of 80 wt.% of pyrolusite concentrate and 4 or 8 wt.% H_2O, microsphere clusters may have recrystallized to form the round shaped, 100 µm large particles with cracked polyhedral surface present in the Pyro/Hs blends (Fig. 4.20B and Fig. 4.19 C, D). However, the apparent porosity of hausmannite given by the Heckel curves (Fig. 4.8) shows little variations. On the other hand, Heckel curves for the three other materials indicate ongoing deformation with increasing pressure (Fig. 4.8).

The Py for bentonite (143 MPa) is below the pressure applied, allowing for plastic deformation. However, Py is higher for kaolinite and pyrolusite concentrate (715 and 954 MPa, respectively). Our results on pyrolusite concentrates indicate bimodal composition, with soft and plastically deforming minerals (lithiophorite) and hard mineral like pyrolusite and cryptomelane. Those hard grains form the skeleton of the tablet and give it its compressive strength. No data are available for the mechanical behavior of pure lithiophorite. However, it has a layered structure like clays, that can be explained crystallographically by alternating brucite like layers with MnO_2 octahedron layers. Therefore, lithiophorite should display plastic deformation up to 400 MPa applied pressure.

It thus grants the tablet its cohesiveness, occupying the interstitial spaces between the grains and bonding the particles together.

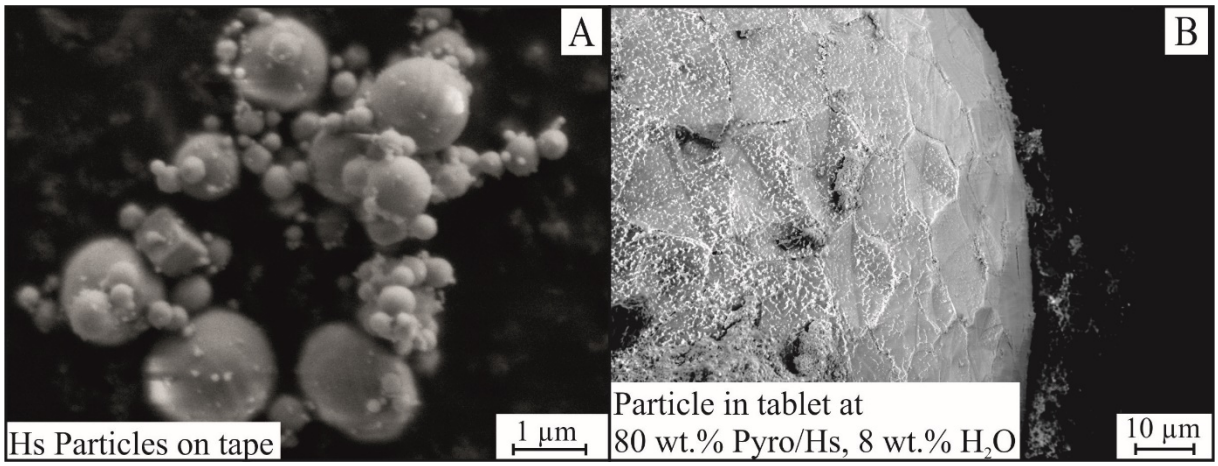

Fig. 4.20. SEM pictures of A) Hausmannite particles before agglomeration on carbon tape and B) Zoom on a particle with hausmannite signature, after agglomeration.

He *et al.* (He et al., 2019) found that an enhanced tablet strength is generally achieved for lower Py and higher interparticle frictional forces. However, the literature and our experiments highlight two major exceptions. The first one is pre-agglomerated material that will break-up during tableting, because it creates fresh surfaces that will increase the interparticle bonding of the particles. It beneficiates from less interparticle frictional forces enabling better distribution in the agglomerate (Kawashima et al., 1994). This may also apply to fragmentary material with low hardness that will break-up even without pre-agglomeration. The second exception concerns the material displaying elastic recovery behavior, occurring during pressure release. Comparing Rd for kaolinite and pyrolusite concentrate tablets, the latter displays better results at pressures above ~200 MPa. Kaolinite undergoes elastic deformation at pressures below 200 MPa, leading to elastic recovery of about 25 % (Awad et al., 2019). The elastic recovery of a material, associated with the anisotropy of the contacts (discussed in section 5.1.1), is related to the capping (horizontal cleavage) of the tablet (Ahmed, 2014). This deleterious effect decreases Rd and the integrity of a tablet. An increase in dwelling time is usually introduced to decrease the elastic recovery, dissipating it over time. However, despite introducing a 5000 ms dwelling time, clay minerals continued to display a capping above 100 MPa. Hence this elastic recovery counteracts the increase in bonding size due to pressure increase and can explain why kaolinite Rd does not increase with applied pressure. In contrast, bentonite shows less capping and cleavages under similar decompression conditions, as it has higher surface charges and bonding strength.

Our findings are in agreement with models developed by He et al (He et al., 2019), who show that larger tablet strength is achieved for high average bond size and low bond size distribution, high interparticle frictional forces, high non-convexity and low yield pressure.

However, it has to be taken into account that the study of He et al (He et al., 2019) was performed on uniform material. Complex materials such as the pyrolusite concentrate may deviate from these conclusions and require deeper understanding for their tableting potential to be predicted.

7.2 Water impact

In the agglomeration industry, moisture is commonly added, either to disperse the binder, or as a binder itself. It is also useful to reduce dust generation from tablets by increasing their

cohesiveness through the formation of capillary bridges. Moisture addition impacts both particle rearrangement and material and particle deformation, but it highly depends on the material (Louati et al., 2017).

In this study, water addition (up to 4 wt.% H_2O) to hausmannite and bentonite resulted in an increase in final density and a decrease in Py. Wang *et al.* (Wang et al., 2017) performed studies on synthetic silica spheres and angular silica beach sand, and found that low water saturation (about 25 %) will ease the rearrangement of the particles, facilitating their displacement and reducing the porosity. This is in agreement with our observations and explained by hausmannite low surface charges and conductivity, similar to that of their studied materials (Revil et al., 2015). Bentonite is mainly composed of smectite (montmorillonite), which has interlayer spaces able to accommodate water, but also different types of pore spaces (Matusewicz and Olin, 2019). This facilitates layer separation and particle rearrangement (Halt and Kawatra, 2014), a behavior that is also enhanced by electrostatic forces in the presence of water (Salles, 2006). There is an increase in final density, but of lower amplitude compared to hausmannite.

Water addition to pyrolusite concentrate and kaolinite has less and negligible effect on particle rearrangement and deformation, respectively. In the pyrolusite concentrate, Rd is increased with the addition of water (Fig. 4.11). This can be explained by the formation of capillary bridges leading to particle bonding, which decreases electrostatic forces (Louati et al., 2017).

However, at lower saturation, moisture helps reducing the cleavages by elastic recovery, while its impact on tablet deformation is below the capillary bridges break-up conditions (Rodd et al., 2005).

At high water content (above 8 wt.% H_2O), all materials show the same behavior characterized by a drop in Rd and water exuding from the tablet. Due to the modification of the material to a slurry (Louati et al., 2017), material extrudes from the die. This confirms observations made by Wang *et al.* (Wang et al., 2017) that above 75 % H_2O saturation, water lock-up occurs, preventing particle displacements. It hence stiffens the material and hinders its rearrangement.

7.3 pH impact and surface charges

pH and zeta potential are commonly looked upon in colloidal sciences (Hunter, 1988) and usually not considered in agglomeration processes. It is assumed that close to its IEP a material significantly increases its tendency to agglomerate (Suttiponparnit et al., 2010). The absence of similarly charged surfaces decreases particle repulsion, allowing for higher bond size potential. In this study, pyrolusite concentrate shows improved tableting results at pH 3.8, which coincides with its IEP. The slight improvement during tableting of kaolinite and hausmannite at lower pH correlates with decreasing magnitude in zeta potential.

Bentonite shows better tableting properties at low pH. This most likely finds its explanation in an increase bonding strength. Its zeta potential variations differ from that of the other materials present in this study. Most of the surface charges of bentonite are due to elemental substitutions in its layers, and are therefore negative independently of pH. However, the edges of its layers present pH dependent “broken bonds” and exposed OH groups, but they generally represent only 2-3 % of the exposed surface of the smectite clays (Grim, 1968). Those edges present positive charges at low pH and negative charges at higher pH (Yariv and Cross, 1979), allowing for stronger bonding of inversely charged surfaces as proposed by Halt and Kawatra (Halt and Kawatra, 2014).

At high pH, the peculiar behavior of pyrolusite concentrate is due to the presence of lithiophorite. The lithiophorite has a structure of alternating octahedral MnO_2 and brucite-like layers (Roqué-Rosell et al., 2010). Brucite has an IEP of 11 (Pokrovsky and Schott, 2004), which may translate

to improved agglomerability of lithiophorite at pH 11 due to similar structure. Although no zeta potential variation is visible around pH 11 (Fig. 4.7), reaching lithiophorite IEP, may increase overall pyrolusite concentrate tableting performance results.

Tableting can be impacted by pH through the modification of the (1) bonding size, by preventing particle repulsion due to their surface charge, and (2) bonding strength, by creating bonds between oppositely charged surfaces. In our study bonding size and strength are optimized at low pH. For the pyrolusite concentrate high alkaline pH is favorable, related to the presence of lithiophorite.

7.4 Mixed material behavior

Tableting experiments on blends of pyrolusite with hausmannite were performed to optimize tableting of manganese fines. Additionally, tests were performed on kaolinite and bentonite blended with hausmannite and pyrolusite concentrates for comparative purposes.

The bentonite and kaolinite produced self-adhesive agglomerates when blended with hausmannite, even at low content (10 wt.%; See supplementary material 5 (Appendix 7)). This correlates with independent findings (Ilkka and Paronen, 1993), which shows that plastically deforming material dominates the mixing behavior when blended with a fragmentary material.

Furthermore, the study revealed that by blending two fragmentary materials, the less compressible one dominates the behavior of the blend. This is not entirely the case for the pyrolusite concentrate-hausmannite blend used in this study. At 0 wt.% H_2O, the pyrolusite concentrate largely controls the behavior of the mix up to 50 wt.% hausmannite, based on a simple linear consideration of the Py values (Fig. 4.16). In contrast, Rd from the tableting experiments indicates that tablets are no longer self-adhesive between 33.3 and 50 wt.% hausmannite, because the less coherent hausmannite dominates. The assumption is that the pyrolusite concentrate forms tablets supported by a matrix of fine grained lithiophorite (Fig. 4.21). The added hausmannite will be included in this matrix, until it cannot be accommodated anymore and rapidly decreases the tablets' Rd with increasing content. The mix can accommodate up to 20 wt.% hausmannite before reaching the hardness transportation limit of 700 kPa Rd limit (Fig. 4.17). Above this content, the interparticle space will be filled by hausmannite particles so that lithiophorite cannot act as binder.

At 4 wt.% H_2O, the addition of hausmannite to the pyrolusite concentrate acts similar to the addition of water described by Wang et al (Wang et al., 2017). It first makes particle rearrangement easier, before creating lock-ups and stiffening of the material at higher hausmannite content. Considering the easier rearrangement of hausmannite particles due to their spherical shape and lack of surface charges, it may function as a lubricant at low (20 to 30 wt.%) content when mixed with water. Since water addition stiffens the pyrolusite concentrate and hausmannite particles are quickly rearranged (Fig. 4.15A), this could explain the inefficient rearrangement process at higher hausmannite content (>50 wt.%).

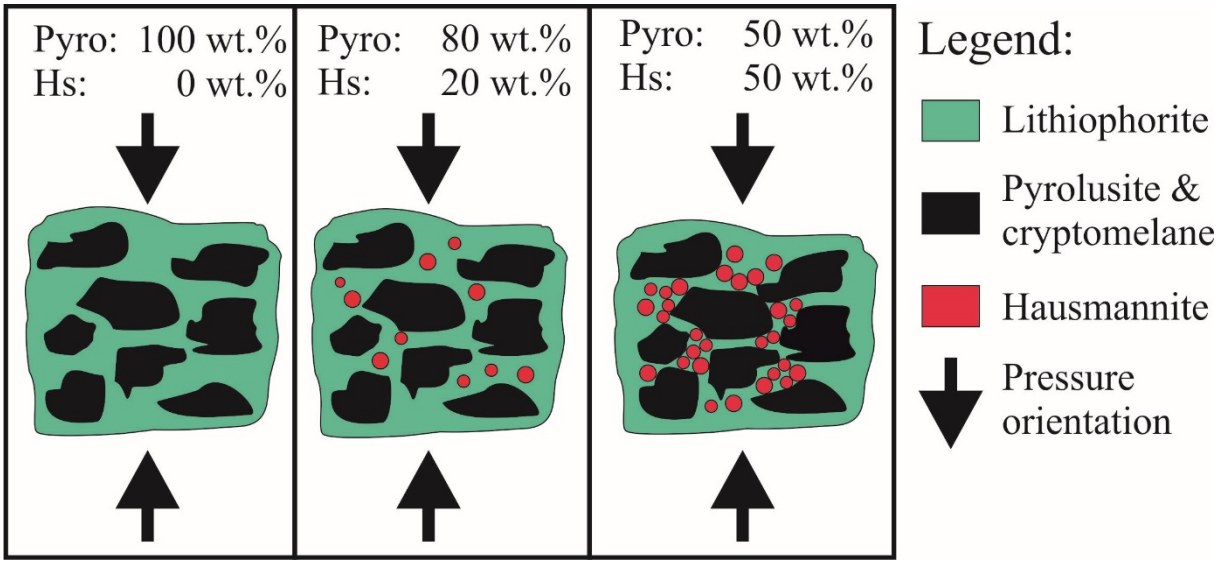

Fig. 4.21. Schematic drawing of the material organization inside a tablet after compaction of Pyrolusite concentrate/Hausmannite blends of various compositions. Lithiophorite grains are represented as a matrix binding the grains together.

Table 4.5 summarizes all the information discussed in this section, associating the different phenomena and their impact on agglomeration.

Table 4.5. Phenomena impacting the agglomeration efficiency, associated with their modifying factors.

Agglomeration	Modifying factors	Phenomena	Impact
Contact Area	Pressure	Final density	Positive
	Mineralogy pressure	Elastic recovery	Negative
		Particle breakage	Positive
	Morphology	Rearrangement	Variable
	Morphology	Rearrangement	Variable
Contact intensity	Moisture	Capillary bridges	Variable
		Charge screening	Negative
	pH + Mineralogy	Surface state	Variable
	Mineralogy + pressure	Fresh surfaces	Positive
	Hardness + Morphology	Interlocking	Positive

8. Conclusion

This study shows that understanding the microprocesses occurring during tableting, and hence the prediction of material behavior, requires an extensive physical and chemical characterization. Mineralogical quantification and micro-textural information are essential.

The operating conditions, investigated in this study, led to the following conclusions:

- High pressure (>250 MPa) is deleterious for clay material agglomerates due to their elastic recovery. However, it is beneficial for pyrolusite concentrate.
- Addition of 2 to 4 wt.% H_2O increases tabletability through higher Rd and lesser elastic recovery and fine generation. However, addition of 6 to 10 wt.% (depending on material) of H_2O, decreases the Rd of agglomerates.
- Best agglomeration results were obtained for pH 4. However, further investigation should be performed to confirm the present findings.

The material properties are the most important factor to achieve tabletization. It has been shown that the presence of soft, plastic material with a high specific surface area is key in determining the tableting potential of fine-grained material, such as the lithiophorite in the pyrolusite concentrate or the bentonite when blended in hausmannite.

Moreover, it has been demonstrated that the pyrolusite concentrate, close in composition to Moanda Mn ore fines, has a high tableting potential and could be easily agglomerated on mine site without binder. It can be used as a matrix to recycle other Mn-bearing products, as would be the case on an Mn processing plant. These two cases are represented by the following recipes:

- Pyrolusite concentrate tablets agglomerate at 4 wt.% H_2O and 450 MPa have a 1200 kPa Rd with 52.9 wt.% Mn.
- An 80/20 blend of pyrolusite concentrate and hausmannite tableted at 4 wt.% H_2O and 350 MPa shows an 850 kPa Rd for a 56.4 wt.% Mn content.

Both recipes give Rd above the industrial grade limit set at 700 kPa. Tableting is thus a viable green recycling alternative to pelletization, briquetting and sintering as it does not require any binder or additional heating.

9. Acknowledgements

We thank Eramet IDEAS, the GEOPS laboratory for hosting this project, and the KIC-EIT RawMaterials for their support through the Go4.0 project (N° 15046). The PhD is supported by a CIFRE project N° 2017/0326 and the ANRT for their logistic and financial support. A. Elmassian, O. Haution and Y Hervé (EID) are thanked for their help preparing the samples prior to agglomeration. S Lafon and O. Laugier (EID) are thanked for their support in preparing the samples for the characterization. We thank EUROTAB and its staff, L. Kirchhoff and J.-L. Layes for the availability of Cassiopée and their valuable advices. We would also like to thank Imerys Ceramic France for their products used in this study.

Chapitre 5 - Assessment of particle size distribution and punch speed impact on DEM-modelling for Mn oxide fines

In cooperation with Maksym Dosta (Hamburg University of Technology, Multiscale Simulation of Granular Materials (V-EXK1), Denickestraße 15 (K), 21073 Hamburg).

1. Introduction

The hypotheses formulated based on the characterization of the materials are strongly supported by the empirical tests performed, supporting the qualitative predictability of agglomeration. Improving the predictability to be quantitative would be the next objective of this study, but the agglomeration processes are complex and hence difficult to model. The simplest is the tableting, which was used to perform the empirical agglomeration tests presented above. This method, widely used in the pharmaceutical sector, has been recently studied for fines produced by Mining and Metallurgical Industries (MMI), (Dubos et al., 2021, 2019). This method gives a better agglomeration parameters control during tablet production. However, it requires a profound understanding of the material and the material behavior during tableting (Wünsch et al., 2019). Data acquired during agglomeration experiments can be used to predict material behavior through modeling. (Dubos et al., 2019; Sonmez et al., 2004; Thornton et al., 2012; Yuksel and Cullinan, 2016)

While compaction behavior is widely modeled in the pharmaceutical sector, it is in its incipient state in MMI. One of the difficulties is the complexity of the materials (heterogeneous phases, morphologies and grain sizes) compared to pharmaceutical products which are mainly monophasic with unique morphologies and grain sizes (Herting and Kleinebudde, 2008b; Kadiri et al., 2005; Kawashima et al., 1994). All modelling approaches have the goal to predict agglomeration/compaction behavior of the materials and finally to optimize the agglomeration/compaction process through parameter control.

In MMI, agglomeration parameters are commonly studied empirically, based on experimental results on the specific materials of the companies (Bizhanov et al., 2014; Rousseau et al., 2016). However, MMI have a growing interest in numerical modelling of agglomeration processes, to increase time- and economic- efficiency, as well as improve process predictability. The Discrete Element Method (DEM) is commonly used in the pharmaceutical sector for roll compactor and uni-axial presses on homogeneous and soft materials (Ketterhagen et al., 2009). It is under investigation for application in MMI (He et al., 2019). DEM models the behavior and properties of each particle. It is mainly used for granular material behavior, such as during their flow (Behjani et al., 2020; Orefice and Khinast, 2020) or their agglomeration (Yuksel and Cullinan, 2016). It allows a good predictability of the process outcomes, although finer calibrations are always required. This type of modeling is restrictive to a certain number of parameters, which need to be defined for the specific agglomeration process applied to the fines. For example, parameters required for briquetting, pelletization and tableting may vary (Pietsch, 2002).

DEM relies on a phenomenological understanding of the agglomeration and requires most reliable and detailed parameters (density, Young and Poisson modulus, sliding friction…) of the material modelled. Furthermore, a deep understanding of the agglomeration mechanisms allows to precisely predict the outcome of the processes, even very complex (Cleary and Sawley, 2002; Licciardi et al., 2020). The major downsides of this method is the computation power and time required. Balakin et al (2015) investigated this method through an approach named “pragmatic modelling”. This method seeks to reduce computational intensity through analytical relations and assumptions such as the particle shape and size, the Particle Size Distribution (PSD), also neglecting some phenomena (such as hydrodynamic fragmentation of the agglomeration).

The experiments presented in this chapter seek to fit DEM modelling experiments with the empirical results obtained in the previous chapter. The comparison point is an agglomerate of dry pyrolusite concentrate, tableted at 450 MPa displaying a Rd between 1148 and 1359 kPa, and a breakage occurring by a net split across the tablet. The fit is based on (1) the Rd of the agglomerate and (2) the way it breaks. In order to modify these results, four parameters are varied: the sliding friction of the particles (Sl), and the normal and tangential strengths (Str), Young Modulus (YM) and Bond Size (BS) of the bonds binding the particles together.

This is the first study applying DEM modelling to manganese oxide fines, a pyrolusite concentrate. Results are critically evaluated also with prediction on agglomeration potential based on detailed material characterization and experiments. These materials were previously studied for their chemical and physical characteristics and tableting experiments were performed on pure and mixed materials (Dubos et al., 2021, 2019).

2. Sample material

The material used as a comparison basis for these modeling tests is the pyrolusite concentrate, already presented in the second part of this thesis. It has been selected for its good agglomeration performances and its industrial interests, due to its proximity with Mn ore fines produced in Moanda (Comilog, Gabon). Additional details on its microtexture and its PSD, relevant for the DEM modelling, are highlighted in Fig. 5.1.

The pyrolusite concentrate is composed of 75 wt.% of pyrolusite, 11 wt.% of cryptomelane, 8.2 wt.% of lithiophorite, 3.6 wt.% of Fe oxy-hydroxide, 1 wt.% of clays and traces of quartz and oxides (Dubos et al., 2021). This sample hosts zoned particles composed of a core of pyrolusite and/or cryptomelane of variable grain size (0.1 -100 µm) surrounded by a very fine-grained mixture (< 2 µm) of pyrolusite and cryptomelane, embedded in a lithiophorite matrix (Fig. 5.1A). The pyrolusite and cryptomelane grains show smooth surfaces and may present porous features. Some lithiophorite grains (< 20 µm) display needle-like features. QICPIC analyses followed by granulomorphological calculations indicate shape descriptors of 0.8 sphericity and 0.85 convexity (Dubos et al., 2021). The particle size distribution (PSD) presented in Fig. 5.1B is subdivided into four granulometries (F1 to F4: 60, 15, 3 and 0.3 µm, respectively) for the needs of this study.

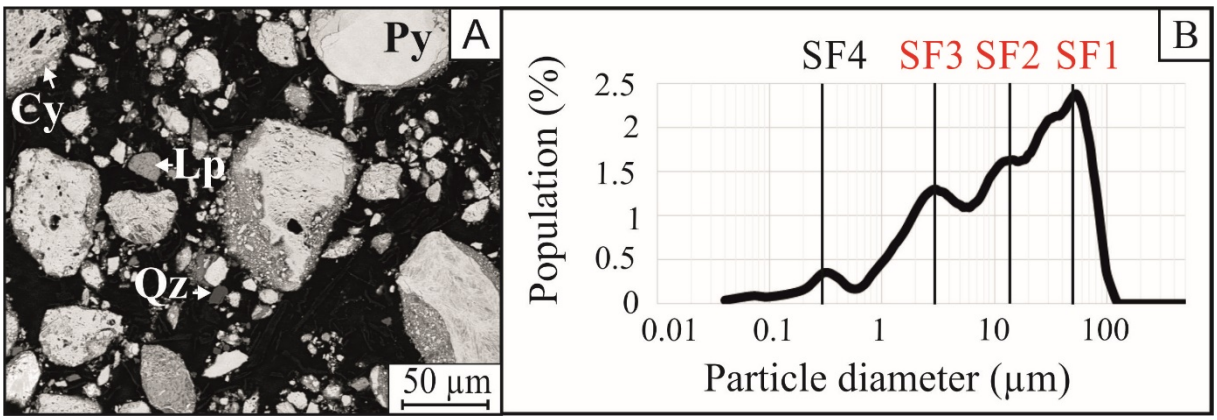

Fig. 5.1. Pyrolusite concentrate characterization with A) SEM picture taken at 15kV using back scattered electrons (BSE) and B) PSD performed using laser granulometry (CILAS1064L).

3. Methodology

3.1 Discret Element Method

The DEM modelling was performed using the MUSEN software v1.64.4. This version was produced by the MUSEN development team in 2019. The tests performed in this study used the Hertz-Mindlin contact model (Hertz, 1882; Tsuji et al., 1992) and the elastic bond model (Dosta et al., 2013; Kozhar et al., 2015; Potyondy and Cundall, 2004; Shen et al., 2016).

The initial state of the model is created by the user, with material and physical objects properties (nature, position, speed). Based on its working equations and their interaction with the system state, a new state is calculated after a fixed interval of time has (virtually) passed. This time interval, called simulation step, is advised by the software depending on the system complexity (PSD of the sample, the particles parameters, the model used). In this study, it ranges between 10^{-7} and 10^{-9} seconds. However, all those intermediary states, called frames, are not saved, to limit data generation and calculation time. They were saved every 10^{-5} s during the compression step and every 5.10^{4} s during the hardness tests.

3.2 Modelling strategy

The objective of this study was to find a correlation point between the experimental tests and the modelling trials. The correlation relies on (1) the diametral resistance (Rd) of the tablet and (2) the way it breaks. The modelling process, presented in Fig. 5.2, is hence achieved in two steps: the compaction step and the hardness test. The compaction step simulates the application of pressure on the material by a punch. The material is generated inside a cylindrical volume with a 0.6 mm height and a 0.657 mm radius with a porosity of 0.6132. The cylinder dimensions are proportional to the matrix used for the agglomeration experimentation, while the porosity is equal to the experimental one. The modelling protocol is presented in Fig. 5.2. The agglomeration process was modeled in two steps: During the compression, the Hertz-Mindlin contact model is used for the particle-particle and particle-die interactions (Fig. 5.2). Once the desired pressure is achieved, the adequate frame is selected to proceed to the second step.

The pressure value selected was 454 MPa. It was calculated from the data extracted, using the ratio between the effort and the surface. In order to have an optimal comparability of the experiments, the extracted frame was used as a common basis for all the hardness tests.

The hardness test begins with the bond generation between particles based on their separation distance. The elastic bond model is used to dictate the bond behaviors. Two plates of tungsten carbides are also modelled, the upper one pressing down on the diameter of the tablet at a set speed. Once the tablet breaks, its diametral hardness is extracted to assess its diametral resistance. It is calculated using the following equation (1):

$$Rd = \frac{2*F*1000}{\pi*h*d} \qquad (1)$$

With F the force applied (in N), h and d the height and diameter, respectively (in mm). The Rd is expressed in kN.

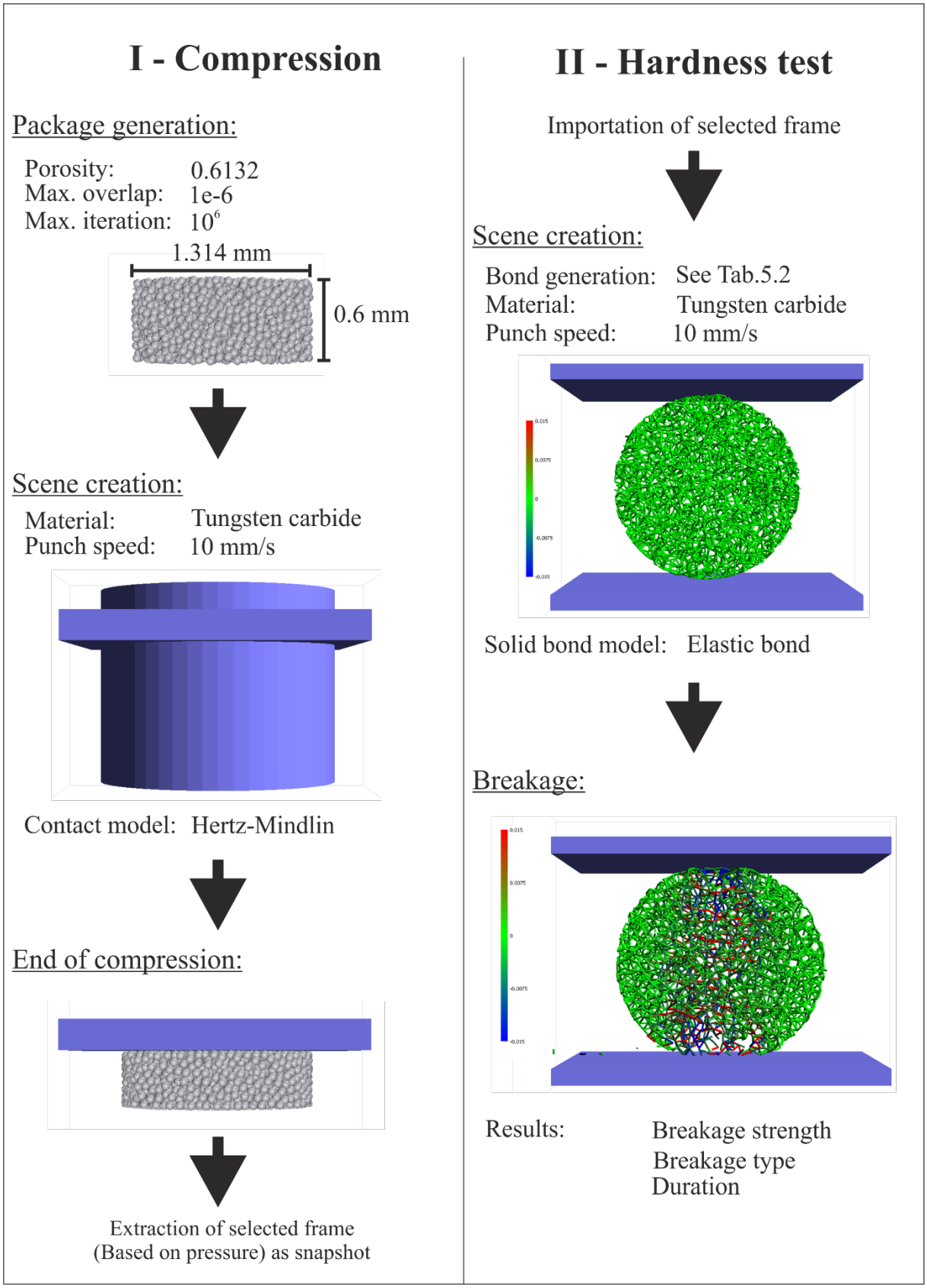

Fig. 5.2. Modelling protocol used to perform this study.

The other result observed is the agglomerate breaking style. During the empirical experiments, the pyrolusite concentrate agglomerated at 450 MPa broke through a diametral crack that split the tablet in two. However, just as the Rd, this varies with the modelling parameters. Three breakage type were observed (Fig. 5.3): (1) the splitting, where a crack occurs through a significant part of the tablet, (2) the cracking, where a simple crack occurs at the edge of the tablet and (3) the crumbling, where the bonds are gradually broken while the punch presses down. There are also mixed behaviors, e.g. the bonds start to crumble before a crack appears. Those behaviors are also reported in the graphs below (e.g. as crumble/crack when the crumbling happens first).

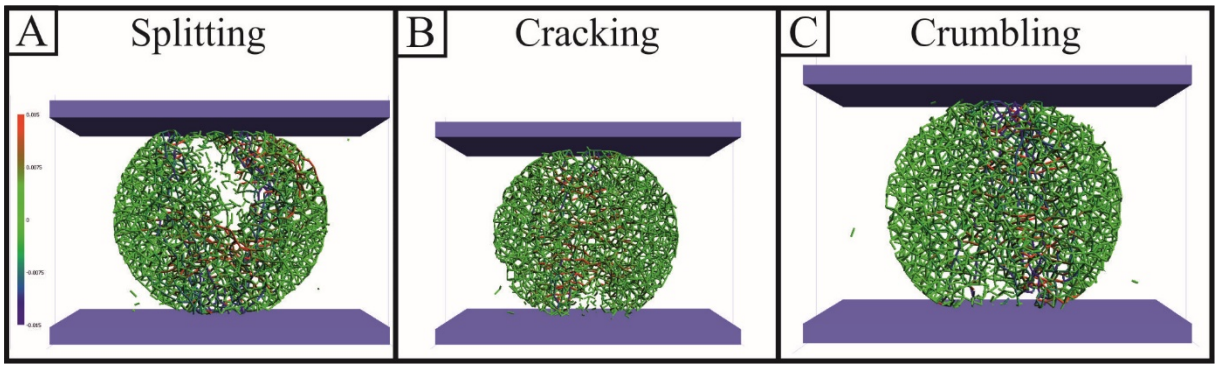

Fig. 5.3. Different breakage types with A) the splitting, B) the cracking and C) the crumbling.

3.3 Parameter definition

The DEM modelling relies on parameters specific to the material and/or the bonds.

3.3.1 Material parameters

The material parameters consist of the PSD, density, Young's modulus, Poisson ratio, rolling and sliding friction. The PSD and density values were based on analytical results. The other values were estimated based on the literature and the agglomeration behavior observed during the empirical tests (Dubos et al., 2021). All these parameters were constant through the experiments, apart from the sliding friction. They are summarized in Table 5.1.

The microtexture of the particles is complex (Dubos et al., 2021, 2019, Fig. 5.1). A layer a lithiophorite covers the surface of pyrolusite/cryptomelane grains. However, based on QICPIC measurement (Fig. 4.6), the overall particle shape is quite simple with sphericity and convexity values higher than 0.8. While it is possible to modify the shape of particles, it requires additional settings and increased computing power, especially if each particle is to be given a unique, randomized shape. Moreover, creating biphasic particles is not possible given the current state of the software. Therefore, it was decided to perform modelling trials using spherical, monophasic particles of pyrolusite and modify their parameters to account for the presence of other minerals (mostly lithiophorite) in the sample.

The measured PSD of the sample can be subdivided in 4 size fractions. However, the smallest size fraction consists of particles with a 0.3 µm diameter representing about 7 % of the sample. The F1/F4 size ratio is about 200, against 20 for the F1/F3 size ratio. According to Furnas (1931), the

optimal density of a system with 4 components and a 200 largest/smallest size ratio, is about 0.78, while for 3 components and a 20 largest/smallest size ratio the optimal density is around 0.74. This results in little difference regarding the packing density, which is the main parameter influencing the agglomeration forces intensity. Additionally, the inclusion of F4 during particle generation only requires too much computing power due to the number of particles, causing computer and software instability. It was hence decided to proceed modelling with 3 size fractions (F1, F2, F3) with particle diameters of 60, 15 and 3 µm. Their respective content in the sample was at 38.9, 33.3 and 27.8 %. The density was set at 4085.5 kg/m^3, accordingly to the measurements.

The other material parameters necessary for DEM modelling (Young's modulus, Poisson ratio, sliding and rolling friction) of pyrolusite concentrate are not available in literature. It was hence necessary to perform assumptions on its mechanical parameters. Assumptions were performed by comparing its agglomeration behavior to that of the other materials (bentonite, kaolinite and hausmannite) used during the empirical experiment (Dubos et al., 2019), for which values are available (Karakaya et al., 2011; Mal'tseva and Vinichuk, 2016). Young's modulus value of 25 GPa was reported for pyrolusite (Sermeus et al., 2014). As pyrolusite and cryptomelane have similar mechanical behavior, pyrolusite Young's modulus may be also applied to cryptomelane. However, 15 wt.% of the sample is composed of minerals with a mechanical behavior close to that of montmorillonite (Young's modulus of 0.43 GPa). Since no value was available for a mix between pyrolusite and soft compounds, an assumption was made to set the Young's modulus at 20 GPa for DEM modelling. A Poisson ratio of 0.3 was assumed based on the average value for oxide minerals (Ji et al., 2018), due to the absence of values specific to Mn-bearing materials.

Sliding friction of 0.5 and 0.7 for kaolinite and montmorillonite (major bentonite compound) respectively are reported (Moore and Lockner, 2007; Skempton, 1985). Since the tableting behavior of the pyrolusite concentrate ressembles that of kaolinite in our study (Dubos et al., 2021), the value of 0.5 for the sliding friction was retained during the compression step. However, it was modified during the hardness test to investigate the potential impact of a removal of the coating during compression and its effect on breaking behavior.

The rolling friction of materials vary from 0 to 0.004, depending on their particle shapes and surface state. As our material is mainly composed of rounded particles, the rolling friction was set at 0.002.

Table 5.1. Mechanical parameters for the pyrolusite concentrate used for DEM modelling.

Parameters	Pyrolusite concentrate
Density (kg/m^3)	4085.80
Young Modulus (GPa)	20.00
Poisson ratio	0.30
Normal strength (GPa)	0.50
Tangential strength (GPa)	0.50
Sliding friction	Variable (0.4 to 0.9)

Rolling friction	0.02

3.3.2 *Bond parameters*

The material parameters consist of the bond diameters and bond lengths, Young's modulus, normal and tangential strengths. The main forces acting during agglomeration are Van der Waals forces (VdW), ElectroStatic forces (ES) and capillary bridges, the latter of which is mainly active in wet media (Dubos et al., 2019; Pietsch, 2002). As this modelling experiment simulated dry agglomeration, capillary forces are negligible. Additionally, the VdW forces are 1000 times stronger than ES (Schulze, 2008). Thus, in order to simplify the calculations, only the VdW forces were modeled. Based on the work of Schulze (2008), the existence range of the VdW forces was discretized in three distance intervals, based on the particle separation distance (Table 5.2). The bond diameter attributed to a bond length was based on their intensity. When the bond diameter was modified during the tests, the ratio between the different distance intervals was kept constant. The initial ratio is presented in Table 5.2.

Table 5.2. Bond diameters for the different distance intervals. The initial ratio is presented in the diameter column.

Bond	Min distance (mm)	Max distance (mm)	diameter (mm)
VdW1	-1.00E-03	4.00E-06	1.00E-02
VdW2	4.00E-06	1.00E-05	2.00E-05
VdW3	1.00E-05	1.00E-04	2.00E-07

The Young modulus of an object defines its deformation behavior. Bonds with a lower Young modulus will accommodate more deformation before breaking. This parameter was varied between 2 and 20 GPa in order to try and approach the breaking type observed during empirical tests.

For the normal and tangential strength, the following strategy was applied: The pyrolusite concentrate has a mechanical behavior intermediary to kaolinite and bentonite. Since the strength values for these materials are $2.6.10^9$ and $1.48.10^8$, the value for the pyrolusite concentrate were varied between these values. The range for all the parameter variations is presented in Table 5.3.

Table 5.3. Variation range of the different bond parameters.

Bond parameters	Min	Max
VdW1 diameter	0.005	0.075
Young Modulus (GPa)	2	20.0
normal strength (GPa)	0.5	3.0
tangential strength (GPa)	0.5	3.0

4. Results

The Fig. 5.4 presents their variation across a range of Sl and Str values, with the BS being 0.012 and 0.010 mm in Fig. 5.4 A and B, respectively. The strength plays an important role in the Rd of the agglomerate. With a BS of 0.012, a Str increase from 10 to 20 and 30 MPa increases the average Rd from 220 to 670 (3 times higher) and 1180 (5.4 times higher) kPa, respectively. With a BS of 0.010, a similar Str variation increases the average Rd from 140 to 450 (3.2 times higher) and 780 (5.6 times higher) kPa, respectively. Identical increase of Str gives similar increases of Rd, independently of BS.

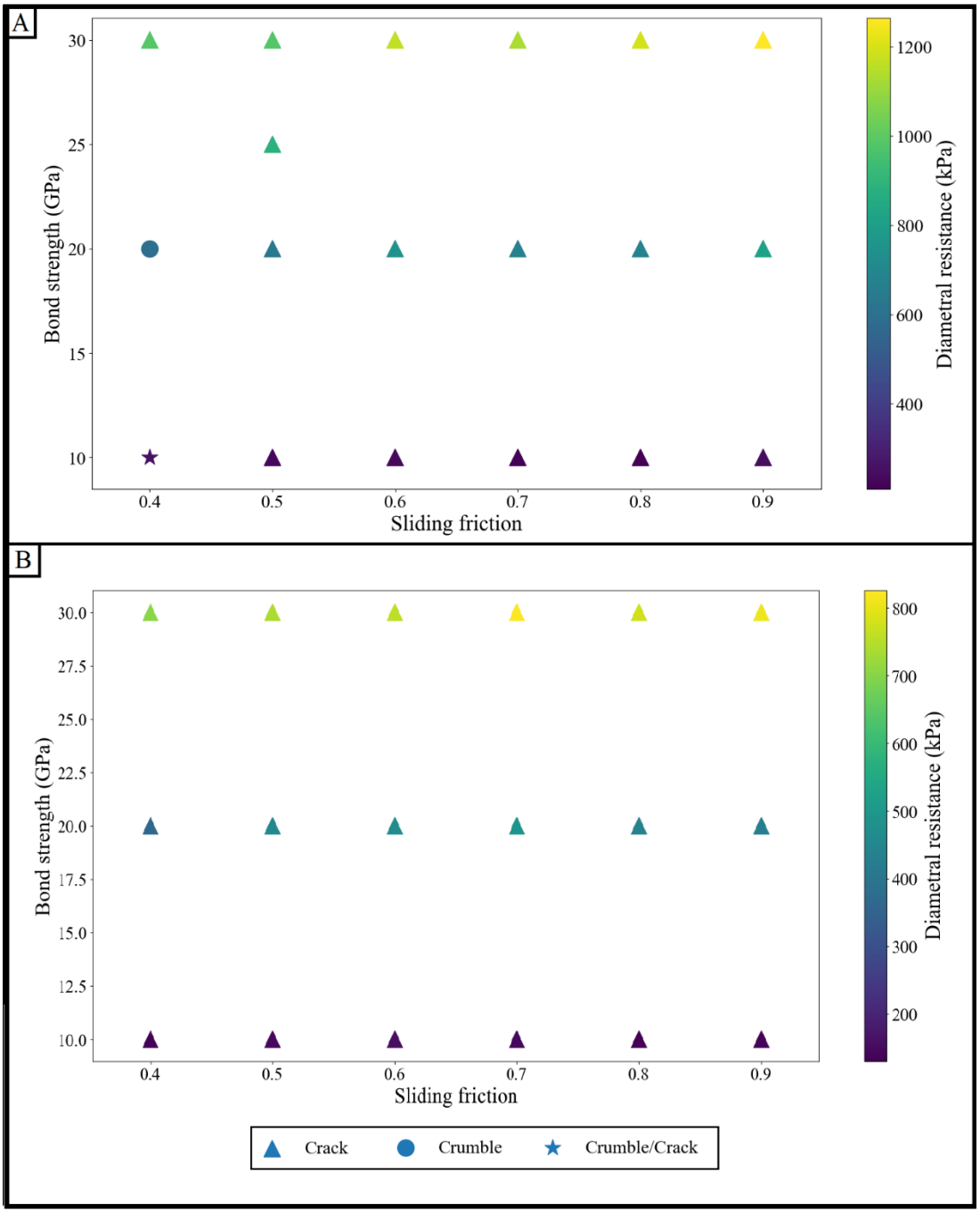

Fig. 5.4. Rd and breaking style variations across a range of Sl and Str values, for a YM of 20 GPa and a BS of 0.012 (A) and 0.010 (B).

On the other hand, the sliding friction does not appear to have a significant impact on Rd, independently of the BS value. Additionally, both of those parameters do not appear to have a significant impact on the breaking style of the agglomerates, as all those experiments resulted in cracks with the exception of those performed at Sl 0.4, BS 0.012 for Str 10 and 20.

The Fig. 5.5 (see next page) presents the Rd and breakage style variations across a range of Str and YM. For BS of 0.012, the Rd between 10 and 20 GPa Str is 2.5 times higher on average. However, the increase from 10 to 30 GPa shows a slightly higher increase ratio at lower YM (5.4 and 4 at YM 2 and 20 GPa, respectively). For BS of 0.010, the Rd between 10 and 20 Str is lower, at 2.3 times higher on average. The same tendency is observed for a Str increase from 10 to 30 GPa, with values 6 and 3.5 times higher for YM of 5 and 20 GPa, respectively.

The YM also has a significant impact on Rd: at it decreases, the Rd appears to increase exponentially. For BS 0.012, a YM decrease from 20 to 8 GPa increases the Rd 1.4 times (from 950 to 1330 kPa), while a decrease from 8 to 2 GPa increases the Rd 2.9 times (from 1330 to 3850 kPa).

Additionally, it appears that decreasing the YM modifies the breakage behavior. High YM (20 GPa) experiments end with a cracking of the tablet. However, a lower YM tend to display a more crumbling behavior. If the strength is high enough, the crumbling can also lead into a splitting of the tablet, the stress being concentrated along the diameter of the tablet.

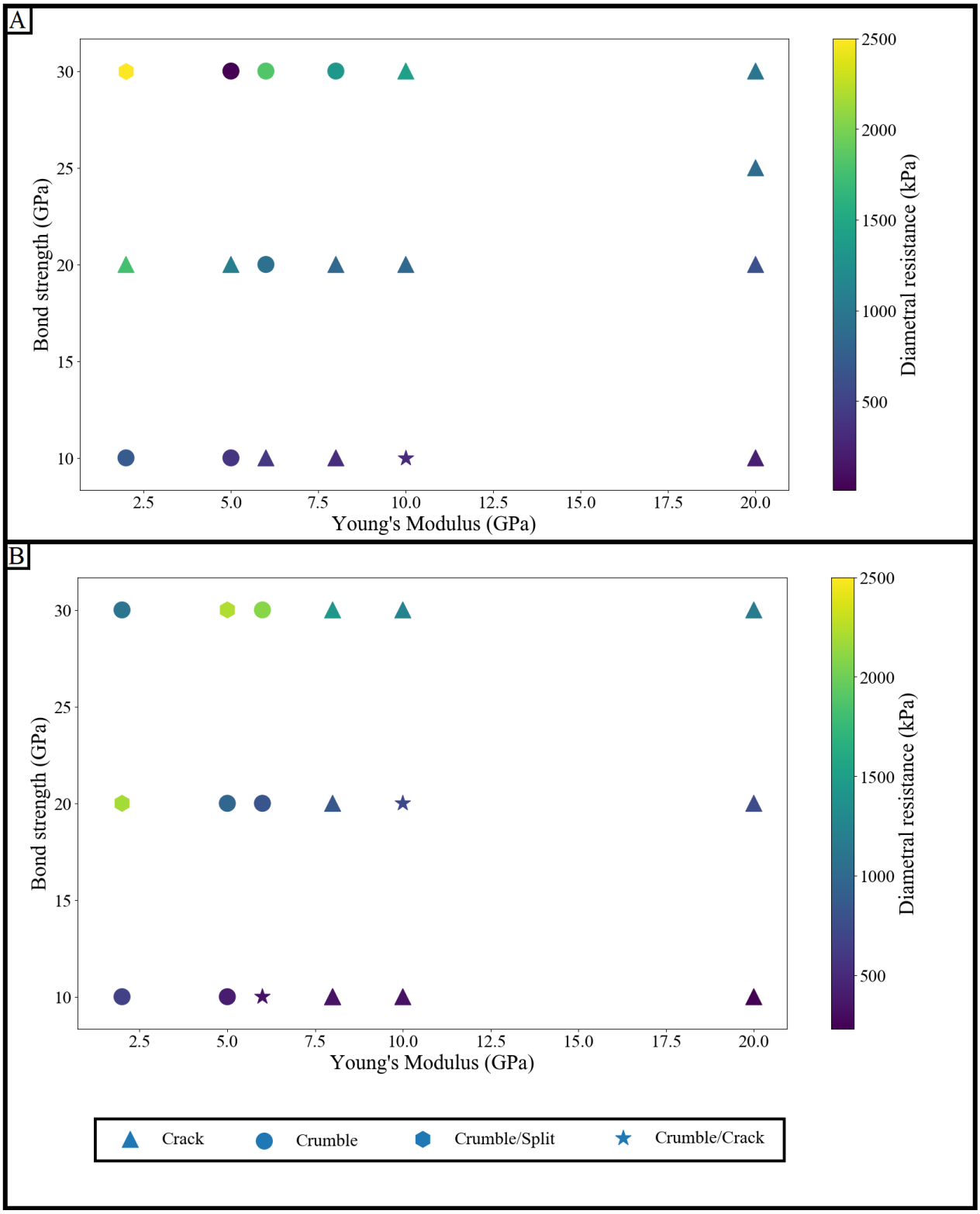

Fig. 5.5. Rd and breaking style variations across a range of YM and Str values, for a BS 0.012 and a Sl of 0.5 (A) and 0.6 (B).

The Fig. 5.6 shows the Rd and breaking style variations across a range of BS and Str values, a YM of 5 GPa and a sliding friction of 0.5. Similarly to Fig. Fig. 5.5, Str has, proportionally speaking, a bigger impact at lower BS (for BS 0.005, the Rd is 2.9 and 6.2 times higher for 10 to 20 and 10 to 30 GPa, respectively) compared to what can be observed at higher BS (for BS of 0.05, the Rd is 2.4 and 4.1 times higher for 10 to 20 and 10 to 30 GPa

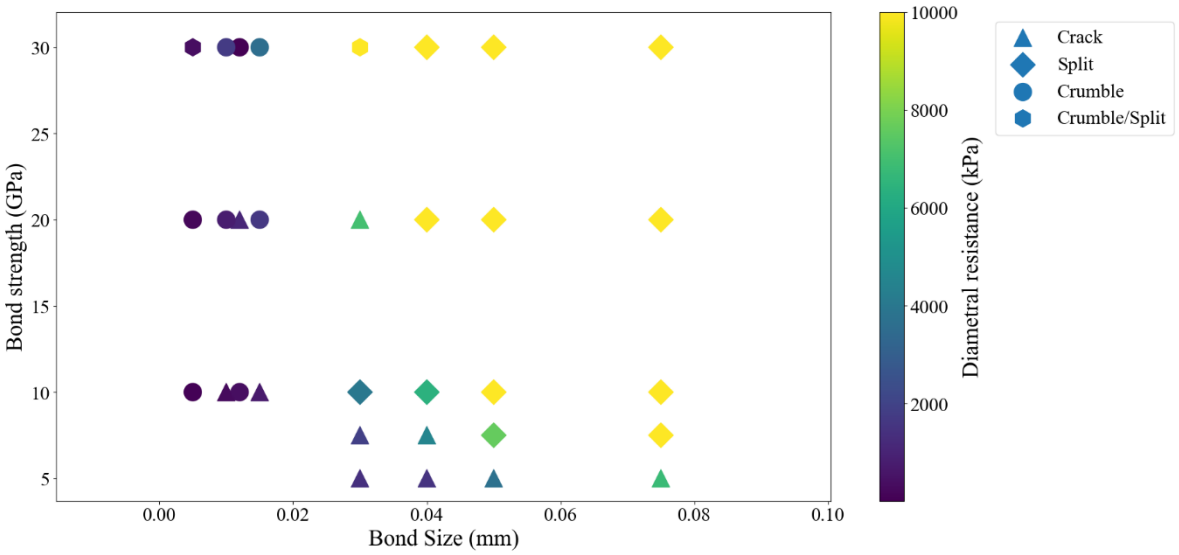

Fig. 5.6. Rd and breaking style variations across a range of BS and Str values, for a YM of 5 GPa and a Sl of 0.5.

5. Discussion

This modelling study aimed at fitting DEM simulation results with empirical agglomeration experiment performed in the previous chapter. However, no point was reached that fitted both the expected Rd and breaking style of the agglomerates. This is likely due to the numerous assumptions performed on the material parameters used in this study. The discrepancy between the literature material and the studied sample must be analytically quantified through adapted methods rather than estimated. It is hence necessary to measure the pyrolusite concentrate YM, Poisson ratio, and sliding and rolling frictions to improve the model accuracy.

Additionally, the bond parameters were explored empirically through numerical simulation results, based on calculations of the VdW force intensity performed by Schulze (2008). Further work should be conducted to determine the adequate bond parameters (normal and tangential strengths, BS, YM) of the VdW bonds formed by the pyrolusite concentrate. It would help narrow the range of values to be investigated as well as improve model accuracy and robustness.

However, the modelling strategy used in the present study still enables a better understanding of the impact of the parameters used on the Rd and breaking style of the agglomerates.

The breaking style variation is linked to the stress distribution in the agglomerate.

The breaking parameters are strongly influenced by the bonds YM variations, due to the elastic bond model used. The bond ability to deform changes the stress repartition in the agglomerate. At low YM (< 7.5, depending on the force), the stress applied to a tablet during the breaking test

creeps through the tablets through bond deformation and the load is shared by the bonds (Antonyuk et al., 2005). When the bonds in the agglomerate are unable to absorb more stress, they will gradually break, causing the crumbling of the agglomerate. This stress load sharing explains why low YM experiments display a much higher Rd despite similar strength. However, at higher YM (20 GPa), the stress sharing is less efficient, and the strain is concentrated at the edge of the tablet, overcoming the bonds resistance before the stress can be shared by the entire tablet. This results in a lower Rd and a breaking style shifted toward a crack.

Antonyuk (2005) described the breaking mechanism of a sphere by the formation of a cone representing the stress distribution inside it. It is likely that the bond parameters change the cone properties by altering the stiffness of the agglomerate. An agglomerate with low stiffness (low YM, low BS) will present a better distribution of the stress. This could result in a crack of moderate depth with a wide angle. However, increasing the agglomerate stiffness would give a narrower and deeper crack. The maximum amplitude of such phenomena would be a split, i.e. a very narrow cone with a depth is bigger than the diameter, where the stress is focused along the diameter, where it is generated.

Furthermore, those behaviors are strength dependent. If the bonds are too weak, they will require an adequately low stiffness to transmit the stress received to neighboring bonds. A higher bond strength would result in a more important stress transmission across the agglomerate.

6. Conclusion

This study was unable to reach a fitting point between the DEM modelling and the agglomeration experiments performed in the previous chapter. Additional characterization of the mechanical parameters of the pyrolusite concentrate and further work on the expression of its normal and tangential strengths based on its chemical and physical parameters are required.

However, it helped to improve the understanding the role each bond parameter plays in the breakage behavior of agglomerates. The BS and the bond YM positively correlate with the stiffness of the agglomerate, while the bond strength enables the stress transmission through the agglomerate.

This study is a first step toward the modelling of pyrolusite concentrate, but it only considers dry agglomeration conditions. Once the pyrolusite concentrate has been properly characterized, considering the impact of moisture addition on the breakage behavior would broaden the experimental conditions that can be investigated.

Chapitre 6 - General discussion

The volume of dust generated in the manganese industry induces an important environment impact and a high cost. The 80 000 t per year needing to be landfilled by Eramet Norway lead to an important risk of heavy metals leaching, and to manage that risk, a cost of 8 M€ per year. These costs can be avoided and converted into incomes through recycling of the material back into the FeMn process chain using agglomeration.

The Go-4-0 project proved the feasibility of the briquetting of fine materials. A variety of different dust and sludge blends were tested, using various binders or binder mixes, which respective amounts were based on a literature review, the fabricant's recommendation and economic viability of the overall process. The tested binders were: (1) 8 wt.% molasses + 1.6 wt.% hydrated lime, (2) 0.64 wt.% FE10 (binder from alcotac) with 0.128 wt.% calcium carbonate, (3) 0.84 wt.% Peridur 300D (cellulose-based binder from AkzoNobel), and (4) 11.73 wt.% cement CEM I. Briquettes properties were evaluated through fall test (hardness), tumbling index (fine generation) and heat test (thermal behavior). The best results were obtained with the Peridur 300D, which was later used in the pilot tests (Banchet and Blaffart, 2018).

However, during the uniaxial compaction tests performed during this work, satisfactory agglomeration of Mn ore fines was easily achieved without the use of binder. It was also performed successfully on mixes of various compositions containing ore fines and refining dusts, although the latter is unable to give satisfactory agglomeration results on its own. The optimal properties were reached with 80 wt.% Mn ore fines for 20 wt.% refining dusts regarding the solid materials, and an added 4 wt.% of the solid mass of moisture. at an 80/20 weight ratio between the Mn ore fines and refining dusts.

The agglomeration results obtained during those experiments were conform to the hypotheses formulated (Dubos et al., 2019). Indeed, thanks to an extended, multi-disciplinary characterization of the materials and a comparison to commercial binders, it was possible to correlate their respective properties and theorize the important properties impacting their agglomeration behavior. Although this step was qualitative, the experiments performed on pure materials under controlled conditions enabled a semiquantitative qualification of the agglomeration potential for the studied materials. Additionally, to their agglomeration potential, it is possible to predict the optimal agglomeration conditions based on the material. While the ore fines and refining dusts presented a high linear correlation between agglomeration efficiency and applied pressure, the elastic properties of the clay materials tend to reduce the agglomerate strength at higher pressure by forming capping and cleavages (Dubos et al., 2019).

The impact of the environmental conditions and the importance of the moisture properties were also highlighted by the pH experimentations, showing how the modification of the surface state may impact agglomerate strength. For example, the zeta potential of bentonite with respect to pH, presented in the Chapter 3, reveals a shift in the charge polarity at the edge of the layers of the montmorillonite it contains (Yariv and Cross, 1979). This shift allows forming stronger electrostatic bonds between these edges and the surface of the montmorillonite layers, which are negatively charged.

As stated above, experiments have been performed on material blends, with an emphasis on pyrolusite concentrate and refining dusts. They reveal the potential of natural ore fines (at least in the case of Mn laterites in Moanda) to be used as natural binders along the whole process chain. Their high content of hydroxized and layered materials (clays, lithiophorite) is transformed and "lost" during the first pyrometallurgical step above a drying >100 °C. This gives them unique properties compared to all the other dusts produced during the transformation from ore to metal.

These process dusts present oxides (often spinels) and silicates (except phyllosilicates). Those mineralogical families possess low specific surface area and surface charge, with hard and brittle physical properties. Those characteristics, close to that of hausmannite presented in this work, results in a low agglomeration potential. Each mineral transition that the material undergoes during pyrometallurgical processes decreases its agglomeration potential.

However, the manganese mine at Moanda in Gabon produces more than 4 Mt of ores per year. In the first chapter of this thesis, it was found that the ore contains about 10 wt.% of very fine particles (<100 µm). This amounts to roughly 400 000 t of ore fines per year. It was stated in the introduction that the Eramet Norway plants produce 80 000 t of fine-grained wastes each year. The experiments performed in this work showed that the optimal blend to maximize fine recycling while retaining sufficient hardness is a mix with 80 wt.% pyrolusite concentrates and 20 wt.% refining dusts. Thus, it is theoretically possible to recycle the entirety of the Mn process dusts through agglomeration, using the Mn ore fines as sole binders.

It is important to note that this is a rough estimation, which approximates the pyrolusite concentrate for ore fines. However, the pyrolusite concentrate was jigged to enrich it in Mn oxides and reduces its lithiophorite and clay content. Since the latter minerals are responsible for the pyrolusite concentrate agglomeration potential, raw ore fines should have a higher binding potential that the concentrate used in this study. It also considers that all the process dusts are equivalent to the refining dusts in terms of agglomeration efficiency.

1. A new, systematic approach

Mineral agglomeration studies are mostly empirical: when a company needs to recycle its fine-grained materials, it considers the materials separately or mixed together, choose one or more binders according to its restrictions and perform tests to estimate the best recipe. This is the case of the Go-4-0 project (Banchet and Blaffart, 2018), among many other studies (Bizhanov et al., 2014; Johansson and Alderborn, 2001; Zhu et al., 2014). While this method produces results, the lack of theoretical considerations prevents the transferability of the results. The present work has a theoretical approach to agglomeration completed by experiments to obtain results pertinent in other case scenarios. This is achieved through the combination of an extended chemical, physical and mineralogical characterization of the materials, theoretical considerations on agglomeration (Pietsch, 2002; Schulze, 2008) and agglomeration tests. It is the first time that agglomeration is approached in such a systematic way, which allows to reach conclusions that would not be possible otherwise. It is an intensive work, but it allows this methodology to be applicable to various materials. Additionally, each new study applying this methodology can be used to improve the accuracy of the findings of the present work. This thesis is an important step toward a conclusive model of agglomeration.

1.1 Characterization methods

An important aspect of this work is the cross-checking of the various methods. The results of different methods overlap to some extents, such as the XRD and the Qemscan that both studies the mineralogy of a sample. However, while the XRD is essential to analyze the crystallography, it hardly allows to quantify the mineralogy. Through the calibration of QEMSCAN analyzes by XRD and analytical chemistry, it is possible to obtain an accurate quantification. While each method brings unique information on the material properties, those overlaps allow a critical consideration of the results. The contradictions arising between the method force the user to reflect about the

physical meaning of their results. It may not always be possible to have results that are numerically coherent across the different methods but being able to explain those differences results in a better understanding of the materials. It was the case when studying the grain morphology of hausmannite through QICPIC, SEM: the SEM enabled the observation of each particles separately, while the QICPIC measured the shape parameters of small clusters of those particles that could not be separated by ultrasounds (Dubos et al., 2019).

1.2 Agglomeration mechanisms

In the literature review presented in chapter 1, it was shown that the Capillary forces and the electrostatic forces, including the Van der Waals forces, are considered to be the most important forces partaking in agglomeration (Pietsch, 2002; Schulze, 2008). However, understanding the forces that comes into play is not sufficient to model a process. They must be decomposed into their influencing parameters, and those parameters must be correlated to the material properties, and the agglomeration process being considered. Those properties must be integrated into the force expressions, so that the strength of the forces can accurately describe the agglomerate strength.

This work has been built around the deconstruction of the forces into their constituting parameters. The main parameters are: (1) the separation distance, common to all forces and most impacting parameter, (2) the surface charges of the material, (3) the liquid saturation of the material. The material properties intervene in the expression of all three parameters, and forces.

The separation distance is the first parameters to consider during agglomeration due to its importance regarding the force intensities. For example, an increase of the separation distance from 10^{-7} to 10^{-5} mm decreases the intensity of the Van der Waals forces by 4 orders of magnitude (Schulze, 2008). It makes the physical properties of the material and the pressure applied to the material essentials. Indeed, a hard, brittle particle (such as the hausmannite in the present work) will maintain a high separation distance in the sample, due to its inability to fill the voids. This is especially true if all the particles are spherical, due to the low compacity inherent to a structure composed of such particles (Gauß, 1831). However, a soft and/or plastic material will be able to fill the empty spaces more easily by deforming and/or breaking down into smaller pieces. However, this is dependent on the pressure being applied to the material, which needs to be higher than its resistance thresholding. Additionally, an important PSD can help fill the void, providing a ratio effective to reduce the porosity of the agglomerated material (McGEARY, 1961). Reducing the separation distance is the best way to increase the “bonding density”, i.e. the number of bonds present in a sample to hold it together.

Additionally, the surface state of the material, which results from the interaction between the material and its local environment, plays a key role agglomeration. This was showcased with the pH-based experiments performed on the concentrates, which demonstrated a significant change in the resistance of the bentonite and pyrolusite concentrates with pH variations. It had been shown that montmorillonite, contained in the bentonite, see their surface properties altered by pH (Grim, 1968; Yariv and Cross, 1979). It has now been demonstrated that this modification impacts its agglomeration behavior. Those observations could be performed at a finer scale and expanded to other materials using X-ray Photo Spectrometry (XPS), which allows to measure the surface properties and bondings. With a proper protocol, it could be possible to assess the particle surface alterations occurring after the application of different pH.

The moisture is also a key element as it forms capillary bridges, which increases the cohesiveness of a sample, but do not increase its compressive strength. This increase of cohesiveness of a sample decreases its fine generation. This property of water reducing the fine generation is well known,

as it is the reason lorries wheels and cargo are sprayed with water when exiting the mines and quarries for transportation. However, this was not quantified in this thesis. It is usually measured by the tumbling index and is an important value to consider in order to assess the quality of an agglomerate. The presence of water also decreases the intensity of the electrostatic forces by screening them (Louati et al., 2017).

This study presents the first available data for CEC, BET and Zeta potential on Mn oxide materials (pyrolusite concentrate, hausmannite). CEC and Zeta potential measurement are usually used for clay minerals and colloidal suspension. For the first time, these values are used as an indicator for the agglomeration potential of fine materials.

1.3 Agglomeration methods

Agglomeration methods classically used in the mining and metal industries are the pelletization, which present the highest throughput from all methods, and sintering, which is the most robust despite material variations. However, pelletization, the most used agglomeration method for iron ores, also require an additional roasting step for the agglomerates to achieve sufficient hardness for transportation. Due to the high content of combined water of Mn ores, this roasting would be deleterious its pellets. Therefore, sintering is the most used agglomeration method in the Mn industry (Zhu et al., 2014).

However, extrusion of Mn fines as also been observed and empirically studied (Beloborodov et al., 2016) with satisfactory results. Moreover, Blancher et al (2015) performed a characterization study on briquetted Ni ore fines revealing that the smectites acted as a natural binder. Additionally, the Go-4-0 project obtained satisfactory briquetting results, although using binders.

However, the briquetting agglomeration only present an indirect control over the pressure applied to the sample and no instrumented machine have been found. Therefore, this study performed the first uniaxial compression experiments on Mn ore fines. It allowed a finer control over the agglomeration parameters than briquetting or pelletization, thanks to a direct control over the pressure applied. Thus, it presents a solution to perform binder free agglomeration.

Despite the control and repeatability this machine offers, important variations of agglomeration results were observed despite identical operating conditions. This can be explained by the mixing of the materials when adding moisture. The fine particles form clusters due to the addition of moisture, which persist during the mixing phase. This leads to a heterogeneous humidification of the material, significantly impacting the agglomeration results stability. In order to obtain a homogeneous material and moisture distribution, the mixing should be performed using an adequate technology, such as a bladed mixing drum.

1.4 Predictability – Modelling

In this work, preliminary modelling of the agglomeration behavior of Mn fines in dry conditions was undertaken using DEM. Although the splitting breaking style observed during the hardness measurements could be reproduced, the obtained diametral resistance of the agglomerates is X times higher than the experimental values.

Such discrepancies are mostly due to the mechanical properties of the materials not being fully investigated. While Heckel curves were performed in order to evaluate the material tendencies toward a brittle or viscoelastic behavior, no measurement have been performed regarding Young's modulus nor Poisson ratio for the here-studied materials. Some values were available in the

literature for pure materials, but nothing was found for more complex materials. For example, the pyrolusite concentrate used in this study has been determined to have lithiophorite coating pyrolusite and cryptomelane grains. However, no model was found in the literature to calculate the resulting Young modulus of such bimodal material, barring the fact that no data were available for lithiophorite in itself. Moreover, the impact of moisture on both Young's modulus and Poisson ratio should be investigated (Chamrova, 2010) in order to perform a finer modelling at different moisture content.

A theoretical database on pure minerals has started to be implemented and completed by ELATE (Gaillac et al., 2016). Building a complementary database with data from experiments on pure and mixed industrial materials would be interesting to improve the availability of agglomeration modelling.

Additionally, the bond parameters were explored empirically for the pyrolusite concentrate due to the absence of measurement or literature source. Due to an absence of adequate model, the characterization performed during the chapter 2 could not be used to their full potential in this study. Otherwise, it should be possible to estimate the bond parameters properties (Bond size, normal and tangential strengths, Young's Modulus) based on the characterization of the material, thus easing the process of modelling the agglomeration by circumventing, or at least reducing, the need for empirical exploration of the optimal bond parameters.

In the meantime, the present work can be helpful to decrease the exploratory work by highlighting the impact of the different bond parameters on agglomeration results. The most impactful parameters appear to be Young's modulus and the bond size, which are the main contributors to the breaking style of the agglomerates.

2. Extrapolation of the prediction to other ore fines

The material properties studied in this thesis and used to predict their agglomerability can be measured in other Mn ores, but also in materials linked to other commodities, such as iron or nickel value chains. Thus, the method developed in this work can theoretically be applied to other materials. It should hence be possible to product their agglomeration potential, at least qualitatively.

2.1 Case of other Mn ores

One of the main issues of agglomeration processes is the susceptibility to feed changes, which will degrade the agglomerate properties. However, adapting the functioning parameters of the agglomeration process to the new feed properties can be sufficient to restore agglomerate properties, as long as the feed's mineralogy stays similar.

For example, the experiments in this work were performed on Mn ores from Moanda, Gabon enriched in pyrolusite and cryptomelane. It means that the raw ore feed presents higher content of lithiophorite and clay minerals. Additionally, Eramet COMILOG has expressed its will to expand its mining activities near Moanda. The new prospect of Okouma has been studied through XRD, XRF and Qemscan, revealing similar mineralogy than the present feed, dominated by pyrolusite, cryptomelane, lithiophorite and clay minerals (illite and kaolinite). It also presents important variability: for example, its lithiophorite content varies from 10 to 70 wt.% depending on the location and depth in the deposit (Blancher, 2018).

The presence of lithiophorite and clay minerals are considered to be the most important element allowing the self-agglomeration of the pyrolusite concentrate, it can be predicted that this material should agglomerate properly without binder. However, its variability increases the need to keep improving the modelling to reach a numerical prediction and be able to adapt the process according to the feed variations.

However, the main Mn ore is the Kalahari deposit, which represents 75 wt.% of the world's known Mn resources. It is a semi-carbonated ore, with lower Mn content than Moanda's ore. The products of the two mines studied in the present work (Gloria and Asman ores, ASMANG, South Africa; Dubos et al., 2019) contain mostly kutnohorite, calcite, braunite and hausmannite. They both produce little fines (~ 1 wt.%; Dubos et al., 2019).

Therefore, agglomeration experiments were not performed on the semi-carbonated ore fines from the Kalahari deposit. It is suggested to perform experiments on fine materials from the Kalahari deposits in order to define their agglomeration behavior. At a first glance, it can be suggested that their low hardness combined to their brittle properties are more favorable to agglomeration than that of the here studied hausmannite.

2.2 Case of new commodities

A definitive prediction applied to new commodities would require performing additional tests. However, predictions can already be formulated for some ore types, based on the shared properties of mineralogical families. The layered structures minerals (phyllosilicates mostly), swelling and non-swelling clays play a key role in agglomeration. Surface deposits in chemically weathered areas are favorable to their formation. For example, the Ni laterites are rich in clay minerals such as nontronite, saponite, sepiolite and pimelite (Galí et al., 2012; Tauler et al., 2009; Traoré, 2005; Wells et al., 2009). Similar observation can be performed for bauxite (Negrão et al., 2018), a laterite type Al-rich ore and Nb-Ta laterites (Sadiq and Umrao, 2020), both containing clay minerals with their valuable minerals.

In some cases, the elements of interests are directly contained in the clay minerals, such as in a number of Rare Earth Elements (REE)-rich deposits in the Nanling area in Southern China, called "ion adsorption clay" deposits (Kanazawa and Kamitani, 2006; Kynicky et al., 2012).

3. Extrapolation to other agglomeration methods

It was stated that uniaxial compaction is the agglomeration method which parameters are easiest to control. When the machine is instrumented, the measured values are directly translatable to the material (e.g. the pressure applied by the punch is the pressure received by the material). The other methods, presented in the chapter 1 of this thesis, possesses mostly controls that are indirect. For example, a tangential wheel press can control the spacing between its wheels, which will in turn modify the linear pressure applied to the material, which is different from the actual pressure received by the material. Moreover, the pressure is applied differently compared to uniaxial compaction. It is hence possible to control the spacing between the wheels directly, but new models would have to be developed to (1) translate it into the effective pressure applied to the material and (2) understand the way the material would react to a pressure applied this way. All agglomeration present different level of acquired knowledge, but none of them is well known to the point of having perfectly functional models.

Due to the machines relying on different working principles, their builds and hence their functioning parameters are also different. The work presented here and the resulting predictability is hence not directly transferable to other methods. However, the methodology is still valid: by identifying the main mechanisms on which rely each method, it is possible to analyze how those mechanisms would impact the main agglomeration forces based on the material properties and the agglomeration parameters.

Moreover, this does not render the analyses performed in this work useless, as some properties identified as key for uniaxial compaction result prediction may also intervene in another agglomeration process, although in a different way. For example, a low hardness, plastic particle may (1) deform easily during uniaxial compaction, thus increasing its contact surface with other particles and hence the bonding strength and (2) inefficiently transfer kinetic energy due to deformation, hence more readily sticking to other particles dur pelletization by preventing a rebound after the shock between the two particles.

The agglomeration processes which do not rely on pressure in order to bring the particles together will probably require the most work compared to the present thesis, since the underlying mechanisms are the most different.

4. Conclusion and perspectives

The present thesis approaches the agglomeration from a new, material-centric angle. The objective is to be able to predict the agglomeration potential based on the material parameters. The characterization study performed in the second chapter made a qualitative estimation of the agglomeration potential possible. The hypotheses formed were confirmed by the experimental compaction tests performed in the third chapter, thus contributing to the understanding of agglomeration processes. However, additional work is required to reach a quantitative predictability of the material's potential. Moreover, tools for numerical modelling of agglomeration, such as DEM, already exists and are suitable for use by the Mining and metallurgical industries, provided the necessary analyses are performed on the studied material.

Furthermore, the results show that tableting is suitable for materials generated by the mining and metallurgical industries. It has also been shown that binder-free agglomeration can be achieved in the manganese industry and can be used to recycle materials that are difficult to agglomerate.

The present work hence represents one more step toward a robust predictability of agglomeration potential of materials. However, a number of additional steps can be taken to go further on the subject, besides the realization of additional agglomeration tests.

In order to predict a material behavior, it must be properly known. The characterization is an essential part of the prediction task. Despite an extensive number of analyses performed in the present work, the mechanical aspect of their properties was overlooked. The absence of characterization of the Young's modulus, Poisson ratio and frictions parameters for the materials studied limited the potential of the DEM modelling undertaken during this study. Determining those parameters, especially for the pyrolusite concentrate, at various moisture content would improve the robustness of the modelling and allow for additional agglomeration conditions to be studied. Although this work is complex (Chamrova, 2010), it is essential to improve modelling stability.

It is also interesting to consider the surface state of the particles after interacting with different environmental conditions. Performing XPS measurement on the surface of particles before and after exposing it to various environmental conditions (moisture with different pH and/or chemistry,

binders, etc.) could provide interesting insight regarding agglomeration potential modification with respect to environmental variations.

Additionally, the present study's objective was to predict the agglomerate strength directly from the material characteristic, thus overlooking the bonds development. This should be corrected by dividing the modelling in two steps with (1) the estimation of the bond generation potential based on the material characteristics, in terms of both strength and volume and (2) the estimation of the agglomerate strength based on the bond generation potential and the agglomeration procedure (pressure, moisture, etc.). The first part of this study relies heavily on the characterization of the material, as presented in the second chapter of this work, and could benefit from additional XPS analyses, as discussed above. The second part would rely more heavily on the mechanical characterization of the material coupled to the bond generated. However, by using a pre-existing software such as MUSEN, the priority of the second part could be shifted to optimize the force expression in the software based on its empirical properties.

Finally, the measurement of the forces at this intermediary step would be essential to constraint models developed for both the first and second parts. A recent study has been able to measure the Van der Waals forces (Kawai et al., 2016). If applied to the cross-section and surfaces of the tablets generated through uniaxial compaction, it could be possible to measure the strength developed by the bonds at different location of the tablet, hence characterizing its "intermiediary state".

References

Ahmed, H., 2014. Relationship Between Crystal Structure and Mechanical Properties in Cocrystals and Salts of Paracetamol. Luleå University of Technology, Luleå.

Al Mahrouqi, D., Vinogradov, J., Jackson, M.D., 2017. Zeta potential of artificial and natural calcite in aqueous solution. Adv. Colloid Interface Sci. 240, 60–76. https://doi.org/10.1016/j.cis.2016.12.006

Alkrad, J.A., Abu Shmeis, R., Alshwabkeh, I., Abazid, H., Mohammad, M.A., 2017. Investigation of the potential application of sodium bentonite as an excipient in formulation of sustained release tablets. Asian J. Pharm. Sci. 12, 259–265. https://doi.org/10.1016/j.ajps.2017.01.004

Antonyuk, S., Palis, S., Heinrich, S., 2011. Breakage behaviour of agglomerates and crystals by static loading and impact. Powder Technol. 206, 88–98. https://doi.org/10.1016/j.powtec.2010.02.025

Antonyuk, S., Tomas, J., Heinrich, S., Mörl, L., 2005. Breakage behaviour of spherical granulates by compression. Chem. Eng. Sci. 60, 4031–4044. https://doi.org/10.1016/j.ces.2005.02.038

Aschner, M., Aschner, J.L., 1991. Manganese neurotoxicity: cellular effects and blood-brain barrier transport. Neurosci. Biobehav. Rev. 15, 333–340. https://doi.org/10.1016/s0149-7634(05)80026-0

Awad, M.E., López-Galindo, A., Medarević, D., Đuriš, J., El-Rahmany, M.M., Ibrić, S., Viseras, C., 2019. Flow and Tableting Behaviors of Some Egyptian Kaolin Powders as Potential Pharmaceutical Excipients. Minerals 10, 23. https://doi.org/10.3390/min10010023

Bacher, C., Olsen, P.M., Bertelsen, P., Sonnergaard, J.M., 2008. Compressibility and compactibility of granules produced by wet and dry granulation. Int. J. Pharm. 358, 69–74. https://doi.org/10.1016/j.ijpharm.2008.02.013

Balakin, B.V., Shamsutdinova, G., Kosinski, P., 2015. Agglomeration of solid particles by liquid bridge flocculants: Pragmatic modelling. Chem. Eng. Sci. 122, 173–181. https://doi.org/10.1016/j.ces.2014.09.003

Banchet, J., Blaffart, F., 2018. GO 4 0 – Deliverable 0_0006 – 2018 Optimized Agglomerates for testing in pilot scale. Go-4-0 Project.

Behjani, M.A., Motlagh, Y.G., Bayly, A.E., Hassanpour, A., 2020. Assessment of blending performance of pharmaceutical powder mixtures in a continuous mixer using Discrete Element Method (DEM). Powder Technol. 366, 73–81. https://doi.org/10.1016/j.powtec.2019.10.102

Beloborodov, R., Pervukhina, M., Luzin, V., Delle Piane, C., Clennell, M.B., Zandi, S., Lebedev, M., 2016. Compaction of quartz-kaolinite mixtures: The influence of the pore fluid composition on the development of their microstructure and elastic anisotropy. Mar. Pet. Geol. 78, 426–438. https://doi.org/10.1016/j.marpetgeo.2016.09.030

Bizhanov, A., Kurunov, I., Podgorodetskyi, G., Dashevskyi, V., Pavlov, A., 2014. Extruded Briquettes – New Charge Component for the Manganese Ferroalloys Production. ISIJ Int. 54, 2206–2214. https://doi.org/10.2355/isijinternational.54.2206

Blancher, S.B., Laugier, O., 2014. Briquetage de minerai Weda Bay : Analyse Qemscan (No. 68.14.114). Eramet IDEAS.

Blancher, S.B., Laugier, O., Bouchet, A., 2015. Clay Mineral Characterization on Ni-Laterite: Qemscan Imaging of Alteration Processes, in: MINERAL RESOURCES IN A SUSTAINABLE WORLD. Presented at the 13th SGA Biennial Meeting 2015.

Bondouy, N., Milazzo, J.-M., 2016. COMPTE RENDU DE LA VISITE D'EUROTAB: RESULTATS DE FAISABILITE DE TABLETTE (No. 52.16.024). Eramet IDEAS.

Bouchet, A., Meunier, A., Sardini, P., 2000. Minéraux argileux: structure cristalline; identification par diffraction de rayons X = Clay minerals: crystal structure; X-ray diffraction identification, Bulletin des Centres de Recherches Exploration - Production Elf-Aquitaine : Mémoires. Elf EP Ed, Pau.

Brunauer, S., Emmett, P.H., Teller, E., 1938. Adsorption of Gases in Multimolecular Layers. J. Am. Chem. Soc. 60, 309–319. https://doi.org/10.1021/ja01269a023

By, Thomas, 2017. 2017_BY_Briquetting of Manganese Oxide Fines.pdf.

By, T., 2017. Briquetting of Manganese Oxide Fines. (Master thesis). Norwegian University of Science and Technology, Trondheim, Norway.

Caricchi, L., Burlini, L., Ulmer, P., Gerya, T., Vassalli, M., Papale, P., 2007. Non-Newtonian rheology of crystal-bearing magmas and implications for magma ascent dynamics. Earth Planet. Sci. Lett. 264, 402–419. https://doi.org/10.1016/j.epsl.2007.09.032

Chaim, R., 2017. Particle Surface Softening as Universal Behaviour during Flash Sintering of Oxide Nano-Powders. Materials 10, 179. https://doi.org/10.3390/ma10020179

Chamrova, R., 2010. Modelling and Measurement of Elastic Properties of Hydrating Cement Paste. ÉCOLE POLYTECHNIQUE FÉDÉRALE DE LAUSANNE, Suisse.

Charinpanitkul, T., Tanthapanichakoon, W., Kulvanich, P., Kim, K.-S., 2008. Granulation and tabletization of pharmaceutical lactose granules prepared by a top-sprayed fluidized bed granulator. J. Ind. Eng. Chem. 14, 661–666. https://doi.org/10.1016/j.jiec.2008.03.005

Chen, D.T.N., Wen, Q., Janmey, P.A., Crocker, J.C., Yodh, A.G., 2010. Rheology of Soft Materials. Annu. Rev. Condens. Matter Phys. 1, 301–322. https://doi.org/10.1146/annurev-conmatphys-070909-104120

Chetty, D., Gutzmer, J., 2012. REE redistribution during hydrothermal alteration of ores of the Kalahari Manganese Deposit. Ore Geol. Rev. 47, 126–135. https://doi.org/10.1016/j.oregeorev.2011.06.001

Cleary, P.W., Sawley, M.L., 2002. DEM modelling of industrial granular flows: 3D case studies and the effect of particle shape on hopper discharge. Appl. Math. Model. 26, 89–111. https://doi.org/10.1016/S0307-904X(01)00050-6

Cooper, A.R., Eaton, L.E., 1962. Compaction Behavior of Several Ceramic Powders.

Darab, J.G., Linehan, J.C., Matson, D.W., 1994. Effect of Agglomerate Size on the Catalytic Activity of an Iron Oxyhydroxide Nanocrystalline Powder toward Carbon-Carbon Bond Scission in Naphthylbibenzylmethane. Energy Fuels 8, 1004–1005. https://doi.org/10.1021/ef00046a028

Darde, B., Tang, A.M., Pereira, J.-M., Roux, J.-N., Dangla, P., Talandier, J., Vu, M.N., 2018. Hydro-mechanical behaviour of high-density bentonite pellet on partial hydration. Géotechnique Lett. 8, 330–335. https://doi.org/10.1680/jgele.18.00114

Davis, J.M., Behar, J.V., Braddock, J., Durkee, S., Graham, J.A., Hasselblad, V., Jarabek, A., Mage, D., Ott, W., Svendsgaard, D., Wallace, L., 1994. Reevaluation of Inhalation Health Risks Associated With Methylcyclopentadienyl Manganese Tricarbonyl (MMT) in Gasoline (No. 600R94062). U.S. Environmental Protection Agency.

Day, N., n.d. Crystallography Open Database [WWW Document]. Crystallogr. Open Database. URL http://www.crystallography.net/cod/ (accessed 7.9.19).

Debrincat, D.P., Solnordal, C.B., Van Deventer, J.S.J., 2008a. Influence of particle properties on the size of agglomerated metallurgical powders. Int. J. Miner. Process. 87, 17–27. https://doi.org/10.1016/j.minpro.2008.01.003

Debrincat, D.P., Solnordal, C.B., Van Deventer, J.S.J., 2008b. Influence of particle properties on the size of agglomerated metallurgical powders. Int. J. Miner. Process. 87, 17–27. https://doi.org/10.1016/j.minpro.2008.01.003

Dhanalakshmi, K., Ghosal, S., Bhattacharya, S., 2011. Agglomeration of Food Powder and Applications. Crit. Rev. Food Sci. Nutr. 51, 432–441. https://doi.org/10.1080/10408391003646270

Diamond, S., 1956. Surface Areas of Clay Minerals as Derived from Measurements of Glycerol Retention. Clays Clay Miner. 5, 334–347. https://doi.org/10.1346/CCMN.1956.0050128

Dixon, J.B., Weed, S.B., Dinauer, R.C. (Eds.), 1977. Minerals in soil environments. Soil Science Society of America, Madison, Wis.

Dosta, M., Antonyuk, S., Heinrich, S., 2013. Multiscale Simulation of Agglomerate Breakage in Fluidized Beds. Ind. Eng. Chem. Res. 52, 11275–11281. https://doi.org/10.1021/ie400244x

Dražić, S., Sladoje, N., Lindblad, J., 2016. Estimation of Feret's diameter from pixel coverage representation of a shape. Pattern Recognit. Lett. 80, 37–45. https://doi.org/10.1016/j.patrec.2016.04.021

Dubos, J.-L., Orberger, B., Banchet, J., Milazzo, J.-M., Blancher, S.B., Wallmach, T., Lützenkirchen, J., 2021. Binder-free tableting experiments on manganese oxides and industrial mineral powders. Powder Technol. 377, 194–211. https://doi.org/10.1016/j.powtec.2020.08.032

Dubos, J.L., Orberger, B., Milazzo, J.M., Blancher, S.B., Wallmach, T., Lützenkirchen, J., Banchet, J., 2019. Agglomeration potential evaluation of industrial Mn dusts and sludges based on physico-chemical characterization. Powder Technol. https://doi.org/10.1016/j.powtec.2019.10.101

Dutta, G., Bose, D., 2012. Effect of Sintering Temperature on Density, Porosity and Hardness of a Powder Metallurgy Component. Int. J. Emerg. Technol. Adv. Eng. 2.

Eisele, T. C., Kawatra, S.K., 2003. A review of binders in iron ore pelletization. Miner. Process. Extr. Metall. Rev. 24, 1–90. https://doi.org/10.1080/08827500390198190

Eisele, T.C., Kawatra, S.K., 2003. A review of binders in iron ore pelletization. Miner. Process. Extr. Metall. Rev. 24, 1–90.

Eissa, M., Ghali, S., Ahmed, A., El-Faramawy, H., 2012. Optimum condition for smelting high carbon ferromanganese. Ironmak. Steelmak. 39, 419–430. https://doi.org/10.1179/1743281211Y.0000000062

eit.RawMaterials, n.d. Innovation themes. URL https://eitrawmaterials.eu/innovation-themes/ (accessed 6.4.20).

Eramet Norway, 2018. Expertise and growth: Sustainability report 2017 (Annual report). Eramet Norway, Norway.

European Commission, 2020. Circular Economy Action Plan: For a cleaner and more competitive Europe. European Union, Brussels.

Fernández, A.I., Chimenos, J.M., Raventós, N., Miralles, L., Espiell, F., 2003. Stabilization of Electrical Arc Furnace Dust with Low-Grade MgO Prior to Landfill. J. Environ. Eng. 129, 275–279. https://doi.org/10.1061/(ASCE)0733-9372(2003)129:3(275)

Fernández-González, D., Piñuela-Noval, J., Verdeja, L.F., 2018. Iron Ore Agglomeration Technologies, in: Shatokha, V. (Ed.), Iron Ores and Iron Oxide Materials. InTech. https://doi.org/10.5772/intechopen.72546

Furnas, C.C., 1931. Grading Aggregates - I. - Mathematical Relations for Beds of Broken Solids of Maximum Density. Ind. Eng. Chem. 23, 1052–1058. https://doi.org/10.1021/ie50261a017

Gaillac, R., Pullumbi, P., Coudert, F.-X., 2016. ELATE: an open-source online application for analysis and visualization of elastic tensors. J. Phys. Condens. Matter 28, 275201. https://doi.org/10.1088/0953-8984/28/27/275201

Galí, S., Soler, J.M., Proenza, J.A., Lewis, J.F., Cama, J., Tauler, E., 2012. Ni Enrichment and Stability of Al-Free Garnierite Solid-solutions: A Thermodynamic Approach. Clays Clay Miner. 60, 121–135. https://doi.org/10.1346/CCMN.2012.0600203

Garcês Gonçalves, P.R., De Abreu, H.A., Duarte, H.A., 2018. Stability, Structural, and Electronic Properties of Hausmannite (Mn_3O_4) Surfaces and Their Interaction with Water. J. Phys. Chem. C 122, 20841–20849. https://doi.org/10.1021/acs.jpcc.8b06201

Gaudin, A., Ansan, V., Rigaudier, T., 2015. Mineralogical and δ18O–δD isotopic study of kaolinized micaschists at Penestin, Armorican Massif, France: New constraint in the kaolinization process. CATENA 133, 97–106. https://doi.org/10.1016/j.catena.2015.05.006

Gauß, C.F., 1831. "Besprechung des Buchs von L. A. Seeber: Untersuchungen über die Eigenschaften der positiven ternären quadratischen Formen usw" [Discussion of L. A. Seeber's book: Studies on the characteristics of positive ternary quadratic forms etc].

Gensch, M., Weber, A.P., 2017. Rebound behavior of nanoparticle-agglomerates. Adv. Powder Technol. 28, 1930–1942. https://doi.org/10.1016/j.apt.2017.05.003

Gonzalez, S., Windows-Yule, C.R.K., Luding, S., Parker, D.J., Thornton, A.R., 2014. Shaping Segregation: Convexity vs. Concavity. ArXiv14106286 Cond-Mat.

Grim, R.E., 1968. Clay mineralogy, 2nd ed. ed. McGraw-Hill, New York.

Grosshans, H., Papalexandris, M.V., 2017. On the accuracy of the numerical computation of the electrostatic forces between charged particles. Powder Technol. 322, 185–194. https://doi.org/10.1016/j.powtec.2017.09.023

Gul, A., Sirkeci, A.A., BOYLU, F., Guldan, G., Burat, F., 2014. IMPROVEMENT OF MECHANICAL STRENGTH OF IRON ORE PELLETS USING RAW AND ACTIVATED BENTONITES AS BINDERS. Physicochem. Probl. Miner. Process. 51, 23–26. http://dx.doi.org/10.5277/ppmp150203

Gulbinska, M.K. (Ed.), 2014. Lithium-ion Battery Materials and Engineering: Current Topics and Problems from the Manufacturing Perspective, Green Energy and Technology. Springer London, London. https://doi.org/10.1007/978-1-4471-6548-4

Halt, J.A., Kawatra, S.K., 2017. Does the Zeta Potential of an Iron Ore Concentrate Affect the Strength and Dustiness of Unfired and Fired Pellets? Miner. Process. Extr. Metall. Rev. 38, 132–141. https://doi.org/10.1080/08827508.2017.1288114

Halt, J.A., Kawatra, S.K., 2014. Review of organic binders for iron ore concentrate agglomeration. Min. Metall. Explor. 31, 73–94. https://doi.org/10.1007/BF03402417

He, Y., Li, Y.Y., Evans, T.J., Yu, A.B., Yang, R.Y., 2019. Effects of particle characteristics and consolidation pressure on the compaction of non-spherical particles. Miner. Eng. 137, 241–249. https://doi.org/10.1016/j.mineng.2019.04.007

He, Y., Wang, Z., Evans, T.J., Yu, A.B., Yang, R.Y., 2015. DEM study of the mechanical strength of iron ore compacts. Int. J. Miner. Process. 142, 73–81. https://doi.org/10.1016/j.minpro.2015.05.005

Heckel, R.W., 1961a. 1961_Heckel_Al_Density_pressure relationships in powder compaction.pdf.

Heckel, R.W., 1961b. Density-pressure relationship in powder compaction. Trans. Metall. Soc. AIME 221, 5.

Heim, A., Obraniak, A., Gluba, T., 2005. Changes of feed bulk density during drum granulation of bentonite. Physicochem. Probl. Miner. Process. 219–228.

Heim, A., Obraniak, A., Gluba, T., 2004. The effect of equipment and process parameters on torque during disk granulation of bentonite. Physicochem. Probl. Miner. Process. 157–166.

Herting, M., Kleinebudde, P., 2008a. Studies on the reduction of tensile strength of tablets after roll compaction/dry granulation. Eur. J. Pharm. Biopharm. 70, 372–379. https://doi.org/10.1016/j.ejpb.2008.04.003

Herting, M., Kleinebudde, P., 2008b. Studies on the reduction of tensile strength of tablets after roll compaction/dry granulation. Eur. J. Pharm. Biopharm. 70, 372–379. https://doi.org/10.1016/j.ejpb.2008.04.003

Herting, M.G., Kleinebudde, P., 2007. Roll compaction/dry granulation: Effect of raw material particle size on granule and tablet properties. Int. J. Pharm. 338, 110–118. https://doi.org/10.1016/j.ijpharm.2007.01.035

Hertz, H., 1882. Ueber die Berührung fester elastischer Körper. J. Für Reine Angew. Math. Crelles J. 1882, 156–171. https://doi.org/10.1515/crll.1882.92.156

Hooper, R.T., 1968. The production of ferromanganese. JOM 20, 88–92. https://doi.org/10.1007/BF03378712

Horiba, 2020. Zeta Potential: Layout, Calculating, Analysis. Horiba. URL https://www.horiba.com/en_en/zeta-potential/ (accessed 8.12.20).

Hou, J., Li, H., Zhu, H., Wu, L., 2009. Determination of Clay Surface Potential: A More Reliable Approach. Soil Sci. Soc. Am. J. 73, 1658. https://doi.org/10.2136/sssaj2008.0017

Hunter, R.J., 1988. Zeta potential in colloid science: principles and applications, 3. print. ed, Colloid science. Academic Pr, London.

Ilkka, J., Paronen, P., 1993. Prediction of the compression behaviour of powder mixtures by the Heckel equation. Int. J. Pharm. 94, 181–187. https://doi.org/10.1016/0378-5173(93)90022-8

IMnI, 2020. IMnI Annual Review 2019 (Annual review). International Manganese Institute.

International Energy Agency, 2007. World Energy Outlook 2007: China and India Insights, World Energy Outlook. OECD. https://doi.org/10.1787/weo-2007-en

Ji, S., Li, L., Motra, H.B., Wuttke, F., Sun, S., Michibayashi, K., Salisbury, M.H., 2018. Poisson's Ratio and Auxetic Properties of Natural Rocks: Poisson's Ratio and Auxetic Properties of Natural Rocks. J. Geophys. Res. Solid Earth 123, 1161–1185. https://doi.org/10.1002/2017JB014606

Johansen, A., Schæfer, T., 2001. Effects of physical properties of powder particles on binder liquid requirement and agglomerate growth mechanisms in a high shear mixer. Eur. J. Pharm. Sci. 14, 135–147. https://doi.org/10.1016/S0928-0987(01)00164-6

Johansson, B., Alderborn, G., 2001. The effect of shape and porosity on the compression behaviour and tablet forming ability of granular materials formed from microcrystalline cellulose. Eur. J. Pharm. Biopharm. Off. J. Arbeitsgemeinschaft Pharm. Verfahrenstechnik EV 52, 347–357.

Kabata-Pendias, A., Pendias, H., 2001. Trace elements in soils and plants, 3rd ed. ed. CRC Press, Boca Raton, Fla.

Kadiri, M.S., Michrafy, A., Dodds, J.A., 2005. Pharmaceutical powders compaction: Experimental and numerical analysis of the density distribution. Powder Technol. 157, 176–182. https://doi.org/10.1016/j.powtec.2005.05.025

Kanazawa, Y., Kamitani, M., 2006. Rare earth minerals and resources in the world. J. Alloys Compd. 408–412, 1339–1343. https://doi.org/10.1016/j.jallcom.2005.04.033

Karakaya, M.Ç., Karakaya, N., Bakır, S., 2011. Some properties and potential applications of the Na- and Ca-bentonites of ordu (N.E. Turkey). Appl. Clay Sci. 54, 159–165. https://doi.org/10.1016/j.clay.2011.08.003

Karland, O., 2010. Chemical and mineralogical characterization of the bentonite buffer for the acceptance control procedure in a KBS-3 repository.

Kawai, S., Foster, A.S., Björkman, T., Nowakowska, S., Björk, J., Canova, F.F., Gade, L.H., Jung, T.A., Meyer, E., 2016. Van der Waals interactions and the limits of isolated atom models at interfaces. Nat. Commun. 7. https://doi.org/10.1038/ncomms11559

Kawakita, K., Lüdde, K.-H., 1971. Some considerations on powder compression equations. Powder Technol. 4, 61–68. https://doi.org/10.1016/0032-5910(71)80001-3

Kawashima, Y., Cui, F., Takeuchi, H., Niwa, T., Hino, T., Kiuchi, K., 1994. Improvements in flowability and compressibility of pharmaceutical crystals for direct tabletting by spherical crystallization with a two-solvent system. Powder Technol. 78, 151–157. https://doi.org/10.1016/0032-5910(93)02772-3

Kero, I.T., Eidem, P.A., Ma, Y., Indresand, H., Aarhaug, T.A., Grådahl, S., 2019. Airborne Emissions from Mn Ferroalloy Production. JOM 71, 349–365. https://doi.org/10.1007/s11837-018-3165-9

Ketterhagen, W.R., am Ende, M.T., Hancock, B.C., 2009. Process Modeling in the Pharmaceutical Industry using the Discrete Element Method. J. Pharm. Sci. 98, 442–470. https://doi.org/10.1002/jps.21466

Klein, C., Dutrow, B., 2008. Mineral science, John Wiley & Sons. ed.

Komarek, 2020. briquetting machines and compaction, granulation solutions. URL https://komarek.com/ (accessed 6.8.20).

Kopeliovich, D., 2012. Methods of shape forming ceramic powders. Subst. Technol. URL http://www.substech.com/dokuwiki/doku.php?id=methods_of_shape_forming_ceramic_powders&s=compaction (accessed 6.8.20).

Kotzé, I.., 2002. Pilot plant production of ferronickel from nickel oxide ores and dusts in a DC arc furnace. Miner. Eng. 15, 1017–1022. https://doi.org/10.1016/S0892-6875(02)00127-9

Kozhar, S., Dosta, M., Antonyuk, S., Heinrich, S., Bröckel, U., 2015. DEM simulations of amorphous irregular shaped micrometer-sized titania agglomerates at compression. Adv. Powder Technol. 26, 767–777. https://doi.org/10.1016/j.apt.2015.05.005

Kynicky, J., Smith, M.P., Xu, C., 2012. Diversity of Rare Earth Deposits: The Key Example of China. Elements 8, 361–367. https://doi.org/10.2113/gselements.8.5.361

Lastra, R., Paktunc, D., 2016. An estimation of the variability in automated quantitative mineralogy measurements through inter-laboratory testing. Miner. Eng. 95, 138–145. https://doi.org/10.1016/j.mineng.2016.06.025

Leroy, P., Tournassat, C., Bernard, O., Devau, N., Azaroual, M., 2015. The electrophoretic mobility of montmorillonite. Zeta potential and surface conductivity effects. J. Colloid Interface Sci. 451, 21–39. https://doi.org/10.1016/j.jcis.2015.03.047

Li, H., Robertson, D.G.C., 1997. Effect of Moisture, Combined Water, and Volatile Elements on Fixed Carbon Requirement in a Ferro-Manganese Smelting Furnace. Presented at the Electric Furnace Conference Proceedings, The Iron & Steel Society (IOM3), pp. 269–279.

Licciardi, A., Gallagher, K., Clark, S.A., 2020. Estimating uncertainties on net erosion from well-log porosity data. Basin Res. 32, 51–67. https://doi.org/10.1111/bre.12366

Liebman, M., 2000. The treatment and disposal of electric arc furnace dust in North America. Presented at the Proc., Electric Furnace Conf., Iron & Steel Society, Warrendale, PA, 58, 781–792.

Lifshitz, E.M., 1956. The theory of molecular attractive forces between solids.

Linhares, F.M., Victor, C.C.F., Lemos, L.R., Bagatini, M.C., 2019. Effect of three different binders and pellet feed on granulation behaviour of sintering mixtures. Ironmak. Steelmak. 1–7. https://doi.org/10.1080/03019233.2019.1659001

Logan, D.L., 2015. A first course in finite element method, 6th edition. ed. Cengage Learning, Mason, OH.

Louati, H., Oulahna, D., de Ryck, A., 2017a. Effect of the particle size and the liquid content on the shear behaviour of wet granular material. Powder Technol. 315, 398–409. https://doi.org/10.1016/j.powtec.2017.04.030

Louati, H., Oulahna, D., de Ryck, A., 2017b. Effect of the particle size and the liquid content on the shear behaviour of wet granular material. Powder Technol. 315, 398–409. https://doi.org/10.1016/j.powtec.2017.04.030

Lowke, D., Gehlen, C., 2017. The zeta potential of cement and additions in cementitious suspensions with high solid fraction. Cem. Concr. Res. 95, 195–204. https://doi.org/10.1016/j.cemconres.2017.02.016

Lu, G.W., Gao, P., 2010. Emulsions and Microemulsions for Topical and Transdermal Drug Delivery, in: Handbook of Non-Invasive Drug Delivery Systems. Elsevier, pp. 59–94. https://doi.org/10.1016/B978-0-8155-2025-2.10003-4

Lyman, G.J., 2014. Determination of the complete sampling distribution for a particulate material. Proc. Sampl. 2014 17–24.

Mal'tseva, V.E., Vinichuk, B.G., 2016. Methods of Testing Bentonite Clays for Agglomerating Iron-Ore Concentrates. Metallurgist 60, 237–242. https://doi.org/10.1007/s11015-016-0280-0

Manceau, A., Tommaseo, C., Rihs, S., Geoffroy, N., Chateigner, D., Schlegel, M., Tisserand, D., Marcus, M.A., Tamura, N., Chen, Z.-S., 2005. Natural speciation of Mn, Ni, and Zn at the micrometer scale in a clayey paddy soil using X-ray fluorescence, absorption, and diffraction. Geochim. Cosmochim. Acta 69, 4007–4034. https://doi.org/10.1016/j.gca.2005.03.018

Mansa, R.F., Bridson, R.H., Greenwood, R.W., Barker, H., Seville, J.P.K., 2008. Using intelligent software to predict the effects of formulation and processing parameters on roller compaction. Powder Technol. 181, 217–225. https://doi.org/10.1016/j.powtec.2007.02.011

Mars Mineral, 2020. Pelletizing technology. URL https://www.marsmineral.com/ (accessed 6.8.20).

Martin, C.., Bouvard, D., Shima, S., 2003. Study of particle rearrangement during powder compaction by the Discrete Element Method. J. Mech. Phys. Solids 51, 667–693. https://doi.org/10.1016/S0022-5096(02)00101-1

Matusewicz, M., Olin, M., 2019. Comparison of microstructural features of three compacted and water-saturated swelling clays: MX-80 bentonite and Na- and Ca-purified bentonite. Clay Miner. 54, 75–81. https://doi.org/10.1180/clm.2019.1

Maxbauer, D.P., Feinberg, J.M., Fox, D.L., 2016. Magnetic mineral assemblages in soils and paleosols as the basis for paleoprecipitation proxies: A review of magnetic methods and challenges. Earth-Sci. Rev. 155, 28–48. https://doi.org/10.1016/j.earscirev.2016.01.014

Maximenko, A.L., Olevsky, E.A., Shtern, M.B., 2008. Plastic behavior of agglomerated powder. Comput. Mater. Sci. 43, 704–709. https://doi.org/10.1016/j.commatsci.2008.01.011

McGEARY, R.K., 1961. Mechanical Packing of Spherical Particles. J. Am. Ceram. Soc. 44, 513–522. https://doi.org/10.1111/j.1151-2916.1961.tb13716.x

Melhus, M.F., Aranson, I.S., 2012. Effect of vibration on solid-to-liquid transition in small granular systems under shear. Granul. Matter 14, 151–156. https://doi.org/10.1007/s10035-012-0314-7

Mergler, D., Baldwin, M., Bélanger, S., Larribe, F., Beuter, A., Bowler, R., Panisset, M., Edwards, R., de Geoffroy, A., Sassine, M.P., Hudnell, K., 1999. Manganese neurotoxicity, a continuum of dysfunction: results from a community based study. Neurotoxicology 20, 327–342.

Mielniczuk, B., Millet, O., Saïd El Youssoufi, M., 2017. Analysis of capillary bridges using imaging techniques and recent analytical model. Presented at the 35èmes Rencontres Universitaires de Génie Civil, hal-01674600, Nantes, France.

Moore, D.E., Lockner, D.A., 2007. Friction of the smectite clay montmorillonite. Seism. Zone Subduction Thrust Faults 317–345.

Moraes, S.L. de, Lima, J.R.B. de, Ribeiro, T.R., 2018. Iron Ore Pelletizing Process: An Overview, in: Shatokha, V. (Ed.), Iron Ores and Iron Oxide Materials. InTech. https://doi.org/10.5772/intechopen.73164

Mu, F., Su, X., 2007. Analysis of liquid bridge between spherical particles. China Particuology 5, 420–424. https://doi.org/10.1016/j.cpart.2007.04.006

Muurinen, A., 2011. Measurements on Cation Exchange Capacity of Bentonite in the Long-Term Test of Buffer Material (LOT). Posiva Oy, Olkiluoto, Eurojaki, Finland.

Negrão, L.B.A., Costa, M.L. da, Pöllmann, H., 2018. The Belterra Clay on the bauxite deposits of Rondon do Pará, Eastern Amazon. Braz. J. Geol. 48, 473–484. https://doi.org/10.1590/2317-4889201820180128

Nosrati, A., Addai-Mensah, J., Robinson, D.J., 2012. Drum agglomeration behavior of nickel laterite ore: Effect of process variables. Hydrometallurgy 125–126, 90–99. https://doi.org/10.1016/j.hydromet.2012.05.016

Olsen, S.E., Tangstad, M., Lindstad, T., 2007. Production of Manganese Ferroalloys. tapir academic press, Trondheim.

Orberger, B., Wagner, C., Tudryn, A., Baptiste, B., Wirth, R., Morgan, R., Miska, S., 2017. Iron (oxy)hydroxide and hematite micro- to nano-inclusions in diagenetic dolomite from a 2.4 Ga banded iron formation (Minas Gerais, Brazil). Eur. J. Mineral. 29, 971–983. https://doi.org/10.1127/ejm/2017/0029-2679

Ordiales, M., Iglesias, J., Fernández-González, D., Sancho-Gorostiaga, J., Fuentes, A., Verdeja, L., 2016. Cold Agglomeration of Ultrafine Oxidized Dust (UOD) from Ferromanganese and Silicomanganese Industrial Process. Metals 6, 203. https://doi.org/10.3390/met6090203

Orefice, L., Khinast, J.G., 2020. Deformable and breakable DEM particle clusters for modelling compression of plastic and brittle porous materials — Model and structure properties. Powder Technol. 368, 90–104. https://doi.org/10.1016/j.powtec.2020.04.035

Palzer, S., 2011. Agglomeration of pharmaceutical, detergent, chemical and food powders — Similarities and differences of materials and processes. Powder Technol. 206, 2–17. https://doi.org/10.1016/j.powtec.2010.05.006

Pambo, F., 2004. Conditions de formation des carbonates de manganèse protézoïques et analyse minéralogique et géochimique des minerais à bioxydes de manganèse associés dans le gisement de Moanda (Sud-Est, Gabon).

Pan, J., Shi, B., Zhu, D., Mo, Y., 2016. Improving Sintering Performance of Specularite Concentrates by Pre-briquetting Process. ISIJ Int. 56, 777–785. https://doi.org/10.2355/isijinternational.ISIJINT-2015-578

Parker, S.P. (Ed.), 1993. McGraw-Hill encyclopedia of physics, 2nd ed. ed. McGraw-Hill, New York.

Pietsch, W., 2002a. Agglomeration processes: phenomena, technologies, equipment. Wiley-VCH, Weinheim.

Pietsch, W., 2002b. Agglomeration processes: phenomena, technologies, equipment. Wiley-VCH, Weinheim.

Poirier, J., 2014. Vers une nouvelle filière industrielle de recyclage et de valorisation des fines particules minérales. CNRS - Lett. Innov. URL https://www.cnrs.fr/lettre-innovation/actus.php?numero=170 (accessed 2.28.20).

Pokrovsky, O.S., Schott, J., 2004. Experimental study of brucite dissolution and precipitation in aqueous solutions: surface speciation and chemical affinity control. Geochim. Cosmochim. Acta 68, 31–45. https://doi.org/10.1016/S0016-7037(03)00238-2

Potyondy, D.O., Cundall, P.A., 2004. A bonded-particle model for rock. Int. J. Rock Mech. Min. Sci. 41, 1329–1364. https://doi.org/10.1016/j.ijrmms.2004.09.011

Qicpic, n.d. Qicipic shape descriptors [WWW Document]. Sympatec. URL https://www.sympatec.com/en/particle-measurement/glossary/particle-shape/ (accessed 7.8.19).

Quaicoe, I., Nosrati, A., Skinner, W., Addai-Mensah, J., 2013. Agglomeration behaviour and product structure of clay and oxide minerals. Chem. Eng. Sci. 98, 40–50. https://doi.org/10.1016/j.ces.2013.03.034

Rakitskaya, T., Truba, A., Dzhyga, G., Nagaevs'ka, A., Volkova, V., 2018. Water Vapor Adsorption by Some Manganese Oxide Forms. Colloids Interfaces 2, 61. https://doi.org/10.3390/colloids2040061

Revil, A., Jardani, A., Sava, P., Haas, A., 2015. The Seismoelectric Method: Theory and applications. John Wiley & Sons, Ltd, Chichester, UK. https://doi.org/10.1002/9781118660270

Ripke, S.J., Kawatra, S.K., 2000. Can fly-ash extend bentonite binder for iron ore agglomeration? Int. J. Miner. Process. 60, 181–198. https://doi.org/10.1016/S0301-7516(00)00015-6

Rodd, L.E., Scott, T.P., Cooper-White, J.J., McKinley, G.H., 2005. Capillary Break-up Rheometry of Low-Viscosity Elastic Fluids. Appl. Rheol. 15, 12–27. https://doi.org/10.1515/arh-2005-0001

Rondet, E., Cuq, B., Cassan, D., Ruiz, T., 2016. Agglomeration of wheat powders by a novel reverse wet agglomeration process. J. Food Eng. 173, 92–105. https://doi.org/10.1016/j.jfoodeng.2015.10.046

Roqué-Rosell, J., Mosselmans, J.F.W., Proenza, J.A., Labrador, M., Galí, S., Atkinson, K.D., Quinn, P.D., 2010. Sorption of Ni by "lithiophorite–asbolane" intermediates in Moa Bay lateritic deposits, eastern Cuba. Chem. Geol. 275, 9–18. https://doi.org/10.1016/j.chemgeo.2010.04.006

Roskill information services, 2019. Manganese: Outlook to 2029, Fifteenth edition. ed. Roskill.

Rousseau, M., Blancher, S.B., Contessotto, R., Wallmach, T., 2016. BENEFICIATION OF LOW GRADE MANGANESE ORE BY JIGGING IN A SPECIALLY DESIGNED ORE DRESSING UNIT. Presented at the IMPC 2016: XXVIII International Mineral Processing Congress Proceedings, Canadian Institute of Mining, Metallurgy and Petroleum, Québec, Canada.

Sadiq, M., Umrao, R.K., 2020. Nb-Ta-rare earth element mineralization in titaniferous laterite cappings over Sung Valley ultramafic rocks in Meghalaya, India. Ore Geol. Rev. 120, 103439. https://doi.org/10.1016/j.oregeorev.2020.103439

Salles, F., 2006. Hydratation des argiles gonflantes: séquence d'hydratation multi-échelle et détermination des énergies macroscopiques à partir des propriétés microscopiques. Laboratoire de Modélisation des Transferts dans l'Environnement, CEA-Cadarache 13108 Saint Paul lez-Durance - France.

Schoonheydt, R.A., Johnston, C.T., 2011. The surface properties of clay minerals, in: Brigatti, M.F., Mottana, A. (Eds.), Layered Mineral Structures and Their Application in Advanced Technologies. Mineralogical Society of Great Britain and Ireland, London, pp. 335–370. https://doi.org/10.1180/EMU-notes.11.10

Schulze, D., 2008a. Powders and bulk solids: behavior, characterization, storage and flow. Springer, Berlin ; New York.

Schulze, D., 2008b. Powders and bulk solids: behavior, characterization, storage and flow. Springer, Berlin ; New York.

Sermeus, J., Sinha, R., Vanstreels, K., Vereecken, P.M., Glorieux, C., 2014. Determination of elastic properties of a MnO_2 coating by surface acoustic wave velocity dispersion analysis. J. Appl. Phys. 116, 023503. https://doi.org/10.1063/1.4885427

Sezgin, N., Yalçın, A., Köseoğlu, Y., 2016. MnFe2O4 nano spinels as potential sorbent for adsorption of chromium from industrial wastewater. Desalination Water Treat. 57, 16495–16506. https://doi.org/10.1080/19443994.2015.1088808

Shen, Z., Jiang, M., Thornton, C., 2016. DEM simulation of bonded granular material. Part I: Contact model and application to cemented sand. Comput. Geotech. 75, 192–209. https://doi.org/10.1016/j.compgeo.2016.02.007

Shimizu, K., Sokolov, S.V., Compton, R.G., 2016. Agglomeration equilibria of hematite nanoparticles. Colloid Interface Sci. Commun. 13, 19–22. https://doi.org/10.1016/j.colcom.2016.06.003

Shoyama, M., Kawata, T., Yasuda, M., Matsusaka, S., 2018. Particle electrification and levitation in a continuous particle feed and dispersion system with vibration and external electric fields. Adv. Powder Technol. 29, 1960–1967. https://doi.org/10.1016/j.apt.2018.04.022

Skempton, A.W., 1985. Residual strength of clays in landslides, folded strata and the laboratory. Géotechnique 35, 3–18. https://doi.org/10.1680/geot.1985.35.1.3

Sonmez, H., Tuncay, E., Gokceoglu, C., 2004. Models to predict the uniaxial compressive strength and the modulus of elasticity for Ankara Agglomerate. Int. J. Rock Mech. Min. Sci. 41, 717–729. https://doi.org/10.1016/j.ijrmms.2004.01.011

Sonnergaard, J.., 2000. Impact of particle density and initial volume on mathematical compression models. Eur. J. Pharm. Sci. 11, 307–315. https://doi.org/10.1016/S0928-0987(00)00119-6

Spettl, A., Dosta, M., Antonyuk, S., Heinrich, S., Schmidt, V., 2015. Statistical investigation of agglomerate breakage based on combined stochastic microstructure modeling and DEM simulations. Adv. Powder Technol. 26, 1021–1030. https://doi.org/10.1016/j.apt.2015.04.011

Sridharan, A., Rao, S.M., Murthy, N. s., 1986. Compressibility behaviour of homoionized bentonites. Géotechnique 36, 551–564. https://doi.org/10.1680/geot.1986.36.4.551

Stasiak, M., Tomas, J., Molenda, M., Rusinek, R., Mueller, P., 2010. Uniaxial compaction behaviour and elasticity of cohesive powders. Powder Technol. 203, 482–488. https://doi.org/10.1016/j.powtec.2010.06.010

Stellman, J.M., 2000. Encyclopédie de sécurité et de santé au travail. Bureau International du Travail, Genève.

Stewart, R.L., Bradt, R.C., 1995. The Brittle to Ductile Transition In MgAl2O4 Spinel, in: Bradt, R.C., Brookes, C.A., Routbort, J.L. (Eds.), Plastic Deformation of Ceramics. Springer US, Boston, MA, pp. 21–29. https://doi.org/10.1007/978-1-4899-1441-5_2

Suttiponparnit, K., Jiang, J., Sahu, M., Suvachittanont, S., Charinpanitkul, T., Biswas, P., 2010. Role of Surface Area, Primary Particle Size, and Crystal Phase on Titanium Dioxide Nanoparticle Dispersion Properties. Nanoscale Res. Lett. https://doi.org/10.1007/s11671-010-9772-1

Tangstad, M., Olsen, S.E., 1997. Phase relations in ferromanganese slags during melting and reduction. Proc. 5th Int. Conf. Molten Slags Fluxes Salts 549–555.

Tauler, E., Proenza, J.A., Galí, S., Lewis, J.F., Labrador, M., García-Romero, E., Suarez, M., Longo, F., Bloise, G., 2009. Ni-sepiolite-falcondoite in garnierite mineralization from the Falcondo Ni-laterite deposit, Dominican Republic. Clay Miner. 44, 435–454. https://doi.org/10.1180/claymin.2009.044.4.435

Tay, J.Y.S., Kok, B.W.T., Liew, C.V., Heng, P.W.S., 2019. Effects of Particle Surface Roughness on In-Die Flow and Tableting Behavior of Lactose. J. Pharm. Sci. 108, 3011–3019. https://doi.org/10.1016/j.xphs.2019.04.028

Thornton, A., Weinhart, T., Luding, S., Bokhove, O., 2012. MODELING OF PARTICLE SIZE SEGREGATION: CALIBRATION USING THE DISCRETE PARTICLE METHOD. Int. J. Mod. Phys. C 23, 1240014. https://doi.org/10.1142/S0129183112400141

Traoré, D., 2005. Serpentinisation hydrothermale et altération latéritique des roches ultrabasiques en milieu tropical : évolution géochimique et minéralogique de la minéralisation en platine de la rivière des Pirogues (Nouvelle-Calédonie). Université de la Nouvelle-Calédonie.

Tsuji, Y., Tanaka, T., Ishida, T., 1992. Lagrangian numerical simulation of plug flow of cohesionless particles in a horizontal pipe. Powder Technol. 71, 239–250. https://doi.org/10.1016/0032-5910(92)88030-L

Tuck, C., Virta, R., 2015. Minerals yearbook: Iron ore.

Udo, M., Esezobor, D., Apeh, F., Afolalu, A., 2018. Factors Affecting Ballability of Mixture Iron Ore Concentrates and Iron Oxide Bearing Wastes in Metallurgical Processing. J. Ecol. Eng. 19, 235–242. https://doi.org/10.12911/22998993/86158

U.S. Geological Survey, 2020. Mineral Commodity Summaries. U.S. Geological Survey.

Veyera, G.E., 1994. Veyera, G. E. (1994). Uniaxial stress-strain behavior of unsaturated soils at high strain rates (No. WL-TR-93-3523). WRIGHT LAB TYNDALL AFB FL.

Vodyanitskii, Y.N., 2009. Mineralogy and geochemistry of manganese: A review of publications. Eurasian Soil Sci. 42, 1170–1178. https://doi.org/10.1134/S1064229309100123

von Smoluchowski, M., 1903. Contribution to the theory of electro-osmosis and related phenomena. Bull Int Acad Sci Crac. 3, 184–199.

Wallmach, T., 2017. 2017_Wallmach_A QEMSCAN® BASED STUDY ON THREE PARTICLE SIZE FRACTIONS CONTAINING COPPER SULPHIDES AND GANGUE MINERALS.

Wang, S., Shen, L., Maggi, F., El-Zein, A., Nguyen, G.D., 2017. Uniaxial compressive behavior of partially saturated granular media under high strain rates. Int. J. Impact Eng. 102, 156–168. https://doi.org/10.1016/j.ijimpeng.2016.12.018

Webmineral, n.d. Montmorillonite mineral data. URL http://webmineral.com/data/Montmorillonite.shtml#.Xw61N0HgpEY (accessed 7.15.20a).

Webmineral, n.d. Kaolinite mineral data. URL http://webmineral.com/data/Kaolinite.shtml#.Xw70ckHgpEY (accessed 7.15.20b).

Wells, M.A., Ramanaidou, E.R., Verrall, M., Tessarolo, C., 2009. Mineralogy and crystal chemistry of “garnierites” in the Goro lateritic nickel deposit, New Caledonia. Eur. J. Mineral. 21, 467–483. https://doi.org/10.1127/0935-1221/2009/0021-1910

Wollborn, T., Schwed, M.F., Fritsching, U., 2017. Direct tensile tests on particulate agglomerates for the determination of tensile strength and interparticle bond forces. Adv. Powder Technol. 28, 2177–2185. https://doi.org/10.1016/j.apt.2017.05.024

World Health Organization (Ed.), 2000. Air quality guidelines for Europe, 2nd ed. ed, WHO regional publications. World Health Organization, Regional Office for Europe, Copenhagen.

Worldsteel, 2020. Steel data viewer. WorldSteelAssociation. URL https://www.worldsteel.org/steel-by-topic/statistics/steel-data-viewer/C_asu_cse/CHN/IND (accessed 6.5.20).

Wünsch, I., Finke, J., John, E., Juhnke, M., Kwade, A., 2019. A Mathematical Approach to Consider Solid Compressibility in the Compression of Pharmaceutical Powders. Pharmaceutics 11, 121. https://doi.org/10.3390/pharmaceutics11030121

Yang, L., Hu, J., Bai, K., 2016a. Capillary and van der Waals force between microparticles with different sizes in humid air. J. Adhes. Sci. Technol. 30, 566–578. https://doi.org/10.1080/01694243.2015.1111834

Yang, L., Hu, J., Bai, K., 2016b. Capillary and van der Waals force between microparticles with different sizes in humid air. J. Adhes. Sci. Technol. 30, 566–578. https://doi.org/10.1080/01694243.2015.1111834

Yariv, S., Cross, H., 1979. Colloid Geochemistry of Clay Minerals, in: Geochemistry of Colloid Systems. Springer Berlin Heidelberg, Berlin, Heidelberg, pp. 287–333. https://doi.org/10.1007/978-3-642-67041-1_8

Yuksel, A., Cullinan, M., 2016. Modeling of nanoparticle agglomeration and powder bed formation in microscale selective laser sintering systems. Addit. Manuf. 12, 204–215. https://doi.org/10.1016/j.addma.2016.07.002

Zabava, B.-S., Voicu, G., Dinca, M.-N., Ungureanu, N., Ferdes, M., 2018. Durability of pellets obtained from energy plants: review. Presented at the 17th International Scientific Conference Engineering for Rural Development. https://doi.org/10.22616/ERDev2018.17.N419

Zhu, D., Yu, W., Zhou, X., Pan, J., 2014. Strengthening pelletization of manganese ore fines containing high combined water by high pressure roll grinding and optimized temperature elevation system. J. Cent. South Univ. 21, 3485–3491. https://doi.org/10.1007/s11771-014-2326-4

Zhu, X., Zhu, Z., Lei, X., Yan, C., 2016. Defects in structure as the sources of the surface charges of kaolinite. Appl. Clay Sci. 124–125, 127–136. https://doi.org/10.1016/j.clay.2016.01.033

Appendices

Sample Description	Al (wt%)	Ba (wt%)	Ca (wt%)	Cu (wt%)	Fe (wt%)	K (wt%)	Mg (wt%)	Mn (wt%)	Na (wt%)	P (wt%)	Pb (wt%)	Si (wt%)	Sr (wt%)	Ti (wt%)	Zn (wt%)	LOI (wt%)	S (wt.%)	C (wt.%)	B (wt.%)	Cl (wt.%)
Gabon ore C	2.84	0.15	0.08	0.04	2.95	0.74	< d.l.	51.8	< d.l.	0.12	< d.l.	1.49	0.014	0.08	0.06	14.28	0.02	0.05	< d.l.	< d.l.
Gabon ore M	2.57	0.14	0.14	0.04	3.75	0.67	0.28	46.7	< d.l.	0.11	< d.l.	4.92	< d.l.	0.08	0.05	12.86	0.03	0.10		
Gabon ore F	6.66	0.21	0.19	0.06	8.16	1.01	0.15	36.2	0.12	0.15	< d.l.	3.69	0.019	0.25	0.06	15.63	0.04	0.10		
Asman ore C	0.19	0.27	4.56	< d.l.	8.93	< d.l.	0.85	46.8	< d.l.	0.02	< d.l.	2.86	0.092	0.01	< d.l.	7.51	0.09	1.38	0.07	< d.l.
Asman ore M	0.20	0.37	4.43	0.02	10.30	< d.l.	1.93	44.3	< d.l.	0.02	< d.l.	2.95	0.160	0.03	0.02	7.09	0.12	1.52		
Asman ore F	0.28	1.13	6.53	0.02	9.77	< d.l.	0.82	41.7	0.15	0.03	< d.l.	2.15	0.310	0.02	0.02	9.61	0.48	2.00		
Gloria ore C	0.15	0.12	9.06	< d.l.	4.84	< d.l.	2.01	40.8	< d.l.	0.01	< d.l.	2.72	0.010	< d.l.	< d.l.	14.38	0.05	3.83	0.04	< d.l.
Gloria ore M	0.19	0.08	9.47	< d.l.	5.97	< d.l.	2.31	37.7	< d.l.	0.01	< d.l.	3.01	0.018	0.01	< d.l.	15.55	0.04	4.32		
Gloria ore F	0.38	0.37	10.3	< d.l.	7.01	< d.l.	2.19	33.8	0.11	0.02	< d.l.	2.99	0.043	0.02	0.03	16.94	0.20	4.52		
Sinter C	3.70	0.23	0.16	0.05	4.40	0.66	0.14	56.1	< d.l.	0.11	< d.l.	3.48	0.015	0.32	0.06	-0.60	0.02	0.57		
Sinter M	3.58	0.24	0.19	0.05	5.51	0.59	0.13	54.7	< d.l.	0.10	< d.l.	3.78	0.013	0.13	0.08	-0.15	0.04	0.83		
Sinter F	3.72	0.24	0.33	0.05	4.18	0.49	0.11	57.3	0.10	0.12	< d.l.	2.81	0.017	0.13	0.06	-0.23	0.06	0.37		
Remelt C	3.30	0.32	6.03	0.02	6.35	0.31	1.48	48.8	0.14	0.06	< d.l.	6.32	0.090	0.11	< d.l.	-7.93	0.25	7.31		
Remelt M	3.16	0.32	5.59	0.02	5.89	0.23	5.89	41.9	0.11	0.05	< d.l.	8.11	0.090	0.11	< d.l.	-8.20	0.21	3.36		
Remelt C	3.81	0.53	7.26	0.02	5.62	0.34	2.97	38	0.23	0.05	< d.l.	7.12	0.153	0.16	0.04	1.01	0.23	3.97	0.04	0.07
Spill mix C	0.31	< d.l.	0.47	0.06	13.90	0.06	3.52	68.6	< d.l.	0.13	< d.l.	1.33	< d.l.	0.03	< d.l.	-25.83	0.04	3.21		
Spill mix M	0.30	< d.l.	0.27	0.02	8.18	0.06	20.70	22.3	< d.l.	0.04	< d.l.	13.20	< d.l.	0.02	0.02	-5.81	0.02	1.24		
Spill mix F	1.11	0.08	1.65	0.03	8.56	0.12	10.80	34.9	0.11	0.06	< d.l.	6.31	0.023	0.04	0.14	2.92	0.07	2.44	< d.l.	< d.l.
Hood dust	2.04	0.16	1.58	0.03	2.94	6.59	1.28	29.4	1.44	0.06	< d.l.	3.00	0.030	0.07	2.88	22.01	0.98	10.80	0.09	1.56
Sludge	0.80	0.07	1.17	0.02	1.56	1.26	1.10	34.1	0.86	0.05	< d.l.	1.20	0.020	0.03	2.73	35.40	0.32	12.70	0.03	< d.l.
Tapping dust	0.76	< d.l.	0.20	< d.l.	1.17	2.17	1.03	55.3	0.23	< d.l.	< d.l.	3.42	< d.l.	0.04	2.23	3.90	1.14	1.62	0.03	0.33
Cooler dust C	< d.l.	< d.l.	0.02	0.05	12.40	< d.l.	1.60	71.1	< d.l.	0.12	< d.l.	1.03	< d.l.	0.01	0.02	-22.67	0.02	1.54		
Cooler dust M	< d.l.	< d.l.	0.03	0.02	6.88	< d.l.	0.53	66.8	< d.l.	0.06	< d.l.	0.35	< d.l.	< d.l.	0.05	-3.98	0.02	0.26		
MOR Dust	< d.l.	< d.l.	< d.l.	0.01	2.06	< d.l.	0.10	70.3	< d.l.	0.02	< d.l.	< d.l.	< d.l.	< d.l.	0.15	-0.06	< d.l.	0.02	< d.l.	< d.l.
Metal crushing	0.16	< d.l.	0.11	0.05	12.40	< d.l.	4.25	67.8	< d.l.	0.12	< d.l.	3.25	< d.l.	< d.l.	< d.l.	-26.06	0.02	1.57	< d.l.	< d.l.
Detection limite (d.l)	0.11	0.04	0.02	0.01	0.04	0.06	0.06	0.02	0.07	0.01	0.28	0.14	0.009	0.01	0.01		0.01	0.01	50 ppb	0.05
Uncertainty (+/-)	0.01	0.01	0.005	0.005	0.005	0.01	0.01	0.005	0.01	0.01	0.01	0.01	0.0005	0.005	0.005	0.05	0.01	5% (re	5 ppb	0.005

Appendix 1. Bulk chemistry of the different fractions of the different samples.

ref ddb	Phase	formula	Gabon ore			Sinter			Asman ore			Gloria ore			Remelt			Spill mix			Hood	tapping	Sludge	MOR	cooler		metal
			C	M	F	C	M	F	C	M	F	C	M	F	C	M	F	C	M	F	F	F	F	F	F	M	F
96-901-1109	Manganese-alpha	Mn58.00																+							+	+	+
96-101-0990	Manganosite	MnO				+	+	+							+	+	+	+	+	+	+	+		+	+	+	
96-900-9082	Pyrolusite	Mn2.00 O4.00	+	+	+																						
96-900-2354	Brucite	Mg1.00 O2.00																									+
96-900-7648	Cryptomelane	K1.30 Na0.22 Sr0.16 Mn7.52 Fe0.32 Al0.16 O16.00	+	+																							
96-900-1964	hausmannite	Mn3O4				+	+	+	+	+	+	+	+	+	+	+	+	+		+	+	+		+	+	+	+
96-900-0877	Galaxite	Mn7.12 Al16.88 O32.00				+	+	+							+	+	+										
96-901-2447	Hercynite	Al8.00 Fe16.00 O32.00				+	+	+																			
96-900-5294	Jacobsite	Mg3.80 Mn3.57 Fe16.54 Zn0.05 Ti0.02 O32.00																									
96-900-7024	Gahnite	Zn8.00 Al16.00 O32.00																					t				
96-900-7523	Bixbyite	Fe20.16 Mn11.84 O48.00							+	+	+																
96-900-9783	Hematite	Fe12.00 O18.00							+	+	+																
96-900-6543	Braunite	Mn56.00 Si8.00 O96.00							+	+	+	+	+	+													
96-900-0789	Tephroite	Mn7.32 Mg0.68 Si4.00 O16.00				+	+	+																			
96-900-0639	Glaucochroite	Mn3.48 Mg0.40 Zn0.20 Ca3.92 Si4.00 O16.00													+	+	+										
96-900-7378	Forsterite	Mg8.00 Si4.00 O16.00													+	+	+		+	+						+	+
96-900-4118	Enstatite	Si16.00 Mg16.00 O48.00																									
96-101-0145	Quartz	SiO2	+	+	+	+	+	+							+	+	+					+	+				
96-101-1046	Kaolinite 2M	Al8.00 Si8.00 O36.00 H0.00			+				+	+	+	+	+	+													
96-900-9666	Illite	K4.00 Al16.00 Si8.00 O48.00			+																						
96-900-9775	Manganite	Mn4.00 O8.00 H4.00							+	+	+																
96-900-1591	Lithiophorite	Mn3.00 Al1.95 Li0.99 O12.00 H6.00	+	+	+																						
96-100-8767	Goethite	Fe4.00 O8.00 H2.00	+	+	+																						
96-120-0017	Gibbsite	Al8.00 O24.00 H24.00			+																						
96-901-2231	Graphite	C																	+			+		+			
96-900-0098	Rhodochrosite	Mn6.00 C6.00 O18.00																					+				
96-900-0967	Calcite	Ca6.00 C6.00 O18.00							+	+	+	+	+	+		+	+			+	+						
96-900-0100	Smithsonite	Zn6.00 C6.00 O18.00																					+				
96-900-1048	Kutnohorite	Ca3.06 Mn2.94 C6.00 O18.00							+	+	+	+	+	+							+		+				
96-900-3524	Dolomite	Ca3.00 Mg3.00 C6.00 O18.00							+	+	+			+	+		+	+									
96-900-3126	Sylvite	K4.00 Cl4.00																			+	+	+				
96-901-0368	Berlinite	Al3.00 P3.00 O12.00																					+				

Appendix 2. XRD results for the different fractions of the different samples.

Sieve	Gabon	Sinter	Asman	Gloria	Spillmix	Remelt
Moisture (Thermobalance) (wt%)(+/- 0.01%)	10.53	0.60	0.29		4.32	2.60
>1mm	1957.0	2013.5	1368.0	2669.4	2453.2	2578.1
1mm - 500µm	35.5	6.4	7.0	8.9	377.6	137.0
500-250µm	33.8	3.6	5.4	9.0	260.6	90.0
250-100µm	39.2	9.6	6.4	10.9	73.8	60.4
<100µm	210.8	70.0	8.8	7.6	104.7	107.8
Total	**2276.3**	**2103.1**	**1395.6**	**2705.8**	**3269.9**	**2973.3**

Appendix 3. Sieving results, for the Gabon ore, sinter, Asman ore, Gloria ore, Spillmix and Remelt samples used for the characterization of the ferromanganese byproducts.

	pH	Zeta Potential (mV)	Mobility (µ/s)/(V/cm)
Gabon ore	4.22	-2.87	-0.22
Gabon ore	3.98	4.15	0.32
Gabon ore	3.98	6.61	0.52
Gabon ore	3.10	26.87	2.10
Gabon ore	4.80	-20.57	-1.61
Gabon ore	4.80	-16.59	-1.30
Sludge	1.32	-0.79	-0.06
Sludge	2.00	2.23	0.17
Sludge	2.20	-1.63	-0.13
Sludge	2.41	-9.49	-0.74
Sludge	2.65	-4.22	-0.33
Sludge	2.95	-11.61	-0.91
Sludge	3.20	-9.28	-0.73
Sludge	4.68	-15.21	-1.19
Sludge	3.70	-17.60	-1.37
Sludge	5.20	-17.35	-1.36
MOR	2.98	-18.25	-1.43
MOR	2.13	-3.99	-0.31
MOR	2.56	-10.55	-0.82
MOR	3.85	-22.24	-1.74
MOR	3.09	2.71	0.21
MOR	4.72	-3.30	-0.26
Metal dust	2.13	-0.23	-0.02
Metal dust	2.51	-0.05	0.00
Metal dust	2.74	-5.64	-0.44
Metal dust	2.97	-11.62	-0.91
Metal dust	2.97	-11.62	-0.91
Metal dust	6.17	-23.40	-1.83

Appendix 4. Zeta potential measurement at various pH values, for the Gabon ore, sludge, MOR and metal dusts sampled at the Eramet Norway Sauda ferromanganese production plant.

Sample Description	Fe (wt.%)	Mn (wt.%)	Si (wt.%)	Al (wt.%)	K (wt.%)	Ca (wt.%)	Na (wt.%)	Mg (wt.%)	LOI (wt.%)	Ti (wt.%)	Zn (wt.%)	Ba (wt.%)	P (wt.%)
Bento	1.21	0.08	32.3	7.25	0.53	1.24	1.94	1.6	6.67				0.012
Kao	0.61	<0.02	23.5	17.9	2.25	<0.08	<0.11	0.18	10.86				0.029
Pyro	2.47	52.9	0.82	2.56	0.69	<0.08	<0.11	<0.06	13.46	0.07	0.06	0.3	0.092
Hs	2.06	70.3	<0.14	<0.11	<0.06	<0.02	<0.07	0.1	-0.06	<0.01	0.15	<0.1	0.02

Appendix 5. XRF analysis of the bentonite, kaolinite, pyrolusite concentrate and hausmannite samples, including traces (Ti, Zn, Ba, P).

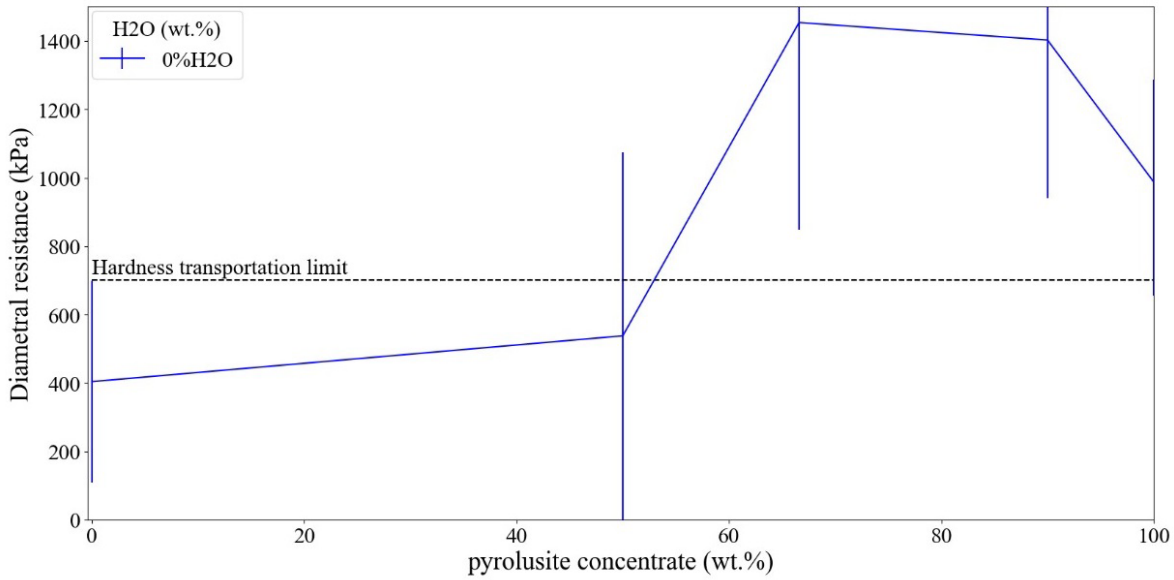

Appendix 6. Rd versus the pyrolusite concentrate content in the blend, at 0 wt.% H_2O

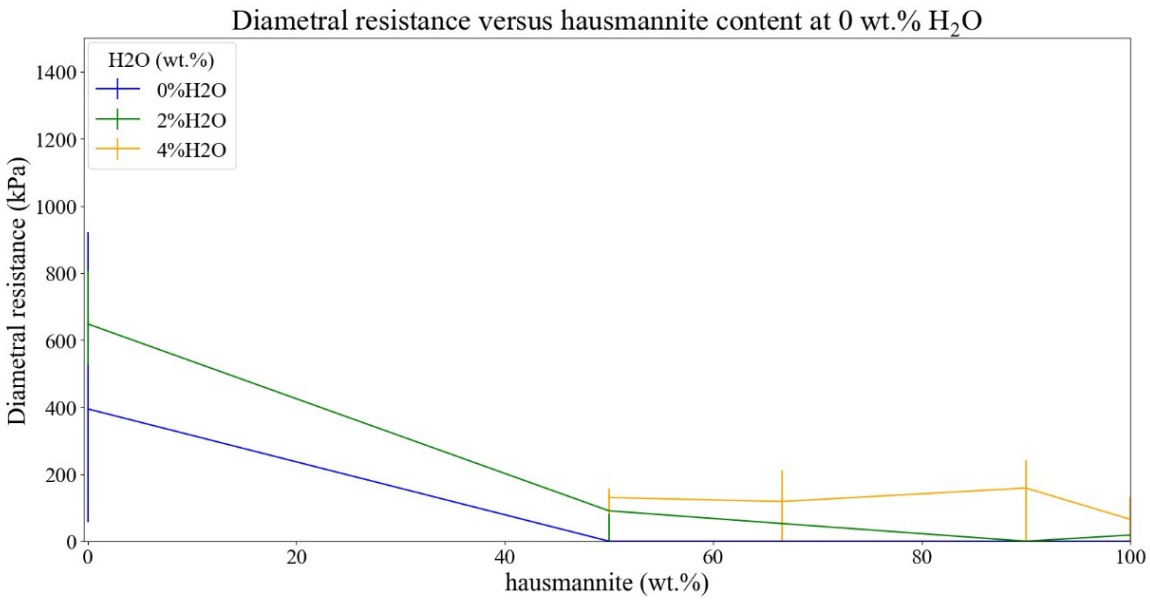

Appendix 7. Rd versus the hausmannite content in the blend, at 0, 2 and 4 wt.% H_2O

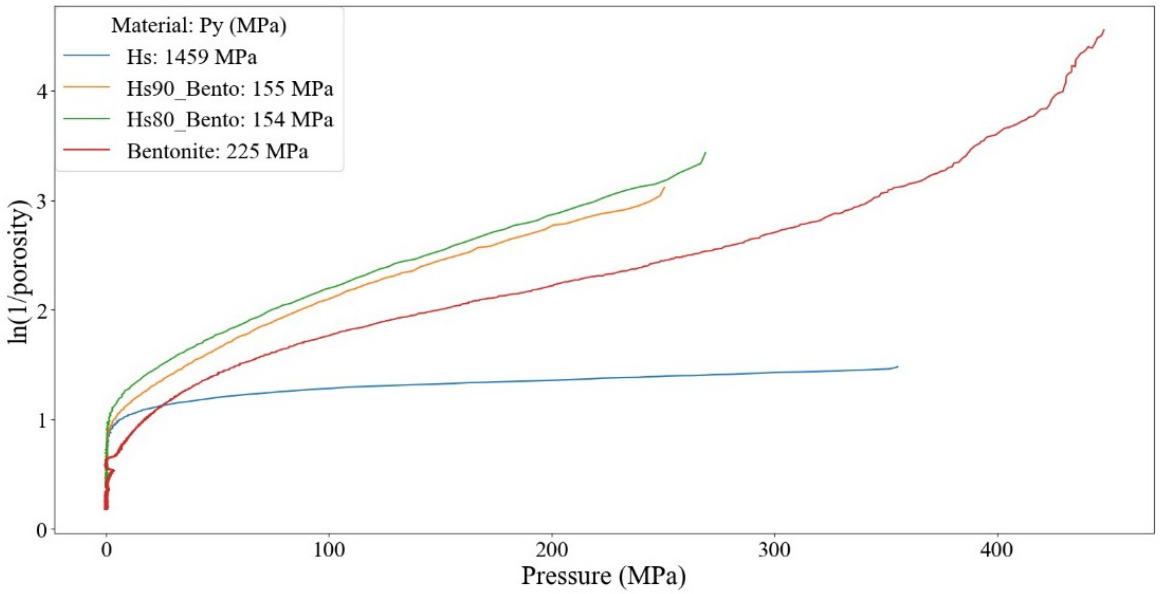

Appendix 8. Heckel curves for different hausmannite-bentonite mixes at 2 wt.% H_2O

Sample	Convexity	Sphericity	Aspect ratio
Bentonite	0.68	0.59	0.69
Kaolinite	0.63	0.48	0.66
Enriched ore	0.84	0.82	0.69
Hausmannite	0.7856	0.76	*0.71*

Appendix 9. Morphological parameters measured by QICPIC for the bentonite, kaolinite, hausmannite and pyrolusite samples used for the agglomeration tests.

pH	Bentonite	Kaolinite	Hausmannite	Pyrolusite
2.2	-35.17	-13.52		
2.39	-34.8			
2.44	-36.8			
2.5		-24.57		
2.6			5.57	
2.85	-34.27			
2.88		-31.13		
3.19			-9.05	
3.22			-9.05	
3.33			-11.64	
3.46			-24	
3.47	-35.54			
3.56				17.12
3.78		-42.09		
3.88				3.04
3.88				5.42
4.16				-1.7
4.33				-4.14
4.45	-39.36			
4.73				-14.7
4.8			-30.3	
5.03				-18.29
5.57			-27.71	
5.65	-37.21			
5.97	-36.99			
6.01			-31.62	
6.17	-37.1			
6.76				-35.57
7.07		-49.45		
7.17			-36.98	
9.09				-46.22
9.28	-41.92			
9.31	-38.02			
9.51			-38.25	
9.76				-48.95
9.79		-50.8		
10.15		-50.77		
10.75				-45.44
11.11			-38.08	

Appendix 10. Zeta potential measurement at various pH values, for the bentonite, kaolinite, hausmannite and pyrolusite samples used for the agglomeration tests.

Appendix 11. Proceedings published for the IMPC 2018 in Moscow (see below).

PHYSICO-CHEMICAL CHARACTERISATION OF INDUSTRIAL MANGANESE DUSTS AND SLUDGES AND ITS IMPLICATION FOR AGGLOMERATION: FROM ORE TO METAL

J.L. Dubos[1/2,*], B. Orberger[1/3], J.M. Milazzo[1], S. B. Blancher[1], J. Lützenkirchen[4]

1. *Eramet Research, 1 Avenue Albert Einstein, 78190 Trappes-en-Yvelines, France.*
2. *GEOPS, Université Paris Sud-Université Paris Saclay, Bât 504, 91405 Orsay, France*
3. *Catura Geoprojects, 2 rue Marie Davy, 75014 Paris, France*
4. *INE, Karlsruhe Institute of Technology, 76344 Eggenstein-Leopoldshafen, Germany*

*(*corresponding author: john-lee.dubos@eraметgroup.com)*

ABSTRACT

Industrial dusts are commonly agglomerated using empirical recipes with binders such as bentonite, while sludges are used into mixes. Those materials contaminate the products, are expensive and generate significant amounts of slag. Achieving cold dust agglomeration with little or no binder requires understanding the controlling parameters in order to predict and optimize the process behavior. This in turn necessitates a comprehensive dust characterization to base those predictions on measurable characteristics. Hence we collected 13 Mn-rich dusts over all the process chain: ore fines, smelting, tapping and refining dusts, as well as ferromanganese alloy powder. Those samples were analyzed for their chemical, physical and mineralogical characteristics.

The X-Ray Diffraction and Qemscan® analyses show that the mineralogy of the primary ore dusts are the most complex, showing various hydroxides, oxides, carbonates, tectosilicates and phyllosilicates. The furnace dusts contain oxides, tectosilicates and carbonates with number of volatiles, while the refining dusts present only few oxides and metal. Finally, the metal dust is near pure metal. We can observe a chemical and mineralogical simplification across the process chain. This simplification is accompanied by morphological changes: particles shapes and PSD vary from jagged, irregular particles with broad PSD (>1 mm to <0.3 µm) to smooth and spherical with very narrow PSD (100 µm to <0.3 µm). The metal dust is an exception, due to its crushed nature. The Cationic Exchange Capacities (CECs) of the samples range from 0 to 22 meq/100g. Specific surface areas (SSA) range <0.1 to 27m²/g, and seem to decrease with mineral simplification. This may be due to the disappearance of hydrated and/or sheet-bearing minerals, since a smaller grain size should mean an increased of SSA. Zeta potential varies strongly over the range of the samples tested. However, besides Gabon that has a Point of Zero Charge (PZC) ~ 4.1, the other samples' PZC is between 2 and 2.5.

From previous studies, feed material dusts, with intrinsic properties close to that of binders, agglomerate better than process dusts. It may hence be interesting to use the process dusts as additives mixed into the feed.

KEYWORDS

Cold agglomeration, dust, sludge, metallurgy, ferromanganese, characterization, mineralogy.

INTRODUCTION

Dusts, here defined as particles below 3 mm, and sludges, suspended material composed of fine particles, are the most important non-recyclable wastes of the mining and pyrometallurgical industries. For example, the Mn-waste production over all the treatment process of the ERAMET Norway production plant amounts to 20 kt/y of dried sludge and 15 kt/y of dust. This excludes dust produced during mining, beneficiation and handling of ore fines (B. Ravary, personal communication). These materials, classified as hazardous, can be considered as secondary raw material due to their significant Mn content. E.g. MOR fumes contains up to 70 % of Mn, which is about 20 % more than the metal content in the primary Mn-laterite ore. Each company hence recycles its own waste. However, the introduction of loose dust and water bearing sludges into furnaces will decrease the gas permeability in the burden and hinder processes. Hence, agglomeration needed. Good agglomeration produces a material with (i) sufficient mechanical strength to be handled without generating new dust, and (ii) a chemical and mineralogical composition providing good reducibility (iii) do not deteriorate gas permeability. Today, each company agglomerates its own dust and sludges based on empirical experiments (e.g. (Pietsch, 2002).

Agglomeration theory has been deeply studied in pharmacology (Herting and Kleinebudde, 2008a; Johansen and Schæfer, 2001), food (Rondet et al., 2016) and material industries (Kotzé, 2002; Wollborn et al., 2017). Most of those studies performed on cold agglomeration used homogeneous materials, while complex materials were studied using high temperature agglomeration. Industrial dusts and sludge are complex materials, but would necessitate cold binderless agglomeration. They are systematically investigated for their chemical composition and particle size, and to a lesser degree for qualitative mineralogy (Herting and Kleinebudde, 2008a). Particle size is determined through laser granulometry (Debrincat et al., 2008; Shimizu et al., 2016). Physical parameters (Cation Exchange Capacity (CEC), specific surface area (SSA, using the Brunauer-Emmet-Taylor (BET) method) and the zeta potential are rarely investigated (Johansen and Schæfer, 2001).

This paper presents for the first time results on dust and sludge sampled along the process chain for ferromanganese pyrometallurgical processes, including dusts from the primary raw material. We investigated in total 13 samples representative of those wastes. Systematic mineralogical, chemical, physico-chemical and textural analyses were performed. Our final objective is to evaluate the key-parameters to design an appropriate agglomeration process.

MATERIALS AND METHODS

Thirteen samples were studied from the Manganese pyrometallurgical plant of ERAMET in Norway (Sauda; Figure 1). Six samples represent the feed material: (i) lateritic oxide ore and its sintered, reduced product from Moanda (Gabon, 1, 6 in Fig. 1), (ii) raw mixed carbonate-oxide ore from Gloria and Asman (both from South Africa; 2, 3 in Fig. 1), (iii) Recycled MOR slag and onsite material spilled during handling (Respectively Remelt, 4 and Spill mix+Metal, 5 in fig. 1). The raw materials are named hereafter: GO (Gabon ore), AO (Asman ore) and GlO (Gloria ore). Those materials are converted into Mn alloy in the furnaces. More samples come from: (i) the environmental

hood (located above the furnaces hall, 7, Fig. 1), (ii) the dust generated during metal tapping (8), (iii) the sludge produced in the water treatment plant, which processes dust collected in the Venturi filters (9). Samples 7, 8 and 9 are referred to as furnace dusts hereafter. MOR low density ultrafines (<100 µm) do not contain metal droplets (10). However, two types of cooler dusts (medium density ultrafines, <100 µm, and high density medium sized fines, 100-500 µm contain metal droplets (11, 12). Samples 10, 11 and 12 are hereafter referred to as refining dusts. The last sample is ferromanganese dust, generated during the crushing of the alloy. Besides MOR and the cooler dusts, sampled from big bags, all other samples were taken inline.

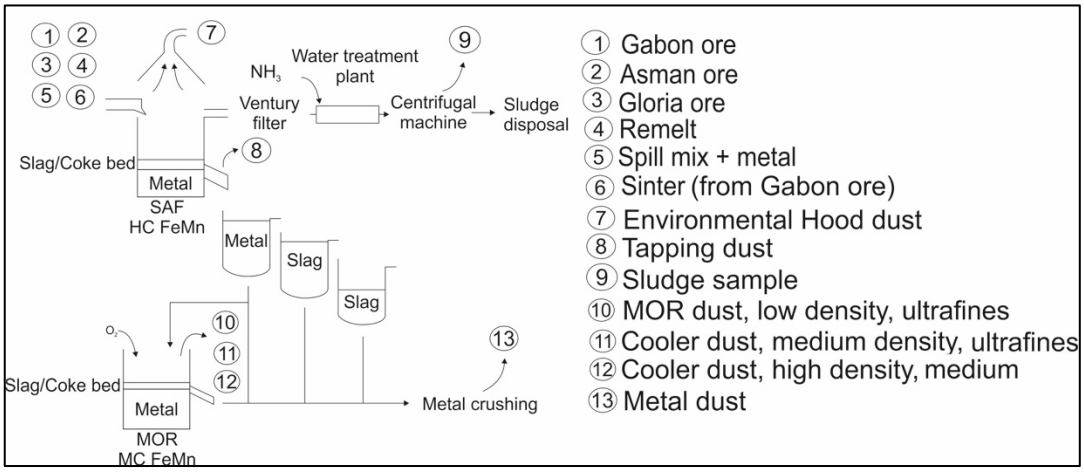

Figure 1: Sampling location across the treatment process of Sauda ferromanganese production plant.

Upon reception, all the samples were wet sieved to separate the fractions >1 mm, 1-0.1 mm, and <100 µm. Chemical and mineralogical analyses were performed at ERAMET Research, France. Each of the samples and their different size fractions were analyzed for bulk chemistry through X-Ray Fluorescence (XRF; equipped with a Co-anode), combustion for C and S, and Loss On Ignition (LOI) for the moisture content. LOI has both positive (loss of volatiles) and negative (gain of weight due to reoxidation of reduced/metal phases) values. Cl was determined by chromatography (881 Compact IC Pro. Colonne anionique Metrosep A Sup3- 250/4.6 from Metrohm and B with ICP-OES (720 from Agilent). Mineralogical analyses were performed using X-Ray Diffraction (XRD, PANalytical X'PERT PRO, with a Cu-anode, measuring time of 1 h). Polished sections of 26 samples (all particle fractions) were carbon-coated and analyzed by QEMSCAN® (FEI Quanta 650F SEM, 2 Brucker Xflash 30 mm silicon drift EDX detectors, at 25kV and 10 nA, average couting time 5h**).** Wet laser granulometry was used on all sample fractions < 100 µm (Cilas 1064L) but the Gloria and Asman ores.

The fractions <100 µm (except cooler dust, similar to MOR) were analyzed at the laboratory Étude Recherches Matériaux (ERM, Poitiers) for: (i) SSA using BET method (TRISTAR II 3020 from Micromeritics®), (ii) CEC (according to the NF X31-130 (1999) norm).

Zeta potential measurements (Nanobrook 9000plus PALS with green laser) were performed at the Karlsruhe Institute of Technology (KIT, Germany). The analyzed samples included the fraction <100 µm of Gabon ore, sinter, tapping dust, sludge, MOR dust, metallic dust samples. The material was suspended in milliQ water, and the part of the suspension that was not settling was extracted to proceed for measurements.

RESULTS

Chemistry

Feed material

The Gabon ore shows the highest Mn content (around 50 wt.%) for primary ore. Mn varies strongly from 51.8 wt.% in the fraction > 1mm, to 36.2 wt.% in the fraction <100 µm. Iron increases from 3 wt.% (> 1 mm) to 8.2 wt.% (< 100µm). The Al (2.8 to 6.7 wt.%) and K (0.7 to 1 wt.%) contents are highest in the fraction < 100 µm. The Si content does not seem to be controlled by the grain size (based on three analyses): 1.5 wt.% for > 1 mm, 5 wt.% for 1 mm-100 µm, and 3.7 wt.% for < 100 µm. The LOI is related to hydrous phases. Combining the observations on Al, Si, K and LOI, the fraction < 100 µm is the one richest in clay minerals (Al+Si = 10.4 wt.%). The P content is high and stable at about 0.1 wt.%. Sulphur and Carbon are low at 0.03 and 0.1 wt.%.

The AO and GlO are poorer in Mn than the GO, and it decreases gradually with grain size (from 47 wt.% to 42 wt.% and 41 wt.% to 34 wt.%, respectively). In the AO, Fe is constant ~ 10 wt.%, while in GlO Fe increases (from 5 to 7 wt.%.) with Mn decrease. The Al content in the AO and the GlO is about a factor 10 lower than in the GO (~ 0.3 wt.%), while Si is similar but stable (~ 3 wt.%). Potassium is below the detection. However, their content in Ca, Mg and total C are high (Ca: 5 wt.%; Mg: 1.2 wt.%; C: 1.8 wt.% for AO; Ca: 9 wt.%; Mg: 2.2 wt.%; C: 4.3 wt.% for GlO). Ca is highest in the smallest fraction, Mg in the intermediate fraction. The LOI ranges from 7 to 9.5 wt.% in AO and 14 to 17 wt.% in GlO and is highest in the fraction < 100 µm. We can assume that a third is related to carbonates, and the remainder to clays and hydroxides. In the AO and GlO, for the fraction <100 µm: (i) S reaches respectively 0.5 wt.% and 0.2 wt.%, (ii) Sr increases to ~0.4 wt.%. The B- content is 0.07 and 0.04 wt.%, respectively.

The sinter material show very little chemical variation over the different fractions. All metals increase (averages: Al: 3.5 wt.%; K: 0.6 wt.%; Mg: 0.1 wt.%; Ca: 0.2 wt.%) due to the elimination of volatiles. The Mn content is the highest average of the feed material (56 wt. %). The Fe content is intermediate to the values of GO, with an average value of 4.3 wt.%, and a maximum at 5.5 wt.% for the medium fraction. The LOI is close to 0 wt.%.

In the Remelt sample, the chemistry is homogeneous for Al (3.3 wt.%) and K (0.3 wt.%). The obvious elements affected by the grain size reduction are: Fe, decreasing from 6.4 to 5.6 wt.%, Mn, decreasing from 49 to 38 wt.%, and the LOI, increasing from -7.9 to 1 wt.%. The Ca contents are around 5.8 wt.%, with maximum 7.3 wt.% for the smallest fraction. The Mg and Si reach their maximum values for the medium fraction (5.9 and 8.1 wt.% respectively). The C content is around 3.6 wt.%, but reaches 7.3 wt.% in the fraction > 1 mm; the S content is constant at 0.2wt.%.

In the Spill mix sample; the Fe and Mn contents are as high as 14 wt.% and 69 wt.% in the fraction > 1mm, while only averaging at 8.4 wt.% and around 28 wt.% for the other grain sizes. Al and Ca are highest in the fraction < 100 µm (1.11 wt.% and 1.65 wt.% respectively). The Mg, Si and C amounts do not show any pattern: 3.52, 1.3 and 3.2 wt.% (>1 mm); 20.7, 13 and 3.2 wt.% (1 mm-100 µm); 10.8, 6.3 and 2.4 wt.% (<100 µm), respectively. The S and B contents are below detection limit, the P content is around 0.1 wt.%. Only the LOI is controlled by the grain size, going from -25.8 (> 1 mm) to 2.9 wt.% (< 100 µm).

Process dust

Hood, tapping and sludge dust, coming from the ferromanganese furnace, have a similar chemistry. The same is true for the MOR and the two cooler dusts, which come from the refining step of the alloy. The furnace dusts are rich in Zn (2.2 to 2.9 wt.%), K (1.3 to 6.6 wt.%), Si (1.2 to 3.4 wt.%), B (0.03 to 0.09 wt.%) and S (0.3 to 1.1 wt.%). They are also higher in Al (0.8 to 2 wt.%), Ca (0.2 to 1.6 wt.%), Mg (1 to 1.3 wt.%) and Cl (0.3 to 1.6 wt.%) than the refining dusts. The hood dust and sludge have the highest LOI (22.0 and 35.4 wt.%) and C content (about 12 wt.%), but the lowest Mn content (29 and 35 wt.% respectively). On the other hand, the tapping dust has only 3.9 wt.% LOI for 55 wt.% Mn.

For the refining samples, the Mn content is high (67 to 71 wt.%). The Fe (2 to 12 wt.%), Mg (0.1 to 1.6 wt.%), P (0.02 to 0.12 wt.%), Si (0 to 1 wt.%), C (0.02 to 1.50 wt.%) and S (0 to 0.02 wt.%) content increase with density from MOR to coarse cooler dust. Conversely, the Zn content and LOI decrease with density: 0.15 wt.% to 0.02 wt.%. and -0.1 to -22.7 wt.%, respectively.

The crushed metal contains 68 wt.% of Mn, and 12.4 wt.% of Fe. The Al and Si contents are 0.2 wt.% and 3.3 wt.% respectively. Ca is lower than Mg (0.11 and 4.25 wt.% respectively). The C content is 1.6 wt.%. Potassium is still significant (0.12 wt.%) while S is close to the detection limit. (0.02 wt.%). The LOI is about -26 wt.%, which is the most negative value among all samples.

Mineralogy

Feed material

In GO, the main Mn carriers (in all fractions) are pyrolusite (MnO_2), lithiophorite ($AlMn^{4+}O_2(OH)_2$) and cryptomelane ($K(Mn^{4+},Mn^{2+})_8O_{16}$). This last mineral is not found in the fraction < 100 µm. Goethite($FeO(OH)$) and quartz (SiO_2) are present in all three size fractions, whereas gibbsite ($Al(OH)_3$, illite ($K(Al,Mg,Fe^{2+})_2(Si,Al)_4O_{10}(OH)_2\ H_2O$) and kaolinite ($Al_2Si_2O_5(OH)_4$) are only present in the smallest fraction. In the Gabon sinter, the mineralogy is very homogeneous: all fractions contain manganosite (MnO), Mn-bearing spinels (solid solution between hausmannite (Mn_3O_4), galaxite ($Mn^{2+}Al_2O_4$) and hercynite ($Fe^{2+}Al_2O_4$)), tephroite ($Mn^{2+}SiO_4$) and quartz. In AO all fractions contain manganite (MnO(OH), hausmannite, braunite ($Mn^{2+}Mn^{3+}{}_6(SiO_4)O_8$) and kutnohorite ($CaMn^{2+}(CO_3)_2$, as well as calcite ($CaCO_3$), dolomite ($CaMg(CO_3)_2$), kaolinite and hematite (Fe_2O_3) in various amounts. In GO, a very similar mineralogy is observed as in the AO (hausmannite, braunite, kutnohorite, calcite and kaolinite). The smallest fraction also shows dolomite.

In the remelt sample, the main Mn carriers are glaucochroïte ($CaMn^{2+}SiO_4$), manganosite, and galaxite. Forsterite (Mg_2SiO_4) may be present. The sample also contains quartz. Carbon is related to calcite (1 mm-100 µm and <100 µm) and dolomite (>1 mm and <100 µm). In the spill mix sample, the main Mn carrier is manganosite. Both coarse and fine fractions also contain hausmannite, while the coarse sample additionally includes Mn metal. The C is

hosted in dolomite (>1 mm), graphite (1 mm-100 µm) and calcite (<100 µm). The fractions 1 mm-100 µm and <100 µm also show olivine ($(Mg,Fe)SiO_4$).

Process dusts

In the furnace dust, Hood and tapping dusts contain Manganosite and hausmannite as Mn-bearers. Sludges show rhodochrosite ($MnCO_3$) and kutnohorite, the last of which is shared with hood dusts. Sylvite (KCl) is common to all three samples. Other minerals are observed: (i) calcite in hood dust and (ii) quartz and graphite in tapping dust. In the refining dusts, mostly manganosite and hausmannite are present, with Mn metal appearing in the cooler dusts (both medium and coarse). The MOR dust shows graphite as an additional phase. The metal dust is mainly composed of metallic Mn, FeMn alloy?), but forsterite is also observed.

Particle Size Distribution

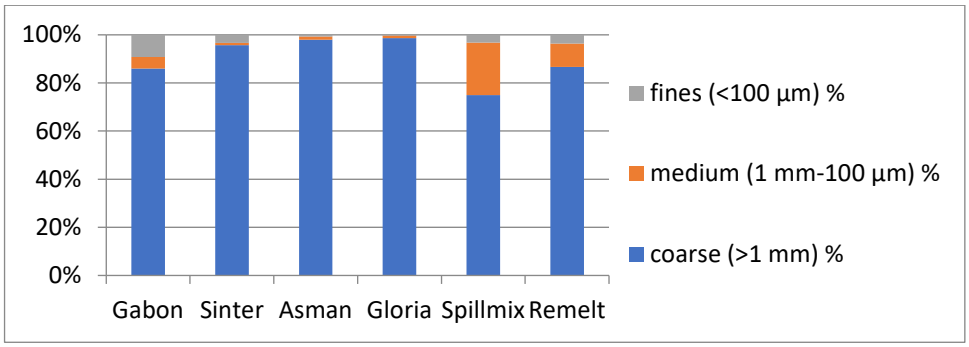

Figure 2 - Sieving of the feed materials. Wet sieving was performed to separate three fractions: material >1 mm, 1 mm-100 µm and <100 µm.

Upon reception, the material was wet screened to have a first understanding of the granulometry (see fig. 2). Laser granulometry has then been performed on the < 100 µm fraction on almost all samples (see chapter: material and methods). Two types of particle size distribution can be distinguished: (1) samples with a main population between 1 and 10 µm (GO, Sludges, Hood, Tapping, MOR and cooler fine dusts), and (2) main population between 10 and 100 µm (Sinter, Remelt, Spill mix, and metal dust).

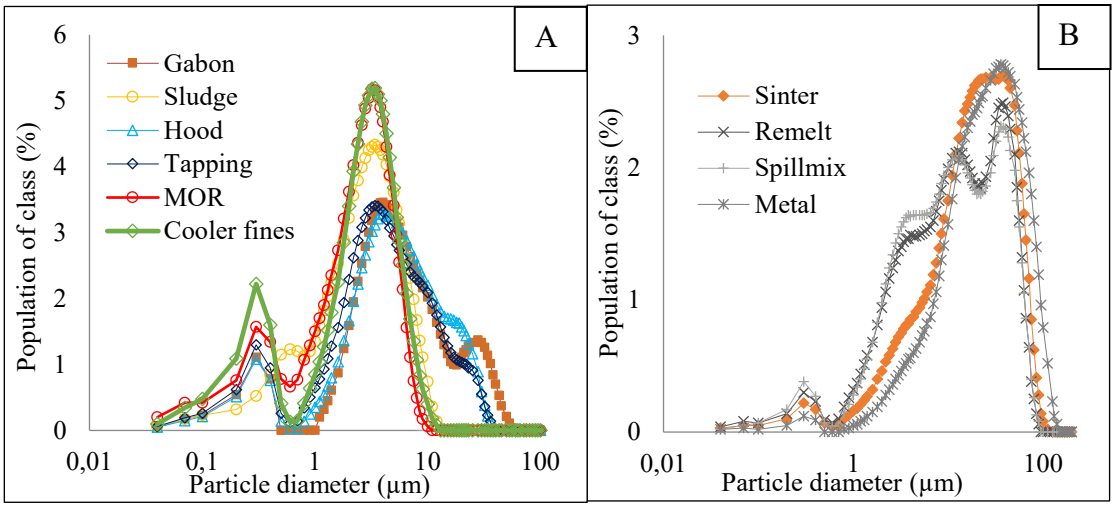

Figure 3 - Particle Size Distribution (PSD) of the measured samples. A) Samples with a main population between 1 and 10 µm. B) Samples with a main population between 10 and 100 µm.

In the first population, all samples show bimodal distribution (fig.3A). All dusts cumulate at 0.3 µm, except the sludges (0.6 µm). GO, tapping and hood dust show a population centered at 30, 22 and 18 µm, respectively. A peak can be seen at 18 µm for both Hood and Tapping dusts, and at 30 µm for GO. The second group of dust (fig. 3B), also has a population centered at 0.3 µm and a peak at 3.4 µm. For Remelt and Spill mix, and sinter and metal, the main population can be sub-divided: (i) at 13 and 20 µm respectively and (ii) 36 µm. The sinter and metal are more homogeneous, but still show two populations: (i) around 20 µm, and (ii) at 36 µm, like the Spill mix and remelt samples.

BET and CEC

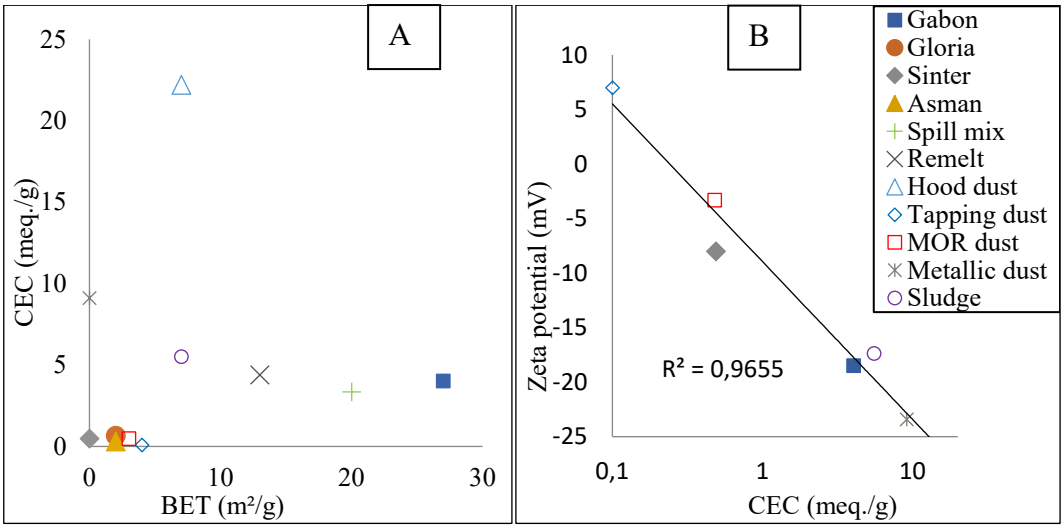

Figure 4 - Graphs presenting A) BET versus CEC. B) Zeta potential versus CEC. Significant relative variations can be observed, but it is hardly possible to relate them to a process evolution

The feed has a high variability: The GO shows the highest values (27 meq./g; see fig.4A). GO, AO and Sinter are very low (between 0 and 2 meq./g). Spill mix and Remelt, show intermediate BET (20 and 13 m²/g, respectively).

In the process dusts, the BET decreases with the distance from the feed (fig. 4A). The CEC values for the feed are positively correlated with the BET values (fig. 4A). However, in the process dusts CEC is not controlled by the BET. The hood dust has the highest value (22.2 meq./g). The metallic dust and the sludges have low CEC (respectively 9.11 and 5.52 meq./g) and BET. The values for MOR is low (0.48 meq./g respectively), the tapping dust is below the detection limit (<0.1 meq/g). Based on QEMScan analyses the feed material shows a broad PSD and grain morphologies varying from fibres to nanoparticles to rounded quartz and oxyhydroxides crust. However the processing dusts show narrower PSD and more rounded grain morphologies. Metal shows angular grain shapes.

.

Zeta Potential

The AO and GO did not generate enough fines, only values for GO are available. The GO has a value of -18.5 mV, while the Sinter has a -8 mV potential (fig. 4B). The tapping dust has a positive value of 7 mV when suspended in milliQ water. The two tests performed on MOR show values around 0 (-3.3 and 2.7 mV) potential. The Cooler dusts, metallic dusts and Sludges have widely negative values (fig. 4B). The values determined in milliQ water pertain to widely varying pH conductivity values among the samples, so that the observed linear relationship may not be significant (fig. 4B).

The Point of Zero Charge (PZC) was determined for four samples along the processing chain: GO fines, Sludges, MOR dusts and metallic dusts. The GO's zeta potential has a sharp evolution with the pH, from 27 mV at pH 3.1 to -21 mV at pH 4.8. The PZC is at ~pH 4.1. For the Sludges, the potential is -18 mV at pH ~4. It seems to increase in a straight line toward pH 2 where the potential is zero. Although the metal dust potential reaches 0 around the same values (~pH 2.5), its evolution is not as linear. The slope is steeper between pH 2.5 and 3 (0 to -12 mV) than for Sludges (around -7 to -11 mV). The MOR dust behavior is peculiar: the points pH 3.9/2.7 mV and pH 4.7/-3.3 mV, close to zero, are measured by simply suspending the sample in milliQ water. However, when acid or base is added, the values change drastically and align themselves on a curve that has a behavior close to that of metal and dusts. The PZC was not achieved, but it seems to be around pH 1.9-2, following the curve.

DISCUSSION

The major results on each dust type are summarized in Fig. 5. The composition of the feed (half Sinter and GO (high P, low B), half AO and GlO (low P, high B)) was made to fit the pyrometallurgical industry requirements. Its mineralogy, grain morphologies, PSD and chemistry, due to the different ore deposit types (e.g. Chetty and Gutzmer, 2012 for the GlO and AO, ; Pambo, 2004 for GO), are highly variable. The further into the process, the simpler those parameters become. Furnace dusts still contain volatiles, with carbonate and high water content in Sludges. Refining dusts have very simple chemistry and mineralogy, as does metal. Its silicates come from the casting bed, made of forsterite sand.

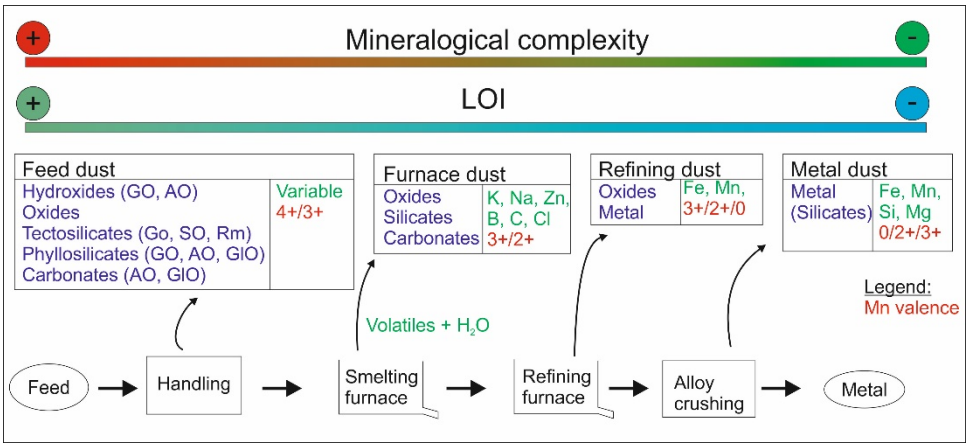

Figure 5 - Summary of the chemical and mineralogical characteristics of the different types of dusts, based on their location in the ferromanganese production process.

Eisele and Kawatra (2003), showed bentonite, mostly composed of montmorillonite (swelling clay), as a commercial binder. Agglomeration tests on Ni laterite ore dust bearing smectite (swelling clay) were successful without binder (Internal report, ERAMET Research, 2014). The Mn-ore feed contain no swelling clays, but phyllosilicates (illite, kaolinite) and hydroxides (goethite, manganite, gibbsite, and lithiophorite). These minerals have high adsorption potential, as do swelling clays and natural binders (bentonite). Granulometry on agglomeration was investigated by (Pietsch, 2002; Yang et al., 2016): They showed that broad PSD leads to better agglomeration results. Johansen and Schæfer (2001) worked on the effect of particle shape, showing that angular, jagged shapes improves agglomeration efficiency over rounder particles. This fits with the feed material, which has heterogeneously shaped particles with broad diameters range. The process dusts show spherical particle, with narrower size range: this is less suitable for agglomeration. The SSA, the area available for interaction between the materials, helps agglomeration (Pietsch, 2002). CEC is taken as a measurement of the interaction potential for negatively charged surfaces: a particle adsorbing elements may adhere to another particle. Zeta potential was measured to correlate: it is reasonable to think that the more negative a surface charge, the higher its potential to adsorb cations. The figure 4B shows a good correlation between both values for negative zeta potential: it seems physically reasonable. Conversely to the other parameters, the BET and CEC do not evolve linearly through the treatment process. The hood dust CEC value may be due to an interaction between sylvite and cobaltihexamine chloride used for the measurement.

CONCLUSIONS

Those different measurement show that the material simplification across the treatment process decreases agglomeration potential. Feed material seems to have intrinsic binder properties. Taking advantage of those, it may be sensible to proceed through additivation for the other materials: they could be mixed in small amount for their respective advantageous properties: Reductant content (carbonates in Sludges), Mn content (70 wt% in refining dusts) or shape factor (angularity of metal dusts). Their hindering properties for agglomeration would be diluted into the agglomeration potential of the feed material. A modelling of the different parameters having an impact during agglomeration would be needed, to evaluate the acceptable variability to keep achieving successful agglomeration.

ACKNOWLEDGEMENTS

We thank ERAMET Research, the GEOPS laboraty, the KIC, the EITRawMaterials and the ANRT for their logistic financial support. A. Salaün, S Lafon and Q. Jallet (ER) are thanked for their help handling the samples. We thank the staff of ENS (B. Ravary, E.-D. Fatnes, D.-O. Hjertenes and E.-V. Hansen) for their help during the sampling mission.

REFERENCES

Ahmed, H., 2014. Relationship Between Crystal Structure and Mechanical Properties in Cocrystals and Salts of Paracetamol. Luleå University of Technology, Luleå.

Al Mahrouqi, D., Vinogradov, J., Jackson, M.D., 2017. Zeta potential of artificial and natural calcite in aqueous solution. Adv. Colloid Interface Sci. 240, 60–76. https://doi.org/10.1016/j.cis.2016.12.006

Alkrad, J.A., Abu Shmeis, R., Alshwabkeh, I., Abazid, H., Mohammad, M.A., 2017. Investigation of the potential application of sodium bentonite as an excipient in formulation of sustained release tablets. Asian J. Pharm. Sci. 12, 259–265. https://doi.org/10.1016/j.ajps.2017.01.004

Antonyuk, S., Palis, S., Heinrich, S., 2011. Breakage behaviour of agglomerates and crystals by static loading and impact. Powder Technol. 206, 88–98. https://doi.org/10.1016/j.powtec.2010.02.025

Antonyuk, S., Tomas, J., Heinrich, S., Mörl, L., 2005. Breakage behaviour of spherical granulates by compression. Chem. Eng. Sci. 60, 4031–4044. https://doi.org/10.1016/j.ces.2005.02.038

Aschner, M., Aschner, J.L., 1991. Manganese neurotoxicity: cellular effects and blood-brain barrier transport. Neurosci. Biobehav. Rev. 15, 333–340. https://doi.org/10.1016/s0149-7634(05)80026-0

Awad, M.E., López-Galindo, A., Medarević, D., Đuriš, J., El-Rahmany, M.M., Ibrić, S., Viseras, C., 2019. Flow and Tableting Behaviors of Some Egyptian Kaolin Powders as Potential Pharmaceutical Excipients. Minerals 10, 23. https://doi.org/10.3390/min10010023

Bacher, C., Olsen, P.M., Bertelsen, P., Sonnergaard, J.M., 2008. Compressibility and compactibility of granules produced by wet and dry granulation. Int. J. Pharm. 358, 69–74. https://doi.org/10.1016/j.ijpharm.2008.02.013

Balakin, B.V., Shamsutdinova, G., Kosinski, P., 2015. Agglomeration of solid particles by liquid bridge flocculants: Pragmatic modelling. Chem. Eng. Sci. 122, 173–181. https://doi.org/10.1016/j.ces.2014.09.003

Banchet, J., Blaffart, F., 2018. GO 4 0 – Deliverable 0_0006 – 2018 Optimized Agglomerates for testing in pilot scale. Go-4-0 Project.

Behjani, M.A., Motlagh, Y.G., Bayly, A.E., Hassanpour, A., 2020. Assessment of blending performance of pharmaceutical powder mixtures in a continuous mixer using Discrete Element Method (DEM). Powder Technol. 366, 73–81. https://doi.org/10.1016/j.powtec.2019.10.102

Beloborodov, R., Pervukhina, M., Luzin, V., Delle Piane, C., Clennell, M.B., Zandi, S., Lebedev, M., 2016. Compaction of quartz-kaolinite mixtures: The influence of the pore fluid composition on the development of their microstructure and elastic anisotropy. Mar. Pet. Geol. 78, 426–438. https://doi.org/10.1016/j.marpetgeo.2016.09.030

Bizhanov, A., Kurunov, I., Podgorodetskyi, G., Dashevskyi, V., Pavlov, A., 2014. Extruded Briquettes – New Charge Component for the Manganese Ferroalloys Production. ISIJ Int. 54, 2206–2214. https://doi.org/10.2355/isijinternational.54.2206

Blancher, S.B., Laugier, O., 2014. Briquetage de minerai Weda Bay : Analyse Qemscan (No. 68.14.114). Eramet IDEAS.

Blancher, S.B., Laugier, O., Bouchet, A., 2015. Clay Mineral Characterization on Ni-Laterite: Qemscan Imaging of Alteration Processes, in: MINERAL RESOURCES IN A SUSTAINABLE WORLD. Presented at the 13th SGA Biennial Meeting 2015.

Bondouy, N., Milazzo, J.-M., 2016. COMPTE RENDU DE LA VISITE D'EUROTAB: RESULTATS DE FAISABILITE DE TABLETTE (No. 52.16.024). Eramet IDEAS.

Bouchet, A., Meunier, A., Sardini, P., 2000. Minéraux argileux: structure cristalline; identification par diffraction de rayons X = Clay minerals: crystal structure; X-ray diffraction identification, Bulletin des Centres de Recherches Exploration - Production Elf-Aquitaine : Mémoires. Elf EP Ed, Pau.

Brunauer, S., Emmett, P.H., Teller, E., 1938. Adsorption of Gases in Multimolecular Layers. J. Am. Chem. Soc. 60, 309–319. https://doi.org/10.1021/ja01269a023

By, Thomas, 2017. 2017_BY_Briquetting of Manganese Oxide Fines.pdf.

By, T., 2017. Briquetting of Manganese Oxide Fines. (Master thesis). Norwegian University of Science and Technology, Trondheim, Norway.

Caricchi, L., Burlini, L., Ulmer, P., Gerya, T., Vassalli, M., Papale, P., 2007. Non-Newtonian rheology of crystal-bearing magmas and implications for magma ascent dynamics. Earth Planet. Sci. Lett. 264, 402–419. https://doi.org/10.1016/j.epsl.2007.09.032

Chaim, R., 2017. Particle Surface Softening as Universal Behaviour during Flash Sintering of Oxide Nano-Powders. Materials 10, 179. https://doi.org/10.3390/ma10020179

Chamrova, R., 2010. Modelling and Measurement of Elastic Properties of Hydrating Cement Paste. ÉCOLE POLYTECHNIQUE FÉDÉRALE DE LAUSANNE, Suisse.

Charinpanitkul, T., Tanthapanichakoon, W., Kulvanich, P., Kim, K.-S., 2008. Granulation and tabletization of pharmaceutical lactose granules prepared by a top-sprayed fluidized bed granulator. J. Ind. Eng. Chem. 14, 661–666. https://doi.org/10.1016/j.jiec.2008.03.005

Chen, D.T.N., Wen, Q., Janmey, P.A., Crocker, J.C., Yodh, A.G., 2010. Rheology of Soft Materials. Annu. Rev. Condens. Matter Phys. 1, 301–322. https://doi.org/10.1146/annurev-conmatphys-070909-104120

Chetty, D., Gutzmer, J., 2012. REE redistribution during hydrothermal alteration of ores of the Kalahari Manganese Deposit. Ore Geol. Rev. 47, 126–135. https://doi.org/10.1016/j.oregeorev.2011.06.001

Cleary, P.W., Sawley, M.L., 2002. DEM modelling of industrial granular flows: 3D case studies and the effect of particle shape on hopper discharge. Appl. Math. Model. 26, 89–111. https://doi.org/10.1016/S0307-904X(01)00050-6

Cooper, A.R., Eaton, L.E., 1962. Compaction Behavior of Several Ceramic Powders.

Darab, J.G., Linehan, J.C., Matson, D.W., 1994. Effect of Agglomerate Size on the Catalytic Activity of an Iron Oxyhydroxide Nanocrystalline Powder toward Carbon-Carbon Bond Scission in Naphthylbibenzylmethane. Energy Fuels 8, 1004–1005. https://doi.org/10.1021/ef00046a028

Darde, B., Tang, A.M., Pereira, J.-M., Roux, J.-N., Dangla, P., Talandier, J., Vu, M.N., 2018. Hydro-mechanical behaviour of high-density bentonite pellet on partial hydration. Géotechnique Lett. 8, 330–335. https://doi.org/10.1680/jgele.18.00114

Davis, J.M., Behar, J.V., Braddock, J., Durkee, S., Graham, J.A., Hasselblad, V., Jarabek, A., Mage, D., Ott, W., Svendsgaard, D., Wallace, L., 1994. Reevaluation of Inhalation Health Risks Associated With Methylcyclopentadienyl Manganese Tricarbonyl (MMT) in Gasoline (No. 600R94062). U.S. Environmental Protection Agency.

Day, N., n.d. Crystallography Open Database [WWW Document]. Crystallogr. Open Database. URL http://www.crystallography.net/cod/ (accessed 7.9.19).
Debrincat, D.P., Solnordal, C.B., Van Deventer, J.S.J., 2008a. Influence of particle properties on the size of agglomerated metallurgical powders. Int. J. Miner. Process. 87, 17–27. https://doi.org/10.1016/j.minpro.2008.01.003
Debrincat, D.P., Solnordal, C.B., Van Deventer, J.S.J., 2008b. Influence of particle properties on the size of agglomerated metallurgical powders. Int. J. Miner. Process. 87, 17–27. https://doi.org/10.1016/j.minpro.2008.01.003
Dhanalakshmi, K., Ghosal, S., Bhattacharya, S., 2011. Agglomeration of Food Powder and Applications. Crit. Rev. Food Sci. Nutr. 51, 432–441. https://doi.org/10.1080/10408391003646270
Diamond, S., 1956. Surface Areas of Clay Minerals as Derived from Measurements of Glycerol Retention. Clays Clay Miner. 5, 334–347. https://doi.org/10.1346/CCMN.1956.0050128
Dixon, J.B., Weed, S.B., Dinauer, R.C. (Eds.), 1977. Minerals in soil environments. Soil Science Society of America, Madison, Wis.
Dosta, M., Antonyuk, S., Heinrich, S., 2013. Multiscale Simulation of Agglomerate Breakage in Fluidized Beds. Ind. Eng. Chem. Res. 52, 11275–11281. https://doi.org/10.1021/ie400244x
Dražić, S., Sladoje, N., Lindblad, J., 2016. Estimation of Feret's diameter from pixel coverage representation of a shape. Pattern Recognit. Lett. 80, 37–45. https://doi.org/10.1016/j.patrec.2016.04.021
Dubos, J.-L., Orberger, B., Banchet, J., Milazzo, J.-M., Blancher, S.B., Wallmach, T., Lützenkirchen, J., 2021. Binder-free tableting experiments on manganese oxides and industrial mineral powders. Powder Technol. 377, 194–211. https://doi.org/10.1016/j.powtec.2020.08.032
Dubos, J.L., Orberger, B., Milazzo, J.M., Blancher, S.B., Wallmach, T., Lützenkirchen, J., Banchet, J., 2019. Agglomeration potential evaluation of industrial Mn dusts and sludges based on physico-chemical characterization. Powder Technol. https://doi.org/10.1016/j.powtec.2019.10.101
Dutta, G., Bose, D., 2012. Effect of Sintering Temperature on Density, Porosity and Hardness of a Powder Metallurgy Component. Int. J. Emerg. Technol. Adv. Eng. 2.
Eisele, T. C., Kawatra, S.K., 2003. A review of binders in iron ore pelletization. Miner. Process. Extr. Metall. Rev. 24, 1–90. https://doi.org/10.1080/08827500390198190
Eisele, T.C., Kawatra, S.K., 2003. A review of binders in iron ore pelletization. Miner. Process. Extr. Metall. Rev. 24, 1–90.
Eissa, M., Ghali, S., Ahmed, A., El-Faramawy, H., 2012. Optimum condition for smelting high carbon ferromanganese. Ironmak. Steelmak. 39, 419–430. https://doi.org/10.1179/1743281211Y.0000000062
eit.RawMaterials, n.d. Innovation themes. URL https://eitrawmaterials.eu/innovation-themes/ (accessed 6.4.20).
Eramet Norway, 2018. Expertise and growth: Sustainability report 2017 (Annual report). Eramet Norway, Norway.
European Commission, 2020. Circular Economy Action Plan: For a cleaner and more competitive Europe. European Union, Brussels.
Fernández, A.I., Chimenos, J.M., Raventós, N., Miralles, L., Espiell, F., 2003. Stabilization of Electrical Arc Furnace Dust with Low-Grade MgO Prior to Landfill. J. Environ. Eng. 129, 275–279. https://doi.org/10.1061/(ASCE)0733-9372(2003)129:3(275)
Fernández-González, D., Piñuela-Noval, J., Verdeja, L.F., 2018. Iron Ore Agglomeration Technologies, in: Shatokha, V. (Ed.), Iron Ores and Iron Oxide Materials. InTech. https://doi.org/10.5772/intechopen.72546

Furnas, C.C., 1931. Grading Aggregates - I. - Mathematical Relations for Beds of Broken Solids of Maximum Density. Ind. Eng. Chem. 23, 1052–1058. https://doi.org/10.1021/ie50261a017

Gaillac, R., Pullumbi, P., Coudert, F.-X., 2016. ELATE: an open-source online application for analysis and visualization of elastic tensors. J. Phys. Condens. Matter 28, 275201. https://doi.org/10.1088/0953-8984/28/27/275201

Galí, S., Soler, J.M., Proenza, J.A., Lewis, J.F., Cama, J., Tauler, E., 2012. Ni Enrichment and Stability of Al-Free Garnierite Solid-solutions: A Thermodynamic Approach. Clays Clay Miner. 60, 121–135. https://doi.org/10.1346/CCMN.2012.0600203

Garcês Gonçalves, P.R., De Abreu, H.A., Duarte, H.A., 2018. Stability, Structural, and Electronic Properties of Hausmannite (Mn_3O_4) Surfaces and Their Interaction with Water. J. Phys. Chem. C 122, 20841–20849. https://doi.org/10.1021/acs.jpcc.8b06201

Gaudin, A., Ansan, V., Rigaudier, T., 2015. Mineralogical and δ18O–δD isotopic study of kaolinized micaschists at Penestin, Armorican Massif, France: New constraint in the kaolinization process. CATENA 133, 97–106. https://doi.org/10.1016/j.catena.2015.05.006

Gauß, C.F., 1831. "Besprechung des Buchs von L. A. Seeber: Untersuchungen über die Eigenschaften der positiven ternären quadratischen Formen usw" [Discussion of L. A. Seeber's book: Studies on the characteristics of positive ternary quadratic forms etc].

Gensch, M., Weber, A.P., 2017. Rebound behavior of nanoparticle-agglomerates. Adv. Powder Technol. 28, 1930–1942. https://doi.org/10.1016/j.apt.2017.05.003

Gonzalez, S., Windows-Yule, C.R.K., Luding, S., Parker, D.J., Thornton, A.R., 2014. Shaping Segregation: Convexity vs. Concavity. ArXiv14106286 Cond-Mat.

Grim, R.E., 1968. Clay mineralogy, 2nd ed. ed. McGraw-Hill, New York.

Grosshans, H., Papalexandris, M.V., 2017. On the accuracy of the numerical computation of the electrostatic forces between charged particles. Powder Technol. 322, 185–194. https://doi.org/10.1016/j.powtec.2017.09.023

Gul, A., Sirkeci, A.A., BOYLU, F., Guldan, G., Burat, F., 2014. IMPROVEMENT OF MECHANICAL STRENGTH OF IRON ORE PELLETS USING RAW AND ACTIVATED BENTONITES AS BINDERS. Physicochem. Probl. Miner. Process. 51, 23–26. http://dx.doi.org/10.5277/ppmp150203

Gulbinska, M.K. (Ed.), 2014. Lithium-ion Battery Materials and Engineering: Current Topics and Problems from the Manufacturing Perspective, Green Energy and Technology. Springer London, London. https://doi.org/10.1007/978-1-4471-6548-4

Halt, J.A., Kawatra, S.K., 2017. Does the Zeta Potential of an Iron Ore Concentrate Affect the Strength and Dustiness of Unfired and Fired Pellets? Miner. Process. Extr. Metall. Rev. 38, 132–141. https://doi.org/10.1080/08827508.2017.1288114

Halt, J.A., Kawatra, S.K., 2014. Review of organic binders for iron ore concentrate agglomeration. Min. Metall. Explor. 31, 73–94. https://doi.org/10.1007/BF03402417

He, Y., Li, Y.Y., Evans, T.J., Yu, A.B., Yang, R.Y., 2019. Effects of particle characteristics and consolidation pressure on the compaction of non-spherical particles. Miner. Eng. 137, 241–249. https://doi.org/10.1016/j.mineng.2019.04.007

He, Y., Wang, Z., Evans, T.J., Yu, A.B., Yang, R.Y., 2015. DEM study of the mechanical strength of iron ore compacts. Int. J. Miner. Process. 142, 73–81. https://doi.org/10.1016/j.minpro.2015.05.005

Heckel, R.W., 1961a. 1961_Heckel_Al_Density_pressure relationships in powder compaction.pdf.

Heckel, R.W., 1961b. Density-pressure relationship in powder compaction. Trans. Metall. Soc. AIME 221, 5.

Heim, A., Obraniak, A., Gluba, T., 2005. Changes of feed bulk density during drum granulation of bentonite. Physicochem. Probl. Miner. Process. 219–228.
Heim, A., Obraniak, A., Gluba, T., 2004. The effect of equipment and process parameters on torque during disk granulation of bentonite. Physicochem. Probl. Miner. Process. 157–166.
Herting, M., Kleinebudde, P., 2008a. Studies on the reduction of tensile strength of tablets after roll compaction/dry granulation. Eur. J. Pharm. Biopharm. 70, 372–379. https://doi.org/10.1016/j.ejpb.2008.04.003
Herting, M., Kleinebudde, P., 2008b. Studies on the reduction of tensile strength of tablets after roll compaction/dry granulation. Eur. J. Pharm. Biopharm. 70, 372–379. https://doi.org/10.1016/j.ejpb.2008.04.003
Herting, M.G., Kleinebudde, P., 2007. Roll compaction/dry granulation: Effect of raw material particle size on granule and tablet properties. Int. J. Pharm. 338, 110–118. https://doi.org/10.1016/j.ijpharm.2007.01.035
Hertz, H., 1882. Ueber die Berührung fester elastischer Körper. J. Für Reine Angew. Math. Crelles J. 1882, 156–171. https://doi.org/10.1515/crll.1882.92.156
Hooper, R.T., 1968. The production of ferromanganese. JOM 20, 88–92. https://doi.org/10.1007/BF03378712
Horiba, 2020. Zeta Potential: Layout, Calculating, Analysis. Horiba. URL https://www.horiba.com/en_en/zeta-potential/ (accessed 8.12.20).
Hou, J., Li, H., Zhu, H., Wu, L., 2009. Determination of Clay Surface Potential: A More Reliable Approach. Soil Sci. Soc. Am. J. 73, 1658. https://doi.org/10.2136/sssaj2008.0017
Hunter, R.J., 1988. Zeta potential in colloid science: principles and applications, 3. print. ed, Colloid science. Academic Pr, London.
Ilkka, J., Paronen, P., 1993. Prediction of the compression behaviour of powder mixtures by the Heckel equation. Int. J. Pharm. 94, 181–187. https://doi.org/10.1016/0378-5173(93)90022-8
IMnI, 2020. IMnI Annual Review 2019 (Annual review). International Manganese Institute.
International Energy Agency, 2007. World Energy Outlook 2007: China and India Insights, World Energy Outlook. OECD. https://doi.org/10.1787/weo-2007-en
Ji, S., Li, L., Motra, H.B., Wuttke, F., Sun, S., Michibayashi, K., Salisbury, M.H., 2018. Poisson's Ratio and Auxetic Properties of Natural Rocks: Poisson's Ratio and Auxetic Properties of Natural Rocks. J. Geophys. Res. Solid Earth 123, 1161–1185. https://doi.org/10.1002/2017JB014606
Johansen, A., Schæfer, T., 2001. Effects of physical properties of powder particles on binder liquid requirement and agglomerate growth mechanisms in a high shear mixer. Eur. J. Pharm. Sci. 14, 135–147. https://doi.org/10.1016/S0928-0987(01)00164-6
Johansson, B., Alderborn, G., 2001. The effect of shape and porosity on the compression behaviour and tablet forming ability of granular materials formed from microcrystalline cellulose. Eur. J. Pharm. Biopharm. Off. J. Arbeitsgemeinschaft Pharm. Verfahrenstechnik EV 52, 347–357.
Kabata-Pendias, A., Pendias, H., 2001. Trace elements in soils and plants, 3rd ed. ed. CRC Press, Boca Raton, Fla.
Kadiri, M.S., Michrafy, A., Dodds, J.A., 2005. Pharmaceutical powders compaction: Experimental and numerical analysis of the density distribution. Powder Technol. 157, 176–182. https://doi.org/10.1016/j.powtec.2005.05.025
Kanazawa, Y., Kamitani, M., 2006. Rare earth minerals and resources in the world. J. Alloys Compd. 408–412, 1339–1343. https://doi.org/10.1016/j.jallcom.2005.04.033
Karakaya, M.Ç., Karakaya, N., Bakır, S., 2011. Some properties and potential applications of the Na- and Ca-bentonites of ordu (N.E. Turkey). Appl. Clay Sci. 54, 159–165. https://doi.org/10.1016/j.clay.2011.08.003

Karland, O., 2010. Chemical and mineralogical characterization of the bentonite buffer for the acceptance control procedure in a KBS-3 repository.
Kawai, S., Foster, A.S., Björkman, T., Nowakowska, S., Björk, J., Canova, F.F., Gade, L.H., Jung, T.A., Meyer, E., 2016. Van der Waals interactions and the limits of isolated atom models at interfaces. Nat. Commun. 7. https://doi.org/10.1038/ncomms11559
Kawakita, K., Lüdde, K.-H., 1971. Some considerations on powder compression equations. Powder Technol. 4, 61–68. https://doi.org/10.1016/0032-5910(71)80001-3
Kawashima, Y., Cui, F., Takeuchi, H., Niwa, T., Hino, T., Kiuchi, K., 1994. Improvements in flowability and compressibility of pharmaceutical crystals for direct tabletting by spherical crystallization with a two-solvent system. Powder Technol. 78, 151–157. https://doi.org/10.1016/0032-5910(93)02772-3
Kero, I.T., Eidem, P.A., Ma, Y., Indresand, H., Aarhaug, T.A., Grådahl, S., 2019. Airborne Emissions from Mn Ferroalloy Production. JOM 71, 349–365. https://doi.org/10.1007/s11837-018-3165-9
Ketterhagen, W.R., am Ende, M.T., Hancock, B.C., 2009. Process Modeling in the Pharmaceutical Industry using the Discrete Element Method. J. Pharm. Sci. 98, 442–470. https://doi.org/10.1002/jps.21466
Klein, C., Dutrow, B., 2008. Mineral science, John Wiley & Sons. ed.
Komarek, 2020. briquetting machines and compaction, granulation solutions. URL https://komarek.com/ (accessed 6.8.20).
Kopeliovich, D., 2012. Methods of shape forming ceramic powders. Subst. Technol. URL http://www.substech.com/dokuwiki/doku.php?id=methods_of_shape_forming_ceramic_powders&s=compaction (accessed 6.8.20).
Kotzé, I.., 2002. Pilot plant production of ferronickel from nickel oxide ores and dusts in a DC arc furnace. Miner. Eng. 15, 1017–1022. https://doi.org/10.1016/S0892-6875(02)00127-9
Kozhar, S., Dosta, M., Antonyuk, S., Heinrich, S., Bröckel, U., 2015. DEM simulations of amorphous irregular shaped micrometer-sized titania agglomerates at compression. Adv. Powder Technol. 26, 767–777. https://doi.org/10.1016/j.apt.2015.05.005
Kynicky, J., Smith, M.P., Xu, C., 2012. Diversity of Rare Earth Deposits: The Key Example of China. Elements 8, 361–367. https://doi.org/10.2113/gselements.8.5.361
Lastra, R., Paktunc, D., 2016. An estimation of the variability in automated quantitative mineralogy measurements through inter-laboratory testing. Miner. Eng. 95, 138–145. https://doi.org/10.1016/j.mineng.2016.06.025
Leroy, P., Tournassat, C., Bernard, O., Devau, N., Azaroual, M., 2015. The electrophoretic mobility of montmorillonite. Zeta potential and surface conductivity effects. J. Colloid Interface Sci. 451, 21–39. https://doi.org/10.1016/j.jcis.2015.03.047
Li, H., Robertson, D.G.C., 1997. Effect of Moisture, Combined Water, and Volatile Elements on Fixed Carbon Requirement in a Ferro-Manganese Smelting Furnace. Presented at the Electric Furnace Conference Proceedings, The Iron & Steel Society (IOM3), pp. 269–279.
Licciardi, A., Gallagher, K., Clark, S.A., 2020. Estimating uncertainties on net erosion from well-log porosity data. Basin Res. 32, 51–67. https://doi.org/10.1111/bre.12366
Liebman, M., 2000. The treatment and disposal of electric arc furnace dust in North America. Presented at the Proc., Electric Furnace Conf., Iron & Steel Society, Warrendale, PA, 58, 781–792.
Lifshitz, E.M., 1956. The theory of molecular attractive forces between solids.
Linhares, F.M., Victor, C.C.F., Lemos, L.R., Bagatini, M.C., 2019. Effect of three different binders and pellet feed on granulation behaviour of sintering mixtures. Ironmak. Steelmak. 1–7. https://doi.org/10.1080/03019233.2019.1659001
Logan, D.L., 2015. A first course in finite element method, 6th edition. ed. Cengage Learning, Mason, OH.

Louati, H., Oulahna, D., de Ryck, A., 2017a. Effect of the particle size and the liquid content on the shear behaviour of wet granular material. Powder Technol. 315, 398–409. https://doi.org/10.1016/j.powtec.2017.04.030
Louati, H., Oulahna, D., de Ryck, A., 2017b. Effect of the particle size and the liquid content on the shear behaviour of wet granular material. Powder Technol. 315, 398–409. https://doi.org/10.1016/j.powtec.2017.04.030
Lowke, D., Gehlen, C., 2017. The zeta potential of cement and additions in cementitious suspensions with high solid fraction. Cem. Concr. Res. 95, 195–204. https://doi.org/10.1016/j.cemconres.2017.02.016
Lu, G.W., Gao, P., 2010. Emulsions and Microemulsions for Topical and Transdermal Drug Delivery, in: Handbook of Non-Invasive Drug Delivery Systems. Elsevier, pp. 59–94. https://doi.org/10.1016/B978-0-8155-2025-2.10003-4
Lyman, G.J., 2014. Determination of the complete sampling distribution for a particulate material. Proc. Sampl. 2014 17–24.
Mal'tseva, V.E., Vinichuk, B.G., 2016. Methods of Testing Bentonite Clays for Agglomerating Iron-Ore Concentrates. Metallurgist 60, 237–242. https://doi.org/10.1007/s11015-016-0280-0
Manceau, A., Tommaseo, C., Rihs, S., Geoffroy, N., Chateigner, D., Schlegel, M., Tisserand, D., Marcus, M.A., Tamura, N., Chen, Z.-S., 2005. Natural speciation of Mn, Ni, and Zn at the micrometer scale in a clayey paddy soil using X-ray fluorescence, absorption, and diffraction. Geochim. Cosmochim. Acta 69, 4007–4034. https://doi.org/10.1016/j.gca.2005.03.018
Mansa, R.F., Bridson, R.H., Greenwood, R.W., Barker, H., Seville, J.P.K., 2008. Using intelligent software to predict the effects of formulation and processing parameters on roller compaction. Powder Technol. 181, 217–225. https://doi.org/10.1016/j.powtec.2007.02.011
Mars Mineral, 2020. Pelletizing technology. URL https://www.marsmineral.com/ (accessed 6.8.20).
Martin, C.., Bouvard, D., Shima, S., 2003. Study of particle rearrangement during powder compaction by the Discrete Element Method. J. Mech. Phys. Solids 51, 667–693. https://doi.org/10.1016/S0022-5096(02)00101-1
Matusewicz, M., Olin, M., 2019. Comparison of microstructural features of three compacted and water-saturated swelling clays: MX-80 bentonite and Na- and Ca-purified bentonite. Clay Miner. 54, 75–81. https://doi.org/10.1180/clm.2019.1
Maxbauer, D.P., Feinberg, J.M., Fox, D.L., 2016. Magnetic mineral assemblages in soils and paleosols as the basis for paleoprecipitation proxies: A review of magnetic methods and challenges. Earth-Sci. Rev. 155, 28–48. https://doi.org/10.1016/j.earscirev.2016.01.014
Maximenko, A.L., Olevsky, E.A., Shtern, M.B., 2008. Plastic behavior of agglomerated powder. Comput. Mater. Sci. 43, 704–709. https://doi.org/10.1016/j.commatsci.2008.01.011
McGEARY, R.K., 1961. Mechanical Packing of Spherical Particles. J. Am. Ceram. Soc. 44, 513–522. https://doi.org/10.1111/j.1151-2916.1961.tb13716.x
Melhus, M.F., Aranson, I.S., 2012. Effect of vibration on solid-to-liquid transition in small granular systems under shear. Granul. Matter 14, 151–156. https://doi.org/10.1007/s10035-012-0314-7
Mergler, D., Baldwin, M., Bélanger, S., Larribe, F., Beuter, A., Bowler, R., Panisset, M., Edwards, R., de Geoffroy, A., Sassine, M.P., Hudnell, K., 1999. Manganese neurotoxicity, a continuum of dysfunction: results from a community based study. Neurotoxicology 20, 327–342.

Mielniczuk, B., Millet, O., Saïd El Youssoufi, M., 2017. Analysis of capillary bridges using imaging techniques and recent analytical model. Presented at the 35èmes Rencontres Universitaires de Génie Civil, hal-01674600, Nantes, France.

Moore, D.E., Lockner, D.A., 2007. Friction of the smectite clay montmorillonite. Seism. Zone Subduction Thrust Faults 317–345.

Moraes, S.L. de, Lima, J.R.B. de, Ribeiro, T.R., 2018. Iron Ore Pelletizing Process: An Overview, in: Shatokha, V. (Ed.), Iron Ores and Iron Oxide Materials. InTech. https://doi.org/10.5772/intechopen.73164

Mu, F., Su, X., 2007. Analysis of liquid bridge between spherical particles. China Particuology 5, 420–424. https://doi.org/10.1016/j.cpart.2007.04.006

Muurinen, A., 2011. Measurements on Cation Exchange Capacity of Bentonite in the Long-Term Test of Buffer Material (LOT). Posiva Oy, Olkiluoto, Eurojaki, Finland.

Negrão, L.B.A., Costa, M.L. da, Pöllmann, H., 2018. The Belterra Clay on the bauxite deposits of Rondon do Pará, Eastern Amazon. Braz. J. Geol. 48, 473–484. https://doi.org/10.1590/2317-4889201820180128

Nosrati, A., Addai-Mensah, J., Robinson, D.J., 2012. Drum agglomeration behavior of nickel laterite ore: Effect of process variables. Hydrometallurgy 125–126, 90–99. https://doi.org/10.1016/j.hydromet.2012.05.016

Olsen, S.E., Tangstad, M., Lindstad, T., 2007. Production of Manganese Ferroalloys. tapir academic press, Trondheim.

Orberger, B., Wagner, C., Tudryn, A., Baptiste, B., Wirth, R., Morgan, R., Miska, S., 2017. Iron (oxy)hydroxide and hematite micro- to nano-inclusions in diagenetic dolomite from a 2.4 Ga banded iron formation (Minas Gerais, Brazil). Eur. J. Mineral. 29, 971–983. https://doi.org/10.1127/ejm/2017/0029-2679

Ordiales, M., Iglesias, J., Fernández-González, D., Sancho-Gorostiaga, J., Fuentes, A., Verdeja, L., 2016. Cold Agglomeration of Ultrafine Oxidized Dust (UOD) from Ferromanganese and Silicomanganese Industrial Process. Metals 6, 203. https://doi.org/10.3390/met6090203

Orefice, L., Khinast, J.G., 2020. Deformable and breakable DEM particle clusters for modelling compression of plastic and brittle porous materials — Model and structure properties. Powder Technol. 368, 90–104. https://doi.org/10.1016/j.powtec.2020.04.035

Palzer, S., 2011. Agglomeration of pharmaceutical, detergent, chemical and food powders — Similarities and differences of materials and processes. Powder Technol. 206, 2–17. https://doi.org/10.1016/j.powtec.2010.05.006

Pambo, F., 2004. Conditions de formation des carbonates de manganèse protézoïques et analyse minéralogique et géochimique des minerais à bioxydes de manganèse associés dans le gisement de Moanda (Sud-Est, Gabon).

Pan, J., Shi, B., Zhu, D., Mo, Y., 2016. Improving Sintering Performance of Specularite Concentrates by Pre-briquetting Process. ISIJ Int. 56, 777–785. https://doi.org/10.2355/isijinternational.ISIJINT-2015-578

Parker, S.P. (Ed.), 1993. McGraw-Hill encyclopedia of physics, 2nd ed. ed. McGraw-Hill, New York.

Pietsch, W., 2002a. Agglomeration processes: phenomena, technologies, equipment. Wiley-VCH, Weinheim.

Pietsch, W., 2002b. Agglomeration processes: phenomena, technologies, equipment. Wiley-VCH, Weinheim.

Poirier, J., 2014. Vers une nouvelle filière industrielle de recyclage et de valorisation des fines particules minérales. CNRS - Lett. Innov. URL https://www.cnrs.fr/lettre-innovation/actus.php?numero=170 (accessed 2.28.20).

Pokrovsky, O.S., Schott, J., 2004. Experimental study of brucite dissolution and precipitation in aqueous solutions: surface speciation and chemical affinity control. Geochim. Cosmochim. Acta 68, 31–45. https://doi.org/10.1016/S0016-7037(03)00238-2

Potyondy, D.O., Cundall, P.A., 2004. A bonded-particle model for rock. Int. J. Rock Mech. Min. Sci. 41, 1329–1364. https://doi.org/10.1016/j.ijrmms.2004.09.011

Qicpic, n.d. Qicipic shape descriptors [WWW Document]. Sympatec. URL https://www.sympatec.com/en/particle-measurement/glossary/particle-shape/ (accessed 7.8.19).

Quaicoe, I., Nosrati, A., Skinner, W., Addai-Mensah, J., 2013. Agglomeration behaviour and product structure of clay and oxide minerals. Chem. Eng. Sci. 98, 40–50. https://doi.org/10.1016/j.ces.2013.03.034

Rakitskaya, T., Truba, A., Dzhyga, G., Nagaevs'ka, A., Volkova, V., 2018. Water Vapor Adsorption by Some Manganese Oxide Forms. Colloids Interfaces 2, 61. https://doi.org/10.3390/colloids2040061

Revil, A., Jardani, A., Sava, P., Haas, A., 2015. The Seismoelectric Method: Theory and applications. John Wiley & Sons, Ltd, Chichester, UK. https://doi.org/10.1002/9781118660270

Ripke, S.J., Kawatra, S.K., 2000. Can fly-ash extend bentonite binder for iron ore agglomeration? Int. J. Miner. Process. 60, 181–198. https://doi.org/10.1016/S0301-7516(00)00015-6

Rodd, L.E., Scott, T.P., Cooper-White, J.J., McKinley, G.H., 2005. Capillary Break-up Rheometry of Low-Viscosity Elastic Fluids. Appl. Rheol. 15, 12–27. https://doi.org/10.1515/arh-2005-0001

Rondet, E., Cuq, B., Cassan, D., Ruiz, T., 2016. Agglomeration of wheat powders by a novel reverse wet agglomeration process. J. Food Eng. 173, 92–105. https://doi.org/10.1016/j.jfoodeng.2015.10.046

Roqué-Rosell, J., Mosselmans, J.F.W., Proenza, J.A., Labrador, M., Galí, S., Atkinson, K.D., Quinn, P.D., 2010. Sorption of Ni by "lithiophorite–asbolane" intermediates in Moa Bay lateritic deposits, eastern Cuba. Chem. Geol. 275, 9–18. https://doi.org/10.1016/j.chemgeo.2010.04.006

Roskill information services, 2019. Manganese: Outlook to 2029, Fifteenth edition. ed. Roskill.

Rousseau, M., Blancher, S.B., Contessotto, R., Wallmach, T., 2016. BENEFICIATION OF LOW GRADE MANGANESE ORE BY JIGGING IN A SPECIALLY DESIGNED ORE DRESSING UNIT. Presented at the IMPC 2016: XXVIII International Mineral Processing Congress Proceedings, Canadian Institute of Mining, Metallurgy and Petroleum, Québec, Canada.

Sadiq, M., Umrao, R.K., 2020. Nb-Ta-rare earth element mineralization in titaniferous laterite cappings over Sung Valley ultramafic rocks in Meghalaya, India. Ore Geol. Rev. 120, 103439. https://doi.org/10.1016/j.oregeorev.2020.103439

Salles, F., 2006. Hydratation des argiles gonflantes: séquence d'hydratation multi-échelle et détermination des énergies macroscopiques à partir des propriétés microscopiques. Laboratoire de Modélisation des Transferts dans l'Environnement, CEA-Cadarache 13108 Saint Paul lez-Durance - France.

Schoonheydt, R.A., Johnston, C.T., 2011. The surface properties of clay minerals, in: Brigatti, M.F., Mottana, A. (Eds.), Layered Mineral Structures and Their Application in Advanced Technologies. Mineralogical Society of Great Britain and Ireland, London, pp. 335–370. https://doi.org/10.1180/EMU-notes.11.10

Schulze, D., 2008a. Powders and bulk solids: behavior, characterization, storage and flow. Springer, Berlin ; New York.

Schulze, D., 2008b. Powders and bulk solids: behavior, characterization, storage and flow. Springer, Berlin ; New York.

Sermeus, J., Sinha, R., Vanstreels, K., Vereecken, P.M., Glorieux, C., 2014. Determination of elastic properties of a MnO_2 coating by surface acoustic wave velocity dispersion analysis. J. Appl. Phys. 116, 023503. https://doi.org/10.1063/1.4885427

Sezgin, N., Yalçın, A., Köseoğlu, Y., 2016. MnFe2O4 nano spinels as potential sorbent for adsorption of chromium from industrial wastewater. Desalination Water Treat. 57, 16495–16506. https://doi.org/10.1080/19443994.2015.1088808

Shen, Z., Jiang, M., Thornton, C., 2016. DEM simulation of bonded granular material. Part I: Contact model and application to cemented sand. Comput. Geotech. 75, 192–209. https://doi.org/10.1016/j.compgeo.2016.02.007

Shimizu, K., Sokolov, S.V., Compton, R.G., 2016. Agglomeration equilibria of hematite nanoparticles. Colloid Interface Sci. Commun. 13, 19–22. https://doi.org/10.1016/j.colcom.2016.06.003

Shoyama, M., Kawata, T., Yasuda, M., Matsusaka, S., 2018. Particle electrification and levitation in a continuous particle feed and dispersion system with vibration and external electric fields. Adv. Powder Technol. 29, 1960–1967. https://doi.org/10.1016/j.apt.2018.04.022

Skempton, A.W., 1985. Residual strength of clays in landslides, folded strata and the laboratory. Géotechnique 35, 3–18. https://doi.org/10.1680/geot.1985.35.1.3

Sonmez, H., Tuncay, E., Gokceoglu, C., 2004. Models to predict the uniaxial compressive strength and the modulus of elasticity for Ankara Agglomerate. Int. J. Rock Mech. Min. Sci. 41, 717–729. https://doi.org/10.1016/j.ijrmms.2004.01.011

Sonnergaard, J.., 2000. Impact of particle density and initial volume on mathematical compression models. Eur. J. Pharm. Sci. 11, 307–315. https://doi.org/10.1016/S0928-0987(00)00119-6

Spettl, A., Dosta, M., Antonyuk, S., Heinrich, S., Schmidt, V., 2015. Statistical investigation of agglomerate breakage based on combined stochastic microstructure modeling and DEM simulations. Adv. Powder Technol. 26, 1021–1030. https://doi.org/10.1016/j.apt.2015.04.011

Sridharan, A., Rao, S.M., Murthy, N. s., 1986. Compressibility behaviour of homoionized bentonites. Géotechnique 36, 551–564. https://doi.org/10.1680/geot.1986.36.4.551

Stasiak, M., Tomas, J., Molenda, M., Rusinek, R., Mueller, P., 2010. Uniaxial compaction behaviour and elasticity of cohesive powders. Powder Technol. 203, 482–488. https://doi.org/10.1016/j.powtec.2010.06.010

Stellman, J.M., 2000. Encyclopédie de sécurité et de santé au travail. Bureau International du Travail, Genève.

Stewart, R.L., Bradt, R.C., 1995. The Brittle to Ductile Transition In MgAl2O4 Spinel, in: Bradt, R.C., Brookes, C.A., Routbort, J.L. (Eds.), Plastic Deformation of Ceramics. Springer US, Boston, MA, pp. 21–29. https://doi.org/10.1007/978-1-4899-1441-5_2

Suttiponparnit, K., Jiang, J., Sahu, M., Suvachittanont, S., Charinpanitkul, T., Biswas, P., 2010. Role of Surface Area, Primary Particle Size, and Crystal Phase on Titanium Dioxide Nanoparticle Dispersion Properties. Nanoscale Res. Lett. https://doi.org/10.1007/s11671-010-9772-1

Tangstad, M., Olsen, S.E., 1997. Phase relations in ferromanganese slags during melting and reduction. Proc. 5th Int. Conf. Molten Slags Fluxes Salts 549–555.

Tauler, E., Proenza, J.A., Galí, S., Lewis, J.F., Labrador, M., García-Romero, E., Suarez, M., Longo, F., Bloise, G., 2009. Ni-sepiolite-falcondoite in garnierite mineralization from the Falcondo Ni-laterite deposit, Dominican Republic. Clay Miner. 44, 435–454. https://doi.org/10.1180/claymin.2009.044.4.435

Tay, J.Y.S., Kok, B.W.T., Liew, C.V., Heng, P.W.S., 2019. Effects of Particle Surface Roughness on In-Die Flow and Tableting Behavior of Lactose. J. Pharm. Sci. 108, 3011–3019. https://doi.org/10.1016/j.xphs.2019.04.028

Thornton, A., Weinhart, T., Luding, S., Bokhove, O., 2012. MODELING OF PARTICLE SIZE SEGREGATION: CALIBRATION USING THE DISCRETE PARTICLE METHOD. Int. J. Mod. Phys. C 23, 1240014. https://doi.org/10.1142/S0129183112400141

Traoré, D., 2005. Serpentinisation hydrothermale et altération latéritique des roches ultrabasiques en milieu tropical : évolution géochimique et minéralogique de la minéralisation en platine de la rivière des Pirogues (Nouvelle-Calédonie). Université de la Nouvelle-Calédonie.

Tsuji, Y., Tanaka, T., Ishida, T., 1992. Lagrangian numerical simulation of plug flow of cohesionless particles in a horizontal pipe. Powder Technol. 71, 239–250. https://doi.org/10.1016/0032-5910(92)88030-L

Tuck, C., Virta, R., 2015. Minerals yearbook: Iron ore.

Udo, M., Esezobor, D., Apeh, F., Afolalu, A., 2018. Factors Affecting Ballability of Mixture Iron Ore Concentrates and Iron Oxide Bearing Wastes in Metallurgical Processing. J. Ecol. Eng. 19, 235–242. https://doi.org/10.12911/22998993/86158

U.S. Geological Survey, 2020. Mineral Commodity Summaries. U.S. Geological Survey.

Veyera, G.E., 1994. Veyera, G. E. (1994). Uniaxial stress-strain behavior of unsaturated soils at high strain rates (No. WL-TR-93-3523). WRIGHT LAB TYNDALL AFB FL.

Vodyanitskii, Y.N., 2009. Mineralogy and geochemistry of manganese: A review of publications. Eurasian Soil Sci. 42, 1170–1178. https://doi.org/10.1134/S1064229309100123

von Smoluchowski, M., 1903. Contribution to the theory of electro-osmosis and related phenomena. Bull Int Acad Sci Crac. 3, 184–199.

Wallmach, T., 2017. 2017_Wallmach_A QEMSCAN® BASED STUDY ON THREE PARTICLE SIZE FRACTIONS CONTAINING COPPER SULPHIDES AND GANGUE MINERALS.

Wang, S., Shen, L., Maggi, F., El-Zein, A., Nguyen, G.D., 2017. Uniaxial compressive behavior of partially saturated granular media under high strain rates. Int. J. Impact Eng. 102, 156–168. https://doi.org/10.1016/j.ijimpeng.2016.12.018

Webmineral, n.d. Montmorillonite mineral data. URL http://webmineral.com/data/Montmorillonite.shtml#.Xw61N0HgpEY (accessed 7.15.20a).

Webmineral, n.d. Kaolinite mineral data. URL http://webmineral.com/data/Kaolinite.shtml#.Xw70ckHgpEY (accessed 7.15.20b).

Wells, M.A., Ramanaidou, E.R., Verrall, M., Tessarolo, C., 2009. Mineralogy and crystal chemistry of “garnierites” in the Goro lateritic nickel deposit, New Caledonia. Eur. J. Mineral. 21, 467–483. https://doi.org/10.1127/0935-1221/2009/0021-1910

Wollborn, T., Schwed, M.F., Fritsching, U., 2017. Direct tensile tests on particulate agglomerates for the determination of tensile strength and interparticle bond forces. Adv. Powder Technol. 28, 2177–2185. https://doi.org/10.1016/j.apt.2017.05.024

World Health Organization (Ed.), 2000. Air quality guidelines for Europe, 2nd ed. ed, WHO regional publications. World Health Organization, Regional Office for Europe, Copenhagen.

Worldsteel, 2020. Steel data viewer. WorldSteelAssociation. URL https://www.worldsteel.org/steel-by-topic/statistics/steel-data-viewer/C_asu_cse/CHN/IND (accessed 6.5.20).

Wünsch, I., Finke, J., John, E., Juhnke, M., Kwade, A., 2019. A Mathematical Approach to Consider Solid Compressibility in the Compression of Pharmaceutical Powders. Pharmaceutics 11, 121. https://doi.org/10.3390/pharmaceutics11030121

Yang, L., Hu, J., Bai, K., 2016a. Capillary and van der Waals force between microparticles with different sizes in humid air. J. Adhes. Sci. Technol. 30, 566–578. https://doi.org/10.1080/01694243.2015.1111834

Yang, L., Hu, J., Bai, K., 2016b. Capillary and van der Waals force between microparticles with different sizes in humid air. J. Adhes. Sci. Technol. 30, 566–578. https://doi.org/10.1080/01694243.2015.1111834

Yariv, S., Cross, H., 1979. Colloid Geochemistry of Clay Minerals, in: Geochemistry of Colloid Systems. Springer Berlin Heidelberg, Berlin, Heidelberg, pp. 287–333. https://doi.org/10.1007/978-3-642-67041-1_8

Yuksel, A., Cullinan, M., 2016. Modeling of nanoparticle agglomeration and powder bed formation in microscale selective laser sintering systems. Addit. Manuf. 12, 204–215. https://doi.org/10.1016/j.addma.2016.07.002

Zabava, B.-S., Voicu, G., Dinca, M.-N., Ungureanu, N., Ferdes, M., 2018. Durability of pellets obtained from energy plants: review. Presented at the 17th International Scientific Conference Engineering for Rural Development. https://doi.org/10.22616/ERDev2018.17.N419

Zhu, D., Yu, W., Zhou, X., Pan, J., 2014. Strengthening pelletization of manganese ore fines containing high combined water by high pressure roll grinding and optimized temperature elevation system. J. Cent. South Univ. 21, 3485–3491. https://doi.org/10.1007/s11771-014-2326-4

Zhu, X., Zhu, Z., Lei, X., Yan, C., 2016. Defects in structure as the sources of the surface charges of kaolinite. Appl. Clay Sci. 124–125, 127–136. https://doi.org/10.1016/j.clay.2016.01.033

Experimental parameter study on Manganese oxides agglomeration's key factors

J.L. Dubos[1/2,*], J.M. Milazzo[1], S. B. Blancher[1], B. Orberger[2/3], · L.Diaz[1]

1. *Eramet Research, 1 Avenue Albert Einstein, 78190 Trappes-en-Yvelines, France.*
2. *GEOPS, Université Paris Sud-Université Paris Saclay, Bât 504, 91405 Orsay, France*
3. *Catura Geoprojects, 2 rue Marie Davy, 75014 Paris, France*

*(*corresponding author: john-lee.dubos@erametgroup.com)*

Abstract

Fine particles are is one of the most important issues of the mining and metallurgical industry, due to its environmental and technological impacts. Companies cope with these materials through agglomeration, which is necessary to reintroduce them into the processing chain. These agglomerates have to answer to mechanical strength criteria. However, agglomeration trials are still hugely empirical, and there is little, if any, predictability in its success. This paper evaluates the impact of various parameters on agglomeration through a parametric study, using in the first step, four monomineralic samples. The parameters we chose are: the particles mineralogy and shape, the moisture of the sample, and the mean radius ratio of two populations of different grain sizes mixed together.

Those parameters are chosen to fit the operating conditions of medium-pressure agglomeration systems. The moisture content is set to vary from 0 to 20 wt.% by 5% steps. Particle shape is considered either spherical or angular, analyzed from optic granulometry measurements. The mean radius ratio changes between 1 (same particle size) to 0.1 (one population has a radius 10 times smaller than the other). Since the target materials are metallurgical manganese dust, the monomineralic samples were chosen accordingly: (1) pyrolusite (MnO_2) and (2) hausmannite (Mn_3O_4) are the major manganese bearing phases, while (3) montmorillonite (known for its binder capacity in bentonite) and (4) kaolinite assess the importance of a foliated structure, with their other parameters (such as the swelling potential of montmorillonite) differing. The resistance of the agglomerates to their storage, transportation and use in the metallurgical processing chain, is evaluated through drop tests, crushing tests and abrasion tests. A set of agglomerates with various performances will be investigated in more details to define the key parameters of agglomeration.

This paper develops in further details how the parameters giving the best mechanical answers have been recognized and linked with their associated physical explanations, such as the optimal packing density and the ratio of the mean radius. Those parameters will be correlated with the main agglomeration forces (Van der Waals, electrostatic and capillary bridges) in order to explain and optimize the efficiency of the agglomeration processes.

Appendix 12. Abstract presented at the PARTEC 2019 conference in Nürnberg.

Potential of 3D Computed tomography for industrial waste agglomerates

Markus Firsching[1], Julija Lucic[1], Rebecca Wagner[1], Christine Bauer[1], Beate Orberger[2/3], Alexander Ennen[1,] John Lee Dubos[4], Julien Banchet[5], Jean-Michel Milazzo[4]

1. Development Center X-ray Technology EZRT, Fraunhofer Institute for Integrated Circuits IIS, Flugplatzstr. 75, 90768 Fürth, Germany
2. GEOPS Université Paris Saclay, Bât 504, 91405 Orsay, France
3. Catura Geoprojects, 2 rue Marie Davy, 75014 Paris, France
4. ERAMET IDEAS, 1 Avenue Albert Einstein, 78190 Trappes, France
5. EUROTAB GROUP, ZAC des Peyrardes BP 211, 42173 St Just St Rambert, France

Mine and processing wastes often present secondary raw materials. For recycling, these wastes need to be agglomerated prior to reprocessing. Agglomerates must mechanically withstand transport, mechanical loading and introduction into the reactor. X-ray computed tomography (CT) on agglomerates gives information on porosity, density, grain size distribution and fractures, which are important factors deteriorating the agglomerates. We studied binder-free tablets of manganese oxyhydroxide, bentonite, kaolinite and slag powder right after production and after 3 months aging. Visible cracks were analyzed and the distribution of highly absorbing particles was investigated. Further, the iron content in the slag agglomerates could be determined.

Acknowledgment: This study was performed in the frame of the KIC-EIT ANCORELOG project led by DMT, Essen, Germany (Carlos Garcia Pina) and GO40 project led by ERAMET (Jean Michel Milazzo).

Appendix 13. Abstract presented by Markus Firsching at the Smart Mining Denver 2020 conference.

université PARIS-SACLAY

ÉCOLE DOCTORALE
Sciences mécaniques et énergétiques, matériaux et géosciences (SMEMAG)

Titre : Détermination des paramètres contrôlant l'agglomération de poussières de Mn pour améliorer la prédictibilité des procédés

Mots clés : Agglomération, Paramètres, Manganèse, Matériaux granulaires, Caractérisation, Compression uniaxiale

Résumé : Les poussières (<3 mm) générées chaque année par les industries minières et métallurgiques ont un impact économique et écologique conséquent. Le recyclage de ces matériaux par l'agglomération à froid et sans liant est la meilleure option, mais ces procédés manquent de prédictibilité. La présente étude vise à améliorer cette prédictibilité grâce à une meilleure compréhension des phénomènes.
Une caractérisation étendue des propriétés chimiques, physiques et morphologiques a été réalisée sur les matériaux fins généré durant la production d'alliages de ferromanganèse. Une prédiction qualitative a pu être développée selon des considérations théoriques et empiriques.
Des tests de compaction uniaxiale ont été réalisés sur des échantillons de bentonite, kaolinite, minerai enrichi et hausmannite pour tester les hypothèses formulées. Ils ont confirmé l'importance de la présence de matériaux en feuillet et/ou qui se déforment de façon plastique. L'ajout d'humidité et l'accroissement de la pression ont une limite maximale d'efficacité, dépendante du matériau.
Des tests de modélisation DEM préliminaires ont été réalisés pour estimer l'impact des variation du module d'Young et de la force et la taille des liens sur la force des agglomérés et leur comportement à la cassure.

Title : Determination of the controlling parameters of agglomeration of Mn dusts in order to improve process predictability

Keywords : Agglomeration, Parameters, Manganese, Granular material, Characterization, Uniaxial compaction

Abstract : The mining and metallurgical industries produce significant amount of fine materials (<3mm) each year, which bears a high economic and ecological impact. Recycling these materials through cold, binder-free agglomeration is the best course of action, but still lacks predictability. The present study aims increases this predictability through a deeper comprehension of the phenomena.
An extensive characterization of the chemical, physical and morphological characteristics of the fine materials generated along the ferromanganese alloy production process was performed. A qualitative prediction of the agglomeration potential of the material was developed based on theoretical and empirical comparisons.
Agglomeration experiments using uniaxial compaction were performed on bentonite, kaolinite, enriched ore and hausmannite samples to test the hypothesis formulated. They confirmed the importance of the presence of materials with a layered structure (such as clays) and/or that deform plastically. The moisture addition and the pressure increase have an upper limit of efficiency, depending on the material.
Preliminary DEM modelling were performed to assess the impact of the variation of young's modulus, bond strength and bond size on the simulation of the agglomerate strength and breakage style.